"An investigation of the wear resistance of bearing materials for nuclear applications"

by

Ruby McCarron

A thesis submitted to Imperial College London for the degree of Doctor of Philosophy and Diploma of Imperial College (D.I.C)

November 2018

Tribology Group

Department of Mechanical Engineering

Imperial College London

DECLARATION OF AUTHORSHIP

I, Ruby McCarron, declare that this thesis titled, “AN INVESTIGATION OF THE WEAR RESISTANCE OF BEARING MATERIALS FOR NUCLEAR APPLICATIONS” and the work presented in it are my own.

I confirm that:

- This work was done wholly or mainly while in candidature for a research degree at the Imperial College of London.
- Where I have consulted the published work of others, this is always clearly attributed.
- Where I have quoted from the work of others, the source is always given. With the exception of such quotations, this thesis is entirely my own work.
- I have acknowledged all main sources of help.
- Where the thesis is based on work done by myself jointly with others, I have made clear exactly what was done by others and what I have contributed myself.

COPYRIGHT DECLARATION

IMPERIAL COLLEGE LONDON

ABSTRACT

Tribology Group

Department of Engineering

Doctor of Philosophy

INVESTIGATION OF THE WEAR RESISTANCE OF BEARING MATERIALS FOR NUCLEAR APPLICATIONS

by Ruby McCarron

Safety is the most important factor in the design of nuclear reactors. The impact of the high temperature, high pressure, corrosive and radioactive environment of a nuclear reactor core is a significant consideration in the selection of materials for application in it. Such materials must have exceptional mechanical properties, critical to safe and reliable operation of the nuclear reactor.

Cobalt-based alloys offer excellent resistance to wear and chemical corrosion in such environments. Due to their exceptional mechanical properties, they are often applied as bearing surfaces in nuclear applications. However, when cobalt is exposed to the radioactive products of the reactions taking place in the nuclear reactor core, an isotope of cobalt, cobalt-60, is produced. Cobalt-60 is a leading contributor to occupational based radiation exposure of maintenance personnel. The impact of this potentially hazardous behaviour would be reduced by minimising the presence of cobalt in the reactor core. To do this, low cobalt or cobalt-free alloys must be assessed for their suitability to replace the existing cobalt-based alloys currently applied in nuclear power plants.

Any such replacement alloys must exhibit equal to or improved mechanical and corrosion resistant properties by comparison. The main objective of this project was to identify such alloys that have the potential to replace current in-service alloys, specifically Stellite 20[1] and Haynes 25, two cobalt-based alloys conventionally applied in rolling element bearings (REBs) that operate in nuclear reactor cores. The first step taken to achieve this objective was to study and explore the wear resistance and tribological performance of Stellite 20 and Haynes 25, used as rolling and raceway components in the REBs. The sliding wear behaviour of the alloys

---

[1] It should be noted here that Stellite 3 balls are conventionally used as rolling elements (balls) in the rolling element bearings of interest to this project. However, it was not possible to obtain Stellite 3 balls for the experiments conducted. After consultation with Rolls Royce, another cobalt-based Stellite alloy, Stellite 20 was selected for this project. Stellite 20 is also designed as a wear resistant alloy and, given the similarity between the two alloys in terms of composition and mechanical properties, its use was deemed acceptable.

was assessed using a bespoke ball-on-disc tribometer, which was enclosed in an autoclave, designed to simulate the environment of a nuclear reactor core. Results from these experiments set a performance benchmark from which the wear behaviour of any alternative alloy could be compared. The wear behaviour of a cobalt-free, iron based, developmental alloy, RR2450 was assessed using the same tribometer and compared to Stellite 20. The results indicated good wear resistance of RR2450, relative to Stellite 20. However, concerns were highlighted as to the machinability of the alloy.

Experiments conducted in the bespoke tribometer were time intensive and in order to increase time efficiency of the testing programme, a preliminary screening experiment was developed, using a commercially available tribometer that wasn't enclosed in an autoclave. The sliding wear resistance of two potential Haynes 25 replacement alloys, Cronidur 30 and Haynes 230, were also conducted in less extreme conditions than those for experiments conducted in the autoclave. Following these experiments, it was recommended that the wear behaviour of Cronidur 30 should be further assessed in the simulated reactor ball-on-disc set-up. The form of Haynes 230 assessed demonstrated very poor wear resistance and no further assessments were deemed appropriate.

Experimental results were then used to develop two sets of wear prediction models. The first set made use of a semi-analytical methodology and the second applied finite element (FE) methods. Further development of the FE model was also conducted, where an interaction in which a component surface, influenced from both mechanical wear and surface oxidation, was simulated. The growth of oxide layers has been linked, in literature, with reducing the impact of mechanical wear on the surfaces of components made from cobalt-based alloys in the nuclear reactor environment. The objective of this development was to explore and gain an understanding of how the FE wear models could be used to reproduce the working environment and the response of bearings in harsh environments. These environments are complex and tribo-chemical characterisation and tests in them are difficult to conduct, therefore design strategies could be improved by adopting FE simulation techniques.

Acknowledgements

Firstly, I would like to thank my supervisor at Imperial, Professor Daniele Dini for welcoming me into the Tribology Research Group. I am extremely grateful that I had the opportunity to work with such a wonderful group of people for the past four years. I would like to sincerely thank Daniele for his enthusiasm and guidance during my PhD and for giving me this wonderful opportunity.

I would like to thank my industrial sponsors, Rolls Royce plc for making this project possible, particularly Dr David Stewart for his endless enthusiasm for the research topic and his support throughout the project. I would also like to sincerely thank Professor Philip Shipway and Mr Deen Zhang for their collaboration on this project and making the experimental phase possible.

I would like to thank the academic staff in Tribology particularly Dr Marc Masen for his support and time in the final stages of my PhD. I would also like to thank Pawel O. for his help, patience and good humour. I would like to thank Chrissy Stevens for all of the hard work, support and kindness extended to me and all students in the group.

I would like to express my sincere gratitude to the team in the Research Development Workshop, particularly Amit Choda and Phil Wilson. The team were so important in helping me get my experiments done and always did their best to accommodate my requests. I would also like to thank Mark Holloway and Ruth Brooker for their support.

I would like to thank the Tribology Group for being part of a fantastic four years. It has been such a lovely working environment and I feel very lucky to have been surrounded by such an amazing group of researchers and friends. I would like to thank Yilun Xu for his help and sharing of ABAQUS expertise. A special thanks to the four wonderful women who made this experience better than I could have hoped; to Annelise, Elze, Harriet and Zhench – thanks!

I would like to thank all the various Whats App groups for keeping me company and entertained; “Benicaslugs”, “Trivial Pursuits”, “Lar Mash”, “Hummus” and “be Crazy”, particularly. I am so happy and lucky to have so many great friends. I would also like to thank the lovely ladies who I have shared a home with during my PhD, the Round Towers ladies and anyone else who has listened to the highs and lows.

I would like to thank Sam for being a rock of support, patience, fun and kindness, particularly in the past year. You have been great – thank you.

Finally, I would like to thank my family. To Jack and Heidi who are a constant inspiration and two of the most ambitious people I know, thanks. To my parents, Claire and John, for their endless support, patience, presence and most importantly, for the great fun we always have. Thank you both. I could not have gotten through the last four years without the two of you and I am so grateful.

Giorraíonn beirt bóthar

Contents

NOMENCLATURE 5

LIST OF TABLES 6

LIST OF FIGURES 8

Chapter 1 Introduction 13

- 1.1 Project background 14
- 1.2 Aims and objectives 17
- 1.3 Thesis scope 19

Chapter 2 Literature Summary 21

- Introduction 22
- 2.1 Cobalt-based alloys and their applications 22
- 2.2 Properties of cobalt-based alloys 23
- 2.3 Cobalt-based alloys in the nuclear environment / industry 30
- 2.4 Wear 31
  - Introduction 31
  - 2.4.1 Mechanical wear 32
    - 2.4.1.1 Wear resistance of cobalt-based alloys 35
    - 2.4.1.2 Experimentally investigation wear in rolling elements 38
  - 2.4.2 Oxidation 38
- 2.5 Replacing cobalt-based alloys in nuclear reactors 44
  - Introduction 44
  - 2.5.1 Analysis of Haynes 25 and identification of potential low cobalt/cobalt-free replacement 45
  - 2.5.2 Analysis of iron based alloy for Stellite 20 replacement 52
- 2.6 Building a wear prediction model 53
  - Introduction 53
  - 2.6.1 Numerical wear prediction models 56
  - 2.6.2 Semi-analytical wear prediction models 58
  - 2.6.3 Incorporating the impact of corrosion in a wear prediction model 58
  - 2.6.4 Review 59
- 2.7 Conclusion 60

Chapter 3 Sliding wear investigation in a simulated nuclear reactor environment 61

- Introduction 62
- 3.1 Materials and Methods 63
  - 3.1.1 Materials 63
    - 3.1.1.1 Stellite 20 ball and Haynes 25 disc 63
    - 3.1.1.2 RR2450 ball and Haynes 25 disc 65
  - 3.1.2 Methods: Ball on disc sliding wear experiment 66

3.1.3 Post experimental analysis method 68
    3.1.3.1 Friction Measurement 68
    3.1.3.2 Wear measurement 68
    3.1.3.3 Microstructural and compositional analysis 69
3.2 Results and discussion 70
  3.2.1 Friction measurement 70
    3.2.1.1 Stellite 20 ball on Haynes 25 disc 70
    3.2.1.2 RR2450 ball on Haynes 25 disc 71
  3.2.2 Wear measurement 73
    3.2.2.1 Stellite 20 ball on Haynes 25 disc 73
    3.2.2.2 RR2450 ball on Haynes 25 disc 82
    3.2.2.3 Comparison of wear resistance of Stellite 20 and RR2450 against Haynes 25 discs ... 89
  3.2.3 Microstructural and compositional analysis 91
    3.2.3.1 Stellite 20 ball on Haynes 25 disc 91
    3.2.3.2 RR2450 ball on Haynes 25 disc 96
Conclusion 102
Chapter 4 Development of a preliminary screening sliding wear experiment 104
Introduction 105
4.1 Materials and Methods 107
  4.1.1 Materials 107
    4.1.1.1 Stellite 20 ball and Haynes 25 disc 107
    4.1.1.2 RR2450 balls 108
    4.1.1.3 Cronidur 30 discs 108
    4.1.1.4 Haynes 230 discs 109
  4.1.2 Method: Ball-on-disc sliding wear experiment 109
    4.1.2.1 Post experimental analysis method 110
    4.1.2.2 Wear measurement 110
    4.1.2.3 Topographical analysis 111
4.2 Results and discussion 111
  4.2.1 Wear measurement 111
    4.2.1.1 Stellite 20 ball and Haynes 25 disc 111
      Validation of the preliminary screening experiment at ICL 114
    4.2.1.2 RR2450 ball and Haynes 25 disc 114
      Validation of the preliminary screening experiment at ICL 116
    4.2.1.3 Stellite 20 ball and Cronidur 30 disc 117
    4.2.1.4 Stellite 20 ball and Haynes 230 disc 119
    4.2.1.5 Comparing the wear performance of the existing cobalt-based alloys to nominated replacement alloys 120

4.2.1.5.1 Replacing the Stellite 20 balls with RR2450 balls 121
4.2.1.5.2 Replacing Haynes 25 disc with discs made from Cronidur 30 and Haynes 230.. 124
4.2.2 Topographical and image analysis of wear surfaces 128
4.2.2.1 Stellite 20 ball on Haynes 25 disc 128
4.2.2.2 RR2450 ball and Haynes 25 disc 130
4.2.2.3 Stellite 20 ball and Cronidur 30 disc 132
4.3 Preliminary investigation of rolling wear resistance 134
4.3.1 Introduction 134
4.3.2 Design of ball holder to facilitate rolling wear experiments 134
4.3.3 Validation of rolling ball holder 135
4.3.4 Next steps 136
4.4 Conclusion 137
Chapter 5 Sliding wear prediction using semi-analytical and numerical methods 139
Introduction 140
5.1 Methodology 141
5.1.1 Semi-analytical wear model 141
5.1.1.1 Model validation 144
5.1.2 Two dimensional numerical wear prediction model 145
5.1.2.1 Model description 146
(i) Model definition 146
(ii) Boundary conditions and steps 148
(a) FE ball wear prediction model 148
(b) FE disc wear prediction model 149
(iii) Application of mesh and mesh refinement studies 150
(a) Mesh size optimisation study 151
(iv) Solving the contact problem defined 152
(v) Wear calculation by UMESHMOTION 152
(a) UMESHMOTION methodology 153
(b) Simulating increased number of cycles within a single sliding step 155
5.1.2.2 Validation 155
5.2 Results and Discussion 156
5.2.1 Semi-analytical wear model 156
5.2.2 Numerical wear model: 2-D ball and disc models 159
5.2.2.1 Mesh optimisation study 161
5.2.2.1 Wear depth prediction 161
5.3 Further development and future work of the numerical wear model 162
5.3.1 Introduction 162

        5.3.2 Method 163
        5.3.3 Further improvements and need for future development 165
            5.3.3.1 Preliminary results capturing oxide layer formation using FE 165
                (i) Growth only numerical model 165
                (ii) Combined numerical model 166
    5.4 Conclusion 167
Chapter 6 Conclusion 169
    6.1 Summary 170
    6.2 Achievements 173
    6.3 Future work 176
References 178
Appendix A 184
Appendix B 185
Appendix C 187
Appendix D 188
Appendix E 190
Appendix F 191
Appendix G 193
Appendix H 195
Appendix I 197

NOMENCLATURE

PWR = Pressurised water reactor

CRDM= Control rod drive mechanism

REB = Rolling element bearing

ORE = Occupational radiation exposure

RR = Rolls Royce plc

UoN = University of Nottingham

ICL = Imperial College London

SEM = Scanning electron microscope

SE = Secondary electron

BSE = Backscattered electron

XRD = X-ray diffraction

EDX = Energy-dispersive x-ray spectroscopy

HIP = Hot iso-static pressing

COF = Coefficient of friction

FE = Finite element

WLI = White light interferometer

V = Wear volume

H = Hardness

R = Ball radius

d = Ball scar diameter

r = Ball wear scar radius

k = Wear coefficient

F or F_n = Normal load

s = Sliding distance

h = Maximum wear depth

COF = Coefficient of friction

a = contact radius (Hertz contact theory)

E_c = Elastic modulus of the equivalent surfaces

p_{ave} = Average contact pressure

h = Wear depth

x = oxide film thickness

LIST OF TABLES

Table 2.1 Chemical composition of four conventional alloys investigated by Kapoor 25

Table 2.2 Chemical composition of Stellite 20 and Haynes 25 27

Table 2.3 Chemical composition of a selected Stellite alloy for comparison to Stellite 20 28

Table 2.4 Comparing some material properties of stainless steels 46

Table 2.5 Alloys selected as those which are most suitable to replace Haynes 25 of those considered in this review 49

Table 2.6 A comparison of some mechanical properties of Haynes 25 and nominated low cobalt of or cobalt-free alloys 51

Table 2.7 Composition of two iron-based alloys part of research to remove cobalt from nuclear reactor environments 52

Table 3.1 Compositional information for Haynes 25, Stellite 20 and RR2450 components used in this experimental study 66

Table 3.2 Environmental conditions applied in ball-on-disc experiments 68

Table 3.3 Average vessel temperature and pressure recorded during experiments 70

Table 3.4 Results measured on the wear surfaces of Haynes 25 and Stellite 20 discs and balls following sliding wear experiments 73

Table 3.5 Ball and disc component information, wear coefficient calculated using experimental data and Archard's wear equation for the first iteration of experiments conducted at each environmental condition 80

Table 3.6 Results measured on the wear surfaces of Haynes 25 and RR2450 discs and balls following sliding wear experiments 83

Table 3.7 EDX chemical compositional analysis of specific locations on disc wear track and ball wear scar surfaces for areas presented in Figure 3.21 – 3.23 95

Table 3.8 EDX chemical compositional analysis of specific locations on disc wear track and ball wear scar surfaces for areas presented in Figure 3.24 – 3.26 100

Table 4.1 Key to the points highlighted in Figure 4.1 and the corresponding pressures recorded during experimentation 106

Table 4.2	Compositional information for Haynes 25 and Stellite 20 used in this study	108
Table 4.3	Chemical composition of RR2450 balls used in this experimental study	108
Table 4.4	Chemical composition of Cronidur 30	108
Table 4.5	Chemical composition of Haynes 230	109
Table 4.6	Experimental conditions applied	110
Table 4.7	Results measured on Haynes 25 disc and Stellite 20 ball following sliding wear experiments	113
Table 4.8	Results measured on Haynes 25 disc and Stellite 20 ball following sliding wear experiments	116
Table 4.9	Results measured on Cronidur 30 disc and Stellite 20 ball following sliding wear experiments	118
Table 4.10	Results measured on Haynes 230 disc and Stellite 20 ball following sliding wear experiments	120
Table 4.11	Details of rolling element bearing selected using the SKF bearing calculator	135
Table 5.1	Ball and disc components information, wear coefficient calculated with Archard’s wear equation	145
Table 5.2	Dimensions and properties of the pin and disc for each wear model	147
Table 5.3	Boundary conditions defined within the step module of ABAQUS	150
Table 5.4	Amplitude table for the sliding boundary conditions	150
Table 5.5	Test values in mesh size optimisation study for ball and disc wear	151
Table 5.6	Results from mesh size optimisation study for ball wear	161
Table 5.7	Results from mesh optimisation study for disc wear	161

LIST OF FIGURES

Figure 1.1	Schematic of a pressurised water reactor	15
Figure 2.1	Wear volume following sliding wear pin-on-disc experiments conducted by Kapoor (a) at room temperature, (b) at 250°C and (c) 450°C	26
Figure 2.2	SEM microstructure at x500 of CoCrW Stellite alloy [13]	27
Figure 2.3	Microstructure of an undamaged Stellite 20 ball taken using the BSE mode of an SEM	29
Figure 2.4	Factors leading to mechanisms of wear of rolling element bearings that operate in the core of a nuclear reactor	33
Figure 2.5	(a) Effect of temperature on the wear volume and the coefficient of friction and (b) evolution of the coefficient of friction in temperature domain I, II and III	36
Figure 2.6	A schematic diagram presented by Stott et al, Ref [63] that demonstrates the development process of wear debris particle layers and "glaze" layers	37
Figure 2.7	Thickness of an oxide film induced by potential jump experiment on the surface of a Stellite 6 component immersed in an LiOH-solution	44
Figure 2.8	Microstructure of Cronidur 30	47
Figure 2.9	Microstructure of Haynes Alloy 230 in an annealed and quenched form	49
Figure 3.1	Microstructure of an undamaged Stellite 20 ball surface taken using the BSE mode of an SEM	64
Figure 3.2	Microstructure of a Haynes 25 disc cross section taken using an optical microscope	65
Figure 3.3	Microstructure of an undamaged RR2450 ball surface	65
Figure 3.4	Ball on disc tribometer located at the University of Nottingham	67
Figure 3.5	Ball-on-disc tribometer enclosed in autoclave for high temperature experiments	67
Figure 3.6	Micrograph of a scar produced on Stellite 20 ball after sliding experiment and (b) schematic of ball used to describe volume loss calculation	69
Figure 3.7	Example of profile of one of the sections of the disc track used to calculate wear volume	69

Figure 3.8 Coefficient of friction measured for first 30m of sliding between Stellite 20 balls and Haynes 25 discs 71

Figure 3.9 (a) Coefficient of friction measured for first 30m of sliding between RR2450 balls and Haynes 25 discs (b): Repeat experimental results and (c) the average COF at each test condition 72

Figure 3.10 Ball and disc wear scar and track under 10 N ((a) and (b)) and 35 N ((c) and (d)) loads in 20°C experiments (e) represents profile of the disc wear tracks produced under each load 76

Figure 3.11 Ball and disc wear scar and track under 10 N ((a) and (b)) and 35 N ((c) and (d)) loads in 100°C experiments (e) represents profile of the disc wear tracks produced under each load 77

Figure 3.12 Ball and disc wear scar and track under 10 N ((a) and (b)) and 35 N ((c) and (d)) loads in 200°C experiments (e) represents profile of the disc wear tracks produced under each load 78

Figure 3.13 Stellite 20 ball against Haynes 25 disc -total wear volume measured for all experimental conditions: inset showing results for 10 N experiments. Note that the two separate series of tests are reported in the plot using filled and empty bars 81

Figure 3.14 Ball and disc wear scar and track under 10 N ((a) and (b)) and 35 N ((c) and (d)) loads in 20°C experiments (e) represents profile of the disc wear tracks produced under each load 85

Figure 3.15 Ball and disc wear scar and track under 10 N ((a) and (b)) and 35 N ((c) and (d)) loads in 100°C experiments (e) represents profile of the disc wear tracks produced under each load 86

Figure 3.16 Ball and disc wear scar and track under 10 N ((a) and (b)) and 35 N ((c) and (d)) loads in 200°C experiments (e) represents profile of the disc wear tracks produced under each load 87

Figure 3.17 RR2450 ball against Haynes 25 disc - total wear volume measured for all experimental conditions: inset showing results for 10 N experiments 88

Figure 3.18 Pits and crevices observed on clean surface of RR2450 ball 89

Figure 3.19 Wear volume measurement for all experimental components under 10 N loading condition 90

Figure 3.20 Wear volume measurement for all experimental components under 35 N loading condition 91

Figure 3.21	(a) and (b) area within disc wear track and (c) and (d) area within ball wear scar from using SE and BSE modes of the SEM of components tested under 35 N at 20°C	93
Figure 3.22	(a) and (b) area within disc wear track and (c) and (d) area within ball wear scar using SE and BSE modes of the SEM of components tested under 35 N at 100°C	93
Figure 3.23	(a) and (b) area within disc wear track and (c) and (d) area within ball wear scar using SE and BSE modes of the SEM of components tested under 35 N at 200°C	94
Figure 3.24	(a) and (b) area within disc wear track and (c) and (d) area within ball wear scar from using SE and BSE modes of the SEM of components tested under 35 N at 20°C	98
Figure 3.25	(a) and (b) area within disc wear track and (c) and (d) area within ball wear scar from using SE and BSE modes of the SEM of components tested under 35 N at 100°C	98
Figure 3.26	(a) and (b) area within disc wear track and (c) and (d) area within ball wear scar from using SE and BSE modes of the SEM of components tested under 35 N at 200°C	99
Figure 4.1	Phase diagram of water highlighting the experimental temperatures applied using the tribometers at the UoN and ICL	106
Figure 4.2	Anton Paar high temperature tribometer at Imperial College London	110
Figure 4.3	Stellite 20 ball against Haynes 25 disc -total wear volume measured for both experimental conditions. Note that the two separate series of tests are reported in the plot using filled and empty bars.	112
Figure 4.4	Wear volume produced on Stellite 20 ball and Haynes 25 disc following experiments conducted at ICL and UoN under a 10 N load at (a): 20°C and (b) 80°C	114
Figure 4.5	Wear volume produced on RR2450 ball against Haynes 25 disc following sliding wear experiments at ICL	115
Figure 4.6	Wear volume produced on RR2450 ball and Haynes 25 disc following experiments conducted at ICL and UoN under a 10 N load at (a): 20°C and (b) 80°C	116
Figure 4.7	Wear volume produced on Stellite 20 ball against Cronidur 30 disc following sliding wear experiments at ICL	117

Figure 4.8 Wear volume produced on Stellite 20 ball against Haynes 230 disc following sliding wear experiments at ICL 119

Figure 4.9 Comparing the wear volume produced on experimental components sliding Stellite 20 and RR2450 balls respectively against Haynes 25 discs at room temperature 121

Figure 4.10 Comparing the wear volume produced on experimental components sliding Stellite 20 and RR2450 balls respectively against Haynes 25 discs at 80°C 121

Figure 4.11 Ball scar, disc track and disc track profiles produced under a normal load of 10 N at room temperature 122

Figure 4.12 Ball scar, disc track and disc track profiles produced under a normal load of 10 N at 80°C 123

Figure 4.13 Comparing the wear volume produced on experimental components with a Stellite 20 ball against Haynes 25, Cronidur 30 and Haynes 230 discs respectively at room temperature 124

Figure 4.14 Comparing the wear volume produced on experimental components with a Stellite 20 ball against Haynes 25 and Cronidur 30 discs respectively at 80°C 125

Figure 4.15 Ball scar, disc track and disc track profiles produced under a normal load of 10 N at room temperature 126

Figure 4.16 Ball scar, disc track and disc track profiles produced under a normal load of 10 N at 80°C 127

Figure 4.17 (a) and (b) area within disc wear track and (c) and (d) area within ball wear scar from using SE and BSE modes of the SEM of components tested under 35 N at 20°C 128

Figure 4.18 (a) and (b) area within disc wear track and (c) and (d) area within ball wear scar from using SE and BSE modes of the SEM of components tested under 35 N at 80°C 129

Figure 4.19 (a) and (b) area within disc wear track and (c) and (d) area within ball wear scar using SE and BSE modes of the SEM of components tested under 35 N load at 20°C 130

Figure 4.20 (a) and (b) area within disc wear track and (c) and (d) area within ball wear scar using SE and BSE modes of the SEM of components tested under 35 N load at 80°C 131

Figure 4.21 (a) and (b) area within disc wear track and (c) and (d) area within ball wear scar from using SE and BSE modes of the SEM of components tested under 35 N at 20°C 132

Figure 4.22 (a) and (b) area within disc wear track and (c) and (d) area within ball wear scar from using SE and BSE modes of the SEM of components tested under 35 N at 80°C 133

Figure 4.23 Anton Paar High Temperature Tribometer with custom rolling ball holder, image of ball holder inset 140

Figure 4.24 Comparison of the coefficient of friction recorded for rolling and sliding tests used to validate the rolling ball holder 136

Figure 5.1	(a) and (b) A point contact and a line contact for two elastic bodies and the resultant contact pressure distribution based on Hertz contact theory	142
Figure 5.2	Schematic of ball demonstrating how the development of the contact area and thus the ball scar geometry was calculated	144
Figure 5.3	(a) Assembly module in ABAQUS CAE; model definition of deformable ball and rigid disc (b) Assembly module in ABAQUS CAE; model definition of deformable disc and rigid ball	147
Figure 5.4	Demonstrating boundary conditions applied to ball constraining movement	148
Figure 5.5	Demonstrating boundary conditions applied to disc constraining movement	149
Figure 5.6	(a) Mesh applied to deformable ball (b) Mesh applied to deformable disc	152
Figure 5.7	Data recorded by UMESHMOTION using data produced in ABAQUS	154
Figure 5.8	Schematic demonstrating material removal from disc surface	155
Figure 5.9	(a) – (f): Results from the wear depth computed by the semi-analytical model are compared to the experimental results	157
Figure 5.10	(a) – (f): Experimental disc width and ball scar diameter comparison with results from semi-analytical wear prediction model at all experimental conditions	158
Figure 5.11	(a) and (b): Initial and final contact pressure over a contact length for the ball and disc wear models	159
Figure 5.12	Von Mises stress distribution in the fully elastic ball, changing as the contact pressure changes as a result of wear	160
Figure 5.13	Comparison between the wear depth calculated for (a) the ball and (b) the disc over the sliding cycles completed using semi-analytical and FE methods	162
Figure 5.14	Data extracted from Figure 2.4 with permission of the authors demonstrating the growth of an oxide layer over time	164
Figure 5.15	FE simulation of oxide layer growth on disc surface using data presented by Benea et al	166
Figure 5.16	Comparing the wear depth of a model that simulated wear only and a model that combined the impact oxidation during latent periods with wear	167

Chapter 1 Introduction

Chapter 1 Introduction

1.1 Project background

Safety is the most important feature in the design of nuclear reactors. Operation of the high temperature, high pressure, and radioactive environment has potential safety risks associated that could impact both people working on site and the general public. To minimise risks associated with the operation of nuclear reactors, much focus is placed on the reliability and performance of all components operating within the nuclear reactor vessel (core). An important part of the design process is the selection of materials for application within the reactor vessel. Any materials selected for application must be capable of safely operating in the high temperature, high pressure, and radioactive environment.

Figure 1.1 presents a schematic of a pressurised water reactor (PWR), a type of nuclear reactor. There are two important circuits in the PWR, the primary and secondary circuits, identified in the schematic. Pressurised water circulates around the primary circuit in the direction indicated by arrows in the Figure 1.1. Nuclear reactions taking place within the primary circuit, in the nuclear reactor vessel, are exothermic, heating the primary water. The rate of reactions is controlled by the movement of control rods in the reactor vessel. All moving parts in the system are lubricated by the water circulating. The water is pressurised and therefore does not boil and evaporate when heated. The pressure and temperature within the primary circuit are approximately 12 MPa and 310°C [1]. As the pressurised water leaves the reactor vessel and moves into the steam generator, heat is exchanged from the primary water to the secondary circuit within which secondary water circulates. As a result, the primary water cools down and the temperature of the secondary water rises. The secondary water boils and the steam produced drives a turbine and generator, generating power. The steam is condensed back to water by the condenser and the circuit is complete.

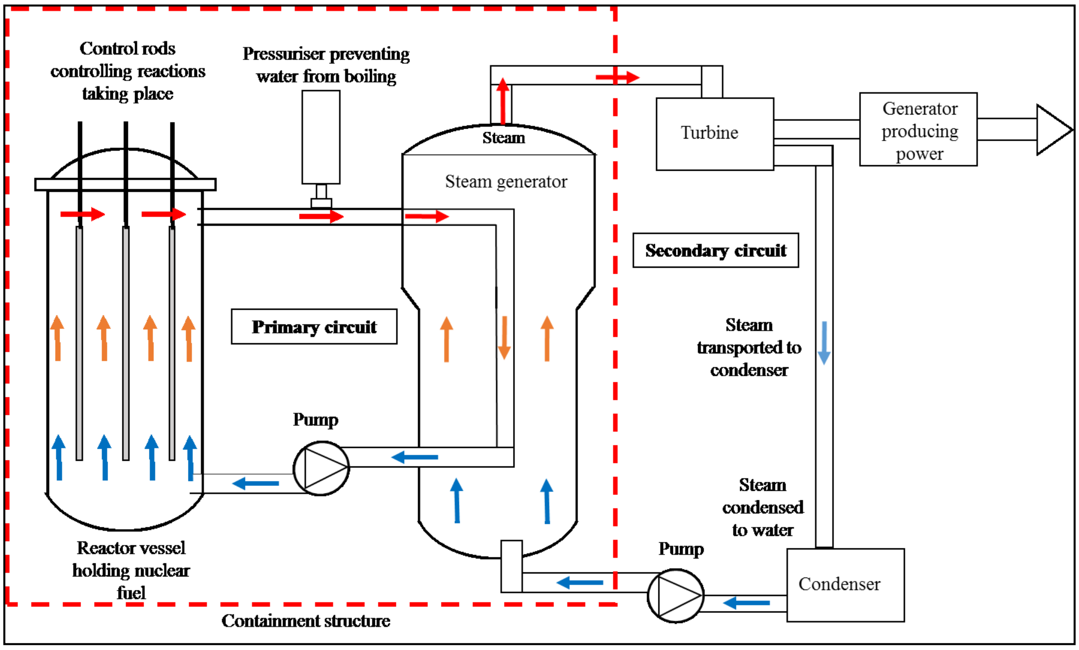

Figure 1.1: Schematic of a pressurised water reactor

A method of incorporating safety in the design of a nuclear reactor relies on simplification of the system design [2]. Various moving components lubricated by the water in the primary circuit facilitate safe and reliable power generation, for example, components facilitating movement of the control rods. A system presented by Ishida and co-workers uses a ‘control rod drive mechanism’ (CRDM) to operate the control rods, which controls the rate of nuclear reactions taking place [1]. The CRDM may be used in marine type nuclear reactor vessels with relatively low energy outputs as well as in typical PWR systems such as that depicted in Figure 1.1. Rolling element bearings (REBs) are used in this CRDM, lubricated by the primary water and facilitate movement by the mechanism. Cobalt-based alloys are used to manufacture such components due to their excellent wear and corrosion resistance and their high hardness in the high pressure, high temperature, water facing environment. These attributes are essential to all materials applied in reactors as any failures in the system could be fatal.

In spite of this, cobalt exhibits unfavourable behaviour in the radioactive environment. When the stable form of cobalt, cobalt-59, is exposed to the products of the nuclear reactions taking place in the reactor vessel, a radioactive isotope of cobalt, cobalt-60 is produced. Cobalt-60 is a highly penetrative isotope with a long half-life of 5.3 years, relative to other elements used in alloys applied in nuclear reactors [3]. Exposure to cobalt-60 is a leading contributor to occupational radiation exposure (ORE) of maintenance personnel during shutdown periods [4]. Wear debris is produced by mechanical interactions taking place in the reactor vessel, some of which consists of this radioactive isotope. The debris becomes suspended in the primary water, transported around the circuit and deposited at various random locations, causing ORE. As a result of this exposure, there is a regulatory and therefore an industry drive to reduce or if possible remove cobalt-based components from the system, removing the risk of ORE to maintenance personnel.

Two cobalt-based alloys, used to manufacture the rolling and race elements of these REBs, are Stellite 20[1] and Haynes 25. In the variable reactor environment, the REBs are exposed to slip, abrasive particle damage or system vibrations causing wear mechanisms that may include sliding, fretting or a combination of mechanisms. These mechanical interactions result in the production of wear debris which, as previously mentioned, may contain the radioactive isotope, cobalt-60. The wear and corrosion behaviour of each alloy should be well understood in order to identify suitable replacement alloy(s). Any cobalt-free or low cobalt alloy nominated to replace either Stellite 20 or Haynes 25 should exhibit equal to or improved relative performance in the relevant environmental conditions.

The wear behaviour of alloys is commonly evaluated by measuring the weight or volume of material loss of components following a wear inducing interaction such as a ball-on-disc sliding wear experiment. Friction related data recorded during such experiments as well as topographical and compositional investigations of post-experimental component surfaces are also used to assess alloy wear behaviour. Understanding the wear behaviour of alloys in an interaction inducing wear, such as sliding, may also be approached using predictive wear models i.e. computational models simulating the wear interactions based on experimental parameters. As wear is an important factor which influences components and product service life, the prediction of wear should have a significant role to play in engineering and material selection [5].

Cobalt-based alloys are used to manufacture structural components for application in nuclear reactors due to their excellent mechanical and corrosion resistant properties. In the radioactive environment, however, they become a safety problem when a radioactive isotope of cobalt is produced exposing maintenance personnel to radiation. The solution to this problem is the reduction or if possible, removal of cobalt from the system, replacing the cobalt-based alloys with alternative alloys with equal to or improved mechanical and corrosion resistant properties, especially wear resistance, in the high temperature, high pressure, water lubricated and radioactive environment. Material selection in the design of a nuclear reactor is critical to safe and reliable operation.

1.2 Aims and objectives

The main objective of this PhD project was to identify such cobalt-free or low cobalt alloys that could replace Stellite 20 or Haynes 25 as the rolling or race elements in the REBs. Assessing the wear behaviour of Stellite 20 and Haynes 25 was an important part of this project as the assessment could be used to set the performance benchmark from which any replacement alloys nominated could be compared.

The experimental work conducted in order to achieve this objective was approached using two different experimental set ups. Firstly, a bespoke ball-on-disc tribometer designed to simulate the environment of a nuclear reactor, located at the University of Nottingham (UoN), was used to conduct sliding wear water lubricated experiments. The tribometer was enclosed in an autoclave which facilitated water lubricated experiments above 100°C. The first cobalt-free alloy investigated using the tribometer at the UoN was RR2450, an iron-based developmental alloy. The alloy was nominated by Rolls Royce plc (RR) as an alloy with the potential to replace Stellite 20 in the rolling element of the REBs having demonstrated relatively good mechanical and corrosion resistant properties in earlier studies.

Conducting experiments in the simulated nuclear reactor environment was time intensive and a preliminary screening experiment was subsequently developed using a tribometer at Imperial College London (ICL). The aim of the preliminary screening experiments was to reduce the volume of the more time intensive experiments conducted in the simulated nuclear reactor environment. The maximum load available using the tribometer for the preliminary screening experiments was 10 N, compared to the upper loading condition available using the tribometer set in the simulated reactor conditions, of 35 N. Preliminary screening experiments could not be enclosed in an autoclave and the temperature of water lubricated experiments was limited to 80°C to prevent evaporation of the water. Any alloys that exhibited sliding wear resistance equal to or better than either Stellite 20 or Haynes 25 in these more limited experimental conditions, would be put forward for further assessment in the more environmentally appropriate tribometer at the UoN. Neither tribometer used to assess the sliding wear behaviour of alloys for the purpose of this project had the capability to conduct rolling wear experiments. A modification to the existing tribometer(s) that would facilitate rolling wear experiments would benefit this work as increased understanding of rolling wear is a relevant part of understanding the wear behaviour of the REBs.

The third section of this project involved the development of wear prediction models using an efficient semi-analytical method and a more versatile but less efficient numerical model using finite element methods. Wear prediction models are useful tools with the potential of reducing the need for complicated and expensive environmentally appropriate material and component validation rigs.

The contribution made by this project is described below;

- The sliding wear behaviour of Stellite 20 and Haynes 25 was investigated using the bespoke ball-on-disc tribometer, designed to simulate the environment of a nuclear reactor. The wear performance of the post experimental components was measured and examined and the impact that different experimental conditions had on the performance of the alloys was compared. The results were used to set a performance benchmark from which any cobalt-free or low cobalt alloys could be compared.
- The Stellite 20 balls were then replaced with RR2450 balls and all experimental conditions were replicated. Results were compared to the performance benchmark set by the Stellite 20-Haynes 25 ball-on-disc experiments. The results were used to make a recommendation for or against further assessment of RR2450 as a cobalt-free, wear resistant alloy to replace Stellite 20 in the rolling element of the REBs.
- A preliminary screening experiment was set up using a tribometer at ICL to assess the suitability of any further cobalt-free or low cobalt alloys nominated to replace Stellite 20 or Haynes 25 in the REBs. Sliding wear experiments were conducted with Stellite 20-Haynes 25 and RR2450-Haynes 25 balls and discs in order to validate the experiment, comparing the results to those produced using the tribometer located at the UoN. Any alloys that exhibited equal to or better wear resistance than the Stellite 20-Haynes 25 alloy combination should be investigated further in the simulated nuclear reactor environment.
- In a review of literature, a cobalt-free and low cobalt alloy, Cronidur 30 and Haynes 230, were identified as suitable alternatives alloys to Haynes 25 due to characteristic mechanical and corrosion resistant properties. The wear resistance of each alloy was investigated using the preliminary screening experiment at room temperature and 80°C under a load of 10 N. The results were used to recommend whether or not the wear behaviour of the alloys should be investigated further in the simulated nuclear reactor environment.
- Rolling wear is of interest in this project as Stellite 20 and Haynes 25 are used in rolling element bearings in the nuclear reactor core. The current set up of both tribometers used in this project facilitate sliding wear experiments only. A ball holder that facilitates rolling

wear tests was designed and made. Preliminary tests were conducted to verify that rolling wear experiments are now possible using the tribometer at ICL.

- Experimental data measured and literature available on the development and application of predictive wear models were used to develop two wear prediction models. A relatively simple, semi-analytical model was developed to predict wear depth on the ball and disc components using the description and implementation procedure presented by Hegadekatte and co-workers [6, 7]. Data measured on post experimental balls and discs was used to validate the model.
- Using the commercial finite element software ABAQUS, numerical wear prediction models were also developed. The basis of wear prediction was similar to that employed in the semi analytical model developed, however, using ABAQUS, a better understanding of stress distribution in the component(s) was possible. It is also possible to use the numerical model to understand other aspects of the interaction such as material plasticity, oxidation of surfaces or thermo-mechanical interaction. The numerical model simulating disc wear was further developed to incorporate the growth of an oxide film on the disc surface. The purpose of this model was to demonstrate the versatility of using ABAQUS to simulate the behaviour of components in the nuclear reactor environment.

1.3 Thesis scope

The structure of this thesis is as follows;

Chapter 2 presents a comprehensive review of literature relevant to the main aspects of this project. Literature covering the application of cobalt-based alloys in nuclear reactor conditions, mechanisms leading to wear of components, the role of oxidation in the wear of cobalt-based alloys and the development of wear prediction models was included.

Chapter 3 describes sliding wear experiments conducted as part of this PhD project using the bespoke ball-on-disc tribometer designed to simulate nuclear reactor conditions. The results from two sets of sliding wear experiments were presented; using Stellite 20-Haynes 25 and RR2450-Haynes 25 balls and discs, over a range of environmental conditions. The results were compared and the suitability of RR2450 as an alloy with the potential to replace Stellite 3 in the rolling element of the REBs was discussed.

Chapter 4 presents results of sliding wear experiments conducted using the preliminary screening experiment. The results from the experiments conducted to validate the tribometer for use as a preliminary screening experiment were presented. Results from two sets of sliding wear experiments that replaced Haynes 25 with Cronidur 30 and then Haynes 230 as the disc alloy are then presented and compared to the Stellite 20-Haynes 25 experimental results. A modification to the tribometer facilitating rolling wear was also presented.

Chapter 5 describes the development of wear depth prediction models using experimental data. The models are validated using experimental data and further development of the numerical model to include the growth of an oxide glaze on component surfaces is presented.

Chapter 6 discusses the conclusions of the present work including further recommendations for future work.

Chapter 2 Literature Summary

Chapter 2 Literature Summary

Introduction

The intent of the following literature review is to provide a comprehensive summary of topics associated with this PhD thesis. A general introduction to cobalt-based alloys is given as well as their relevance to the research question posed. To understand the mechanical and electrochemical behaviour of cobalt-based alloys in a nuclear reactor environment a survey of relevant literature is included, encompassing experimental and computer aided simulation approaches. The replacement of cobalt-based alloys in nuclear reactors is not a new or unique area of research. A wealth of literature is available identifying the problematic behaviour of these alloys in the environment encountered in the prototypical application, with possible solutions investigated and used as a developmental point.

2.1 Cobalt-based alloys and their applications

Until the early 1900s, cutting tools were mainly carbon or tungsten tool steels, the latter used in high speed cutting applications. In the first decade of the twentieth century, Stellites, a new group of chromium–cobalt alloys, were developed by Elwood Haynes [8-10] as an alternative to these existing cutting steels. The superior properties of the Stellites, such as an increase in hardness and resistance to corrosion and oxidation, allowed lathes to operate three times faster than existing high grade steels [8]. These improvements resulted in an increase in popularity of the alloys with the dramatic increase in manufacturing demand caused by WWI. An advantage of using the alloys was that the use of heat treatment was not required owing to their 'inherent hardness'. The alloys could be ground using a normal grinding wheel, an attribute that meant they were not replaced by tungsten carbides when they were initially introduced in the late 1920s [8]. By the early 1920s, the Stellites were in widespread use in the oil well drilling industry.

In the 1930s, their excellent corrosion resistance, endorsed by the addition of molybdenum, was exploited in the dental prosthetic field with the alloy Vitallium [11, 12]. This corrosion resistance, combined with galling and wear resistance has seen ongoing application of cobalt-based alloys in the biomedical implant industry [8]. Derived from Vitallium, the alloy HS-21 was applied in gas turbines in the 1940s with a wrought derivative, S816 used in the blades and vanes of gas turbines [11]. Rolls Royce made use of such alloys in the 1940s in their aerospace division as did the United States aerospace industry [8].

Whilst they have been superseded in some applications by superior or more cost efficient materials, cobalt-based alloys are still used in high temperature applications where corrosion and wear resistance are important [8, 13]. The primary loop of a nuclear reactor core with coolant water circulating is an example of this harsh environment. The excellent high temperature, corrosion and wear resistant behaviour of the cobalt-based alloys has led to their use in some structural components in the reactor core, for example in bearing applications.

2.2 Properties of cobalt-based alloys

The mechanical wear and corrosion resistance of these alloys and their behaviour in the nuclear environment are properties considered to gain an understanding of how they behave in service [3]. The chemical composition, microstructures and manufacturing processes are the significant factors influencing the mechanical properties of Stellite alloys and other cobalt-based alloys [14, 15].

Stellites are generally categorised as cobalt chromium tungsten (CoCrW) or cobalt chromium molybdenum (CoCrMo) systems. The relative carbon content of the Stellites is that which tends to classify them and ranges from 0.1 to 3.2% [10, 16]. Dispersion strengthening by the formation of carbides is made possible by the presence of carbon [17]. These binary compounds are denoted as M_xC_y where M refers to the metallic element(s) forming them. The carbides are the most significant strengthening agents of the alloys. They may, however, have a deleterious impact on alloy ductility [17]. A notable difference between cobalt-based alloys, the carbon content will impact the carbide volume fraction within the microstructure [13, 16], typically lying between 10 and 20% volume [17]. The types of carbides that precipitate in the cobalt-based alloys are $M_{23}C_6$, M_6C , M_7C_3 , MC and M_2C [17].

Stellites with a relatively high carbon content (>1.2 %wt) are used in applications requiring wear resistance, with the low carbon Stellites (<0.35 %wt) selected for applications requiring wear and/or corrosion resistance [13]. In industrial applications, the most significant resistance to wear is observed in alloys with the maximum volume of the hardest carbides that may be supported in the matrix [8]. In general, cobalt-based alloys will be produced in the form of castings, cast rod, powder or powder metallurgy parts [10]. The manufacturing process employed to produce components from the cobalt-based alloys will also be influenced by the carbon content. Below 1.3% carbon content, parts may be wrought. Alloys that have been wrought or cast will contain at least one of the carbide types that has been listed [17]. In the alloy manufacturing process, primary carbides will form during solidification of the molten metal. Secondary carbides, however, will precipitate in the microstructure from the solid solution. Such precipitates positively influence the hot hardness, wear resistance and high temperature creep strength of the alloys [17]. Liu and co-workers [13] relate the wear response of the Stellite alloys to their microstructure and the phases present within it. The composition of the alloys and the balance between constituent elements influents the microstructure, for example, the carbide volume fraction or the presence of intermetallics [6]. Such a balance can be induced or refined in order to produce specific alloy characteristics. Intermetallics, for example, are commonly induced in alloys like the Stellites to increase wear resistance [6]. Another factor that is attributed with contributing to the wear resistance of Stellites is work hardening, which is achieved through the application of a strain induced mechanism [18]. To achieve this, the alloy needs to have a low stacking fault energy and consequently a face-centred-cubic matrix, contributing to the wear resistant characteristics of the alloy [18].

The advent of wrought cobalt-based alloys was in the 1950s with application in forged turbine blades, combustor liners and afterburner tail-pipes [9]. Although nickel-based alloys have since ‘overshadowed’ their use, properties such as wear and hot corrosion resistance, high temperature creep and fatigue strengths have sustained their use across some niche applications, including bearing materials in nuclear reactor applications and some biomedical implant applications [9].

In a review of several Stellite forms, with varying carbon contents from relatively low to high, Liu and co-workers [13] analysed the alloy microstructures by means of SEM and XRD analysis. The data was used to evaluate the relative compositions and identify the phases present. The general microstructure of Stellite alloys is formed of hard carbides, suspended in a tough and ductile matrix [4]. The distribution of these carbides within the cobalt rich matrix as well as their shape and size is dependent on the processing conditions applied [19]. The size and volume fraction and morphology of carbides influences the wear properties; for example, relatively coarse M_7C_3 carbides are related to an increase in component weight loss, i.e. wear [10, 14]. The carbides formed contribute to the room temperature hardness while high temperature hardness is attributed to the matrix [12, 20]. The ‘non-oxidation’ condition of carbides is also credited with further enhancing the corrosion resistance of the alloys [21]. Low presence of tungsten reduces the hardness and increases the toughness of the alloy and vice versa [3]. Tungsten, along with molybdenum promotes solid solution strengthening in cobalt-based alloys [14, 22].

Table 2.1 presents the chemical compositions of four Stellite alloys that were investigated by Kapoor [64]. The four alloys listed are in widespread use in industrial applications where resistance to mechanical wear and corrosion is important. Kapoor's thesis demonstrated the impact these compositions had on the sliding wear behaviour of the alloys for a range of temperatures. The thesis also demonstrated the impact of the compositions on the microstructure of the alloys even though they are from the same family of alloys. The volume fraction of carbides in Stellite 3 for example, was high, relative to the same for Stellite 21, attributed to the difference in %wt carbon in each alloy. This difference was further highlighted following sliding wear experiments conducted, see Figure 2.1. The wear behaviour of cobalt-based alloys will be discussed further in Section 2.4.

Table 2.1: Chemical composition of four conventional alloys investigated by Kapoor [64]

Key	**%wt**	**Co**	**Ni**	**Cr**	**W**	**Fe**	**Mn**	**Si**	**C**	**Mo**
Alloy A	Stellite 3*	Balance	3.5	31.5	12.5	5	2	2	2.4	0
Alloy B	Stellite 6	Balance	3	29	4.5	3	0.5	0.75	1.2	1.5
Alloy C	Stellite 12	Balance	1.5	30	8.3	3	2.5	0.7	1.4	0
Alloy D	Stellite 21	Balance	2.75	27	0	3	1	1	0.24	5.5

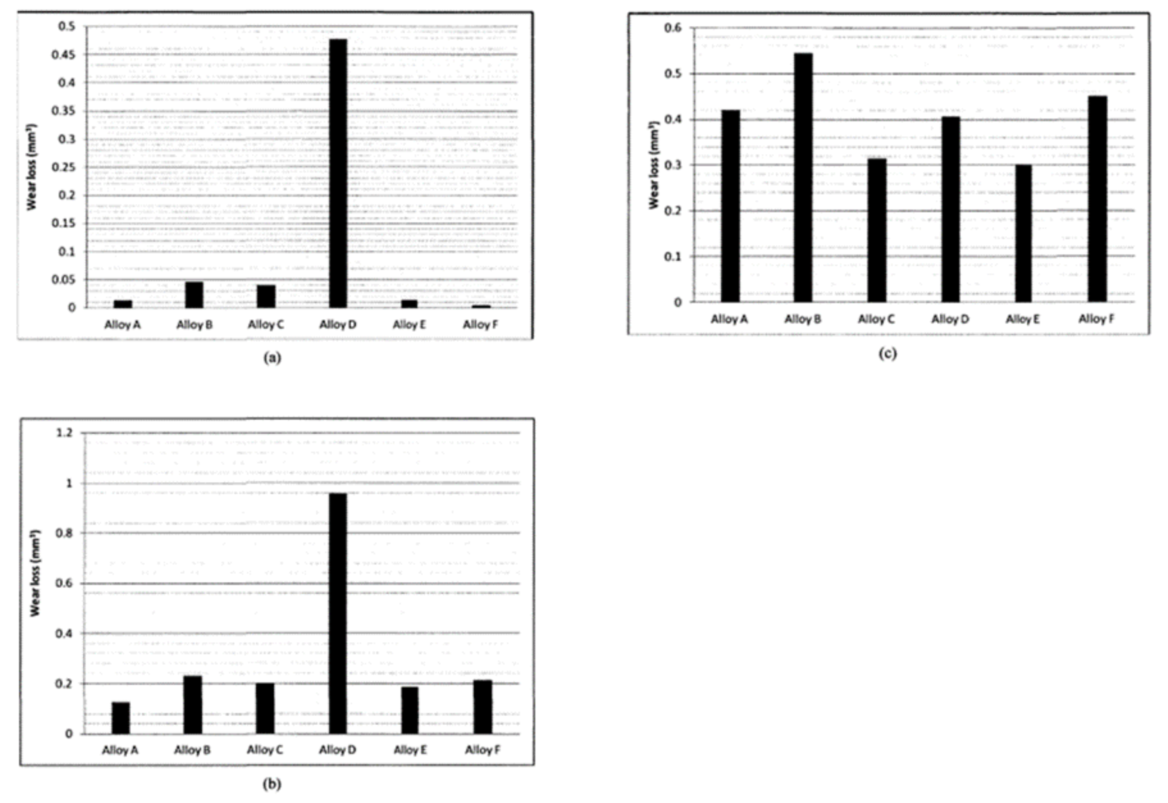

Figure 2.1: Wear volume following sliding wear pin-on-disc experiments conducted by Kapoor (a) at room temperature, (b) at 250°C and (c) 450°C [65]

Due to their excellent wear resistance and corrosion resistance for a range of temperatures and environmental conditions, Stellite 3 and Stellite 6 are two alloys that are found in a range of nuclear reactor applications and as such, literature discussing either of these alloys is relevant for the purpose of understanding the wear behaviour of cobalt-based alloys in prototypical nuclear reactor applications.

Stellite 3 and Haynes 25 are two cobalt-based alloys applied in bearing applications that operate in the nuclear reactor core. It was not possible to obtain Stellite 3 balls for the experiments conducted as part of this PhD thesis. Stellite 20 is an alloy that is very similar to Stellite 3 in terms of composition and mechanical properties. Stellite 20 was available for use in this PhD project and will therefore be referred to throughout the remainder of this thesis chapter.

The two cobalt-based alloys under scrutiny in this review are Stellite 20 and Haynes 25. Each alloy falls into two categories of cobalt-based alloys that have been described *i.e.* a Stellite with a carbon content above 1.3% and a wrought cobalt-based alloy with a carbon content below this. Table 2.2 presents the manufacturer provided nominal composition of the alloys [23, 24].

Table 2.2: Chemical composition of Stellite 20 and Haynes 25

%wt	**Co**	**Ni**	**Cr**	**W**	**Fe**	**Mn**	**Si**	**C**
Stellite 20	Balance	3 **	30-34	13	3 *	0.5 *	1 *	2.8-3
Haynes 25	Balance	10	20	15	3 *	1.5	0.4 *	0.1

**=maximum*

Nickel is attributed with improving ductility, corrosion resistance and high temperature mechanical properties to such alloys [3]. It is also credited with stabilising the face centred cubic matrix that influences the alloy's resistance to sliding wear [9, 25]. Chromium is a major contributor to corrosion and oxidation resistance necessary in this application [3, 9, 14]. Chromium is a principal carbide former, forming metal carbides M_7C_3 and $M_{23}C_6$ as well as intermetallic metals [14, 16, 22]. It also influences the mechanical properties of the alloys as it is important in heat treatment as well as increasing resistance to sulfidation [3, 22]. Chromium, tungsten and molybdenum together are influential on the formation of the strong oxidation resistance matrix [17].

Some of the alloying elements are categorised as refractory metals i.e. metals with a melting point higher than that of chromium [26]. Temperature related strength increases with an increase in the melting point of an alloy. The presence of the refractory metals in the composition of the cobalt-based alloys is thus another contributing factor to their high temperature strength [26]. Cobalt prevents any sudden changes by thermal expansion in the microstructure during heating and cooling, providing stability to the solid solution matrix [8].

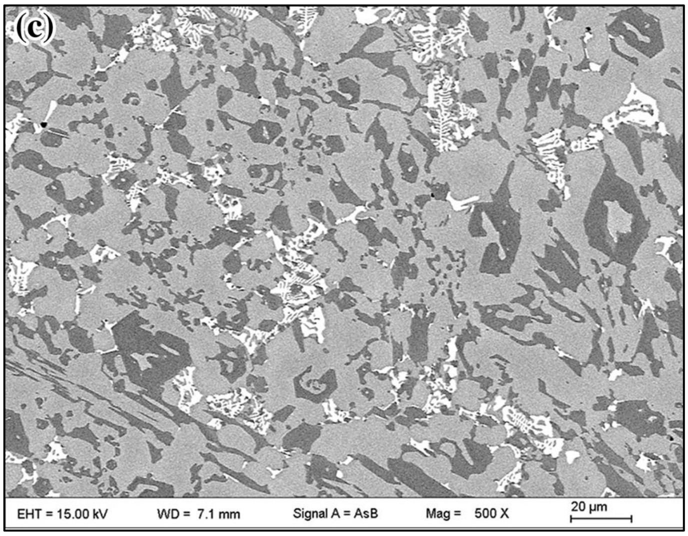

Figure 2.2: SEM microstructure at x500 of CoCrW Stellite alloy [13]

Stellite 20 fits within one of the three categories evaluated by Liu et al [13] *i.e.* it is a high carbon CoCrW alloy. Figure 2.2 presents the microstructure of an alloy within this category that has a similar composition to Stellite 20, see Table 2.3. Using XRD analysis, the dark grey regions in Figure 2.2 are identified as Cr_7C_3 carbides, the light grey phase a face centred cubic cobalt solid solution with the white phase identified as a $(Co,W)_6C$ carbide [13]. The stabilised, face-centred cubic crystal structure is common to the matrix of cobalt-based alloys [10].

Table 2.3: Chemical composition of a selected Stellite alloy for comparison to Stellite 20

%wt	**Co**	**Ni**	**Cr**	**W**	**Fe**	**Mn**	**Si**	**C**
Alloy A3 [13]	Balance	3.5	30.5	12.5	5	2	2	2.4

Stellite 20 is a two phase metal alloy known for its high hardness and excellent resistance to wear and corrosion at elevated temperatures. Figure 2.3 presents the microstructure of an area of a Stellite 20 ball using the backscattered electron mode (BSE) of an SEM. The dark grey chromium rich carbides and the white tungsten rich carbides, earlier identified in Figure 2.2 as Cr_7C_3 and $(Co,W)_6C$, are present. XRD analysis has not been undertaken as part of this body of work but using data and evidence presented in the literature, the assumption is that these carbides are of the form M_7C_3 and M_6C [13]. The medium/light grey portion identified as the cobalt solid solution in Figure 2.2, can once again be identified in Figure 2.3, also rich in chromium and tungsten. It is established by Liu and co-workers that an increase of tungsten in the solid solution will increase tungsten carbide formation due to oversaturation in the matrix.

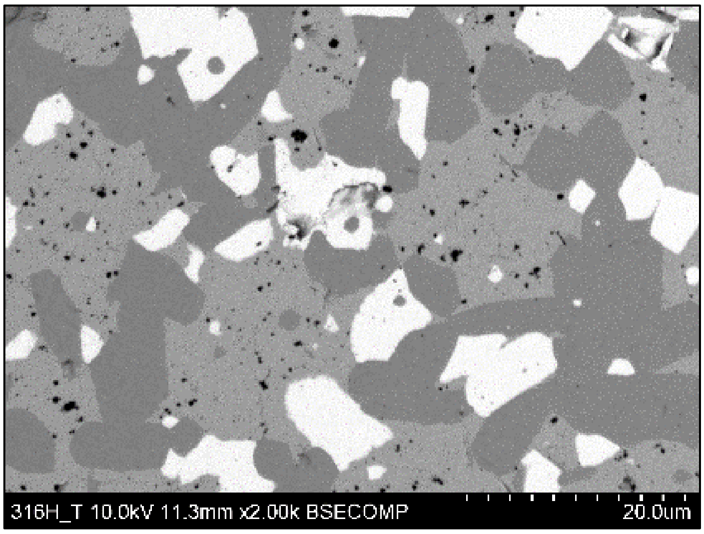

Figure 2.3: Microstructure of an undamaged Stellite 20 ball taken using the BSE mode of an SEM [27]

Haynes 25 is a wrought, ductile, wear and corrosion resistant cobalt-based alloy with excellent high temperature strength [23, 28]. It is also selected by engineers for its ease of fabrication, weldability and resistance to in service galling [29]. In literature the alloy may also be referred to as L605 with a UNS number of R30605.

Wrought cobalt-based alloys tend to have a relatively low level of carbon present in their chemical composition, *i.e.* ≤0.15 %wt [9]. This is to limit the impact that carbon has on manufacturing processes. Improved fabrication and machinability are attributed to tungsten and nickel additions in this alloy [12]. The microstructure of Haynes 25 is generally a single phase face centre cubic system [28]. This may be evolved by the application of mechanical work and temperature treatment [9, 17, 28]. These treatments result in the precipitation of carbides *e.g.* M_7C_3, $M_{23}C_6$ and / or M_6C and other phases in the microstructure while imparting ductility on the alloy [9, 29]. Precipitation of the different phases observed within the Haynes 25 microstructure is dependent on the specific aging temperatures applied in the treatment process [9].

The relatively low carbon content of Haynes 25 however means that the strength of the alloy is less dependent on carbides than for cobalt-based alloys with a high carbon content [12]. Cold working is seen to have a significant impact on the strength of the alloy [12]. Solid solution strengthening is aided by the presence of chromium, tungsten and nickel embedded in the cobalt matrix [21]. Nickel is useful in the stabilisation of the face centred cubic phase with chromium and tungsten stabilising the hexagonal form [30]. An increase creep strength of the alloy by control of the stacking fault energy is observed due to the solid solution composition [30]. For the purpose of this work, the wear behaviour of Haynes 25 in a 30% cold reduced form that has been aged for 6 hours in ~600°C is evaluated. When compared to no or a lower level of cold rolling (5%), Sandrock and Andrews [31] demonstrated that 30% cold reduction of the alloy contributed to an increased level of homogeneity of carbide precipitation during the subsequent aging process.

The Stellite 20 balls in the current investigation have been manufactured by the thermo-mechanical process of hot isostatic pressing (HIPing). This process involves applying high isostatic pressure to the alloy in its powder form at high temperatures instigating diffusion bonding of the powder [32]. A series of studies was conducted by Yu et al. [33-35] to understand the influence of manufacturing process and alloying element content on the tribomechanical properties of cobalt-based alloys. The aim was to comprehend the structure-property relationship of some wear resistant cobalt-based alloys, such as Stellite 6, produced from two different processing routes; powder consolidated and hot isostatic pressing (HIPing) and casting. Microstructural and tribomechanical evaluations involving hardness, impact toughness, abrasive wear, sliding wear and contact fatigue performance tests indicated that, despite the similar abrasive and sliding wear resistance of each alloy, the HIPed alloys exhibited an improved contact fatigue and impact toughness performance in comparison to the cast counterparts.

2.3 Cobalt-based alloys in the nuclear environment / industry

Cobalt-based alloys offer excellent resistance to wear and chemical corrosion. Owing to their exceptional properties in water lubricated environments, the alloys are often used in different bearing surfaces in nuclear applications. Approximately 50% of cobalt in a reactor is found in hardfacing alloys used where resistance to mechanical wear is required e.g. bearing surfaces, valve trim and reactivity control mechanisms [4]. An issue arises with the application of cobalt-based alloys in the radioactive environment when they are exposed to the products of the nuclear reactions taking place.

To describe how likely an interaction between an incident neutron and a target nucleus is, the ‘nuclear cross section’ is established. This is a property of an element with which the reaction rate can be calculated [17]. A low absorption value is preferred to minimise the neutrons absorbed (and wasted) by an element i.e. neutrons that will not be available for nuclear reactions [3]. Minimising neutron absorption of a material will also minimise the irradiation of the material. Relative to the alloying elements of Haynes 25 and Stellite 20, cobalt has a high thermal neutron cross section. When stable cobalt-59 is bombarded with thermal neutrons a radioactive isotope of cobalt, cobalt 60 is produced. Cobalt-60 is an energetic, γ-ray emitting radionuclide with a relatively long half-life of 5.3 years [3]. Iron and chromium have half-lives of 46 days and 26.5 days in comparison [3]. Gamma rays are extremely penetrative emissions and in relation to the high thermal neutron absorption cross section, a relatively high frequency of gamma rays is anticipated from cobalt 60 [3]. Equation 2.1 describes this nuclear activity [4]:

$$ {}^{59}_{27}\mathrm{Co} + {}^{1}_{0}\mathrm{n} \rightarrow {}^{60}_{27}\mathrm{Co} \rightarrow {}^{60}_{28}\mathrm{Ni} + {}^{0}_{-1}\mathrm{e} + \gamma. \qquad \text{Equation 2.1} $$

where *Co* is cobalt, *n* is neutron, *Ni* is nickel, *e* is electron and γ is a gamma ray.

Cobalt-based alloys applied in various applications within the reactor core are exposed to different wear mechanisms producing wear debris, between 1 and 100 μm in size, some of which will be composed of cobalt-60 [36]. The debris is transported around the primary loop of the reactor suspended in the coolant and becomes deposited at different locations throughout. Exposure to cobalt-60 containing wear debris is a leading contributor to occupational radiation exposure of maintenance personnel during shutdown periods [4]. Reducing this exposure is an incentive driving much research in this field. In order to remove the problem, low cobalt or cobalt-free alloys must be identified, their tribological performance examined and compared to the relevant cobalt-based alloys.

2.4 Wear

Introduction

Design goals of nuclear reactors that have relatively low thermal outputs (~100MW) include minimising weight and size [2]. Examples of such reactors include Russian icebreakers with production output ranges from approximately 90 – 150 MWt or some merchant ships such as the NS Savannah with outputs ranging from 30-80 MWt. The safety and reliability of such in vessel reactors is particularly important due to limitations in support from 'the land' [2]. One method of achieving the design goals and reliability of such reactors is simplification of the system design [2]. Ishida and co-workers discuss an in-vessel type control rod drive mechanism designed to meet such requirements [1]. The control rod mechanism presented in the publication may be used in marine type vessels as well as in typical light water and pressurised water reactors [1]. The operation of this mechanism is enabled by components such as ball bearings that allow for thrust and radial supports and have been designed to operate in the high temperature and pressure environment of the reactor [1].

Haynes 25 and Stellite 20 are used in the race and rolling element of rolling element bearings (REBs) operating in the core of such reactors. They are lubricated by the coolant water circulating in the primary loop of the reactor. The alloys from which the bearings are made must be capable of operating in this high pressure and temperature water, 12 MPa and 310°C respectively [1]. Due to the corrosive nature of the primary coolant the alloys must be corrosion resistant [37]. Thermal, physical, chemical, mechanical and environmental properties are those that should be taken into consideration when selecting materials suitable for high temperature bearing applications [26]. Exposed to these conditions, the properties and integrity of such alloys should be maintained for up to 25 years of service life to between 40,000 and 200,000 hours [20, 38].

A critical factor that influences the service life of a component is wear [5]. Wear is defined by Bhushan as the 'surface damage or removal of material from one or both of two solid surfaces in a sliding, rolling or impact motion relative to one another' [39]. The environment described will be influential to the mechanical and electrochemical factors leading to wear of the bearings and will govern the volume of material lost [40]. It has been established that tribocorrosion is active in the wear process of some components located in the reactor core [41, 42]. Tribocorrosion is described as a wear process involving the combination of both mechanical and electrochemical mechanisms [43]. It involves the material degradation of a component surface caused by mechanical interaction between components in contact immersed in a corrosive environment [44].

2.4.1 Mechanical wear

There are several mechanical properties of importance when assessing the suitability of a material to high temperature bearing applications including hot hardness, yield point, creep and work hardening [26]. Fatigue induced failures such as rolling contact fatigue should also be considered [26]. Theoretically, a rolling element bearing that is in a state of pure rolling should be completely unaffected by mechanical wear. However, the scenario whereby the bearings are in a perfect lubrication regime and perpetual state of pure rolling is unlikely due to system control [45-47]. Relative motion between components located in the core is caused by varying operational processes such as positioning adjustment and/or adverse effects such as flow induced vibration [48, 49]. Variable control of the REBs central to this study means that they are exposed to factors leading to mechanical wear such as slip, entry of abrasive particles in the system, poor lubrication regime or system vibrations, see Figure 2.4 [50].

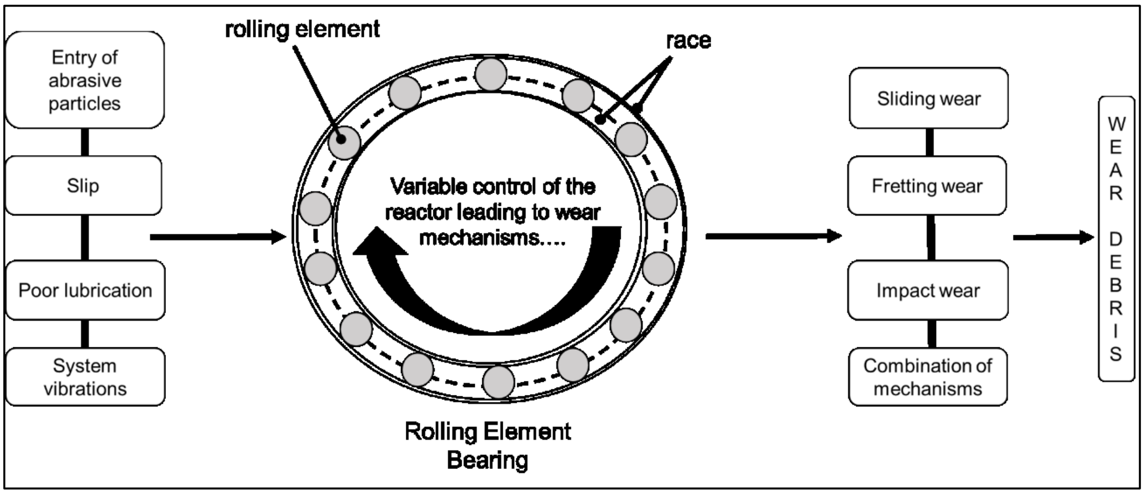

Figure 2.4: Factors leading to mechanisms of wear of rolling element bearings that operate in the core of a nuclear reactor

The resistance of a material or alloy to wear in sliding interactions is important as well as frictional properties and galling resistance [26]. Mechanisms of mechanical wear include adhesion, abrasion, fatigue or impact by erosion [39]. Wear is commonly evaluated by measuring the weight or volume of material loss of components following a wear inducing interaction and by recording and observing the coefficient of friction during the process. Microscopy is used to visually assess the wear patterns and damage produced [39, 51]. Visual interpretation is used to identify mechanisms of wear. Bhushan [39] identifies the cause of scratching or ploughing of the worn surface of the softer material as abrasive wear [39]. Adhesion can be identified with visual microscopic evidence of either debris pull out or retention within the wear track or scar [39]. Using energy-dispersive x-ray spectroscopy (EDX) analysis, the elemental composition of the wear particle and thus its originating component can be confirmed [52].

Sliding wear, which is also of interest for this study and part of the investigation reported in this thesis, can be described as ‘the loss or transfer of a material when contacting surfaces slide’ [53]. It is a complex form of wear that is manifested through a combination of processes [54]. In metals, some common manifestations caused by sliding are seizure, melt wear, mild to severe oxidation wear, as well as wear that is dominated by plasticity of contact surfaces [53]. Functions of wear rate include applied load, component geometry, sliding velocity, surface roughness, material properties, lubrication and temperature [16, 40, 53, 55]. The complexity described is a reason to approach the assessment of material wear behaviour through both experimentation and physical modelling [53]. Lim and Ashby presented this combined approach using empirical data and physical models to categorise wear using ‘wear maps’ [53]. The work involved the creation of wear maps for steels used in pin on disc dry sliding tests. Pressure and sliding velocity were used as the basis for the maps as they could be directly linked to the temperature produced in the contact, dissipated into the experimental components during sliding.

Some early studies established a directly proportional behaviour between wear volume, sliding distance and applied load and an inversely proportional relationship between wear volume and the material hardness [55]. There is much disagreement on the validity of many mathematical wear prediction models however, for instance at low loads and high speeds the volume – hardness relationship mentioned was disproved. A key issue in the application of wear theory is the difficulty in reducing the numerous variables to a practicable number [56]. A study comparing the adhesive wear of nickel against cobalt-based alloys using an unlubricated tribometer, Ref. [57], observed a negative relationship between increased rotational speed and wear volume for the nickel-based alloy and a positive relationship for the cobalt-based alloy. The general dissent against using one generic mathematical model for all sliding wear behaviour further validates the inclination of Lim and Ashby’s work to produce complementary experimental and modelling data.

In studies that compared the impact of load and/or sliding velocities on the wear behaviour of alloys, the production of such maps to categorise wear manifestation was recommended [55]. Rasool and co-workers used this method to understand how chromium content affects the behaviour of dry sliding steels. The work categorised the wear regimes observed into mild, medium and severe wear as well as highlighting factors contributing to transitions between such regimes including changes in sliding speed and load as well as high rates of oxidation [55]. As part of the empirical assessment, different features of wear tracks were associated with different wear mechanisms. A feature of mild wear described as ‘dark’ and ‘smooth’ are glaze layers, contrasting with some bright and rough areas seen in the severe wear regime and large, metallic debris are a condition of adhesive wear [53]. Cutting and ploughing, features of abrasive wear are observed on component surfaces following sliding wear tests as well as adhesion of asperities, production and adhesion of wear debris and material transfer [57.

The most accurate method in matching and comparing mechanical wear models with laboratory experiments is to examine the change in the surface undergoing the effects of mechanical wear with regard to wear rate, friction, appearance, etc. [59]. In general, sliding wear tests using a pin on disc tribometer are employed. Mishina and co-workers utilised pin on disc sliding wear experiments in order to build a database of behaviour observed for use in the development of a wear prediction model *i.e.* how friction data and plastic deformation effect the material performance [60]. Renz and co-workers examined the sliding wear behaviour of Stellite 12 and Tribaloy T400 hardfacing alloys in a pin on disc tribometer under varying test temperatures and initial surface roughness's [61]. The data collected from the work was used to describe phenomologically the severity of the alloy wear, as influenced by the changing test parameters.

The coefficient of friction (COF) recorded throughout the tests was used to correlate wear rates to test temperature and the initial surface roughness [61]. A change in running-in time for both alloys for different temperatures tested was demonstrated and it was concluded that the COF for the alloys tested 'strongly depended' on test temperature [61]. Initial component surface roughness was only seen to impact the coefficient of friction in the lowest test temperature at a level not considered significant [61]. Hardness values measured before and after experiments, inside and outside the worn surface were also investigated and linked to the wear behaviour such as strain hardening of the components within the wear track. Changes in component hardness outside the worn surface were attributed to oxide formation [61].

Lina and co-workers evaluated the impact on flow rate in a PWR on the sliding wear behaviour of reactor components [49]. A positive relationship between wear rate and flow was observed, although the data presented was limited [49]. The flow of water in experiments carried out for the purpose of this PhD thesis will not be measured; however, the relationship observed by Lina and co-workers is still of interest as it should be incorporated into models to achieve a better understanding of the prototypical system in future work.

2.4.1.1 Wear resistance of cobalt-based alloys

In Section 2.2, the impact of chemical composition and microstructure on the behaviour of the cobalt-based alloys, notably the wear resistance, was discussed. Evaluation of the wear behaviour of the cobalt-based alloys will set a performance benchmark for resistance to sliding wear from which the alternative alloys will be measured. The wear resistance of cobalt-based alloys is temperature dependent [21]. Along an increasing temperature profile, the sliding wear rate of these alloys transitions from severe to mild [21]. The spontaneous formation of a 'tribo-layer', when wear rate is in the mild regime has been shown to act as a lubricant in the contact, decreasing the progression of wear. The formation of these glazes and their influence on the rate of wear will be further discussed in Section 2.4.2.

Dréano and co-workers commented on the relatively low volume of work encapsulating the wear behaviour of cobalt-based alloys in a lower temperature, severe wear regime in literature [21]. Their study presented in Ref. [21] investigated the friction and fretting wear behaviour of Haynes 25 for a range of temperatures with a particular focus on 'low' temperatures. The fretting wear behaviour of Haynes 25 against and alumina counter-surface was presented for three temperature domains as indicated in Figure 2.5 (a) (100°C, 300°C and 600°C).

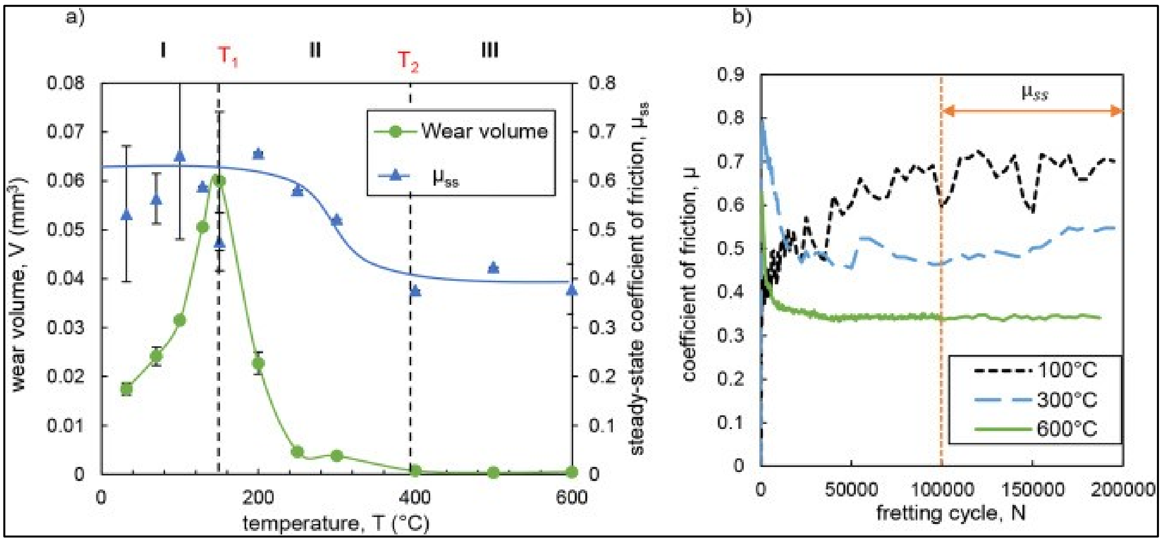

Figure 2.5: (a) Effect of temperature on the wear volume and the coefficient of friction and (b) evolution of the coefficient of friction in temperature domain I, II and III [21]

In the lowest temperature domain, diffusion of metal was not observed and relatively large wear debris were produced and ejected from the contact resulting in a high rate of wear and coefficient of friction throughout the experiment [21]. These researchers hypothesised that this steep increase in wear volume observed up to ~150°C is a result of a complementary interaction between mechanical and oxidational wear. Once diffusion of the metal debris is enabled by the test temperature (>150°C) the wear debris produced is no longer ejected from the contact as rapidly and is broken down into finer particles which may then become compacted [21]. Following the steep drop in wear rate, it remained very low up to the higher temperature limit tested of 600°C. For the highest temperature case, the coefficient of friction stabilised sooner than the intermediate temperature tests and remained relatively low throughout testing. The results presented by Dréano and co-workers confirmed the direct relationship between friction, wear and the presence of a third body structure within the contact.

Inman discussed the production of wear debris for a sliding interaction, and classified it into two categories; passive and active debris [62]. Passive debris, like that discussed by Dréano and co-workers, is 'ejected' from the sliding interface, tends to be metallic, retain its form and structure and does not influence the rate of wear as the interaction continues. This is also echoed by Stott [63] when describing how wear debris may impact the sliding interaction in different ways; identifying debris which may be removed from the contact, thus having no further effect. On the other hand, active debris was described by the author as a more fine manifestation of wear consisting of both metallic and oxide particles [62, 63]. Active debris is that which is retained within the component interface and is likely to influence and probably reduce the rate of wear. Under certain, 'favourable' conditions [64], this active debris forms the oxide glaze, see Section 2.4.2. A further categorisation of wear debris by Stott is that which remains within the contact, free, acting as a third body 'abradant', causing further damage, rather than providing protection from it [63]. Figure 2.6 presented by Stott and co-workers [63] served to demonstrated the step by step process by which wear debris particles develop into "glaze" layers during dry sliding wear.

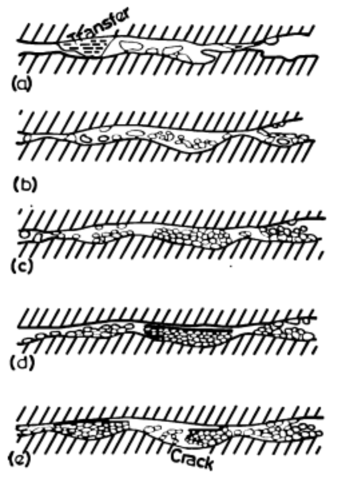

Figure 2.6: A schematic diagram presented by Stott et al, Ref [63] that demonstrates the development process of wear debris particle layers and "glaze" layers

Work by Kapoor and co-workers discussed in Section 2.2 used a pin-on-disc in a furnace to test alloys up to 450°C [16, 65]. The wear behaviour depended on the influence temperature imparted on the microstructural phases i.e. the carbide or the matrix described in Section 2.2. The work established a relationship between carbon content and the resistance to sliding wear of the alloys tested at room temperature. The work also identified the presence of tungsten, molybdenum and nickel important to the wear behaviour. An increase in complexity of the wear mechanisms of these alloys at high temperatures was noted by the authors.

2.4.1.2 Experimentally investigation wear in rolling elements

A large portion of this PhD thesis will be devoted to investigating the sliding wear behaviour of the specific cobalt-based alloys and some cobalt-free or low cobalt alternative alloys. Understanding the wear of rolling elements remains relevant to the work, particularly future work of this project. Twin-disc wear tests are typically used to simulate the rolling sliding contact (wear) behaviour of materials in laboratory environments [51]. In general the post experimental methods used to examine the worn surfaces remain the same as for standard sliding wear tests i.e. coefficient of friction, weight or volume loss and microscopy for visual and compositional inspection [51]. Phenomena likely to be observed as well as traditional manifestations of mechanical wear include Rolling Contact Fatigue (RCF), strain hardening and ratcheting [51]. As previously described, mechanical wear will not manifest in a contact interaction that is in a state of 'pure' rolling [7]. In a twin disc tribometer wear is simulated by 'slip' or 'local sliding' [7]. Hegadekatte and co-workers observe that rolling contacts are actually rolling/sliding contacts caused by slip between the two rolling components and the compressive load applied to the interaction [7].

Cyclical repetition of a 'pure' rolling interaction that exceeds mechanical limits of the rolling element bearing material(s) will eventually lead to failure of the component(s) and the onset of wear [66]. This is initiated by cracks located where the maximum stress occurs, a distance below the surface, which then propagate parallel to the bearing surface [67]. Further development of these cracks leads to the formation of microscopic, 'steep sided' pits or spalls at the contact surfaces [67, 68]. The rolling interaction combined with sliding, as is most common, brings the location of maximum stress closer to the component surface with 'irregular shaped' pits forming at the surface. The formation of cracks on the surface caused by the combined effect of rolling and sliding is accelerated by the presence of stress concentration sites like these pits as well as surface inclusions and corrosion pits for example [67]. Subsurface cracks are observed across sections of the components [68].

2.4.2 Oxidation

The high temperature environment in which the rolling element bearings operate are conducive to chemical reactions [26]. Oxidation is a critical factor effecting the wear rate of metal alloys in elevated temperatures [40]. Lina and co-workers investigated the influence of flow rate on the oxidation of components in simulated PWR environments. Many studies identify the presence of oxide ‘glazes’ on components exposed to varying loading, temperature and sliding velocity conditions [40, 62, 63]. These varying conditions give the glazes characteristic composition and surface roughness [69]. The work by Lina and co-workers established a positive relationship between flow rate and mass loss due to oxidation [49]. They did not explicitly state a reason for the relationship although it conjectured that the flow influences the surface properties. Temperature can refer to the surface temperatures induced by frictional heating as a result of high loads and contact pressures or temperature provided by an external source [63], for example using a high temperature tribometer [69]. Stott [63] investigated the impact of temperature on the mechanism of the wear-protective glaze formation. Frictional heating was maintained at a low level by applying low loads and sliding speeds over the temperature range examined (20°C to 800°C). In the lower temperature range (20°C to 200°C), ‘loosely compacted particles’ on the worn surfaces were established. Where testing temperatures exceeded this range, the ‘very protective’ and hard glaze was observed.

Rasool and co-workers described the phenomenon occurring in many metal alloys exposed to a ‘transition temperature’ when the formation of a smooth oxide glaze in wear tracks leads to a ‘rapid’ decrease in wear rate [55]. Figure 2.3, presented by Dréano and co-workers, depicted the transition of the wear regime over this temperature threshold [21]. Within the mild wear domain, the ‘spontaneous’ formation of the glaze or ‘tribo-layer’ was observed by the authors. Lim and Ashby also confirmed the incidence of oxidation, mild and severe, as a wear manifestation in sliding wear interactions - further validating the discussion in Ref. [63] on the formation of oxide glazes.

The kinetics of growth of such glazes on the surface of a reactor component made from a cobalt-based alloy and how this influences the mechanical wear rate is of interest to this study. The rolling element bearings will not be in a state of perpetual motion throughout the life cycle of the reactor. There will be latent periods when the bearings are not in operation during which oxidation of component surfaces may occur. Glazes formed due to this phenomenon may have an influence on the rate of mechanical wear manifested via the mechanisms detailed in Section 2.4.1. Under non-sliding conditions, high temperature alloys tend to be thermodynamically unstable in air, forming metal oxides with oxygen [63]. At rest, components made of such alloys are likely to depend on slow growing oxide scales on their surface, protecting them from further oxidation, the rate of which will depend on the environment to which they are exposed *i.e.* temperature, in air or in water etc. [63]. The rate of formation of a protective oxide layer can typically be described as a parabolic function of time according to Dréano [21], see Equation 2.2.

$$\xi^2 = k_p t \qquad \text{Equation 2.2}$$

Where ξ is oxide layer thickness, k_p the oxidation or parabolic rate constant and *t* is the time with units in [µm], $[mm^2/s]$ and [s] respectively.

A rate equation for the oxidation phenomenon is given by Equation 2.3.

$$K_p = Aexp(-\frac{Q}{RT}) \qquad \text{Equation 2.3}$$

where *A*, *Q* and *R* are constants and *T* is the absolute temperature [63].

The oxidational mechanism of mild wear is described by Quinn as the formation of 'protective oxide films' in the contact at the local temperature [56]. According to Quinn there is a critical thickness (1-3 µm) at which the oxide film will break off the surface producing wear particles, a characteristic of this wear mechanism. Quinn used Archard's wear equation as a basis to formulate Equation 2.4, an expression for the rate of mild oxidational wear;

$$W = \frac{dAk_{p0e}\exp(-{}^{E_a}/_{RT_0})}{Vf_m{}^2\xi_c{}^2\rho^2} \qquad \text{Equation 2.4 [58]}$$

where W is the rate of wear, *d* is the sliding distance, *A* is the ration of normal applied load to hardness, k_{p0e} is the Arrhenius constant, E_a is the activation energy of oxidation, T_0 is the absolute temperature of the reaction, *V* is the sliding speed, f_m is the mass friction of oxides, ξ_c is the critical thickness for mechanical stability of the oxide layer and ρ is the average density of the oxide.

Limitations of this expression are highlighted by Dréano and co-workers who attempt to establish an alternative expression to Equation 2.4 for wear in lower temperature conditions [21]. This alternative 'oxido-abrasive' wear law for temperature domain I (Figure 2.3) developed as part of that work was 'satisfactorily' validated via experimentation is expressed by Equation 2.5.

$$V_{SS} = \beta\sqrt{\frac{\alpha\delta_0{}^n}{2f}}\exp(-\frac{E_a}{2RT})\frac{P}{H_{softer}}4\delta_0 N \qquad \text{Equation 2.5 [21]}$$

where V_{SS} is the steady-state wear volume,β, α and n are interface dependent constants, f is frequency, P is the applied load, H_{softer} is the hardness of the softer material, δ_0 is displacement and N is the number of cycles.

An interesting review of the level of understanding of the elevated temperature wear resistance of various metals and alloys, including many cobalt-based materials was reported by Pauschitz and co-workers [40]. The formation of the 'glaze' under different alloying temperatures and sliding conditions was identified as a salient feature in a systematic review of all results reported in the recent literature. Different classifications of the 'glaze' formed on the surface of metal components that underwent sliding wear tests in elevated temperatures are identified either as transfer layers, mechanically mixed layers or composite layers. Instances where there was no layer formation were also referred to in the review although it was noted that this was the least common scenario. The comparative chemical composition of the wearing and mating surfaces versus that of the worn surfaces are described as identifying features for each classification. It is indicated that in the case of the transfer and mechanically mixed layers, the oxygen content of the worn surface is low where as a high content is anticipated in the presence of a composite layer. Understanding the formation of such glazes is necessary when trying to identify if such a phenomenon is a feature of experiments performed as part of this PhD thesis.

The glaze has been shown to form from compacted oxide layers and partially oxidised alloy particles within the wear track [40, 63]. The majority of wear debris produced in sliding interactions remain in the wear track and will be often mechanically broken down into finer particles, 'communition' [63]. These particles tend to concentrate around features in the wear track e.g. grooves [63]. The clusters of debris will be subjected to thermo-elastic stresses and become more compacted. Wear will continue to progress on surfaces surrounding these clusters which become load bearing areas. Simultaneously, sintering of these areas may occur, observed in literature at temperatures above 20°C [40, 70]. The process is enhanced under high compressive loads and in temperatures above 150°C it produces solid and smooth glazes [40]. Below this temperature, such layers may still be observed although not as smooth or 'well sintered' [40]. Such layers will lead the wear regime to transition to mild [63]. Another factor that will influence the formation of these glazes is the 'sustainability' of the compacted layers formed [58], which is in turn, influenced by the nature of the debris produced [62]. Work presented in [71] demonstrated the manifestation of the two types of debris described via sliding wear experiments with Nimonic 60 and Incolloy MA956 against a Stellite 6 counterface over a range of temperatures. The test temperature influenced the type of wear debris produced and its influence over the wear rate.

The conditions in which wear is induced will affect the mechanical and microstructural characteristics of these glazes [40]. The speed of sliding is established as a significant factor in glaze formation. The manifestation of at high sliding speeds of abrasive wear will hinder glaze formation as debris will not become compacted and may actually increase the wear rate by further abrasion to the surface [40].

The excellent corrosion resistance of cobalt-based alloys have made them suitable candidates for application in extreme environments. This was observed in a survey by Amateau and Glaeser in the early 1960s on the selection of bearing materials for high temperatures [72]. The survey linked the sliding behaviour of cobalt-based alloys, also considering frictional behaviour, to the presence and structure of oxide phases on component surfaces. Studies by Li and co-workers established a positive effect of low yttrium additions to the oxide film properties and thus the wear resistance of Stellite alloys [40]. Passivable alloys are applied in the nuclear environment partly due to the nature of the oxide films formed on their surfaces [37]. In Stellite 6, for example, the presence of chromium enhances the passivation of the alloy enhancing its corrosion resistance in the oxidising coolant water [37]. The wear of a passivated alloy as a result of experiments such as a pin on disc is likely to yield a different result than from separate corrosion and mechanical wear analyses [37]. A study by So and co-workers [73] on the 'Wear behaviours of laser-clad stellite alloy 6' illustrate the formation of an oxide glaze on the worn surface of a post experimental sliding wear Stellite 6 surface, thickness ranging from 6 to 12 μm.

Tribocorrosion is the term used when describing the combined impact of mechanical and chemical wear on a component [74]. Carbide volume fraction, heat treatment used to produce component, applied normal load and the chemical environment are examples of parameters that affect tribocorrosion [75]. Studies have been carried out to understand the affect tribocorrosion has on Stellite alloys in varying oxidising environments including those of a pressurised water reactor [41, 42, 75]. In such work the relationship between component oxidation and mechanical wear is studied. Generally, a discontinuous sliding wear experiment is undertaken i.e. there are periods of latency between sliding interactions promoting oxidation of component surfaces or even wear debris. These experiments are formed of several procedures; anodic and cathodic measurement tests and open circuit potential measurement tests in a test cell with which the tribometer is equipped [41]. Polarization graphs are developed with the onset of the electrochemical reactions presenting the electrochemical kinetics of the material under scrutiny and how this data changes with the application of a mechanical interaction producing an ‘active wear track’ [41, 42, 76, 77]. The active wear track is where the mechanical interaction has temporarily destroyed the passive layer produced by the electrochemical aspect of the experiment [77]. Measuring and comparing this with surfaces changed by mechanical wear and passivation separately will provide the tribocorrosive relationship. In a study examining the time dependent relationship between the number of mechanical steps, latent period between them and the mass loss of a component in a corrosive environment, Equation 2.6 is presented [35];

$$M_{loss} = N\omega_0 \frac{\tau}{t_0}^{1-n} \qquad \text{Equation 2.6}$$

where M_{loss} is mass loss, *N* is number of mechanical steps, ω_0 is the average mass loss per step, τ is the latency time, t_0 is the time constant and *n* is a dimensionless parameter, given a value of approximately 0.6 for a PWR environment [41, 42, 78].

Tests examining the tribocorrosion of Stellite 6 immersed in 0.5M sulphuric acid and a solution of boric acid and lithia at 20°C and 85°C respectively were carried out by Wenger and co-workers [78]. The value of the dimensionless parameter ‘*n*’ was established for each test condition and the results suggest the value ranks the ‘corrosiveness’ of the environment. The relationship appears to follow the trend that for a smaller value of ‘*n*’, corrosion is more likely and vice versa [78]. The variation in current during the experiments was analysed with respect to oxide film growth. An assumption is made that all variation was due to the growth omitting the effect of any parallel reactions taking place. Garcia and co-workers [77] categorised results of sliding wear tests in a corrosive environment based on the impact the normal load (pressure) had on the passive layer. Under a load of 2N there was no damage observed. In the range of 2 to 10 N, a ‘mild oxidation wear mechanism’ [77, 79] was observed with mechanical delamination of the passive layer and repassivation. For normal loads above 12 N, a sharp increase of corrosive wear was observed with wear damage affecting the layer and the component [77].

Benea and co-workers induced and measured the growth of an oxide film on the surface of a Stellite 6 component over time immersed in LiOH-H_3BO_3 solution using potential jump experiments [37]. The tribocorrosion experiments undertaken by the authors demonstrated that the kinetics of mechanical removal of the passive layer produced and the kinetics of re-passivation of the layer during periods of latency control the wear rate of Stellite 6 in this environment. The growth kinetics extracted from the data produced could be used to develop a wear model incorporating mechanical wear with the passivation kinetics of an oxide film, see Figure 2.7.

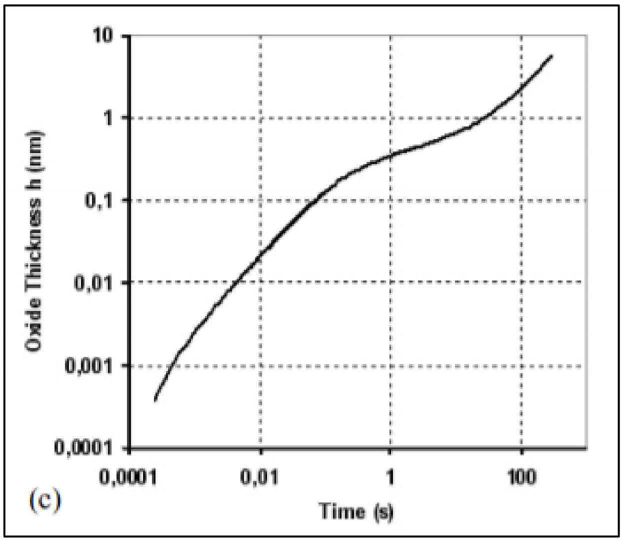

Figure 2.7: Thickness of an oxide film induced by potential jump experiment on the surface of a Stellite 6 component immersed in an LiOH-H_3BO_3 solution [37]

2.5 Replacing cobalt-based alloys in nuclear reactors

Introduction

A key outcome of this work will be a recommendation of cobalt-free or low cobalt alloys that have the potential of replacing cobalt-based alloys in the nuclear reactor system. These alternatives must exhibit equal to if not better than behaviour with respect to strength, hot hardness, resistance to wear, corrosion and thermal shock [22]. Any manufacturing process issues as well as any significant microstructural information will also be encompassed in this. A review of literature makes it clear that the research question faced in this PhD thesis is not new or unique. This literature summary aims to utilise and acknowledge the significant volume of the work already done in an attempt to understand and answer it. Although all available studies will not be directly relevant to this application, the analysis and methods used will be useful.

2.5.1 Analysis of Haynes 25 and identification of potential low cobalt/cobalt-free replacement

The properties of Haynes 25, in the cold rolled and aged form used for the races in the REBs, is the first of the two cobalt-based alloys discussed in this section. The composition of the alloys and the treatments applied to them in their manufacture, significantly influences their mechanical and corrosion resistant properties in the nuclear reactor environment. Such properties of alloys, such as stainless steels (SS), used in typical bearing applications were investigated and compared to properties of the relevant form of Haynes 25.

In stainless steels, chromium provides corrosion resistance by the formation of a protective chromium oxide layer in air. If the chromium content exceeds 12%, this film can reform on the surface after an interaction has induced damage. Haynes 25 is composed of approximately 20% chromium and its corrosion resistance is attributed to this. SS type 440C contains approximately 17% chromium which meets the requirement for film reformation, or repassivation and is commonly used in bearing applications. Another commonly used bearing steel is type AISI 53100 but it has a significantly lower chromium content of range 1.2-1.6% composition. In an online article [12], the corrosion resistance of 440C was described as twice that of AISI 52100. It was also stated however that the superior performance of type 440C may be reduced in an environment with elevated chloride and moisture levels, which may also impact the rolling contact fatigue life of bearings manufactured from the alloy. Cronidur 30 is a relatively new, highly corrosion resistant martensitic cold work steel that is used to manufacture rolling bearings designed to withstand severe stress [80-82]. It was developed as a bearing steel that could accept higher loads than 100Cr6 or type 440C steels in difficult ambient conditions.

For much of the literature reviewed, rather than providing quantitative values for wear and corrosion resistance, alloy performance was compared relatively. Data from [83] is presented in Table 2.4, comparing the relative material properties of several stainless steels using a 100Cr6 stainless steel as the basis (AISI 52100 falls into this category). The review is based on rolling contact fatigue performance of bearings with a steel race.

Table 2.4: Comparing some material properties of stainless steels [83]

	100Cr6	440C	M50NiL	Cronidur 30
Microstructure	Basis	-	+	++
Fatigue life (<150°C)	Basis	-	+	++
Fatigue life (<180°C)	Basis	-	++	+
Fatigue life (>180°C)	Basis	-	+++	+
Corrosion resistance	Basis	+	=	++
Hot hardness/strength	Basis	=	++	+
High speed capability	Basis	-	+++	++

Table 2.4 indicates that both M50NiL and Cronidur 30 display superior performance compared to 100Cr6 stainless steel (e.g. 52100) and type 440C in terms of fatigue life performance in a rolling contact fatigue application. With regard to corrosion resistance, Cronidur 30 was attributed with the best performance of the alloys listed. Cronidur 30 was developed in the aerospace industry where properties of alloys used for bearing applications must incorporate excellent corrosion resistance with fatigue capabilities [80]. It was stated that the bearing life of Cronidur 30 is five times better than M50, another commonly employed bearing steel with a higher ultimate strength than any of those listed in Table 2.4 [84]. The superior characteristics of Cronidur 30 are attributed to the chromium, carbon and nitrogen alloying. The alloying of carbon and nitrogen in martensitic chromium steel, instead of only carbon, was shown to increase alloy hardness and improve resistance to pitting corrosion [85]. The study presented by Gavriljuk and co-workers mainly alludes to the positive mechanical impact of alloying steels carbon and nitrogen instead of carbon alone [85]. The use of classically accepted bearing alloys such as type 440C is limited in aerospace applications due to microstructural properties [80]. Unlike 440C, Cronidur 30 does not contain coarse carbide stringers that provide cracks in components made from 440C with a propagation path. This influences the substantial high strength and isotropic properties of Cronidur 30 [84].

Cronidur 30 is generally applied in a ‘through hardened condition’ in rolling bearing and ball screw applications [84, 86]. The microstructure of the nitrogen rich alloy is different to the classical bearing steels in that it is fine and relatively homogenous [86]. Figure 2.8 presents the microstructure of Cronidur 30 with a uniform dispersion of re-precipitated, fine chromium rich carbides [86]. The absence of large carbides or coarse carbide stringers is attributed to the relatively low carbon composition [84]. In the comparative study by Trojahn and co-workers the average size of carbides present in the microstructure of Cronidur 30 was compared to the same for M50 and type 440C; 10μm compared with 55 μm and 63 μm respectively [84]. This fine grain structure is attributed with minimising component failure as a result of mechanical loading [87]. The alloy has been tested and validated for use in applications up to 320°C according to Bhadeshia [86]. Cronidur 30, used in roller bearings, is less susceptible to contaminants than other bearing steels due to the manufacturing process and damage caused by any contaminants tends to propagate at a slower pace than in other bearing steels [82]. This also lends itself to improved wear resistance by abrasive particles of the alloy. Much of the information readily available about Cronidur 30 tended to include improved properties compared to existing bearing steels. It was difficult to find datasheets or literature discussing limitations of the alloy which leaves a gap in this review.

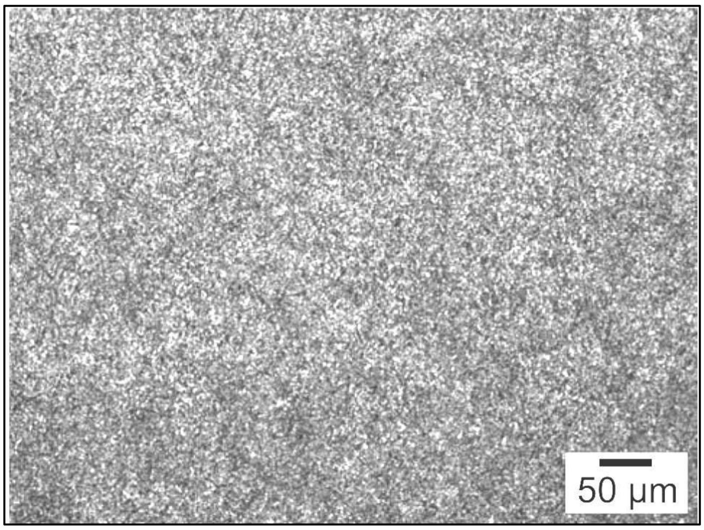

Figure 2.8: Microstructure of Cronidur 30 [86]

The second group of alloys examined with potential for replacing Haynes 25 were nickel-based alloys with a focus on their corrosion resistance, strength and wear properties – where data is available. Nickel-based alloy 625 has outstanding strength and toughness at temperatures up to 1093°C [88]. This is combined with excellent fabrication characteristics [87]. The alloy is exceptionally resistant to fatigue with outstanding corrosion resistance [88]. The resistance to corrosion in flowing seawater was superior to SS 316. The nickel-based alloy, Alloy 825 also demonstrates outstanding performance in seawater as well as excellent resistance in reducing and oxidising acids due to stress corrosion cracking and localised attacks [89]. Hastelloy C276 is a third, highly corrosion resistant alloy that exhibits good strength at high temperatures. The series of Nickel based superalloys, ‘Hastelloy C’ series are commonly used in highly corrosive environments such as nuclear reactors [90]. The corrosion resistance of Hastelloy C276 is considered excellent in seawater as well as excellent resistance to pitting and stress corrosion cracking in temperatures up to 1038°C. The resistance of the alloy to oxidation is considered moderate [91] with the formation of high temperature embrittling precipitates. The relatively low hardness of Hastelloy C276 however discounts it from the list of potential Haynes 25 replacement alloys as this is a key property of an alloy contributing to its wear resistance. Another nickel-based alloy considered is the extremely corrosion and oxidation resistant alloy Haynes 230. This nickel-chromium-tungsten alloy also contains a relatively low volume of cobalt. The alloy is solid solution strengthened with excellent high temperature strength and oxidation resistance [92].

The mechanical properties of the alternative alloys must also be within the range of Haynes 25 in the relevant form. Table 2.6 presents some relevant properties of the appropriate form of Haynes 25 and a selection of alternative alloys for consideration. The values obtained for 0.2% yield strength and the ultimate tensile strength of Haynes 25 in a cold rolled and aged form (20% reduction, aged in 595°C for 2 hours) were set as a benchmark [23]. Similar properties of nominated alternatives were then considered and compared. By comparing these mechanical properties, some of the alloys could be discounted. Stainless steel types 52100 and 440C both met the room temperature requirements. At elevated temperatures however, 52100 steel did not exhibit similar strength and data was unavailable for 440C. Two nickel-based alloys, Inconel 625 and Incoloy 825 respectively, performed in line with what was required at elevated temperatures however did not exhibit the same level of strength at room temperature. At room temperature the mechanical properties of Cronidur 30 were considered acceptable when compared to the same for Haynes 25. Data was unavailable for the highest temperature values that were available for Haynes 25 data. An intermediate strength measurement of Cronidur 30 indicated that the alloy would exhibit acceptable tensile properties at elevated temperatures. Data obtained on a third nickel based alloy under consideration, Hastelloy C276, indicated that it has acceptable, if not superior tensile properties when compared to the relevant form of Haynes 25. The low hardness of Hastelloy C276 however indicated that it was unlikely to exhibit good wear resistance relative to Haynes 25. Finally, low cobalt, nickel-based alloy Haynes 230 was discovered to have close ultimate tensile strength values at the two temperatures considered, but slightly lower 0.2% yield strength at the elevated temperature. Within this remit, the alloys deemed acceptable for further consideration to replace Haynes 25 in this form are Cronidur 30 and Haynes 230. Table 2.5 presents the chemical composition of each of these alloys.

Table 2.5: Alloys selected as those which are most suitable to replace Haynes 25 of those considered in this review

Alloy	Ni	Mo	Cr	Fe	W	Co	Mn	C	N	Other
Cronidur 30	0-0.5	0.85-1.1	14-16	Balance			0-1	0.25-0.35	0.3	0-1
Haynes 230	57 balance	2	22	3 max.	14	5 max.	0.5	0.1		0-1

Figure 2.9 presents the microstructure of an annealed and sample of Haynes 230. Primary carbides are present in the microstructure in the form M_6C both at greain boundaries and dispersed throughout the microstructure [93]. Grain coarsening in prolonged high temperature periods is resisted in the microstructure of the alloy due to these tungsten rich carbides [93]. $M_{23}C_6$ carbides may also precipitate in the microstructure, promoted by carbon and a high tungsten content and are attributed with the good creep strength resistance of the alloy [93].

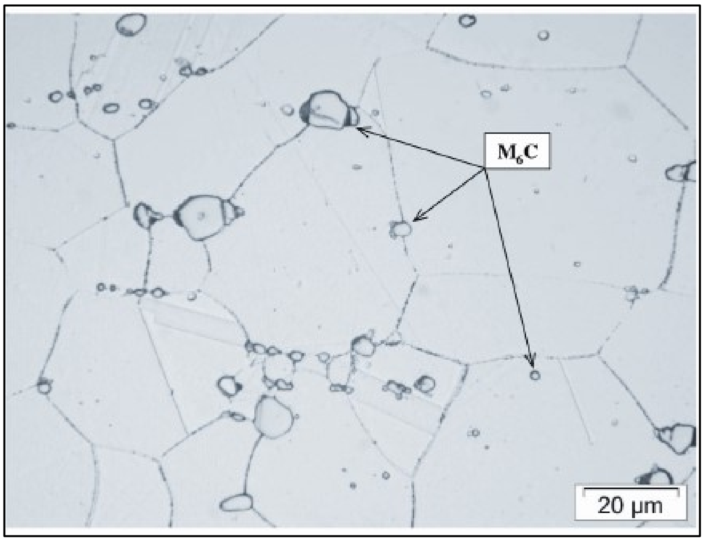

Figure 2.9: Microstructure of Haynes Alloy 230 in an annealed and quenched form [93]

In the Haynes 230 datasheet, made available online by Haynes International, a graph demonstrating the increase in hardness of the alloy as a result of % cold rolling was presented. The increase is significant and indicates the importance of this treatment process to the form of Haynes 230 applied in the bearing application [94]. Obtaining a suitable sample of this alloy for use in ball-on-disc experiments may prove difficult as the cold work formed version of the alloy is readily available in sheet form rather than in bars.

Table 2.6: A comparison of some mechanical properties of Haynes 25 and nominated low cobalt of or cobalt-free alloys

	Description	Hardness [HRC]	0.2Yield Strength [MPa]		Tensile strength [MPa]		Ultimate Strength [MPa]		Density [kg/m^3]	Melting point/range [°C]
Haynes 25 [23]	**Cold rolled (20%) and aged sheet (595°C) for 2 hours**	**47 HRC**	**20°C**	**980°C**			**20°C**	**980°C**	**9051**	**1330-1410**
			1115	**215**			**1315**	**42**		
AISI 52100 [95]		>58 HRC	22°C	1000°C	20°C [86]	1000°C			7810	1424°C
			1410	18.65	1748	33.14				
Stainless steel Type 440C	20°C: Tempered @ 204°C	>58 HRC	20°C				20°C		7650	1482
			1900				2030			
Cronidur 30 [96]	High tempered condition (hardening 1000°C – 1hour/oil, tempering 4hours/ air)	>58 HRC	20°C [84]	640°C [96]			20°C	640°C		
			1850	730			2150	980		
M50NiL *(case hardened)*		>60 HRC	- (1940 for M50)				- (2200 for M50)		7861	
Inconel 625 [97]	20°C: sheet annealed 871°C: hot rolled annealed bar	45 (70% cold reduced form) HRC	20°C	871°C	20°C	871°C			8442	1290-1350
			414-621	529	827-1034	993				
Incoloy 825 [98]	20°C: sheet annealed 1000°C: annealed bar		20°C	1000°C	20°C	1000°C	720 (annealed rod)		8138	1370-1400
			421	200	758	560				
Hastelloy C276 [95]	20°C: Cold reduced (50%), plate annealed at 1177°C 538°C: sheet, heat treated at 1121°C, rapid quenched	86HRB	20°C	538°C			20°C	538°C	8220	1355
			1345	233			1450	613		
Haynes 230 [94]	20°C: 50% cold reduction, no subsequent anneal (3mm sheet) 982°C: Cold rolled and 1250°C solution annealed sheet	40-45 HRC	20°C	982°C			20°C	982°C	8968	1350
			1275	125			1482	172		

2.5.2 Analysis of iron based alloy for Stellite 20 replacement

In a review by Cachon and Denape [22], several cobalt-free alternative alloys were examined and compared to some Stellite alloys to establish their suitability for application in the pressurised water environment. The review listed some iron-based alloys that have been evaluated and discounted. The authors cited two reasons for this; a coefficient of friction significantly higher than that of the Stellite alloys in question and the deterioration of surfaces in contact when contact pressure exceeded 40 MPa [22]. Bowden and co-workers identified the generation of a low stacking fault energy matrix and the % fraction of carbide phases in the microstructure of an alloy as two significant considerations in work related to the identification of cobalt-free alloys to replace Stellites [18].

A thesis by Bowden [20], a project aligned to this research, investigated two cobalt-free alloys, nominated as candidates to replace the cobalt-based alloys, namely Stellites, used in hardfacing applications within the reactor. Bowden presented a study aimed at characterising and assessing the metallurgical properties of two iron-based alloy systems. The first is stainless steel Tristelle 5183 and the second is a that has been developed and patented by Rolls Royce, a derivative alloy of Tristelle 5183, RR2450 [18, 99]. Tristelle 5183 is an alloy with a relatively low cobalt composition, up to 1.5% [99]. The hardness of Tristelle 5183 is in the range 350-450 HV [99]. The development of RR2450 by Rolls Royce plc aimed at providing an alloy that could operate in the nuclear environment, with elevated hardness. Within the patent, see Appendix D, a graph was presented which compared the wear resistance of the alloys and demonstrated superior mechanical performance of RR2450 at 300°C. The study by Bowden, demonstrated the reduced wear resistance of Tristelle 5183 at 190°C, attributed to microstructural properties of the alloy [20]. Table 2.7 presents the composition of both alloys provided in [20].

Table 2.7: Composition of two iron-based alloys part of research to remove cobalt from nuclear reactor environments

	Fe	Cr	Ni	Nb	Si	C	Ti
RR2450	Balance	21.0	9.0	8.5	5.8	1.8	0.5
Tristelle 5183	Balance	21.0	10.0	7.5	5.0	1.9	-

2.6 Building a wear prediction model

Introduction

Understanding the behaviour of the alloys applied in the sliding wear contacts is also approached using predictive wear models. As wear is an important factor which influences component and product service life, the prediction of wear should have a significant role to play in engineering and material selection [5]. There are numerous research groups worldwide with an interest in understanding the wear mechanisms at play when wear is induced in reactor components as a result of the system vibrations discussed in Section 2.4.1. [47]. The data being gathered is being used to understand the phenomena and also to develop versatile wear prediction models [47]. The assessment of the predictive capabilities of existing wear models was relevant in the development of a model that could be useful to this project. The absence of a single wear prediction model for general purpose was documented by Meng and Ludema [100], and was partially attributed to factors such as inaccuracies and being subjective in expressing the mechanisms of wear. The review defined a wear model as 'a listing, description or discussion of the variables that influence wear' [100].

A difficulty in quantitatively assessing fretting wear, for instance, arises from the lack of a well formulated model [101]. Wear experiments are generally considered as being the most reliable sources in understanding the tribological behaviour of contact problems [58]. These experiments are in the place of in situ measurements which can be expensive and time consuming [7]. The literature encapsulating wear prediction models reviewed for this summary was largely based on such laboratory experiments. The volume of experimental wear data identified was not matched by the volume of modelling data. This can be attributed to difficulties that arise when developing contact models of complex engineering surfaces. Complexities that arise include severe local deformations in the contact, the generation of heat by friction, contamination of the interaction by third bodies such as wear debris and changing lubrication regimes [54]. It was therefore a challenge to relate tribological performance to the material properties of components in such systems [102]. The wear rate or the resistance to wear by a material is dependent on the wear mode, a function of the entire tribosystem [69]. Elleuch and Fouvry illustrated that the wear rate in an interaction is composed of the formation of wear debris and the flow of ejected debris from the contact [103, 104].

A survey by Hegadekatte and co-workers categorised wear models available in literature into two categories; 'mechanistic models' and 'phenomenological models' [7]. Mechanistic wear models are those which are based on the failure mechanism of a material whereas the phenomenological models are those based on values arising from contact mechanics [7]. Different analytical and numerical approaches were presented in the literature reviewed using software packages such as ABAQUS [6, 7, 54, 101] and ANSYS [5] as well as less computationally expensive analytical methods [7, 104]. Research into the impact of system loads on the stress fields produced in a contact was initiated by Hertz via an analysis of the stress produced in a contact by two elastic solids [5, 105]. Contacting bodies are regarded as 'elastic half spaces' with an elliptically shaped area of contact. Hertzian contact equations are invoked to calculate contact pressure and subsurface stress distribution in such contacts depending on component geometry and the normal load applied to the interaction.

Models describing wear are mathematically expressed in a variety of ways using straightforward empirical relationships as well as more complicated, physical based expressions [5]. Meng and Ludema listed 100 different variables and constants that have been employed in the literature reviewed, highlighting the variation in parameters employed [100]. Sliding wear, as a quantitative value is a function of load, sliding velocity, temperature, material properties and lubrication regime amongst other parameters [58]. The wide variety of parameters that can influence the behaviour of materials in contact was demonstrated in work presented by Bartosz and co-workers in which a crystal plasticity finite element model was developed to predict galling wear as a result of sliding between two rough, metal contacts under a normal load [106]. The model used crystal plasticity analysis to simulate the interaction and considered several parameters including adhesion, material plasticity, material hardening, surface roughness and asperity geometries and spacing. An example of a more generalised wear analyses was included in the review of wear maps presented by Lim and Ashby [53] that plotted wear regimes as a function of different loads and sliding velocities using dry pin on disc experiments.

A significant volume of the work assessed seeking to build a wear model using experimentally obtained data used Archard's equation for sliding wear as a basis. The equation makes the assumption that the stress fields produced on components in contact interactions and the sliding distance over which the interaction takes place are the most significant parameters to consider when making an assessment of sliding wear [107]. This is an attempt to simplify the complex nature of mechanical wear as discussed in Section 2.4. These models are categorised as phenomenological models. The equation describes the relationship between the material wear volumes lost in a sliding interaction under an applied normal load over a prescribed sliding distance [7]:

$$V = \frac{kFs}{H} \qquad \text{Equation 2.7}$$

where V is the volume of material removed, k is the wear coefficient, F is the normal load applied in the interaction, s is the sliding distance and H is the hardness of the softer material.

The wear coefficient, k, establishes an agreement between experimental and theoretical observations made i.e. factors outside of load, sliding distance and material hardness that affect the wear rate are incorporated in it [5]. The value was defined by Archard as the probability that an asperity interaction will result in the formation of a wear particle. While this model is not strictly applicable to all sliding wear interactions it is used extensively in the form of Equation 2.6 as well as in alternative formulations.

Wear depth produced as a result of such contact interactions is deemed more critical in engineering applications than the wear volume produced [5]. Archard's equation was modified to calculate wear depth instead of wear volume, relating it to the average pressure in the apparent area of contact and the incremental sliding distance [101];

$$\frac{dh}{dS} = k_1 p(x) \qquad \text{Equation 2.8}$$

where dh is the increment of local wear depth produced over *dS*, the increment of sliding distance. k_1 is the local wear coefficient and *p(x)* is the local contact pressure. A derivation of this equation from the original version of Archard's wear equation was provided in [101]. Although the equation used a local value for the wear coefficient, in their numerical wear prediction model, McColl and co-workers used a measured value for k across the complete contact width [101].

In work conducted by Fouvry and co-workers Ref. [108], it was demonstrated that in an interaction where the coefficient of friction did not remain constant, the wear coefficient and therefore Archard's equation were invalid. Instead, the authors implemented a fretting wear model based on wear energy dissipation via heat and/or debris flow and plasticity induced by the interaction. While the authors acknowledged an advanced state of model availability concerned with crack formation and propagation, the same was not observed for the prediction of the production and interaction of wear debris. Producing a wear prediction model that is based upon a relationship between wear rate and the formation and retention or ejection of debris from the contact was the concern of this work [108].

2.6.1 Numerical wear prediction models

Finite element software is acknowledged as a versatile tool which can complete stress analysis calculations as well as simulating the changing geometry of a component due to wear [5]. Hegadekatte and co-workers have conducted significant work on the wear prediction modelling of sliding wear interactions using finite element numerical methods [6, 7, 54].

The first step of building a finite element wear model such as those presented by Hegadekatte, Leen or McColl is the definition of the contact problem [54, 101]. The geometry of the components and their material properties are entered. The surfaces are discretised by applying a fine mesh. The mesh applied to the area of contact will be more refined than the rest of the component to increase computational efficiency [109]. This is done by partitioning each component, gradually refining the mesh toward the contact zone. For a computationally efficient and reasonably accurate 3D wear model it was recommended by Cruzado and co-workers that the optimum mesh size should be approximately 3-4% width of the wear scar [109].

In the second step of the wear model, the FE software solves the contact problem defined in the first [101]. Contact area, pressure and the location of surface nodes within the adaptive mesh domain are calculated and/or recorded. Within the region of contact the mesh applied is 'adaptive'. This means that as wear progresses and the geometry of the test component(s) changes, the mesh will adapt, in a normal direction to the component surface. Adaptive meshing works by running a user defined subroutine UMESHMOTION, written in Fortran, in parallel to the ABAQUS simulation [6, 101]. Adaptive meshing and the subsequent change in geometry of the wearing component, is the result of the application of Equation 2.8, modifying the location of the surface nodes on the mesh through calculating the wear depth for each sliding cycle using the experimentally obtained wear coefficient. As a result of this changing geometry and thus the contact area, variables such as contact pressure and subsurface stresses will update accordingly [101]. The model, presented by McColl and co-workers illustrated that Archard's wear equation could be applied locally in the contact area to predict fretting wear [101, 109].

In the final stage of the process the subroutine uses the recorded values of nodal contact pressure and location to calculate the wear depth produced as a result of the sliding interaction. This wear depth is then used to modify the location of nodes on the surface of the adaptive mesh. This procedure is repeated until the final wear cycle has completed.

The finite element method is considered to be a robust tool in wear investigations as outputs include more than solely wear measurements [110]. Work presented by Gonzalez and co-workers highlighted the opportunity offered by numerical methods to better understand thermo-mechanical properties of a component in sliding wear experiments [111]. This was done by incorporating features of a contact interaction beyond pressure and the wear coefficient such as Coulombic friction, plasticity of a component and heat generated in the contact caused by plastic deformation. The heat produced in the contact is transferred into the test components, negatively impacting the hardness of the alloys, thus increasing the rate of wear. The model indicated that temperature had a more critical effect on the wear rate than the applied pressure. Although the model was not found to agree quantitatively with experimental results, it does provide a good example of the capabilities of the finite element method as a wear prediction model beyond Archard's linear equation.

Arjmandi and his team [110] identified limitations of models presented in [5] and [54] as their high computational expense and their reliance on one wear coefficient which had led to experimental validation inconsistencies. They argued that the changing value of wear coefficient as a result of changing wear regimes, *i.e.* from running in to steady state regimes, should be considered as an important parameter in building a wear model. This theory was backed by research in [112] where it was demonstrated how the accuracy of the finite element model was related to the care with which the running in period was simulated. The solution suggested to account for this was to increase the number of steps in the simulation stage.

Another factor limiting such models is the omission of the physical metallurgical changes in a material which has been exposed to mechanical wear [60, 113]. Suh and colleagues proposed a model that considered phenomena beyond those encompassed by Archard's equation [113]. The work was developed around the concepts of dislocation theory, plastic deformation of the wear surface as well as the significance of the type of wear particles produced. The work also considered crack dimensions and void location following the pin on disc experiments performed. The relationship developed in [113] made a list of assumptions allowing for the incorporation of surface asperities and a link between sliding distance, void and crack formation in component sub surfaces in the wear model.

2.6.2 Semi-analytical wear prediction models

The use of a semi-analytical sliding wear model was presented by Hegadekatte and co-workers as an alternative to computationally expensive finite element wear depth prediction models [7]. While the finite element models discussed in Section 2.6.1 computes wear for each surface node of the finely applied adaptive mesh in each sliding increment, the semi-analytical model determines a 'global' wear depth for each sliding increment. The global scale is applicable to cases with geometry which is relatively easy to calculate. The model is initiated by entering component geometry, material properties (Young's modulus, Poisson's ratio) and experimental parameters (applied load, sliding distance, wear coefficient) [6, 7]. Assuming Hertzian theory for two elastic bodies in contact [6, 105], the contact area dimension(s) and average pressure over this contact are established. The model proceeds to employ Equation 2.8 to calculate wear depth. The work was successful in demonstrating a computationally inexpensive wear prediction model in good quantitative agreement with one produced using numerical methods for wear of components in pin on disc sliding and twin disc rolling configurations.

Done and co-workers also presented a semi analytical wear model that was validated using experimental fretting wear data [104]. Wear was modelled using information presented by Fouvry, discussed in the Introduction to this section (Section 2.6). This model was further developed than the previous model described as it also considered debris entrapment in the contact.

2.6.3 Incorporating the impact of corrosion in a wear prediction model

The phenomena discussed in Section 2.4.2, the formation of an oxide glaze on a component surface, is also considered very relevant to the work conducted for this thesis as it is thought to influence the overall wear rate. Jiang and colleagues highlighted the importance of the synergism between mechanical wear and corrosion wear in a sliding interaction and developed a model with the purpose of demonstrating this [114]. It is generally agreed that there is a relatively low understanding of this phenomenon. Identifying time dependent growth kinetics of the glaze on a component surface in appropriate conditions will allow the author to build a model that simulates mechanical wear and oxide growth together. Déforge and co-workers concluded from their study of tribocorrosion in a PWR environment that any work undertaken to model wear in a nuclear reactor should include both the mechanical and electrochemical phenomena [115]. The work presented by Jiang and co-workers, highlighted that there were significant challenges to be resolved in order to combine the two. To predict the rate of crack propagation or repassivation kinetics of oxide layers on component surfaces, for instance, is already a highly complex process. To consider them as interdependent phenomena further heightens this complexity [114].

The general theory illustrated a sequence starting with passivation of the component surface(s) during periods of latency i.e. no frictional interactions occurring, depassivation of the passive layer via frictional interaction, followed by subsequent repassivation of the surface during latency. Results presented by Wenger and co-workers indicated that the kinetics of repassivation of the passive layer in the active wear track was unaffected by the contact pressure of the test [78]. The latent period of the disc in a continuous sliding wear test may be established based on the path length and the rotational sliding speed. It may not however be calculated for the pin or ball as that component would be in contact with the disc surface throughout the test [78]. Wenger and co-workers investigated the tribocorrosive relationship in sliding wear experiments for Stellite 6 in two electrolytes; 0.5M sulphuric acid and a solution of boric acid with lithia at 20°C and 85°C respectively. Faraday's law was used to find the thickness of the layer formed based on the current transient recorded throughout the experiment integrated to find the charge variation [78]. The work reviewed on this topic as part of this summary was not exhaustive, however, it did highlight its relevance in the consideration of the behaviour of components in the nuclear reactor environment.

2.6.4 Review

Much of the information which has been considered is based around theories and experiments investigating sliding wear. While this is a constituent part of the overall rolling wear phenomenon, it is also important to consider other manifestations of wear applicable in the rolling element bearings. The inherent difficulty in modelling rolling contact wear was identified El Thalji et al [50]. The paper considered the numerous mechanisms of which rolling wear is composed and worked to propose a model which would describe wear over bearing life. This lifetime is divided into five stages; running in, steady state, defect initiation, defect propagation and damage growth. To each of these stages, the active or dominant mechanisms of wear are assigned. Building further on an empirical study of wear progress, work conducted in Ref. [50], moved to incorporate the interaction of the relevant wear mechanisms and stress contact mechanisms such as those developing from asperities, dents and inclusions. The model presented was a probabilistic one i.e. focussed on the wear mechanisms and stress concentrations most likely to occur during the lifetime of the rolling element bearing.

2.7 Conclusion

There are studies that have been conducted in literature included as part of this review that concern the sliding wear behaviour of some cobalt-based alloys in prototypical nuclear reactor environments. The author is unaware, however, of any studies that investigated the sliding wear behaviour of Stellite 20 and Haynes 25 in such an environment, and more specifically, how they interact together. There is also an appreciable gap in the literature on the rolling wear of cobalt-based alloys, in any environment. The gaps identified provided excellent scope for this thesis as the work being conducted could attempt to explore and develop knowledge on the topics, albeit in some cases, at a high level. Work by Dréano et al Ref [21]and Jiang et al Ref [114] provided a good insight into the potential of using mathematical modelling techniques to simulate the mechanical and chemical interactions observed throughout some wear processes. Dréano and co-workers introduced a model developed to combine the influence of oxidation to the sliding wear of alloys, specifically, Haynes 25. This thesis intends to initiate a study that would apply such a model, although significantly less complex in its early stages. The author intends to use information presented throughout literature, including what was presented and discussed by Dréano and co-workers, to build an FE model that would simulate the interplay between sliding wear and the oxide layer formation on component surfaces using FE methods. The interplay between these phenomena is discussed in literature and is attributed with providing some cobalt-based alloys with their exceptional wear resistant properties at elevated temperatures.

Chapter 3 Sliding wear investigation in a simulated nuclear reactor environment

Chapter 3 Sliding wear investigation in a simulated nuclear reactor environment

Part of the work described in this chapter has been published in ***Wear*** *(Ref. [27])*

Introduction

Cobalt-based alloys offer excellent resistance to wear and chemical corrosion and thanks to their exceptional properties in water facing environments they are often used in different bearing surfaces in nuclear applications. Stellite 20 and Haynes 25 are two cobalt-based alloys that are used for the rolling and race component in rolling element bearings (REBs) that facilitate movement of key structural components within the reactor core. Due to unfavourable behaviour in the reactor environment there is a drive to reduce or remove cobalt from the reactor system. The wear behaviour of Stellite 20 and Haynes 25 was investigated in order to set a benchmark from which to compare any low cobalt or cobalt-free alloys nominated as suitable replacement alloys.

The process of understanding the wear behaviour of Stellite 20 and Haynes 25, each consisting of approximately fifty per cent cobalt, was initiated with sliding wear experiments. This investigation was conducted using a bespoke design ball on disc tribometer built with support from Rolls Royce Plc (RR) at the University of Nottingham (UoN). The sliding wear experiments were lubricated by water that had the same chemistry as that of the primary coolant that circulates in a reactor core. This apparatus may be enclosed in an autoclave which facilitates water lubricated experiments above boiling point, an attempt to mimic the high temperature water facing conditions in a reactor core. Although the autoclave adopted in this study is a "static" autoclave, to the best of our knowledge no other test rig (tribometer) exists in the UK that employs a "flow" autoclave, where the primary coolant is circulated around the contact; hence, this was deemed as the best equipment to perform our initial assessment of wear in conditions that mimic a nuclear reactor. Experiments were carried out in a range of environmental conditions to evaluate the impact of increased temperature and/or normal load on the sliding wear behaviour of the alloys. The experiments conducted at the University of Nottingham were supervised by Professor Philip Shipway and Mr Deen Zhang. The experimental results were analysed at Imperial College London (ICL), by measuring the wear volume and depth on the ball and disc components. This was followed by a topographical and compositional investigation using a white light interferometer (WLI) and the Secondary

Electron (SE), Backscattered Electron (BSE) and Energy-dispersive X-ray Spectroscopy (EDX) modes of a Scanning Electron Microscope (SEM).

A performance benchmark was established via the analysis of the post experimental Stellite 20 and Haynes 25 ball on disc components. A cobalt-free iron-based developmental alloy, RR2450 [99] was nominated by RR as an alloy that may have the potential to replace Stellite 20 in the REBs. RR2450 is a complex alloy that was developed by RR, derived from stainless steel Tristelle 5183, with the intention of using it to replace cobalt-based alloys in nuclear applications such as hard facings and bearings [18]. RR2450 balls were manufactured for the purpose of experiments conducted in this project using RR2450 powder supplied by RR. The alloy used has been developed in a way by which production of components by hot-isostatic pressing the powder, will lead to a refined microstructure with grain and carbide size that will lend itself to wear resistance in the nuclear reactor environment [20]. The Stellite 20-Haynes 25 ball on disc experiments were replicated replacing the Stellite 20 balls with RR2450 balls. The same post-experimental analysis was carried out as for the Stellite 20-Haynes 25 ball on disc experiments. The post-experimental analysis of the RR2450-Haynes 25 experiments was compared to the performance benchmark established following the Stellite 20-Haynes 25 experiments. The wear volume and depth measured, visual and compositional analyses were compared. The information and data presented in this chapter was used to make a recommendation for or against the merit(s) of RR2450 as an alloy that has the potential to replace Stellite 20 as the rolling element in bearings to be used for nuclear reactor applications.

3.1 Materials and Methods

3.1.1 Materials

3.1.1.1 Stellite 20 ball and Haynes 25 disc

The 9.525 mm diameter Stellite 20 balls were purchased from RGP balls, Milan. The hardness of the Stellite 20 balls as per the technical data sheet provided by RGP Balls was 56-63 HRC (612-775 HV), see Appendix A for a copy of datasheet. The microstructure of the Stellite 20 balls used in this project is presented in Figure 3.1, obtained using the BSE mode of the SEM. Carbides are noted as the most significant strengthening agents of these alloys and their presence is influenced by the carbon composition in the alloy. The dark grey chromium rich carbides and the white tungsten rich carbides, as discussed in Section 2.2, Chapter 2, have been identified as M_7C_3 and M_6C, respectively. Chromium contributes to the corrosion resistance of the alloy with tungsten making a significant contribution to alloy hardness. The medium/light grey area is the matrix in which these carbides are matrix and is attributed with high temperature hardness of the alloys [12, 20].

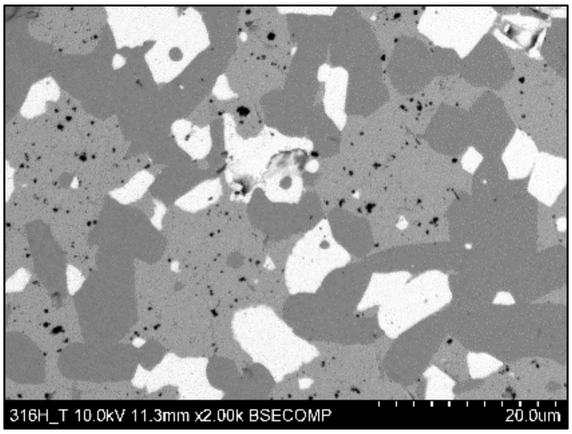

Figure 3.1: Microstructure of an undamaged Stellite 20 ball surface taken using the BSE mode of an SEM

The Haynes 25 balls were cut from a block of Haynes 25 provided by RR in 30% cold reduced form. Prior to machining the discs, the bulk Haynes 25 sample was aged at 605°C (+/- 5°C) for 6 hours in an uncontrolled atmosphere and cooled naturally in air. This treatment method is applied to Haynes 25 used for race material by RR. The approximate hardness of the block after ageing was measured to be 570 Hv30. The minimum UTS is 1586 MPa and the minimum 0.2% proof stress is 1000MPa. The recommended surface roughness for a disc applied in a pin-on-disc experiment is R_a <0.8 µm and the recommended surface roughness for the inner race in an SKF rolling bearing is R_a <0.4 µm [116, 117]. The average final surface roughness of the discs was 0.07 µm which was well within the recommended limits. The microstructures of a cross section of a Haynes 25 disc can be observed in Figure 3.2. The image was obtained using a light microscope. It was necessary to chemically etch the Haynes 25 sample in order to see the microstructure, see Appendix C for the etching method used. Haynes 25 is a single phase alloy and in Figure 3.2, the orientation, shape and size of the grains can be clearly identified. The composition across the alloy was uniform, presented in Table 3.1.

Figure 3.2: Microstructure of a Haynes 25 disc cross section taken using an optical microscope

Table 3.1 provides that compositional data for each of these alloys established using the EDX attachment on a Hitachi S-3400N SEM (Oxford Instruments).

3.1.1.2 RR2450 ball and Haynes 25 disc

RR2450 is a developmental alloy patented by RR, see Appendix 3.4 for patent document. RR2450 was nominated as an alloy with the potential to replace Stellite 20 in nuclear reactor components and was supplied in powder form by RR for use in this experimental study.

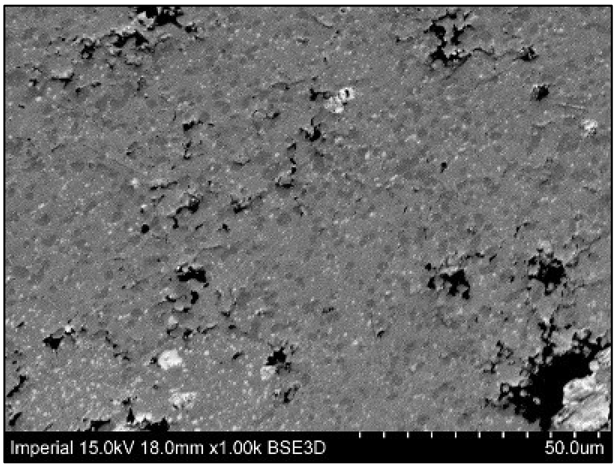

Figure 3.3: Microstructure of an undamaged RR2450 ball surface

The powder was used to produce a bar using hot iso-static pressure at Bodycote, Chesterfield, UK. The bar was then machined and polished into sixteen 10 mm diameter balls by PCS Instruments, London, UK. Figure 3.3 is a BSE image of a section of an RR2450 ball surface prior to any testing. Table 3.1 provides the compositional data of the balls obtained using EDX analysis. RR2450 was designed to have a duplex microstructure with a high proportion of carbides due to the high percentage composition of carbon [20]. These carbides are in the form $(Nb, Ti)CN$ and M_7C_3 , where M represents a combination of chromium and iron. Bowden also identified a silicide phase that made up approximately 20% of the microstructure of RR2450 and going forward from Bowden's work, RR2450 is now considered to have a high strength triplex microstructure, which may be correlated to its superior wear resistance at high temperatures when compared with Tristelle 5183. The dark pit like areas in Figure 3.3 are a consequence of the manufacturing process and will be discussed further in Section 3.2.2.

Table 3.1: Compositional information for Haynes 25, Stellite 20 and RR2450 components used in this experimental study

	Co	**Ni**	**Cr**	**W**	**Fe**	**Mn**	**Si**	**C**
Hayne 25	Bal.	10	20	15	3	1.5	0.4	0.1
Stellite 20	Bal.	3	30-34	13	3	0.5	1	2.8-3
	Fe	**Cr**	**Ni**	**Nb**	**Si**	**C**		
RR2450	47.5	22	9	8	6	7		

3.1.2 Methods: Ball on disc sliding wear experiment

An image and a schematic drawing is presented in Figure 3.4 of the ball on disc tribometer located in the Mechanical Engineering Department at the University of Nottingham. The ball was held, fixed in place in a ball holder and a normal load was applied by the application of free weights. A contact was made between the ball and disc and the load was translated to the disc. The disc was held in a disc carrier attached to a shaft driven at 200 rpm by an external motor. The flexures, or stabilising plates, were designed to provide lateral constraint to the loading system, see Figure 3.4. In the early experimental stage of this project, these plates were inadvertently leading to significant vertical stiffness and the contact load, between the ball and disc, was dependent on vertical positions which resulted in a loss of contact when total wear depth exceeded a certain limit. This was identified due to the relatively high wear that was produced on the Stellite 20 balls in the first set of experiments completed. The design was modified by Professor Philip Shipway and Mr Deen Zhang.

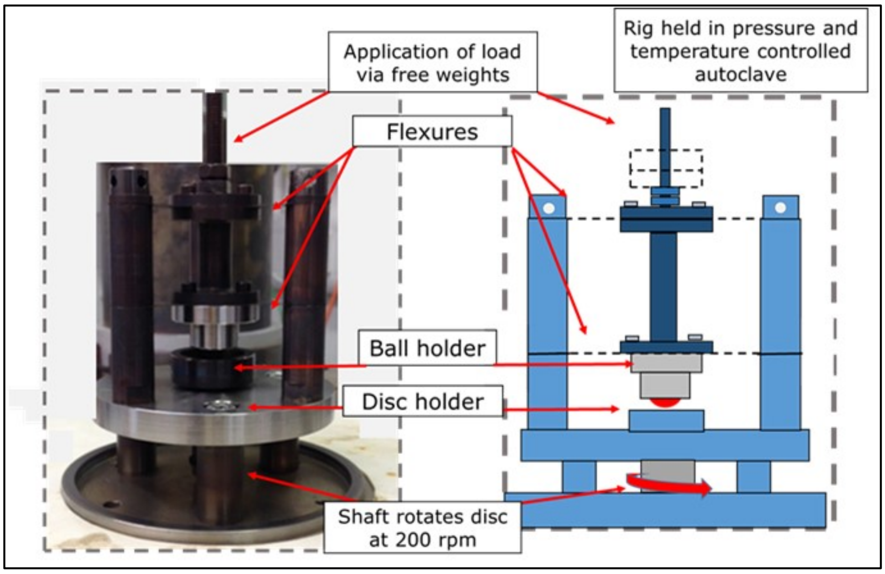

Figure 3.4: Ball on disc tribometer located at the University of Nottingham

The tribometer may be enclosed in an autoclave allowing for water lubricated experiments at elevated temperatures ranging from room temperature to 250°C, see Figure 3.5. Fluid (solution of 10% Li-OH in distilled water) mimicked the coolant that circulates in the relevant nuclear reactor loop. The apparatus is equipped to accommodate experiments using normal loads up to 35 N. Table 3.2 lists the conditions for each experiment conducted in this investigation. Each set of experiments was repeated once.

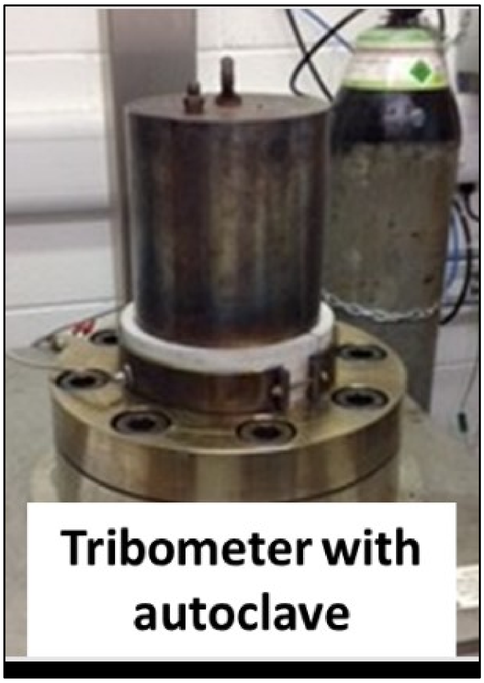

Figure 3.5: Ball-on-disc tribometer enclosed in autoclave for high temperature experiments

Table 3.2: Environmental conditions applied in ball-on-disc experiments

Experimental setup	**Description**					
Time [min]	180					
Speed [rpm]	200					
Sliding distance [m]	2296					
Experimental conditions	**Experimental number**					
Condition reference	1	2	3	4	5	6
Normal load [N]	10	10	10	35	35	35
Corresponding maximum contact pressure [GPa]	1.13	1.13	1.13	1.71	1.71	1.71
Temperature [°C]	RT	100	200	RT	100	200

3.1.3 Post experimental analysis method

Experimental components should be cleaned using non-chlorinated and non-film forming agents and solvents [117] before and following experiments. Ethanol was used for these experiments.

3.1.3.1 Friction Measurement

Data acquisition software recorded torque (Nm), shaft speed (rpm), vessel temperature (°C), pressure (bar) and the number of revolutions completed throughout the experiments. Control experiments were run to establish the average background torque in the system in the absence of experimental components in contact. The value identified was 0.065 Nm which was subtracted from values for torque recorded by the software.

3.1.3.2 Wear measurement

A micrograph was taken of each ball scar and the approximate diameter was measured using ‘ImageJ’ software, see Figure 3.6 (a) [118]. Equation 3.1 (a) and (b) were used to measure the volume lost by the ball:

$$V = \pi h^2 \left[R - \frac{h}{3}\right] \qquad \text{and} \qquad h = R - \sqrt{R^2 - r^2} \qquad \text{Equation 3.1 (a) and (b) [119]}$$

where V is the volume of material lost, h is the maximum wear depth, R is the ball radius and r is the radius of wear scar, as schematically depicted in 3.6 (b).

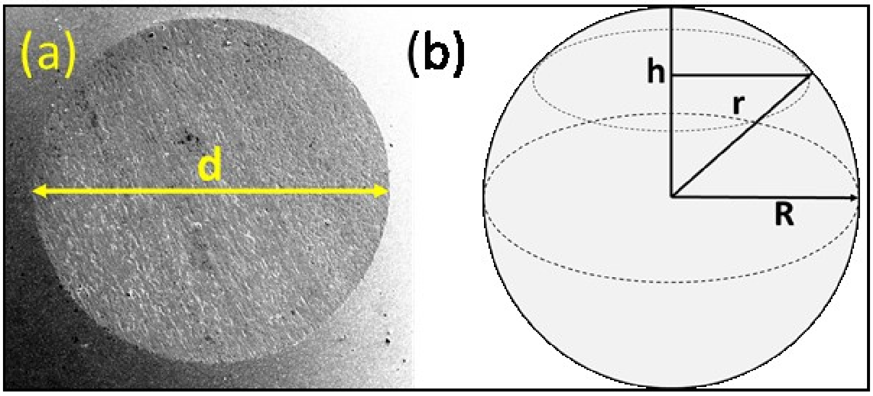

Figure 3.6: Micrograph of a scar produced on Stellite 20 ball after sliding experiment and (b) schematic of ball used to describe volume loss calculation

A VEECO WYCO white light interferometer (WLI) was used to measure the volume loss from the disc by measuring the average wear track profile at ten points along the track and using geometry to calculate the total volume lost [120]. The wear coefficient for the contact pair in each experiment was then calculated using Equation 3.2, Archard's wear law. The WLI was also used to obtain surface roughness of the components prior to experimentation.

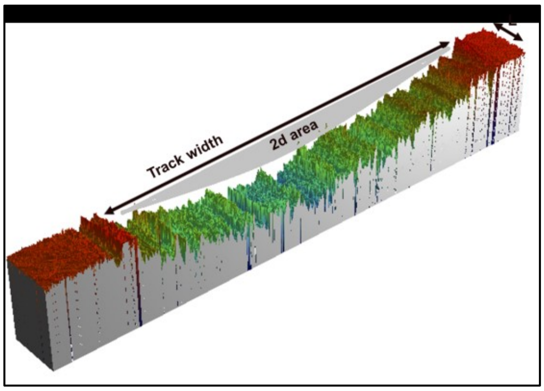

Figure 3.7: Example of profile of one of the sections of the disc track used to calculate wear volume

$$V = \frac{kFs}{H} \qquad \text{Equation 3.1 [7]}$$

where V is the volume of material removed in m^3, k is the wear coefficient, F is the normal load applied in the interaction in N, s is the sliding distance in m and H is the hardness of the softer material.

3.1.3.3 Microstructural and compositional analysis

The secondary (SE) and backscattered electron (BSE) modes of a Hitachi S-3400N scanning electron microscope (SEM) were used to examine the impact of the wear experiments on the post experimental components. The energy dispersive x-ray (EDX) mode was used for compositional analysis of the wear scars and tracks.

3.2 Results and discussion

The average temperature and vessel pressure recorded for each experiment is presented in Table 3.3.

Table 3.3: Average vessel temperature and pressure recorded during experiments

Condition reference	1	2	3	4	5	6
Normal load [N]	10	10	10	35	35	35
Materials: Stellite 20 vs. Haynes 25						
Vessel pressure [bar]	0	2	27	0	2	27
Vessel temperature [°C]	17	102	206	17	102	206
Materials: RR2450 vs. Haynes 25						
Vessel pressure [bar]	0.29	2	20.20	0.38	2	20.54
Vessel temperature [°C]	21	102	200	23	103	201

3.2.1 Friction measurement

3.2.1.1 Stellite 20 ball on Haynes 25 disc

In the early stage of experimentation, the torque meter used to measure frictional changes throughout an experiment was unavailable. Data was therefore only measured from experiments in the upper loading condition (35 N) at room temperature, 100°C and for two 200°C experiments.

Figure 3.8 presents the coefficient of friction (COF) for the first 30 m of the 2296 m experiment. The results are filtered like this to give a clearer view of the early, running in stage of experimentation.

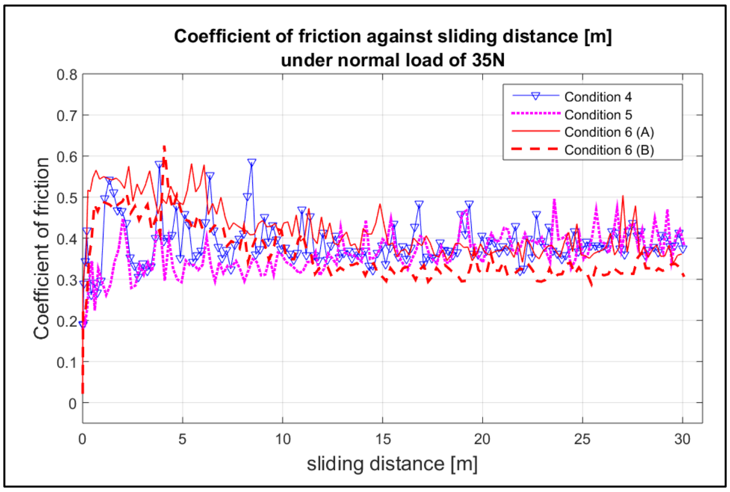

Figure 3.8: Coefficient of friction measured for first 30m of sliding between Stellite 20 balls and Haynes 25 discs

The running in time for each experiment can be seen clearly within the first 10m of sliding. The lines representing the data recorded in the 200°C experiments are consistent in that the COF was slightly elevated compared to the values recorded at lower experimental temperatures. Overall however, in the upper loading condition, temperature did not appear to significantly impact the COF.

3.2.1.2 RR2450 ball on Haynes 25 disc

The torque meter recorded torque throughout the RR2450 vs. Haynes 25 sliding wear experiments under all conditions. The torque values were again converted to produce the coefficient of friction represented throughout the experiment with the results presented in Figure 3.9 (a) and (b).

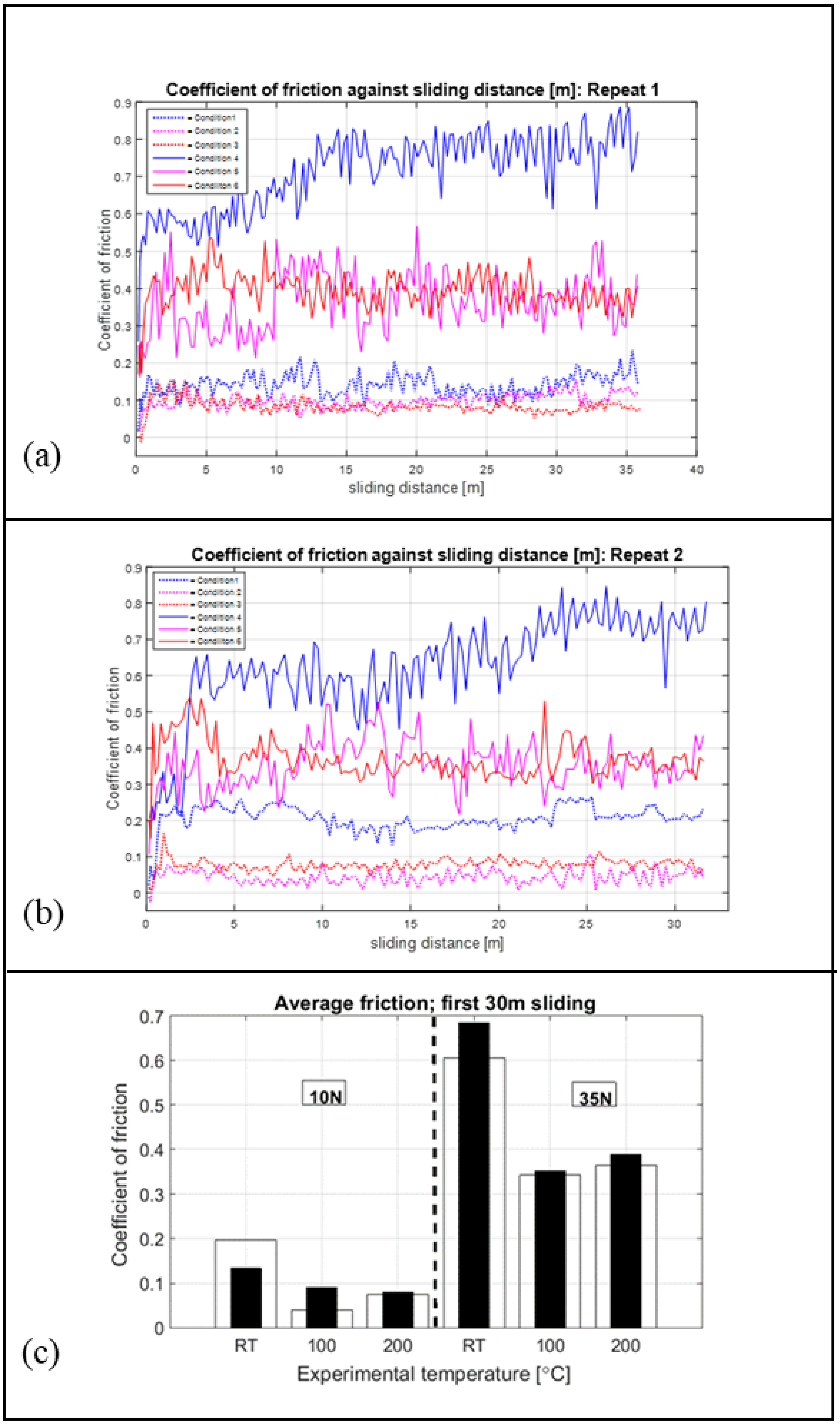

Figure 3.9: (a) Coefficient of friction measured for first 30m of sliding between RR2450 balls and Haynes 25 discs (b): Repeat experimental results and (c) the average COF at each test condition

The relationship between load and friction is clearly demonstrated by the data presented. Comparing the data for repeated experiments, a trend was observed, see Figure 3.9 (c). In both loading conditions, the coefficient of friction measured in the first 30m of sliding at room temperature was notably higher than the same for the 100°C and 200°C experimental temperatures.

3.2.2 Wear measurement

3.2.2.1 Stellite 20 ball on Haynes 25 disc

Figures 3.10 – 3.12 present results for the three temperatures tested under each loading condition. Images of ball wear scars and disc wear tracks are presented for each experimental temperature with the corresponding disc wear track profiles for 10 N and 35 N loads. In Figure 3.10 and 3.11 (a) and (c) the evolution of wear on the ball surface from uneven damage to a distinctive scar can be followed from the 10 N load to the higher 35 N load. At 200°C, where the wear to the ball surface increased significantly under each loading condition, this evolution does not seem as pronounced. The scar radius has increased rather than changing shape, perhaps implying more uniform wear of the ball surface earlier in the interaction in the highest temperature condition. This is likely to be due to a reduction in the wear resistance of the Stellite 20 ball with increased temperature. Figure 3.10 – 3.12 (b) and (d), produced using the white light interferometer, show a clear increase in the width of the disc track with increasing temperature and load. The topographical evolution of wear is interesting. At the most conservative experimental conditions, see Figure 3.10 (b), the track appears smooth. As load and temperature increased, grooves within the tracks appeared, implying a corresponding increase in wear.

As can be seen, under the 10 N normal load, as temperature increased, the width of the track increased. The depth of the track for this loading condition also increased as temperature increased however it was not significant. The track widths also increased with temperature for the 35 N tested discs, see Figure 3.10 – 3.12 (e). The wear depth, however followed a different trend than that observed for the 10 N experiments, see Table 3.4, where it is observed that in the highest temperate condition, the maximum wear depth was shallowest.

Table 3.4: Results measured on the wear surfaces of Haynes 25 and Stellite 20 discs and balls following sliding wear experiments

	Load [N]	**T [°C]**	**Maximum wear depth**		**Track width / scar diameter**		**Wear volume**	
			Disc [μm]	Ball [μm]	Disc [mm]	Ball [mm]	Disc [m^3]	Ball [m^3]

Repeat 1	10	20	**2.12** +/- 0.55	**4.74** +/-0.59	**0.83** +/- 0.29	**0.42** +/- 0.03	**1.24E-10** +/- 5.3E-11	**3.32E-13** +/- 8.26E-14
Repeat 2	10	20	**4.66** +/- 0.31	**8.73** +/- 0.48	**0.84** +/- 0.04	**0.58** +/- 0.02	**2.9E-10** +/- 3.78E-11	**5.63E-11** +/- 1.2E-13
Repeat 1	10	100	**4.56** +/- 0.2	**12.61** +/- 1.19	**1.16** +/- 0.29	**0.69** +/- 0.03	**2.8E-10** +/- 4.31E-11	**4.02E-12** +/- 4.45E-13
Repeat 2	10	100	**5.25** +/- 0.44	**16.55** +/- 1.51	**0.94** +/- 0.06	**0.79** +/- 0.04	**3.1E-10** +/- 6.53E-11	**9.50E-11** +/- 7.2E-13
Repeat 1	10	200	**7.84** +/- 1.24	**253.81** +/- 4.19	**2.55** +/- 0.18	**3.07** +/- 0.03	**6.25E-10** +/- 2.61E-10	**9.47E-10** +/- 3.11E-11
Repeat 2	10	200	**7.45** +/- 0.15	**235.79** +/- 2.61	**2.51** +/- 0.29	**2.96** +/- 0.02	**8.34E-10** +/- 2.13E-10	**8.18E-10** +/- 1.8E-11

	Load [N]	**T [°C]**	**Maximum wear depth**		**Track width / scar diameter**		**Wear volume**	
			Disc [µm]	**Ball [µm]**	**Disc [mm]**	**Ball [mm]**	**Disc $[m^3]$**	**Ball $[m^3]$**
Repeat 1	35	20	**20.24** +/- 1.04	**134.3** +/- 7.61	**2.16** +/- 0.09	**2.26** +/- 0.06	**1.81E-9** +/- 2.03E-10	**2.81E-10** +/- 3.04E-11
Repeat 2	35	20	**25.12** +/- 4.64	**91.25** +/- 15.67	**1.7** +/- 0.19	**1.85** +/- 0.16	**3.12E-9** +/- 4.87E-10	**1.25E-10** +/- 4.3E-11
Repeat 1	35	100	**19.4** +/- 1.63	**455.33** +/- 15.07	**3.76** +/- 0.51	**4.06** +/- 0.06	**2.11E-9** +/- 3.24E-10	**2.02E-9** +/- 1.95E-10

Repeat 2	35	100	**22.13** +/- 3.88	**605.65** +/- 71.32	**3.71** +/- 0.24	**4.64** +/- 0.26	**3.05E-9** +/- 6.45E-10	**4.1E-9** +/- 1.2E-9
Repeat 1	35	200	**14.92** +/- 2.83	**426.4** +/- 264	**4.58** +/- 0.52	**9.46** **+/-** 0.1	**1.78E-9**	**5.82E-9** +/- 1.85E-10
Repeat 2	35	200	**14.52** +/- 2.68	**826.2** +/- 11.74	**5** +/- 0.34	**5.36** +/- 0.03	**1.05E-9** **+/-** 7.45E-10	**9.26E-9** +/- 2.65E-10

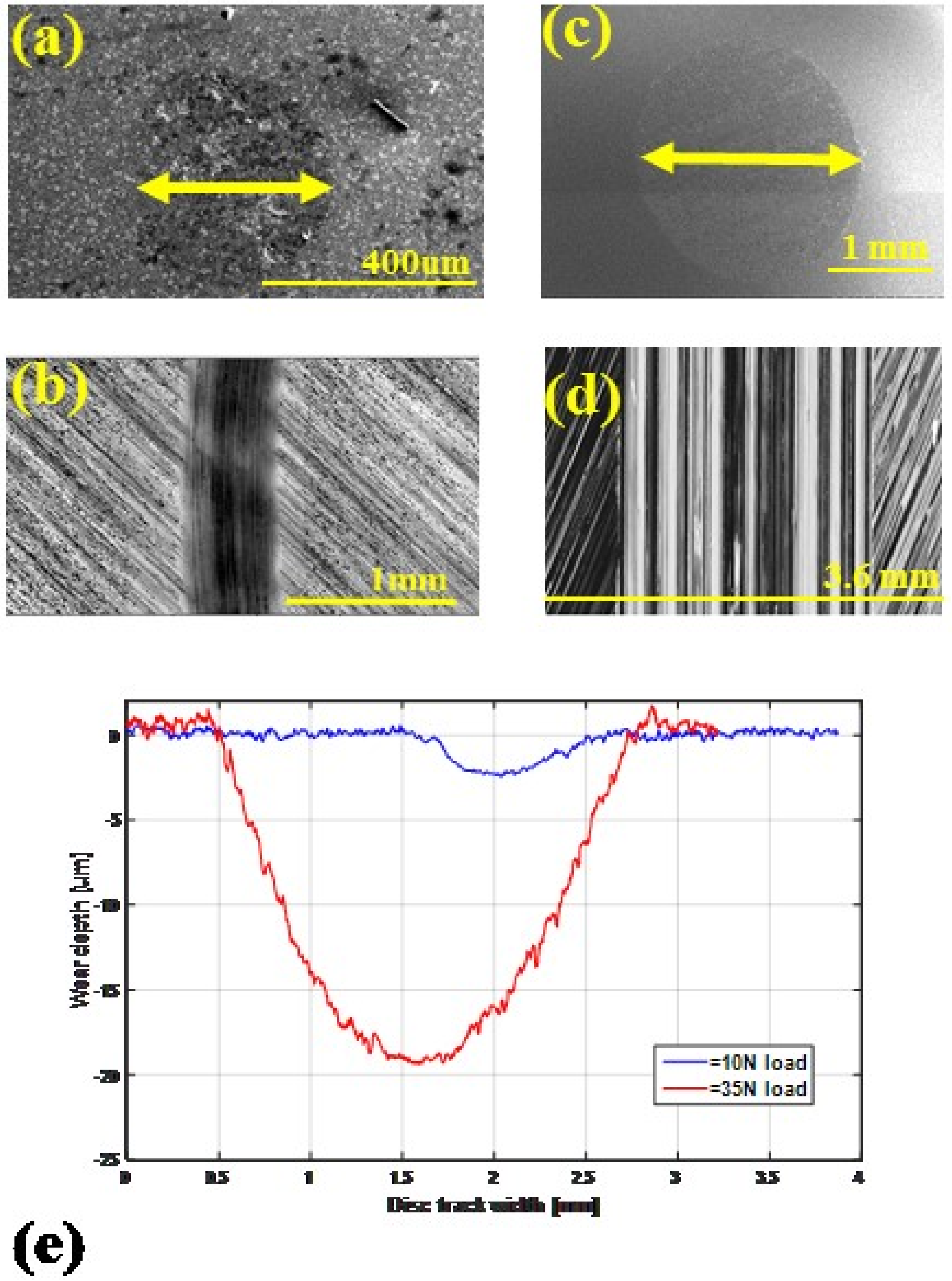

Figure 3.10: Ball and disc wear scar and track under 10 N ((a) and (b))and 35 N ((c) and (d)) loads in 20°C experiments (e) represents profile of the disc wear tracks produced under each load

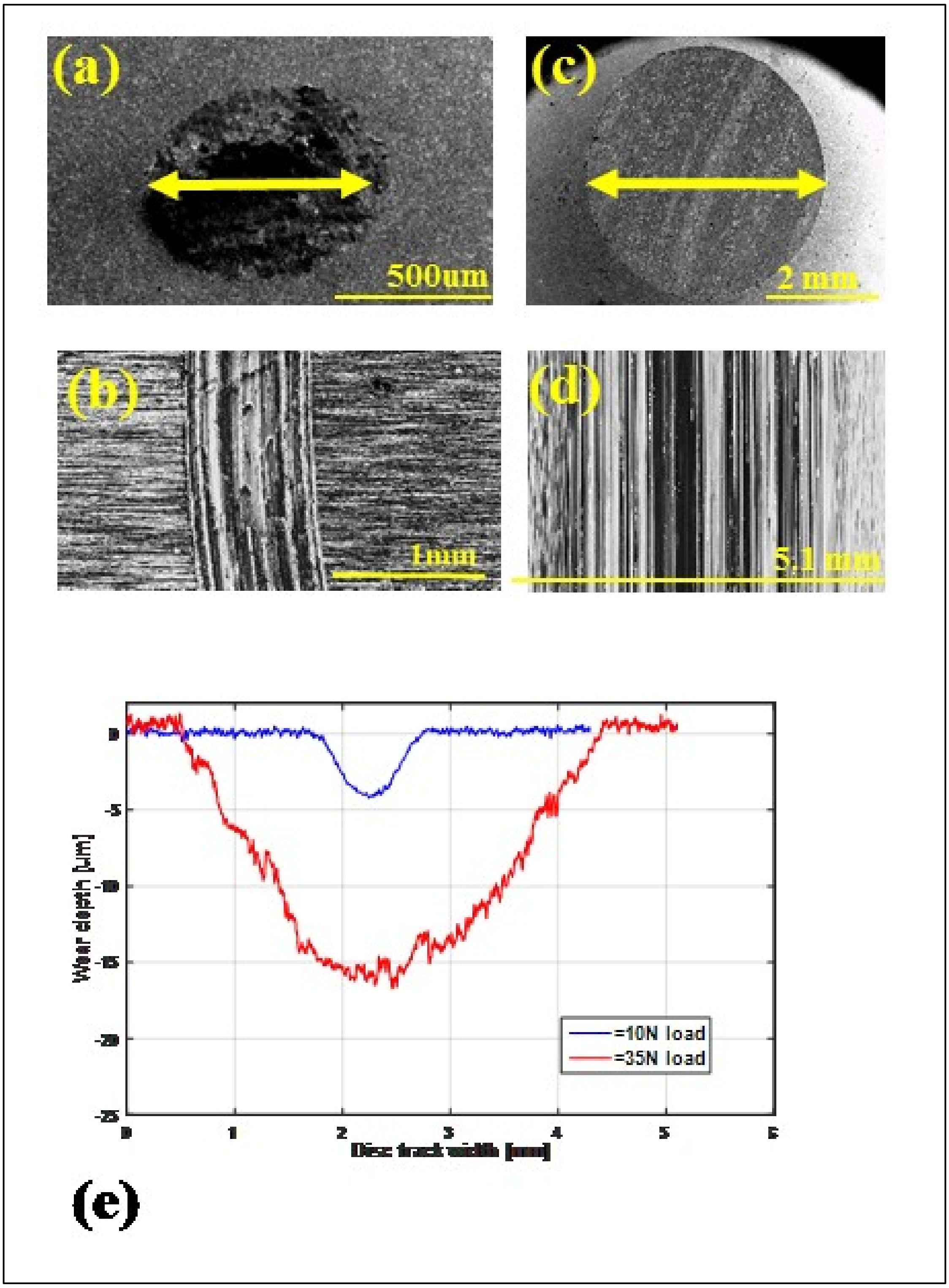

Figure 3.11: Ball and disc wear scar and track under 10 N ((a) and (b)) and 35 N ((c) and (d)) loads in 100°C experiments (e) represents profile of the disc wear tracks produced under each load

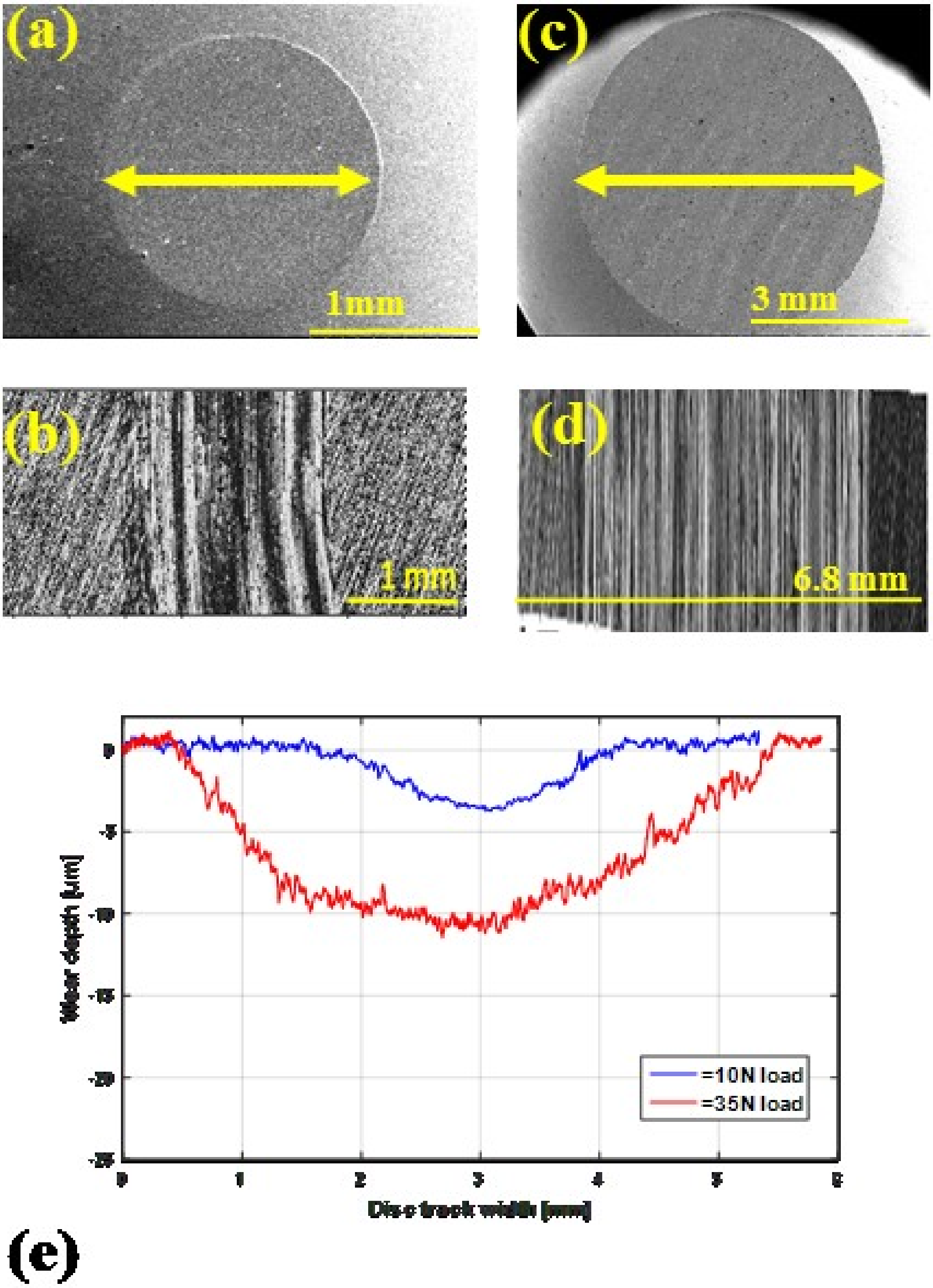

Figure 3.12: Ball and disc wear scar and track under 10 N ((a) and (b))and 35 N ((c) and (d)) loads in 200°C experiments (e) represents profile of the disc wear tracks produced under each load

Figure 3.13 presents the total wear volume measured as a result of the sliding wear experiments; the top portion of each stacked bar representing the ball wear and the bottom the disc wear.

Two sets of experiments are reported on the charts, one using filled bars and the other empty bars (note that this plotting style is also used in the following wear charts). The wear under the lower loading condition can be seen more clearly in the inset to Figure 3.13. As expected, with an increase in temperature and applied load, a clear increase in total wear volume was observed. The wear volume measured for the 10 N experiments increased with increased temperature, rising significantly at 200°C. At room temperature, there was negligible wear of the Stellite 20 ball, not unusual as this is the harder of the two materials. A notable increase in wear of the Stellite 20 ball was observed at higher temperatures for both experiments, implying a reduction in the wear resistance of the Stellite 20 ball at 200°C – more significant than the reduction seen at 100°C which agreed with work presented in Ref. [65]. This might be due to the evolution of the microstructure that can be seen in the images of the ball scar in Figure 3.10 – 3.12 (a) and (c). As the hard, tungsten rich carbide was damaged, the alloy may have become weaker.

Observing the wear volume under the 35 N load, a different pattern was seen. Wear of the Stellite 20 ball increased significantly with an increase in temperature as before. This disagrees with information presented by Stott and co-workers which suggested a decrease in wear for the pin (or ball in this case) would occur [63]. Conducting experiments in temperatures exceeding 200°C may serve to agree with this suggestion. The disc wear volume measured did not follow this pattern. At 20°C, the highest disc wear volume under the upper loading condition was measured. In 100°C, the disc wear measured decreased slightly, although not as significantly as the increase in ball wear measured from the same experiments. In 200°C, the disc wear volume measured was the lowest relative to the room temperature and 100°C disc wear volume in the upper loading condition. This is likely to be linked to the interplay between different wear mechanisms, namely the evolution of microstructure and consequential reduction of wear resistance of the Stellite 20 ball at higher temperatures. The changes in response of Haynes 25 in higher loading conditions may also have an impact as it is an alloy known for its susceptibility to work hardening [121]. If the hardness of Haynes 25 disc increased when the higher load is applied, and plasticity is more likely to occur during loading, the component might have become more resistant to material removal from the sliding interaction. This result agrees with a figure presented by Dréano and co-workers which demonstrated that as temperature increased above approximately 150°C, wear volume of Haynes 25 measured will decrease, see Figure 2.5 [21].

The simultaneous deterioration of the wear resistance of Stellite 20 may have resulted in an increased wear rate for the ball. This in turn resulted in a change to the contact area, increasing the width of the wear track and consequently lowers the contact pressure during the experiments. To be more specific, under the higher loading conditions tested here, a significant increase in material wear of the Stellite 20 ball was observed, see Figure 3.13. This was also apparent from the images of the ball scars presented in Figure 3.10 – 3.12 (a) and (c). This had an impact on the shape of the ball *i.e.* as wear of the ball increases, the surfaces in contact became 'flatter', increasing the contact area and the contact pressure decreased accordingly. The pressure distribution conforms to this. This process would have been more rapid in the higher temperature experiments. The reduced material wear volume of the disc may be attributed to this considering the linear relationship of wear volume and pressure in Equation 3.2.

The material wear volume measured for the components in each experimental condition are applied to Archard's wear equation and an average wear coefficient was calculated, see Table 3.5.

Table 3.5: Ball and disc component information, wear coefficient calculated using experimental data and Archard's wear equation for the first iteration of experiments conducted at each environmental condition

	Diameter [mm]	**Depth [mm]**	**Hardness [Hv]**	**Young's modulus [GPa]**
Stellite 20 ball	9.525		649-867	257
Haynes 25 disc	30	10	572	225
Experimental condition	**Load [N]**	**Temperature [°C]**	**Wear coefficient (ball)**	**Wear coefficient (disc)**
1	10	20	8.281E-15	3.078E-12
2	10	100	1.006E-13	6.898E-12
3	10	200	2.038E-11	2.078E-11
4	35	20	8.898E-13	2.221E-11
5	35	100	1.435E-11	1.59E-11
6	35	200	4.14E-11	1.267E-11

The wear coefficient values were used to develop wear prediction models that will be presented and discussed in Chapter 5.

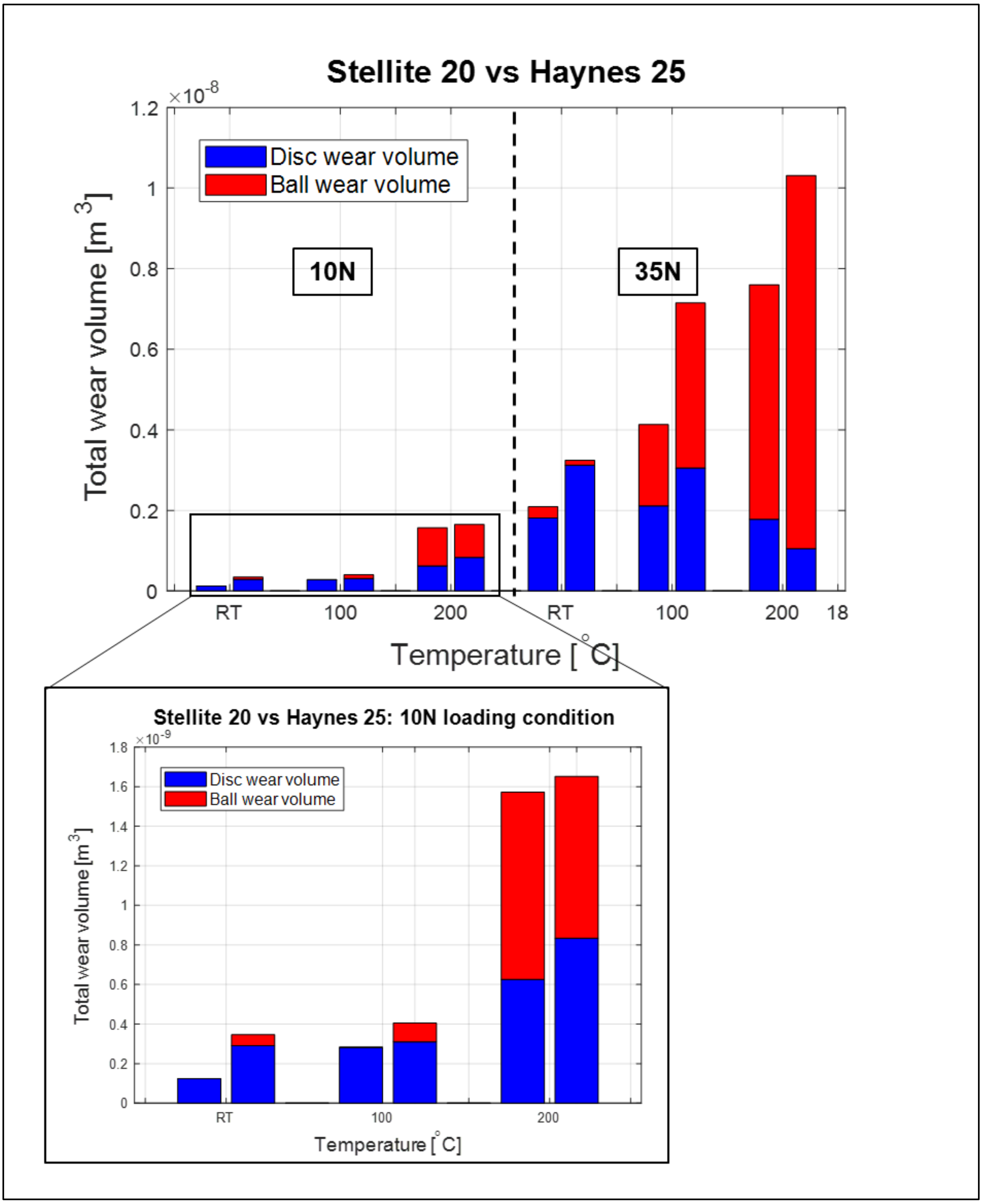

Figure 3.13: Stellite 20 ball against Haynes 25 disc -total wear volume measured for all experimental conditions: inset showing results for 10 N experiments. Note that the two separate series of tests are reported in the plot.

3.2.2.2 RR2450 ball on Haynes 25 disc

The results from the sliding wear experiments using RR2450 balls and Haynes 25 discs were analysed using the same methods as the Stellite 20 and Haynes 25 post experimental components, presented in Section 3.2.2.1. Figure 3.14 – 3.16 (a)-(d) present images of the ball scar produced on an RR2450 ball and a section of the Haynes 25 disc track from an experimental component from one of the repeated experiments carried out in each experimental condition. Figure 3.14 – 3.16 (e) presents the comparative profile of a wear track produced on a disc from each repeated set of experimental conditions. The data presented in Table 3.6 can also be used for reference to understand what is being shown in Figure 3.14 – 3.16.

In Figure 3.14 images of a ball scar and a section of a disc track from components tested at room temperature under each loading condition are presented. It is clear that in the case of the ball, the diameter of the scar increased significantly with an increase in normal load. In the case of the disc, the grooved appearance of the track sections did not vary significantly. Figure 3.14 – 3.16 (e) presents average profiles taken from a disc tested under each condition. An increase in load did not appear to have had a significant impact on the maximum wear depth on the Haynes 25 disc at room temperature. Figure 3.15 and 3.16 present the same for components tested at 100°C and 200°C respectively. In the case of the track produced on discs tested at 100°C no significant in maximum wear depth was observed. In the highest temperature condition, a slight increase in maximum wear depth was observed as normal load increased from 10 N to 35 N. The increase in track width measured increased with load across all temperatures was more significant than the impact of load on the maximum wear depth. For each temperature tested there is a clear increase in the diameter of the ball scar, observe Figure 3.15 and 3.16 (a) and (c). A significant increase in the maximum wear depth on the ball with an increase in the load applied was also observed, see Table 3.6.

Figure 3.17 presents the total wear volume for all post experimental components; the top portion of each bar represents the ball wear volume and the bottom portion represents the disc wear volume measured. The wear under the lower loading condition can be seen more clearly in the inset to Figure 3.17. Each experimental condition was repeated once, and all results are presented on the chart. Except for the room temperature test and particularly for the 100°C experiments under a normal load of 35 N, the tests seem to be repeatable. The lack of repeatability of the 100°C, 35 N experiment may be explained by inconsistencies in the final polishing step of ball manufacture. Figure 3.18 presents SEM images of an area of a RR2450 ball that has been tested, may suggest why the difference in wear in experiments, particularly under the 35 N loading condition may have occurred. The pit observed on the surface of the RR2450 ball, see Figure 3.18 (c) and (d) is a feature observed frequently at random locations on the ball surfaces. The dispersion of these ‘pits’ is not even or uniform and may explain why the lack of repeatability was not seen in all experimental conditions. Prior to this project sliding wear experiments had not been conducted using RR2450, nor had the alloy been used to make balls. If the powder used in ball production was finer, the surface defects may not have occurred which may have an impact on the sliding wear resistance of the alloy.

Table 3.6: Results measured on the wear surfaces of Haynes 25 and RR2450 discs and balls following sliding wear experiments

	Load [N]	**T [°C]**	**Maximum wear depth**		**Track width / scar diameter**		**Wear volume**	
			Disc [μm]	Ball [μm]	Disc [mm]	Ball [mm]	Disc $[m^3]$	Ball $[m^3]$
Repeat 1	10	20	**8.5** +/- 1.1	**50.61** +/- 3.14	**1.16** +/- 0.1	**1.38** +/- 0.04	**3.43E-10** +/- 8.5E-11	**2.8E-11** **+/-** 4.72E-12
Repeat 2	10	20	**11.06** +/- 0.7	**29.17** +/- 4.95	**1.08** +/- 0.12	**1.05** +/- 0.1	**4.68E-10** +/- 7E-11	**1.27E-11** **+/-** 4.36E-12
Repeat 1	10	100	**9.16** +/- 1.13	**107** +/- 4.56	**1.88** +/- 0.11	**2** +/- 0.04	**4.77E-10** +/- 1.16E-10	**1.7E-10** +/- 1.45E-11
Repeat 2	10	100	**12.63** +/- 2.31	**93.7** +/- 5.73	**1.74** +/- 0.12	**1.79** +/- 0.06	**6.75E-10** **+/-** 2.34E-10	**1.31E-10** +/- 1.56 E-11
Repeat 1	10	200	**7.12** +/- 1.41	**153.9** +/- 2.96	**2.41** +/- 0.14	**2.4** +/- 0.02	**4.47E-10** **+/-** 1.22E-10	**3.51E-10** +/- 1.33E-11
Repeat 2	10	200	**7.95** +/- 0.65	**173.82** +/- 4.57	**2.36** +/- 0.08	**2.55** +/- 0.03	**4.74E-10** **+/-** 6.5E-11	**4.47E-10** +/- 2.34E-11

	Load [N]	**T [°C]**	**Maximum wear depth**		**Track width / scar diameter**		**Wear volume**	
			Disc [µm]	**Ball [µm]**	**Disc [mm]**	**Ball [mm]**	**Disc [m^3]**	**Ball [m^3]**
Repeat 1	35	20	**9.4** +/- 0.82	**123.8** +/- 5.24	**2.18** +/- 0.22	**2.16** +/- 0.05	**6.51E-10** **+/-** 8.73E-11	**2.27E-10** +/- 1.9E-11
Repeat 2	35	20	**13.41** +/- 1.38	**133.93** +/- 4.06	**1.73** +/- 0.24	**2.24** +/- 0.03	**7.78E-10** **+/-** 2.67E-10	**2.66E-10** +/- 1.58E-11
Repeat 1	35	100	**11.29** +/- 1.08	**322.02** +/- 107.06	**3.28** +/- 0.24	**3.34** +/- 1.09	**1.1E-9** **+/-** 1.77E-10	**1.67E-9** +/- 5.6E-10
Repeat 2	35	100	**13.54** **+/- 6.6**	**587.7** +/- 177.6	**3.37** +/- 0.53	**4.58** +/- 1.38	**1.34E-9** **+/-** 9.74E-10	**4.96E-9** +/- 2E-10
Repeat 1	35	200	**10.02** +/- 1.73	**405.53** +/- 6.02	**3.02** +/- 0.46	**3.85** +/- 0.03	**7.84E-10** **+/-** 2.21E-10	**2.4E-9** +/- 7E-11
Repeat 2	35	200	**9.95** +/- 0.8	**418.9** +/- 12.4	**3.2** +/- 1.1	**3.9** +/- 0.05	**7.42E-10** **+/-** 1.1E-10	**2.55E-9** +/- 1.5E-10

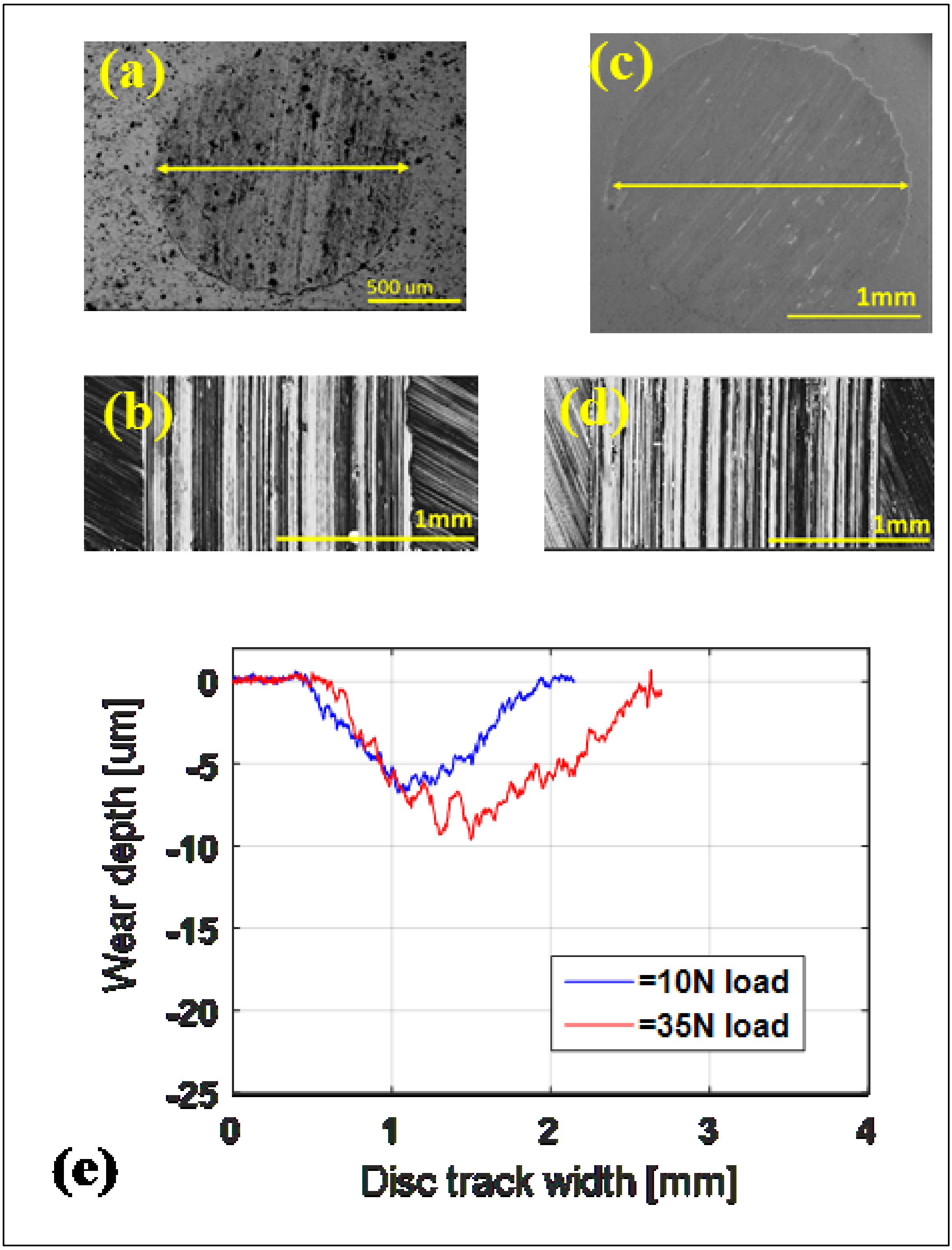

Figure 3.14: Ball and disc wear scar and track under 10 N ((a) and (b))and 35 N ((c) and (d)) loads in 20°C experiments (e) represents profile of the disc wear tracks produced under each load

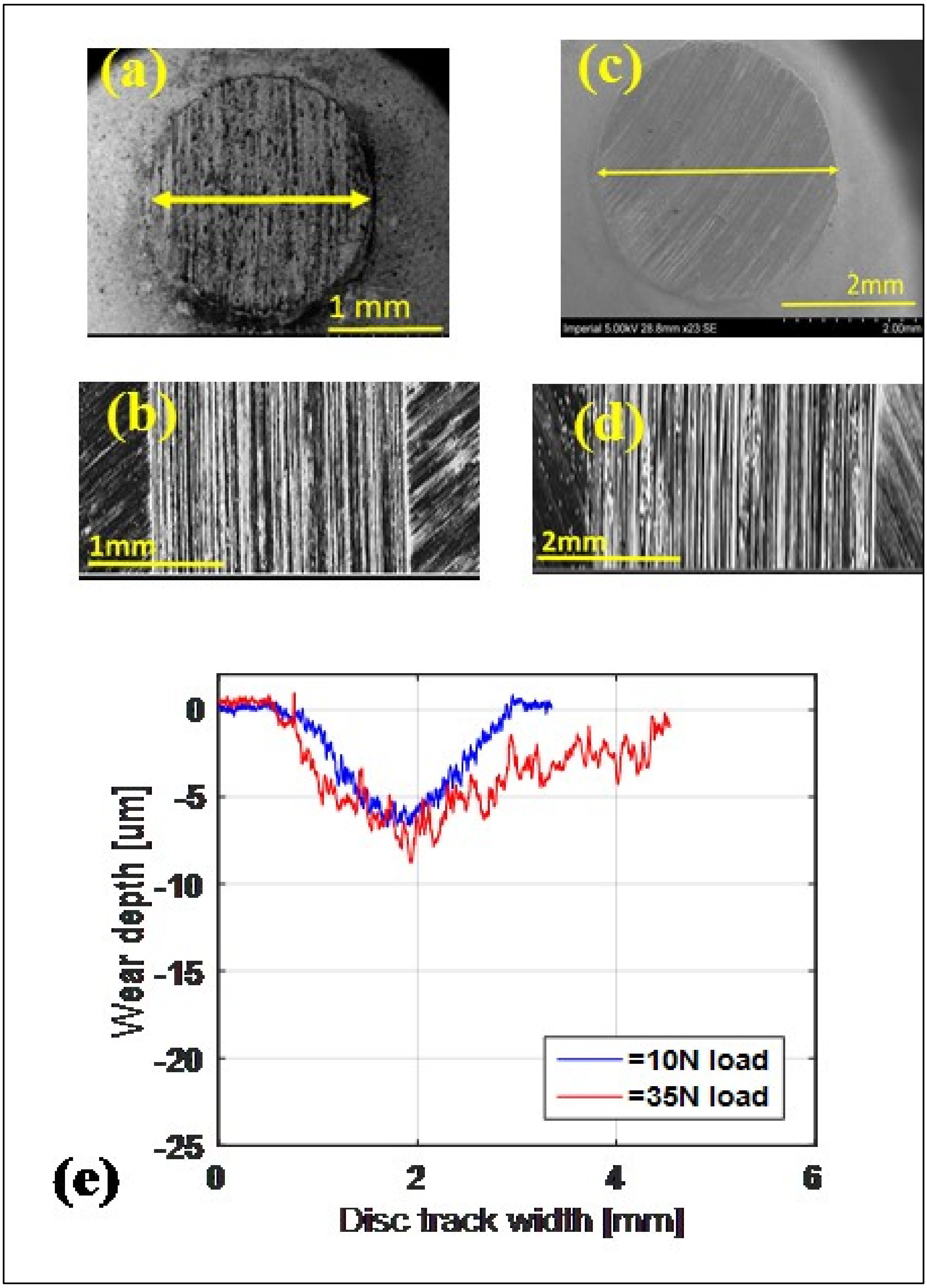

Figure 3.15: Ball and disc wear scar and track under 10 N ((a) and (b))and 35 N ((c) and (d)) loads in 100°C experiments (e) represents profile of the disc wear tracks produced under each load

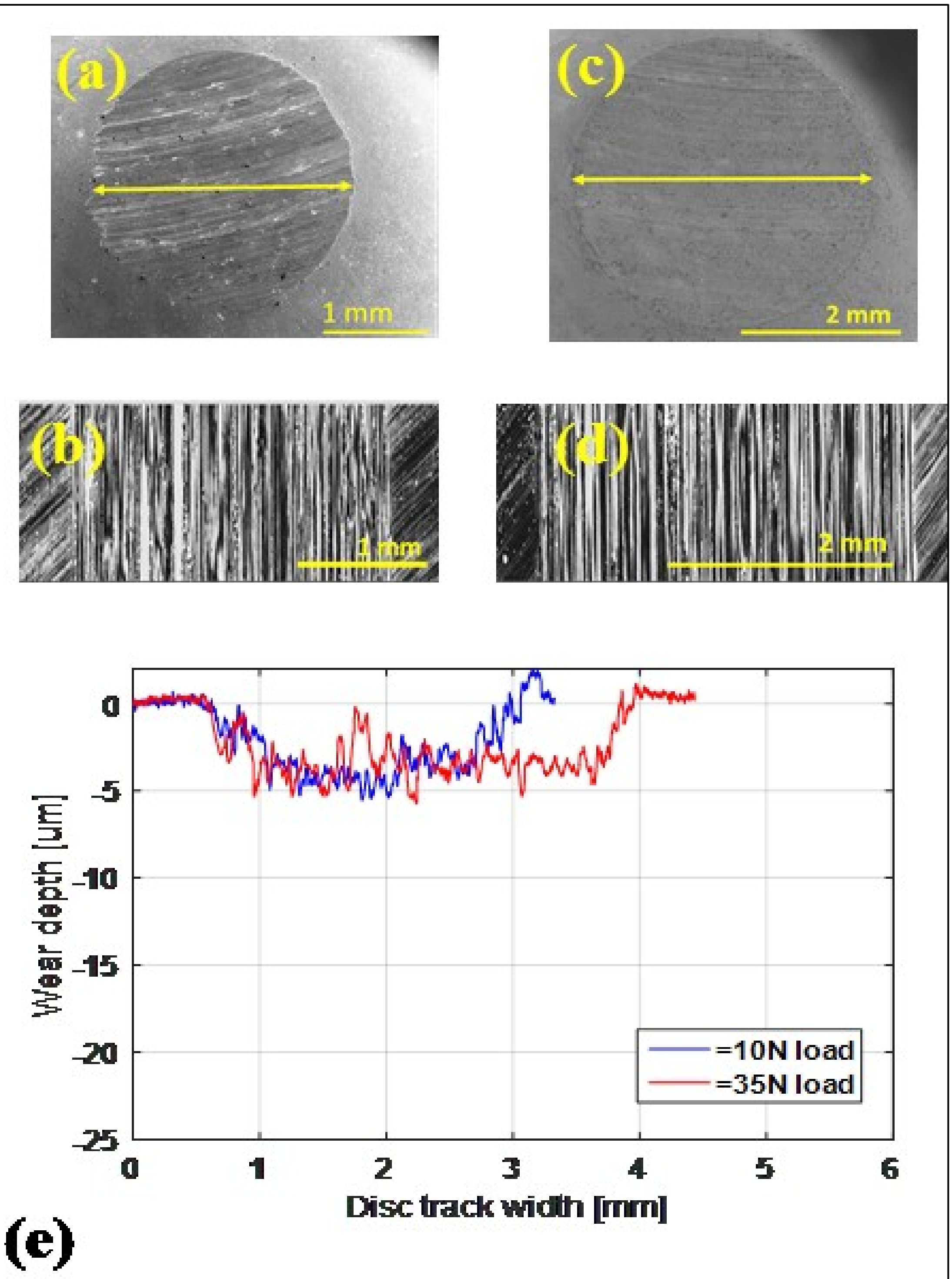

Figure 3.16: Ball and disc wear scar and track under 10 N ((a) and (b)) and 35 N ((c) and (d)) loads in 200°C experiments (e) represents profile of the disc wear tracks produced under each load

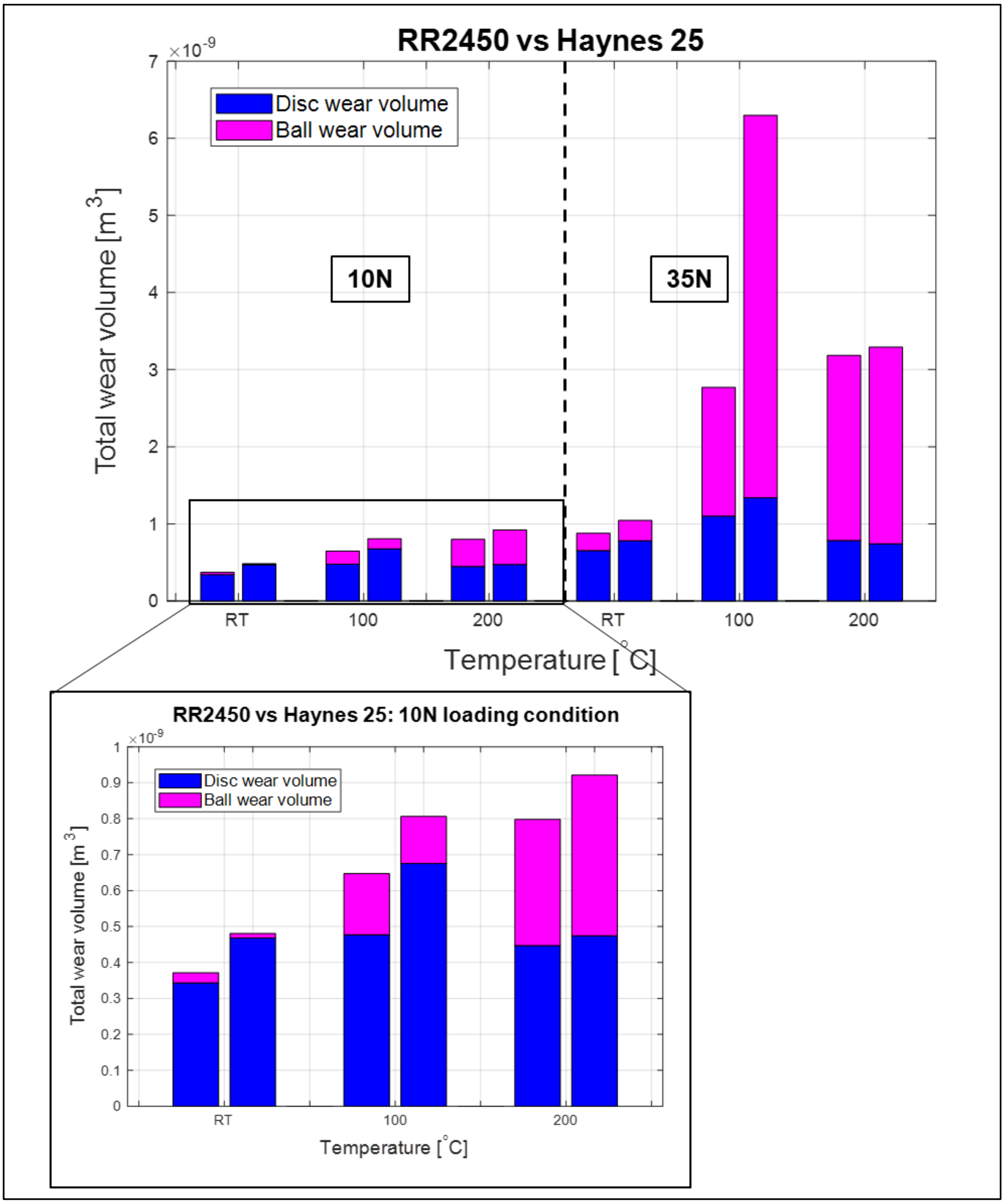

Figure 3.17: RR2450 ball against Haynes 25 disc - total wear volume measured for all experimental conditions: inset showing results for 10 N experiments

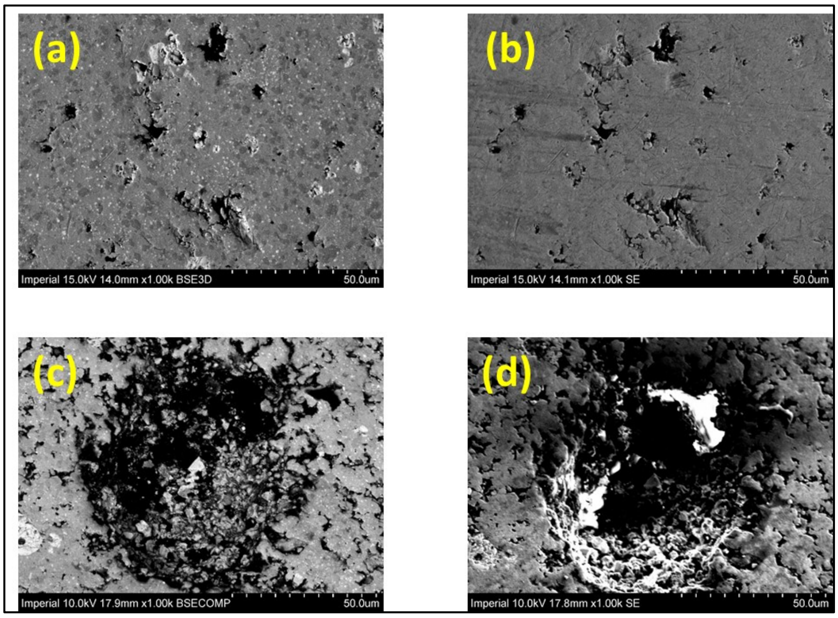

Figure 3.18: Pits and crevices observed on clean surface of RR2450 ball

3.2.2.3 Comparison of wear resistance of Stellite 20 and RR2450 against Haynes 25 discs

Figure 3.19 and Figure 3.20 compare the total wear volume measured for balls and discs from the Stellite 20-Haynes 25 and the RR2450-Haynes 25 ball and disc combinations in all experimental conditions. Figure 3.19 compares the results from the 10 N loading condition and Figure 3.20, the 35 N loading condition. At room temperature, under a normal load of 10 N, more wear volume was measured on the Stellite 20 ball than on the RR2450 ball whereas the former appears to exhibit better wear resistance as temperature increases from room temperature. The combined volume of the ball and disc however was greater for the RR2450-Haynes 25 in each temperature condition apart from one experimental outlier at 200°C. Figure 3.19 indicates an increase in wear for the Haynes 25 disc in the RR2450-Haynes 25 experiments, however due to experimental inconsistency it is difficult to compare behaviour in the highest loading condition.

With an increase in normal load to 35 N, an increase in wear resistance of RR2450 compared to Stellite 20 was observed. As discussed earlier, with an increase in temperature, particularly to 200°C, a significant increase in wear of the Stellite 20 ball was observed. This increase was also observed for the case of the RR2450 ball although not as substantial. Wear volume measured on the Haynes 25 discs was also notably lower from the RR2450-Haynes 25 experiments than from the Stellite 20-Haynes 25 experiments. In both cases, under a load of 35 N, wear of Haynes 25 decreased slightly with an increase in temperature. Both sets of experimental results indicate that RR2450 demonstrates good comparative wear resistance to Stellite 20, particularly in the upper loading condition. There was no noteworthy impact on the wear performance of Haynes 25 in either loading condition, omitting results considered experimental outliers.

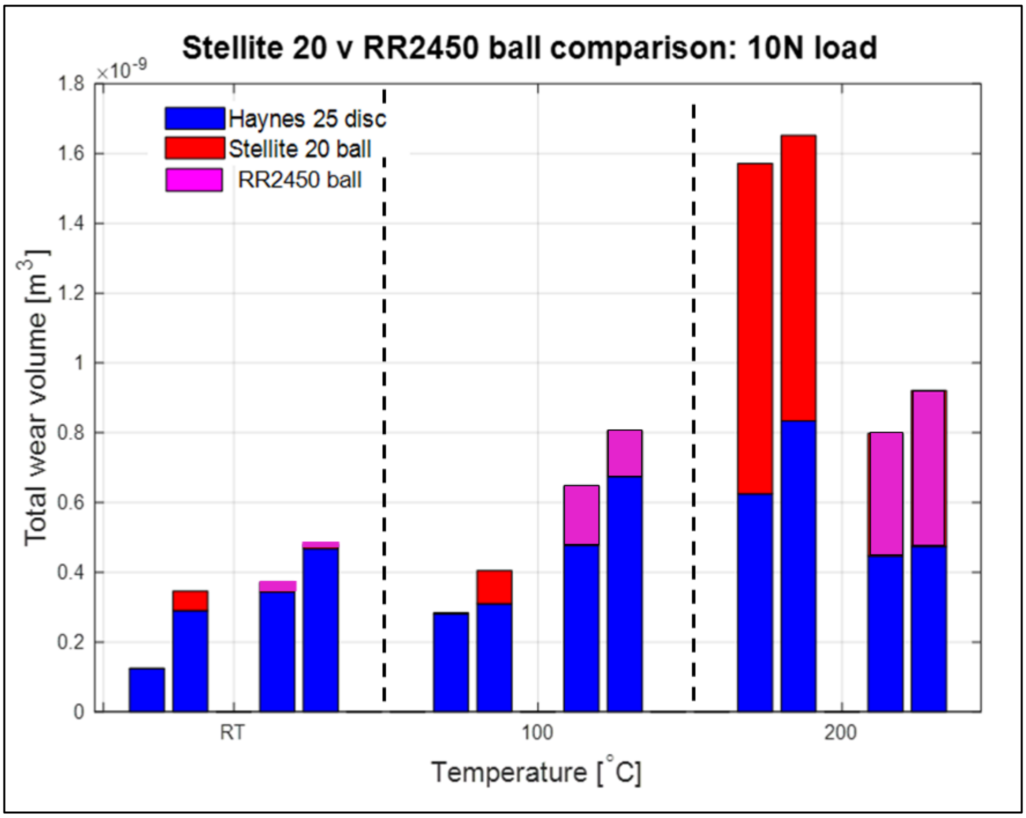

Figure 3.19: Wear volume measurement for all experimental components under 10 N loading condition

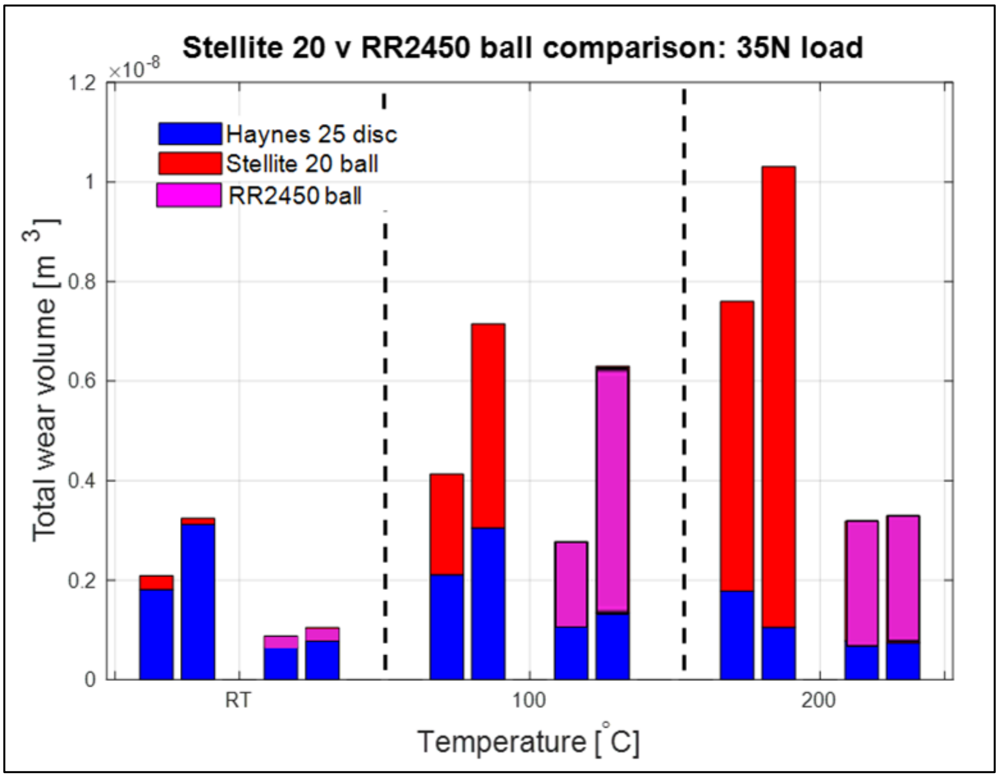

Figure 3.20: Wear volume measurement for all experimental components under 35 N loading condition

3.2.3 Microstructural and compositional analysis

SEM analysis was conducted on disc tracks and scars produced under a load of 35 N in all temperature conditions. The analysis used the SE, BSE and EDX modes of the SEM.

3.2.3.1 Stellite 20 ball on Haynes 25 disc

Figures 3.21-3.23 present locations on the surface of a ball and disc wear scar and track produced under a normal load of 35 N at room temperature, 100°C and 200°C. A distinctive dispersion across the surface of the disc track is seen in Figure 3.21 (a) and (b). EDX analysis of the dispersion revealed increased levels of oxygen and carbon not observed in a bulk analysis of the area. Smooth material removal from the disc surface is represented by the shallow, even grooves and scratches seen in Figure 3.21 (a) and (b). Analysis of points within these scratches revealed notable levels of carbon, levels not seen over the entire track area. This high level of carbon suggests the transfer of from the ball to the disc as Haynes 25 has a carbon composition of approximately 0.1% compared to 3-5% in Stellite 20. In Figure 3.21 (c) and (d) the border between the clean ball and scar is highlighted. The change in microstructure between the two is obvious. In feature 1 in Figure 3.21 (c) and (d), the different phases have not been completely altered, damage appears to have been at the point of initiation. Feature 2 in Figure 3.21 (c) and (d) highlights cracks and topographical damage on the ball surface. The sliding interaction initially induced changes of the surface and alteration of the microstructure giving it a smoother appearance. In feature 2 in Figure 3.21 (c) and (d), the distinct phases can no longer be identified. It seems that the surface cracked as wear progressed. EDX analysis of this, and other similar features in the ball scar revealed a significant level of oxygen (~29% weight), an element not present in analysis of a clean area of the tested ball suggesting that oxidation was initiated, see Table 3.7 for compositional data recorded.

Figure 3.22 (a) and (b) presents a grooved disc track, the grooves appearing slightly deeper than the scratches in Figure 3.21 (a) and (b). A corresponding pattern is seen on the ball scar – see Figure 3.22 (c). EDX analysis within the disc track grooves found a slight increase in carbon although an increase in oxygen was not measured from the 20°C experiment components. The topographical damage highlighted in feature 1 within the disc wear track is a recurring feature observed over the entire track implying that material is not being ploughed as uniformly as during the 20°C experiment. Once again a dispersion was observed over the track surface is visible albeit appearing less frequently, having a similar composition to that seen in Figure 3.21 (a) and (b). The topography of the ball scar is very different to that observed in Figure 3.21 (c) and (d). The scar appears to have been polished by comparison with no indication of the microstructural phases visible on the undamaged area. This corresponds to the significant increase in wear of the Stellite 20 ball at 100°C relative to the room temperature ball wear measurement.

The track produced on the surface of the disc tested at 200°C once again features the same grooved appearance as the 100°C experiment. Topographical damage similar to that observed in feature 1 of Figure 3.22 (a) and (b) is similar in appearance to feature 1 highlighted in Figure 3.23 (a) and (b). The EDX composition of these features was very similar with elevated presence of carbon and oxygen relative to the entire area of the image and the compositional data for Haynes 25. Stott discussed the presence of oxidation and the compaction of 'loose, compact, particles' on metal alloys during sliding wear experiments in a temperature range of 20°C to 200°C [63] which appears to agree with what is observed in both features highlighted on the disc track surface presented in Figures 2.22 and 2.23 (a) and (b). The appearance of the features were also closely compared to images presented by Dréano and co-workers of a thin Co-Cr-W oxide produced under a normal fretting load of 50 N in 100°C ambient temperature [21]. A highly protective glaze layer was not observed in that work until temperatures reached approximately 400°C [21].

In Figure 3.23 (c) and (d) the area of the ball scar presented has grooves in the direction of sliding as observed in Figure 3.22 (c) and (d), corresponding to the topography of the disc track surface. The two phase microstructure of the room temperature tested Stellite 20 ball were also more easily identified in the BSE images than for the 100°C and 200°C experimental conditions. When temperature increased from room temperature the surfaces were polished in appearance suggesting significant damage to the microstructure at the ball surface which agrees with the significant increase in wear volume observed. Unlike the undamaged ball surface presented in Figure 3.1, the tungsten and chromium rich carbides and solid solution strengthened cobalt rich matrix boundaries are no longer identifiable. Plastic deformation of the phases and/or the presence of oxide debris are likely to have contributed to this. This is observed from the 20°C condition through to the 200°C, at which point, the damage became relatively uniform in appearance.

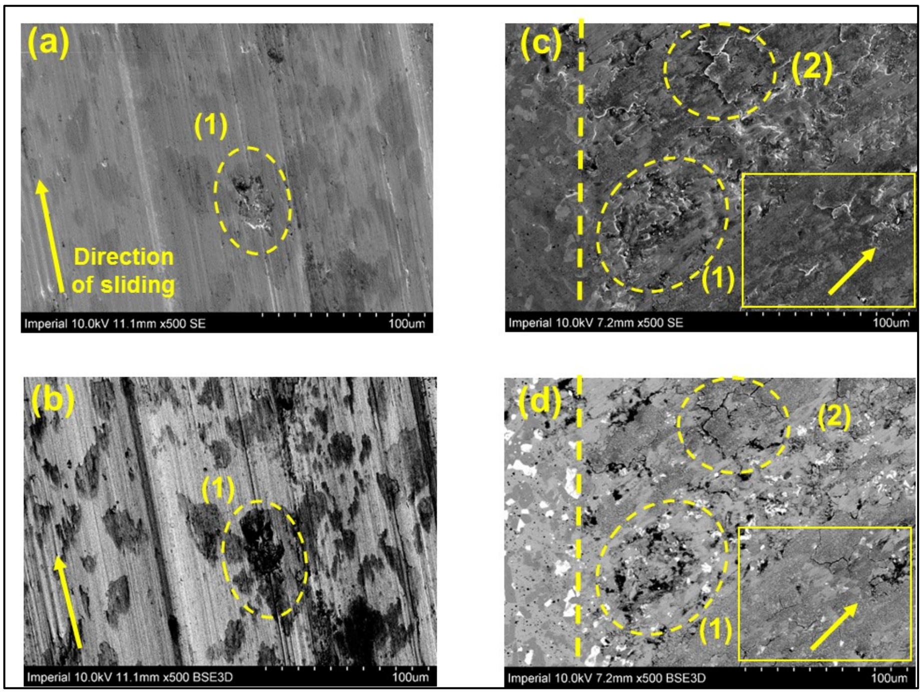

Figure 3.21: (a) and (b) area within disc wear track and (c) and (d) area within ball wear scar from using SE and BSE modes of the SEM of components tested under 35 N at 20°C

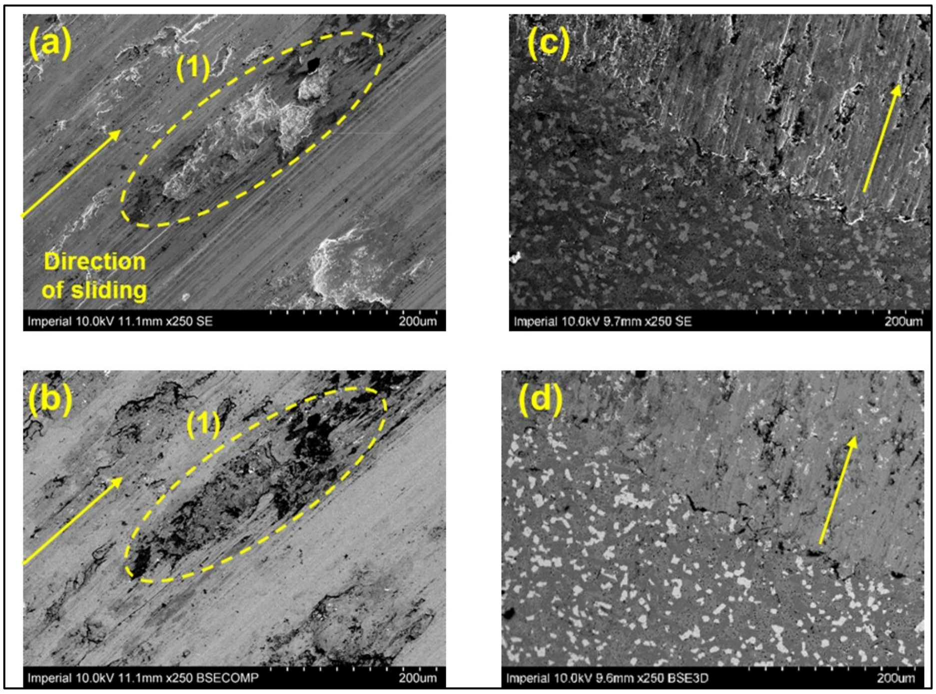

Figure 3.22: (a) and (b) area within disc wear track and (c) and (d) area within ball wear scar using SE and BSE modes of the SEM of components tested under 35 N at 100°C

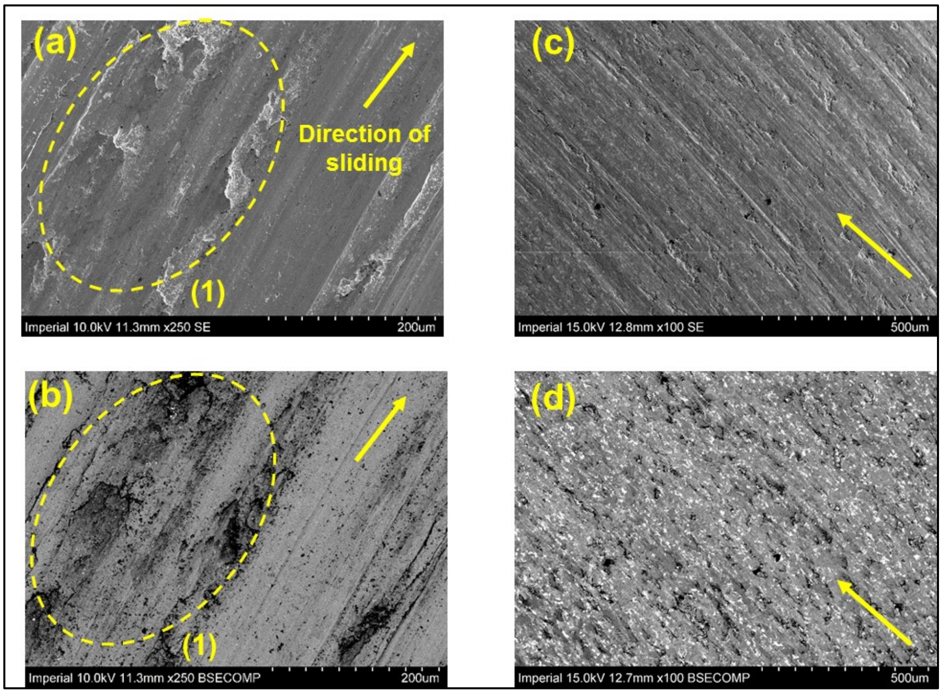

Figure 3.23: (a) and (b) area within disc wear track and (c) and (d) area within ball wear scar using SE and BSE modes of the SEM of components tested under 35 N at 200°C

Table 3.7: EDX chemical compositional analysis of specific locations on disc wear track and ball wear scar surfaces for areas presented in Figure 3.21 – 3.23

18			Carbon	Oxygen	Chromium	Molybdenum	Iron	Cobalt	Nickel	Tungsten	Total
Experiment: 35 N @ 20°C	**Figure**	**Feature**	%wt	%wt	%wt	%wt	%wt	%wt	%wt	%wt	%wt
Disc	3.21 (a) and (b)										
		Average track spectrum	4	2	21	2	1	47	8	15	100
		Dispersion	9	6	16	2	1	44	9	13	100
		Scratches	13	0	17	1	2	44	8	15	100
Ball											
	3.21 (c) and (d)										
		Average scar spectrum	8	15	23	1	1	33	5	14	100
		Feature (2)	7	29	22	0	1	26	1	14	100
		Medium grey area	6	16	21	0	1	37	6	13	100
Experiment: 35 N @ 100°C	**Figure**	**Feature**									
Disc	3.22 (a) and (b)										
		Average track spectrum	6	1	19	2	2	46	9	15	100
		Dispersion	4	6	17	0	0	50	10	13	100
		Within grooves	9	0	20	0	0	45	9	17	100
		Feature (1)	6	6	21	0	0	45	6	16	100
Ball	3.22 (c) and (d)										
		Average scar spectrum	9	6	26	1	2	38	4	14	100
		Within grooves	7	6	26	0	1	41	3	16	100
Experiment: 35 N @ 200°C	**Figure**	**Feature**									
Disc	3.23 (a) and (b)										
		Average track spectrum	4	2	20	2	2	47	8	15	100
		Within grooves	4	0	20	2	1	49	9	15	100
		Dispersion	3	3	20	1	2	47	9	15	100
		Feature (1)	6	6	22	0	1	43	7	15	100
Ball	3.23 (a) and (b)										
		Average scar spectrum	9	15	27	0	2	35	0	12	100

3.2.3.2 RR2450 ball on Haynes 25 disc

Figure 3.24 – 3.26 (a) – (d) present sections of the disc and ball wear track and scars respectively using the SE and BSE mode of an SEM. Specific features have been highlighted and compared to those highlighted on the surface of the Stellite 20-Haynes 25 ball and disc combination. EDX analysis was also conducted and results provided further information about the wear behaviour of the alloy combination and facilitated further comparison to the Stellite 20-Haynes 25 combination. Figure 3.24 (a) and (b) presents a random location on the disc track produced at room temperature under a normal load of 35 N. The direction of sliding can be clearly identified on the disc track surface, similar to the track produced during the Stellite 20-Haynes 25 experiments. The smooth area of the track, implies that material was ploughed smoothly from the disc surface. In feature 1 and 2 in Figure 3.24 (a) and (b), what appear to be fragments of wear debris are observed on the track surface. This was seen at many other locations in the track produced in this experimental condition. EDX analysis of such features revealed that generally, such fragments had a composition agreeing with that expected of Haynes 25 rather than RR2450. This indicates that some debris remained in the contact as the sliding interaction progressed, referred to in literature as active wear debris [62]. From room temperature, the sintering of such areas may occur and in some cases act as load bearing areas although it is not possible to confirm that this happened in these interactions [40, 70].

The dispersion that seen on the disc in the Stellite 20-Haynes 25 experiments was once again observed on the disc surface. In the case of the RR2450–Haynes 25 experiment the wt% of oxygen measured on these features was significantly higher than for a visually similar feature on the surface of the Haynes track for the Stellite 20–Haynes 25 experiments. The ball scar, the border of which can be observed in Figure 3.24 (c) and (d), has a smooth appearance. EDX analysis revealed that there is cobalt present on the scar surface implying that material transferred from the disc to ball surface. Fragments of debris and significant topographical damage were not observed as commonly as on the disc track surface. It was more difficult to confirm transfer and adhesion of wear debris in the Stellite 20-Haynes 25 experiments due to the similar compositions of the alloys.

Similarly to the disc surface produced under a 35 N load at 100°C, the volume of the dark dispersion observed was not a significant feature as for the room temperature condition. Features indicating adhesion of wear debris are observed frequently across the track, an example of which is highlighted in Feature 1, Figure 3.25 (a) and (b). An elevated %wt of iron within this feature, see Table 3.8 was observed and confirmed the presence of debris from the

RR2450 ball in this location. This was also reported at other similar features across the track produced at this experimental temperature. This suggests that the non-uniformity observed across the track surface produced at 100°C may be due to adhesion of wear debris rather than uneven material removal. As the track became less uniform in appearance, the wear volume measured for the disc track decreased. The wear debris that adhered to the surface in the interaction may have protected the disc from further wear which agrees the discussion presented by Stott and Inman [63, 64]. It is possible that this phenomenon also contributed to the reduction in wear volume measured on the disc surfaces from the Stellite 20-Haynes 25 ball and disc experiment as temperature increased. It is not as easy to identify however, as previously mentioned due to compositional similarities of the two cobalt-based alloys.

The damage to the ball surface produced at 100°C was more severe compared to the room temperature condition. The scar also had a more grooved appearance corresponding to the increase in topographical damage observed on the disc surface tested at this condition. The feature highlighted in Figure 3.25 (c) and (d) had slightly elevated levels of cobalt but relative to the average scar spectrum it was not significant.

At the experimental temperature of 200°C under a normal load of 35 N, the topographical non-uniformity on the disc track observed was more severe than at the lower temperature conditions, see Figure 3.26 (a) and (b) as an example. Around significant features of plastic deformation such as this there is what appears to be a fine, powder like debris on the surface. EDX analysis of such features indicated that this contained elevated levels of iron which indicated transfer of debris. The formation of a protective oxide glaze in temperatures above 150°C was discussed by Pauschitz and co-workers. It was noted that these glazes may be formed from wear particles that were mechanically broken down into fine particles by communition and tended to concentrate around features such as grooves in the wear track [40]. The description has similarities to what is observed in Figure 3.26 (a) and (b) suggesting that a protective oxide glaze may form in the sliding experiments presented in this chapter. The literature suggests that wear will transition to a mild wear regime in the presence of these glazes. This also agrees with the reduction in wear volume measured on the disc track in the 200°C temperature condition under a load of 35 N. The polished appearance of the ball scar is once again observed, see Figure 3.26 (c) and (d) agreeing with the significant increase in wear volume observed.

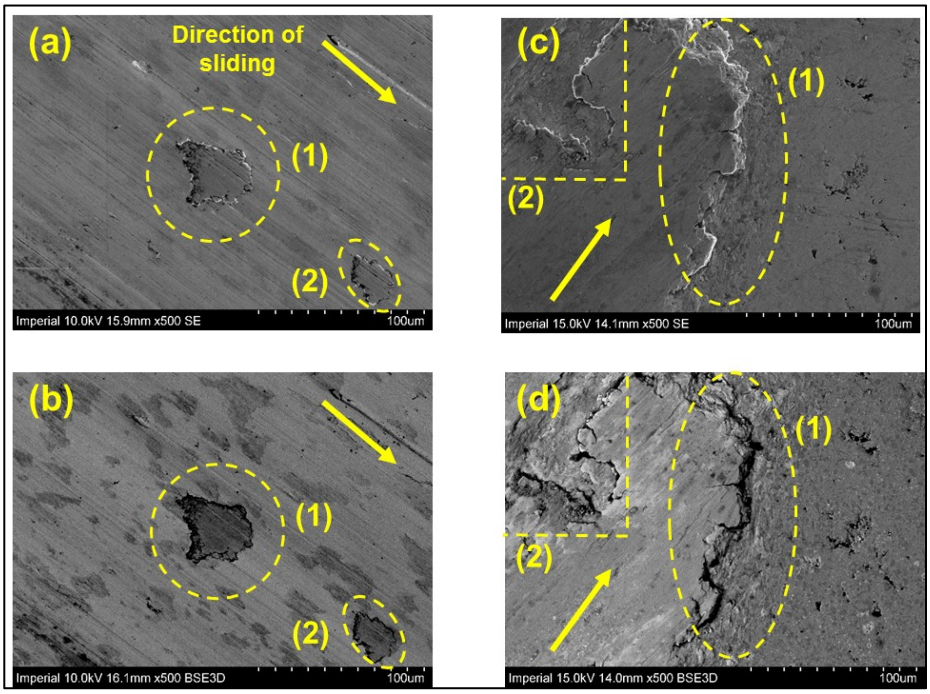

Figure 3.24: (a) and (b) area within disc wear track and (c) and (d) area within ball wear scar from using SE and BSE modes of the SEM of components tested under 35 N at 20°C

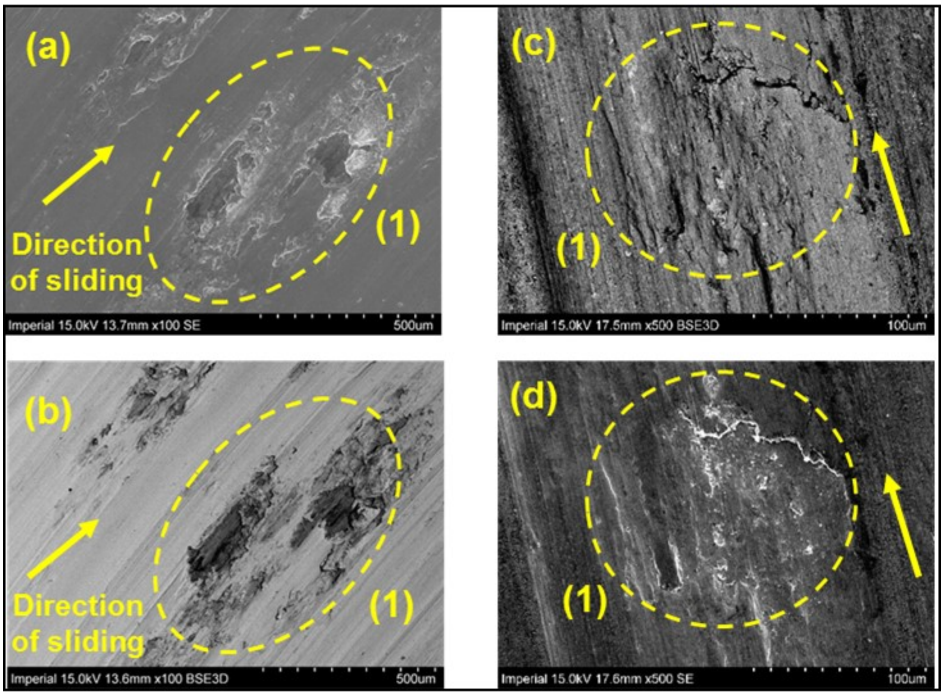

Figure 3.25: (a) and (b) area within disc wear track and (c) and (d) area within ball wear scar from using SE and BSE modes of the SEM of components tested under 35 N at 100°C

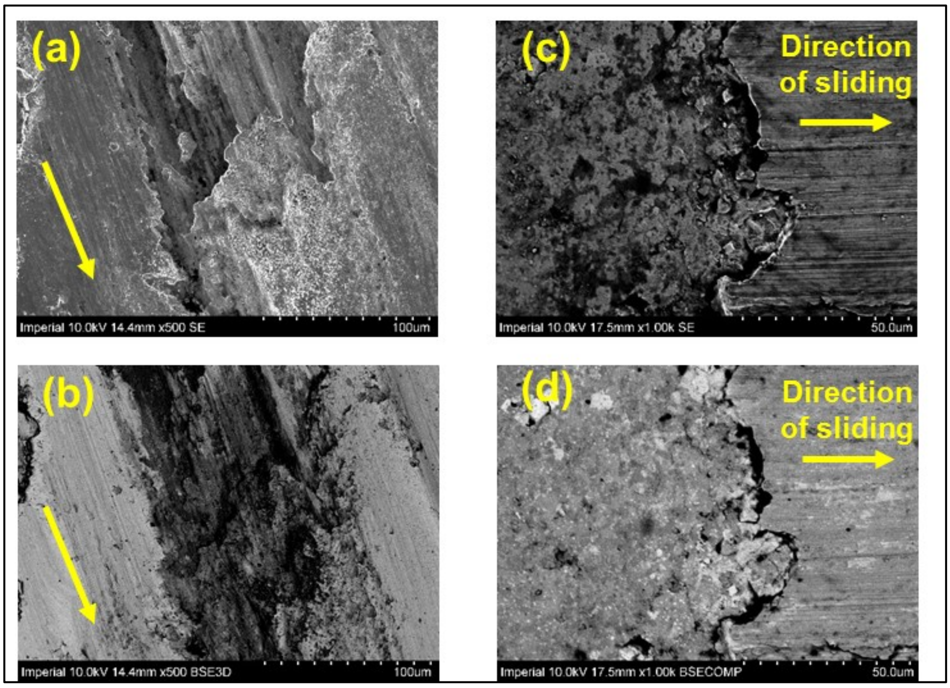

Figure 3.26: (a) and (b) area within disc wear track and (c) and (d) area within ball wear scar from using SE and BSE modes of the SEM of components tested under 35 N at 200°C

Table 3.8: EDX chemical compositional analysis of specific locations on disc wear track and ball wear scar surfaces for areas presented in Figure 3.24 – 3.26

			Carbon	Oxygen	Silicon	Titanium	Chromium	Manganese	Iron	Cobalt	Nickel	Niobium	Tungsten	Total
Experiment: 35 N @ 20°C	**Figure**	**Feature**	%wt	%wt	%wt	%wt	%wt	%wt	%wt	%wt	%wt	%wt	%wt	%wt
Disc	3.24 (a) and (b)													
		Average track spectrum	4	6	0		18	2	3	44	9		14	100
		Smooth track	3	2	0		19	2	2	47	9		16	100
		Feature 1 and 2: fragments of wear debris	5	11	<1		16	1	9	37	9		11	100
		Dispersion	8	28	<1		16	1	6	28	6		7	100
Ball	3.24 (c) and (d)													
		Average scar spectrum	8	10	4	<1	18	<1	32	13	9	4	1	100
		Undamaged surface	7	0	6	<1	22	0	47	0	9	8	0	100
		Smooth scar	5	7	3	<1	18	<1	38	10	9	7	2	100
		Feature 1: significant topographical damage at scar border	3	17	2	<1	16	<1	18	27	9	2	5	100
		Feature 2: topographical damage	0	14	4	0	17	0	40	11	9	4	1	100
Experiment: 35 N @ 100°C	**Figure**	**Feature**												
Disc	3.25 (a) and (b)													
		Average track spectrum	2.39	3.18			19.11	1.42	8.16	42.16	8.97		14.61	100
		Smooth track	2	<1	0	0	20	2	2	48	9	0	16	100
		Feature 1: topographical damage within wear track/ debris	4	11	3	<1	18	<1	31	15	9	4	4	100
Ball	3.25 (c) and (d)													
		Average scar spectrum	6	6	5		21	0	44	2	9	7	0	100
		Smooth scar	6	6	5	<1	22	0	45		8	8	0	100

		Topographical damage with some adhesion of debris	11	11	3	0	16	0	36	9	8	4	2	100
Experiment: 35 N @ 200°C	**Figure**	**Feature**	**Carbon** %wt	**Oxygen** %wt	**Silicon** %wt	**Titanium** %wt	**Chromium** %wt	**Manganese** %wt	**Iron** %wt	**Cobalt** %wt	**Nickel** %wt	**Niobium** %wt	**Tungsten** %wt	**Total** %wt
Disc	3.26 (a) and (b)													
		Average track spectrum	4	6			18	2	6	41	9		14	100
		Smooth track	2	2			19	2	3	47	9		16	100
		Topographical damage	3	17	2		17	1	18	24	8	2	8	100
		Fine, powder like debris	4	10			17	2	9	38	8		12	100
Ball	3.26 (c) and (d)													
		Average scar spectrum	0	12	4	<1	21	<1	39	9	9	4	2	100
		Smooth scar	4	9	4	<1	20	<1	43	5	9	5		100
		Topographical damage at border	4	7	4	<1	<1	20	1	45	5	9	4	100

Conclusion

Stellite 20 and Haynes 25 are two cobalt-based alloys currently employed in REB applications in the core of a nuclear reactor. There is a drive in the nuclear industry to remove or reduce cobalt from reactor environments due to unfavourable behaviour in the primary core. The sliding wear behaviour of these alloys was investigated using a ball on disc tribometer designed to simulate the core of a nuclear reactor in the laboratory environment. The experiments were conducted for a range of temperature and loading conditions to provide an insight of how these variables impact the behaviour of the alloys. The post experimental components were analysed via wear volume measurement and an SEM was used to investigate the impact of wear on the topography and composition of the worn surfaces. The purpose of these experiments was to establish a performance benchmark from which the performance of low cobalt or cobalt-free alternative alloys could be measured. A cobalt-free, iron-based alloy RR2450 was nominated by RR as an alloy with the potential to replace Stellite 20 in the rolling element of the REB systems. The experiments carried out using the Stellite 20-Haynes 25 balls and discs were repeated, replacing Stellite 20 with RR2450. Haynes 25 was used as the disc in both sets of experiments for a consistent comparison of RR2450 to Stellite 20.

The results were compared at each experimental condition for the Stellite 20-Haynes 25 and RR2450-Haynes 25 balls and discs. Under a normal load of 10 N, the total wear volume measured was lower for the Stellite 20-Haynes 25 ball-disc combination than for the RR2450-Haynes 25 combination with one experimental outlier. The difference was not considered significant and the results demonstrated that RR2450 has potential as a wear resistant alloy under the experimental conditions. Under a normal load of 35 N, the RR2450-Haynes 25 combination produced less total wear volume than the Stellite 20-Haynes 25 combination in all temperature conditions, again, with one experimental outlier. Overall the sliding wear behaviour of Haynes 25 did not change significantly at any experimental condition tested when the ball used was changed from Stellite 20 to RR2450 with respect to wear volume measured, topographical and compositional analysis. In the upper loading condition, wear volume of the Haynes 25 discs was slightly lower for the RR2450-Haynes 25 combination. In both sets of experiments, in the upper loading condition, the disc wear volume measured decreased with an increase in temperature. SEM analyses of the disc tracks produced in the RR2450-Haynes 25 experiments, indicated that as temperature increased, ball wear debris transfer and adhere to the disc surface, protecting it from further wear. Due to the compositional similarities between Stellite 20 and Haynes 25 it was not possible to infer if the same phenomena was happening in the prototypical contact pair; however, the evidence available and from discussions in literature indicate that this is likely, see Figures 3.23 and 3.26 and discussions presented by Stott, Inman and Dréano [21, 62, 63].

Due to time limitations of the experimental apparatus and limited quantity of RR2450 balls produced from the original powder the experiments were repeated once. The wear of the RR2450 was not repeatable in all experiments conducted. This is attributed to the poor surface finish of the balls produced. The powder from which they were made is thought to be too coarse and may have impacted the surface finish of the balls. In the latter stages of this project finer RR2450 powder was made available and balls are currently in production using this. An improved surface finish might improve the wear behaviour of the alloy in the sliding ball-on-disc experiments. There is also the risk that manufacturing of RR2450 components was, and will be compromised in the future, by the presence of the large niobium carbides identified in the course of the thesis presented by Bowden [20]. The results presented in this chapter provide evidence that RR2450 has potential as a wear resistant, cobalt-free alloy and warrants further investigation as a replacement for Stellite 20 however, the risks identified to the manufacture and finishing of RR2450 components should be taken into account. The results have provided further scope for the investigation and evaluation of alloys with composition and properties that resemble RR2450. The results also demonstrate significant increase in wear volume for both Stellite 20 and RR2450 with an increase in environmental temperature from room temperature to 100°C and from 100°C to 200°C. The operating temperature of the core of a nuclear reactor is approximately 310°C. The wear behaviour of both alloys should be investigated and compared at this service temperature or as close to it as possible in the laboratory environment.

Chapter 4 Development of a preliminary screening sliding wear experiment

Chapter 4 Development of a preliminary screening sliding wear experiment

Introduction

In Chapter 3 a detailed sliding wear experimental investigation was conducted on two cobalt-based alloys currently in use for rolling element bearings (REBs) operating in the core of nuclear reactors. Sliding wear experiments with Stellite 20 and Haynes 25 balls and discs were conducted using a bespoke design ball-on-disc tribometer. The tribometer, which was designed at the University of Nottingham (UoN) with the support of Rolls Royce plc (RR), could be enclosed in an autoclave facilitating water lubricated sliding wear experiments at temperatures up to 250°C, while still maintaining the lubricating medium (coolant equivalent of the nuclear reactor) below boiling point thanks to the pressurisation of the chamber. The Stellite 20-Haynes 25 ball-on-disc experimental results were used to set a performance benchmark from which cobalt-free or low cobalt alternative alloys could be compared. RR patented developmental alloy RR2450 was nominated to replace Stellite 20 balls and the relative wear resistance exhibited by RR2450 was promising. Recommendations for further investigation into the behaviour of this alloy in the nuclear environment was recommended as a result of the work conducted.

The experiments described in Chapter 3 are time intensive and tribometer availability was limited over the course of this project. A preliminary 'screening' sliding wear experiment was therefore developed at Imperial College London (ICL). The aim of this development was to reduce the volume of more time intensive experiments to be conducted using the autoclave rig at the UoN. The maximum normal load available using the tribometer at ICL was 10 N. The tribometer was not enclosed in an autoclave unlike the tribometer at the UoN and therefore water lubricated experiments were limited to 80°C so that the water wouldn't evaporate. This temperature was selected because it was within reasonable proximity to the 100°C temperature experiments conducted at the UoN and, still immersed in water for a good comparison. Figure 4.1, a simple illustration of the phase diagram of water, demonstrates the points at which tests were conducted using both experimental set-ups, and the proximity of the pressure in the 80°C and 100°C condition was also deemed reasonable, particularly when compared with the significantly higher increase in pressure observed when temperature increased to 200°C, see Table 4.1.

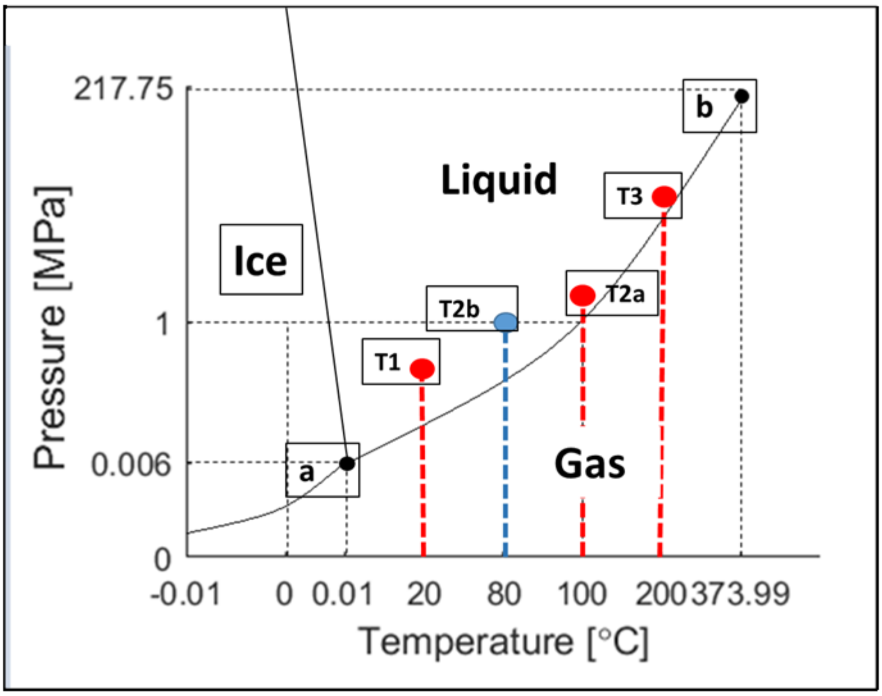

Figure 4.1: Phase diagram of water highlighting the experimental temperatures applied using the tribometers at the UoN and ICL

Table 4.1: Key to the points highlighted in Figure 4.1 and the corresponding pressures recorded during experimentation

T1	Room temperature, lowest experimental temperature ***(0.29MPa recorded)***
T2a	Medium temperature of experiment at UoN; normal boiling point of water ***(2 MPa recorded)***
T2b	Upper temperature of experiments at ICL ***(atmospheric pressure)***
T3	Upper temperature of experiments conducted at UoN ***(20.3 MPa recorded)***
a	Triple point of water
d	Critical temperature

The Stellite 20-Haynes 25 and RR2450-Haynes 25 ball-on-disc combinations were again tested in conditions available using the tribometer at ICL. The sliding wear results were compared to those produced from experiments conducted at the UoN as a means of validating the tribometer at ICL for use as a preliminary screening experiment. Results produced from the Stellite 20-Haynes 25 experiments were used to set the performance benchmark in order to make an assessment of the suitability of potential cobalt-free or low cobalt alternative alloys to replace either Stellite 20 or Haynes 25.

A literature review (see Section 2.5.1, Chapter 2) was conducted to identify commercially available alloys with mechanical and corrosion resistant properties close to those reported for Haynes 25. Cronidur 30 and Haynes 230, a cobalt-free and a low cobalt alloy were identified as candidates to replace Haynes 25. The preliminary screening experiment at ICL was used to investigate the wear performance of each alloy, comparing the results to the Stellite 20-Haynes 25 ball-on-disc experimental results. The ball used in this set of experiments was the cobalt-based Stellite 20 alloy ensuring a consistent comparison to the performance benchmark set. The experimental results were analysed by measuring the wear volume and depth for the ball and disc components. A topographical and in-depth surface imaging analysis was conducted on the worn surfaces using a white light interferometer (WLI) and the SE and BSE modes of an SEM. A comparative analysis of Cronidur 30 and Haynes 230 with Haynes 25 is presented in this chapter and used to make recommendations for or against further investigation of the wear performance of these alloys.

4.1 Materials and Methods

4.1.1 Materials

4.1.1.1 Stellite 20 ball and Haynes 25 disc

Chapter 3 (Section 3.1.1) provides the material description for both the Stellite 20 balls and Haynes 25 discs used in this part of investigation. The Stellite 20 balls were obtained from the same supplier (RGP Balls, Milan, Italy) and the Haynes 25 discs were prepared in the same way as described in Chapter 3. The hardness of the discs used for the purpose of experiments conducted in this chapter was 521 HV30. The datasheets for each alloy are available in Appendices A and B.

Table 4.2: Compositional information for Haynes 25 and Stellite 20 used in this study

%wt	**Co**	**Ni**	**Cr**	**W**	**Fe**	**Mn**	**Si**	**C**
Stellite 20	Balance	3 **	30-34	13	3 *	0.5 *	1 *	2.8-3
Haynes 25	Balance	10	20	15	3 *	1.5	0.4 *	0.1

4.1.1.2 RR2450 balls

Chapter 3 (Section 3.1.2) provides the material description for the RR patented RR2450 balls produced specifically for this PhD project by Bodycote, Chesterfield, UK and PCS Instruments, London, UK. The patent document for this alloy is available in Appendix D.

Table 4.3: Chemical composition of RR2450 balls used in this experimental study

%wt	**Fe**	**Cr**	**Ni**	**Nb**	**Si**	**C**
RR2450	Balance	22	9	8	6	7

4.1.1.3 Cronidur 30 discs

Cronidur 30 is a commercially available alloy nominated to replace Haynes 25 in the race element of the REBs. Cronidur 30 is a martensitic steel, the composition of which is presented in Table 4.4. The iron-based alloy is used in industry for applications including cutting tools and medical instruments *e.g.* drills [122].

Table 4.4: Chemical composition of Cronidur 30 [122]

%wt	**Fe**	**Cr**	**Mo**	**N**	**C**
Cronidur 30	Balance	14-16	0.85-1	0.3-0.4	0.25-0.35

Discs were acquired from Hempel Special Metals Ltd, Berkshire, England for the purpose of these experiments. The discs were cut from a 32.5 mm diameter bar. They were faced with a CNC mill at ICL. The disc samples, average thickness 4.25 mm, were prepared for the sliding wear experiments using a Metserv Grinding and Polishing machine. The recommended surface roughness for a disc applied in a pin-on-disc experiment is R_a <0.8 µm and the recommended surface roughness for the inner race in an SKF rolling bearing is R_a <0.4 µm [116, 117]. To achieve this, silicon carbide grinding papers were used in the following order; Grit size P60, P320, P600, P1200 and finally P2500. The average final surface roughness of the discs was

0.05 μm which was well within the recommended limits. The hardness as per the material datasheet provided by Hempel Special Metals, see Appendix E, and is 55-60 HRC (650-700 HV).

4.1.1.4 Haynes 230 discs

Haynes 230 is the second commercially available alloy nominated as an alloy with the potential to replace Haynes 25 in the race element of the rolling element bearing. It is a nickel-based alloy containing a relatively low quantity of cobalt in its composition. Table 4.5 presents the chemical composition of Haynes 230.

Table 4.5: Chemical composition of Haynes 230

Alloy	Ni	Mo	Cr	Fe	W	Co	Mo	C	Other
Haynes 230	57 balance	2	22.5	3 max.	14.6	5 max.	1.31	0.1	0-1

A bar of diameter 31.75mm was obtained from Haynes International, Manchester, UK for the purpose of this study. The bar was hot rolled solution treated and the hardness of the sample received was 90 HRB (188 HV) - significantly softer than the Haynes 25 and Cronidur 30 discs. In this form, the alloy was unlikely to exhibit acceptable wear resistance however experiments were conducted regardless, to demonstrate the effectiveness of the preliminary screening experiment at ICL. Discs were cut from the bar using an EDM machine. The disc samples with average thickness of 4.4 mm and were prepared for experiments by the same grinding and polishing method as described in Section 4.1.1.3. The average final surface roughness of the discs was 0.05 μm.

4.1.2 Method: Ball-on-disc sliding wear experiment

Figure 4.2 presents an image and schematic diagram of the Anton Paar high temperature tribometer (THT) used for the purpose of these experiments at Imperial College London. The apparatus has been retrofitted to allow for sample immersion in water, see bath labelled in Figure 4.2. The ball is held in the ball holder and contact is made between the ball and disc, held in the bath. Normal load is applied via free weights. The shaft was programmed to rotate at 200 rpm, the same as in the experiments described in Chapter 3. Table 4.6 presents the experimental conditions tested. Each alloy combination was tested in each condition with experiments repeated at minimum twice.

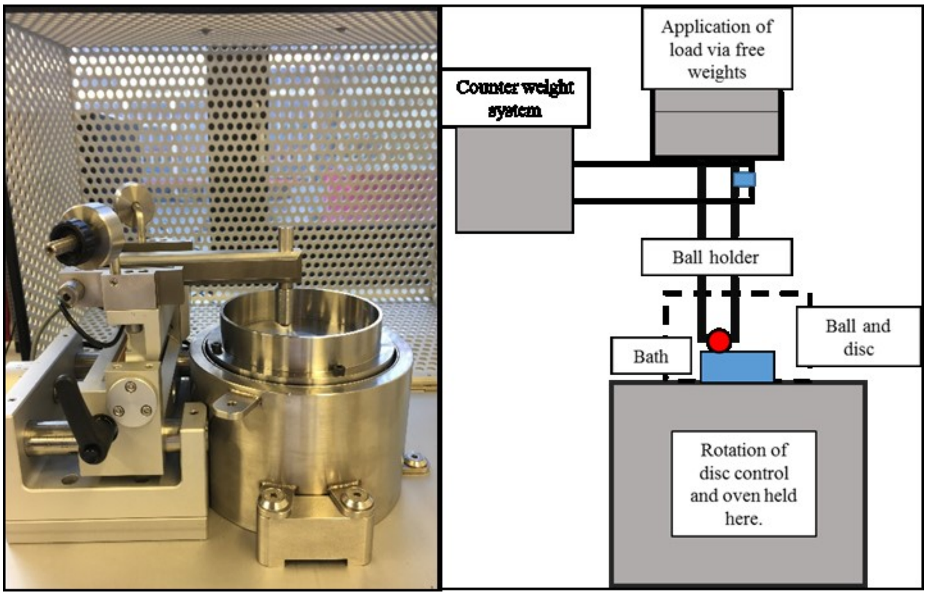

Figure 4.2: Anton Paar high temperature tribometer at Imperial College London

Table 4.6: Experimental conditions applied

Experimental setup	Description	
Time [min]	180	
Speed [rpm]	200	
Sliding distance [m]	2296	
Experimental condition	Experiment number	
Condition reference	1	2
Normal Load	10	10
Corresponding maximum contact pressure [GPa]	1.13	1.13
Temperature [°C]	RT	80

4.1.2.1 Post experimental analysis method

4.1.2.1.1 Wear measurement

The same procedure for measuring wear on the ball and disc components followed in Chapter 3 was followed for experiments presented in this chapter, see Chapter 3 (Section 3.3.2). A VEECO white light interferometer was used to measure disc wear volume and microscope images of scars produced on the balls were used to measure the ball wear volume.

4.1.2.1.2 Topographical analysis

The SE and BSE modes of an SEM (JCM-6000 Neoscope, JEOL USA Inc.) were used to examine the impact of wear experiments on the experimental components. Data obtained using the VEECO white light interferometer were processed to generate profiles of the disc tracks, which were compared across all experimental conditions.

EDX analysis of wear surfaces was not deemed necessary in this investigation. The preliminary screening experiment was developed to reduce the volume of time intensive experiments conducted in an environment more appropriate to that of a nuclear reactor. It is the wear resistance of alloys that is under investigation in this chapter and an understanding of material removal. Any alloys that are recommended to be investigated further in the simulated nuclear reactor will undergo a more intensive topographical and compositional investigation following wear experiments.

4.2 Results and discussion

4.2.1 Wear measurement

The following section presents the wear volume measurements following sliding wear experiments conducted under a normal load of 10 N at room temperature (RT) and 80°C respectively using the Anton Paar high temperature tribometer. For each set of experiments a table is presented of wear data measured on the post experimental ball and disc components. The standard deviation associated with each set of measurements is also provided in these tables. The results from the Stellite 20-Haynes 25 and RR2450-Haynes 25 ball-on-disc experiments were compared to results from experiments conducted using the bespoke tribometer presented in Chapter 3. The comparison was used to validate Anton Paar high temperature tribometer for use as a preliminary screening experiment for cobalt-free or low cobalt alloys.

In Chapter 3, the wear performance exhibited by RR2450 indicated that it has acceptable wear resistant properties when compared to the wear resistance of Stellite 20 in the conditions tested. The wear performance of Cronidur 30 and Haynes 230 were assessed using the preliminary screening experiment developed and the results were compared to Haynes 25 in this chapter.

4.2.1.1 Stellite 20 ball and Haynes 25 disc

Figure 4.3 and Table 4.7 present the wear results measured on the Stellite 20 balls and Haynes 25 discs in both temperature conditions using the Anton Paar high temperature tribometer.

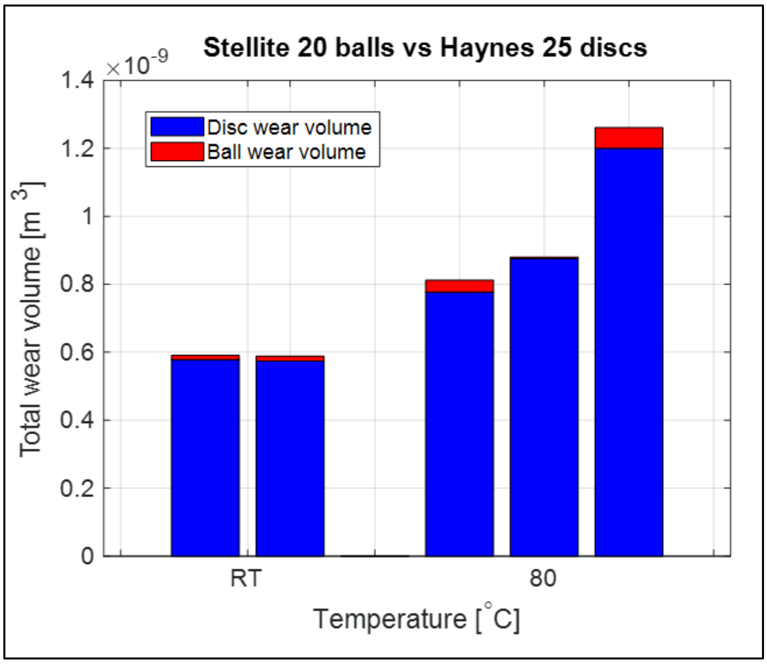

Figure 4.3: Stellite 20 ball against Haynes 25 disc - total wear volume measured for both experimental conditions

Table 4.7: Results measured on Haynes 25 disc and Stellite 20 ball following sliding wear experiments

	Load [N]	**T [°C]**	**Maximum wear depth**		**Track width / scar diameter**		**Wear volume**	
			Disc [μm]	Ball [μm]	Disc [mm]	Ball [mm]	Disc [m^3]	Ball [m^3]
Repeat 1	10	20	**15** +/- 0.51	**28.75** +/- 3.95	**1.1** +/- 0.03	**1.04** +/- 0.07	**5.78E-10** +/- 3.69E-11	**1.26E-11** +/- 3.41E-12
Repeat 2	10	20	**13** +/- 0.59	**30.76** +/- 3.62	**1.57** +/- 0.35	**1.08** +/- 0.06	**5.74E-10** +/- 5.64E-11	**1.43E-11** +/- 3.37E-12
Repeat 1	10	80	**13.43** +/- 0.58	**48.43** +/- 3.29	**1.82** +/- 0.38	**1.35** +/- 0.05	**7.77E-10** +/- 4.37 E-11	**3.51E-11** +/- 4.79E-12
Repeat 2	10	80	**16.44** +/- 1.41	**18.14** +/- 2.26	**1.83** +/- 0.33	**0.83** +/- 0.05	**8.75E-10 +/-** 1.12E-10	**4.98E-12** +/- 1.22E-12
Repeat 3	10	80	**19.12** +/-1.49	**63.81** +/- 2.89	**1.94** +/- 0.36	**1.55** +/- 0.04	**1.2E-9** +/- 1.57E-10	**6.08E-11** +/- 5.42E-12

An increase in total wear volume was observed with an increase in experimental temperature, more notably in the case of the Haynes 25 disc. The maximum wear depth is an important factor to consider when assessing the wear performance of an alloy/mechanical component. It was observed that the maximum disc wear depth did not increase notably with the increase in temperature. For two of the experiments conducted at 80°C, however, the wear depth of the Stellite 20 ball increases substantially with respect to the room temperature experiments.

Validation of the preliminary screening experiment at ICL

The wear volume measurements presented in Table 4.7 were compared to results presented in Chapter 3 from experiments conducted using the bespoke tribometer; the results are reported in Figures 4.4 (a) and (b). The preliminary screening experiment at ICL should serve the purpose of screening materials with mechanical and corrosion resistant properties that indicate that they should be investigated further in a more intense environment at the UoN.

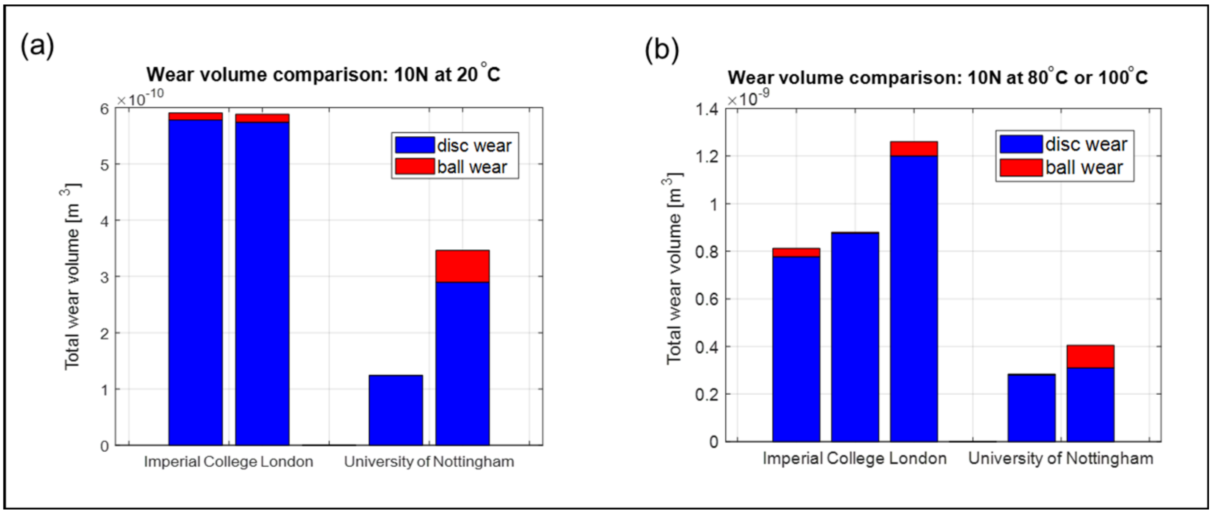

Figure 4.4: Wear volume produced on Stellite 20 ball and Haynes 25 disc following experiments conducted at ICL and UoN under a 10 N load at (a): 20°C and (b) 80°C

Figure 4.4 (a) and (b) compare total wear volume of Stellite balls and Haynes 25 discs that have been tested under a compressive load of 10 N at room temperature and 80°C at ICL and 100°C at the UoN. Figure 4.4 indicates that the preliminary screening experiment, although showing similar trends in terms of wear volume of the two materials tested, gives a more conservative result for wear that is within the range of that measured at the University of Nottingham. It can therefore be used as a means of screening materials at ICL. Cobalt-free and low cobalt alloys that demonstrate wear resistance that is in good comparison to the benchmark set by the Stellite 20-Haynes 25 ball-on-disc experiments, should be investigated further using the tribometer at the UoN where higher loading and temperature experimental conditions are available.

4.2.1.2 RR2450 ball and Haynes 25 disc

Figure 4.5 and Table 4.8 present the wear results measured on the RR2450 balls and Haynes 25 discs in both temperature conditions. In Figure 4.5 it can be observed that there is no significant change in the total wear volume as temperature increases, within the bounds of experimental error. For this material combination the quantity of RR2450 balls available for experimentation was limited however as these experiments were conducted at the UoN this was deemed acceptable. As per the Stellite 20 and Haynes 25 material combination, the maximum wear depth of the disc track did not vary notably with an increase in temperature, see Table 4.8. The wear depth of the ball, unlike wear produced on the Stellite 20 scar, also remained reasonably consistent. This indicated that under the 10 N loading condition, an increase in temperature from room temperature to 80°C did not significantly impact the wear behaviour of the RR2450 balls.

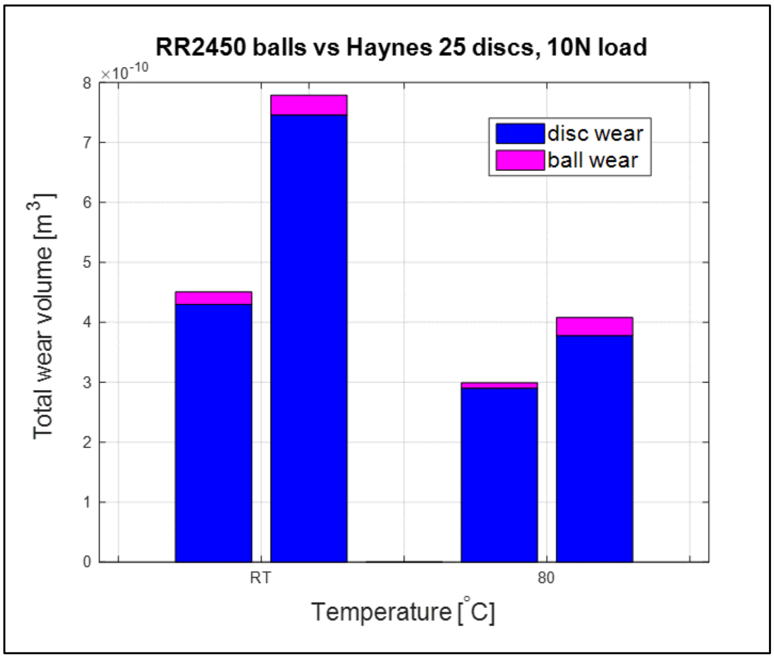

Figure 4.5: Wear volume produced on RR2450 ball against Haynes 25 disc following sliding wear experiments at ICL

Table 4.8: Results measured on Haynes 25 disc and Stellite 20 ball following sliding wear experiments

	Load [N]	**T [°C]**	**Maximum wear depth**		**Track width / scar diameter**		**Wear volume**	
			Disc [µm]	Ball [µm]	Disc [mm]	Ball [mm]	Disc $[m^3]$	Ball $[m^3]$
Repeat 1	10	20	**10.62** +/- 0.45	**37.06** +/- 2.44	**1.14** +/- 0.04	**1.2 +/-** 0.04	**4.3E-10 +/-** 4.1E-11	**2.06E-11** +/- 2.7E-12
Repeat 2	10	20	**15.5** +/- 0.94	**46.71** +/- 4.72	**1.22** +/- 0.05	**1.3** +/- 0.07	**7.46E-10 +/-** 4.3E-11	**3.28E-11** +/- 6.5E-12
Repeat 1	10	80	**10** +/- 1.02	**24.45** +/- 2.1	**0.75** +/- 0.07	**0.96** +/- 0.04	**2.9E-10** +/- 2.74E-11	**8.99E-12** +/- 1.51E-12
Repeat 2	10	80	**9.78** +/- 0.57	**44.8** +/- 2.22	**1.15** +/- 0.04	**1.3** +/- 0.03	**3.78E-10 +/-** 1.62E-10	**3E-11** +/- 2.9E-12

Validation of the preliminary screening experiment at ICL

The wear volume measurements presented in Table 4.8 were compared to results presented in Chapter 3 from experiments conducted using the bespoke tribometer at the UoN, see Figure 4.6 (a) and (b).

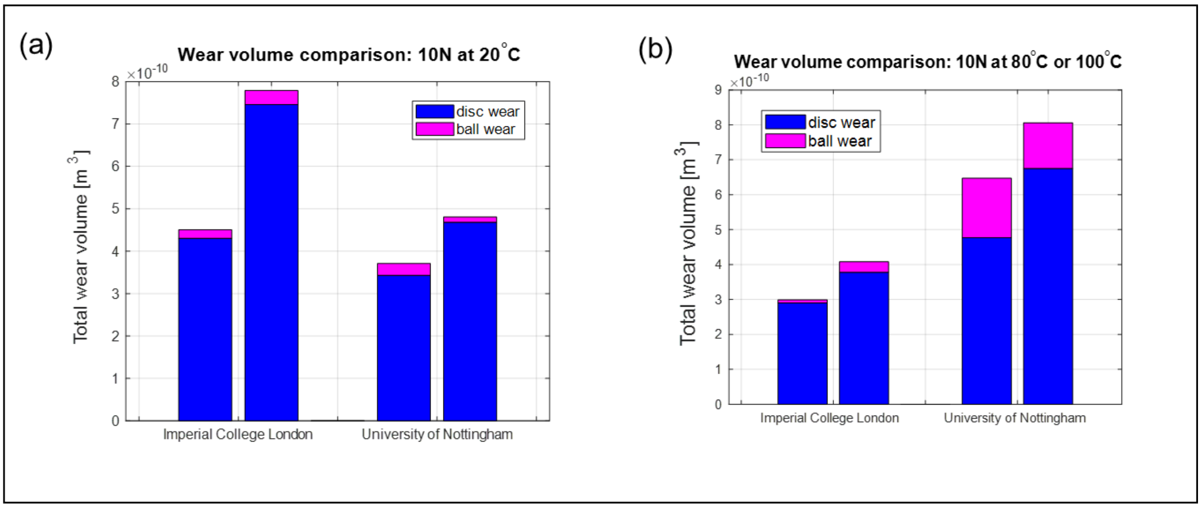

Figure 4.6: Wear volume produced on RR2450 ball and Haynes 25 disc following experiments conducted at ICL and UoN under a 10 N load at (a): 20°C and (b) 80°C

The wear volume measurements compared in Figure 4.6 (a) and (b) do not vary as much when compared relative to the comparison made in Figure 4.4, measured from Stellite 20-Haynes 25 ball-on-disc experiments. Although the results produced at ICL are not as conservative when compared to the same produced at the UoN, they are still comparable to those obtained from experiments conducted at the UoN and therefore both sets of results maintain the validity of the preliminary screening experiment.

4.2.1.3 Stellite 20 ball and Cronidur 30 disc

Figure 4.7 and Table 4.9 present the wear results measured on the Stellite 20 balls and Cronidur 30 discs in both temperature conditions.

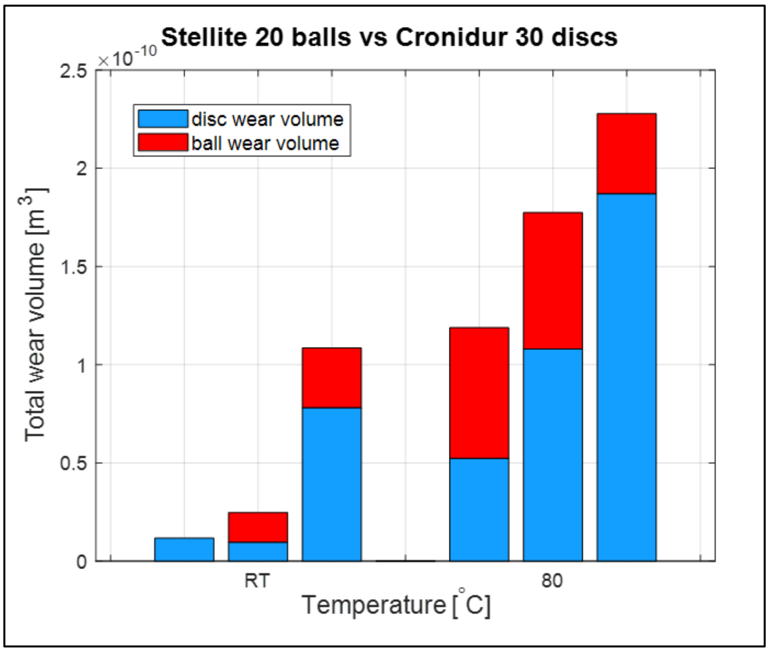

Figure 4.7: Wear volume produced on Stellite 20 ball against Cronidur 30 disc following sliding wear experiments at ICL

Table 4.9: Results measured on Cronidur 30 disc and Stellite 20 ball following sliding wear experiments

	Load [N]	**T [°C]**	**Maximum wear depth**		**Track width / scar diameter**		**Wear volume**	
			Disc [μm]	Ball [μm]	Disc [mm]	Ball [mm]	Disc $[m^3]$	Ball $[m^3]$
Repeat 1	10	20	**1.59** +/- 0.13	**46.85** +/- 1.3	**0.04** +/- 0.01	**1.34** +/- 0.01	**1.17E-11** **+/-** 2.75E-12	**3.27-11** +/- 1.88E-12
Repeat 2	10	20	**3.42** +/- 0.72	**31.81** +/- 1.79	**0.07** +/- 0.014	**1.1** +/- 0.03	**9.66E-12** **+/-** 1.87E-12	**1.51E-11** +/- 1.61E-12
Repeat 3	10	20	**16.73** +/- 0.37	**45.1** +/- 1.74	**0.11** +/- 0.0015	**1.31** +/- 0.03	**7.81E-11** **+/-** 2.68E-12	**3.04E-11** +/- 2.39E-12
Repeat 1	10	80	**14.62** +/- 0.66	**66.88** +/- 1.64	**0.07** +/ 0.002	**1.59** **+/-** 0.02	**5.24E-11** **+/-** 1.81E-12	**6.64E-11** +/- 3.22E-12
Repeat 2	10	80	**20.33** +/- 0.7	**68.22** +/- 2.03	**0.03** +/- 0.03	**1.61** +/- 0.02	**1.08E-10** **+/-** 4.67E-12	**6.94E-11** +/- 4.13E-12
Repeat 3	10	80	**32.33** +/- 0.76	**52.32** +/- 1.65	**0.31** +/- 0.08	**1.41** +/- 0.02	**1.87E-10** **+/-** 2.02E-11	**4.08E-11** +/- 2.56E-12

A notable increase in the total wear volume can be observed for the Stellite 20 and Cronidur 30 ball-on-disc combination with an increase in temperature in Figure 4.7. Taking the largest wear depth measurements into consideration from each set of experimental conditions, the increase in wear depth with an increase in experimental temperature is substantial on both components. Overall the width of the wear tracks produced on the Cronidur 30 discs were narrow relative to wear tracks produced on the Haynes 25 disc surfaces in the Stellite 20-Haynes 25 experiments, as can be observed in Figures 4.11 and 4.12. This explains why the wear volume measured on the discs following the Stellite 20-Cronidur 30 ball-on-disc experiments is significantly lower than the disc wear volume measured following the Stellite 20-Haynes 25 experiments. This is in spite of the experimental measurements demonstrating that the maximum wear depths recorded were not as substantially different, particularly at room temperature.

4.2.1.4 Stellite 20 ball and Haynes 230 disc

Figure 4.8 and Table 4.10 present the wear results measured on the Stellite 20 balls and Haynes 230 discs in both temperature conditions.

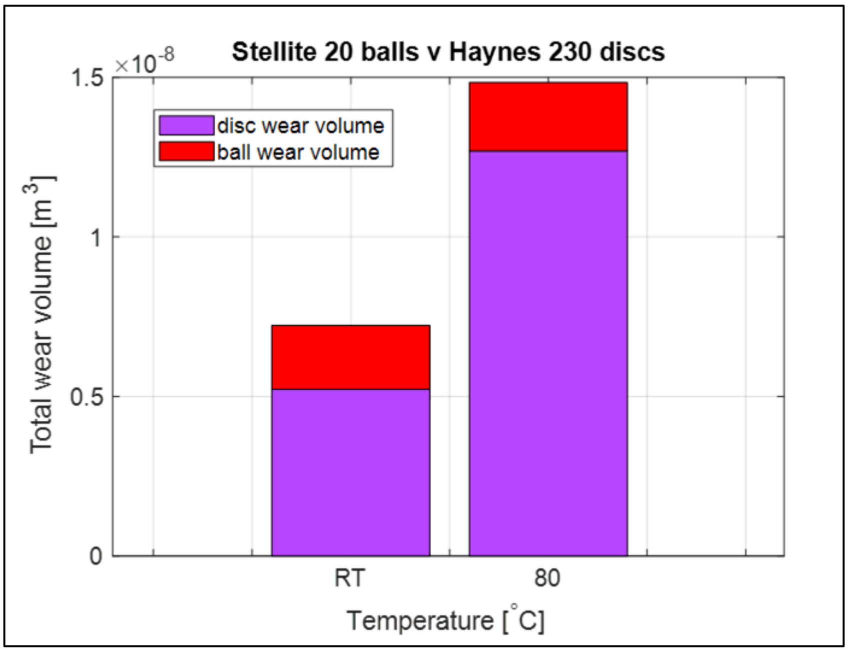

Figure 4.8: Wear volume produced on Stellite 20 ball against Haynes 230 disc following sliding wear experiments at ICL

Table 4.10: Results measured on Haynes 230 disc and Stellite 20 ball following sliding wear experiments

	Load [N]	**T [°C]**	**Maximum wear depth**		**Track width / scar diameter**		**Wear volume**	
			Disc [μm]	Ball [mm]	Disc [mm]	Ball [mm]	Disc [m^3]	Ball [m^3]
Repeat 1	10	20	**48** +/- 3.5	**0.35 +/-** 0.12	**2.8** +/- 0.03	**3.43** +/- 1.14	**5.22E-9 +/-** 1.05E-9	**2.01E-9** +/- 7.28E-10
Repeat 1	10	80	**92** +/- 2.72	**0.38** +/- 0.03	**3.56** +/- 0.05	**3.73** +/- 0.12	**1.27E-08 +/-** 1.27E-8	**2.14E-9** +/- 2.84E-10

Following the first experiments conducted at room temperature and 80°C, it was immediately obvious that Haynes 230 was substantially less wear resistant than either Haynes 25 or Cronidur 30. In each of the conditions tested, the ball scar diameter, disc track depth and width were significantly greater than what was produced on the surface of components from any other material pair examined at those conditions. This has been attributed to the soft condition of the Haynes 230 sample obtained for these experiments. As two experiments were conducted using the alloy albeit at different experimental conditions, the low wear resistance observed by Haynes 230 was anticipated for all prepared samples and therefore repeating these experiments was deemed unnecessary.

4.2.1.5 Comparing the wear performance of the existing cobalt-based alloys to nominated replacement alloys

Sliding wear experiments with the alloys used in the REBs operating in the nuclear reactor environment, Stellite 20 and Haynes 25, were conducted in order to set a performance benchmark from which wear behaviour of cobalt-free or low cobalt alloys nominated to replace them could be compared. The wear behaviour of RR2450 was once again investigated, replacing Stellite 20 balls with RR2450 balls, sliding against Haynes 25 discs for a consistent comparison. The wear volume measured from experiments replacing the Haynes 25 discs with Cronidur 30 and then Haynes 230 discs was also compared to the performance benchmark set. In these experiments Stellite 20 balls were used for a consistent comparison.

4.2.1.5.1 Replacing the Stellite 20 balls with RR2450 balls

Figures 4.9 and 4.10 compare the total wear volume measured from experiments conducted using Stellite 20-Haynes 25 and RR2450-Haynes 25 balls and discs at room temperature and 80°C under a normal load of 10 N.

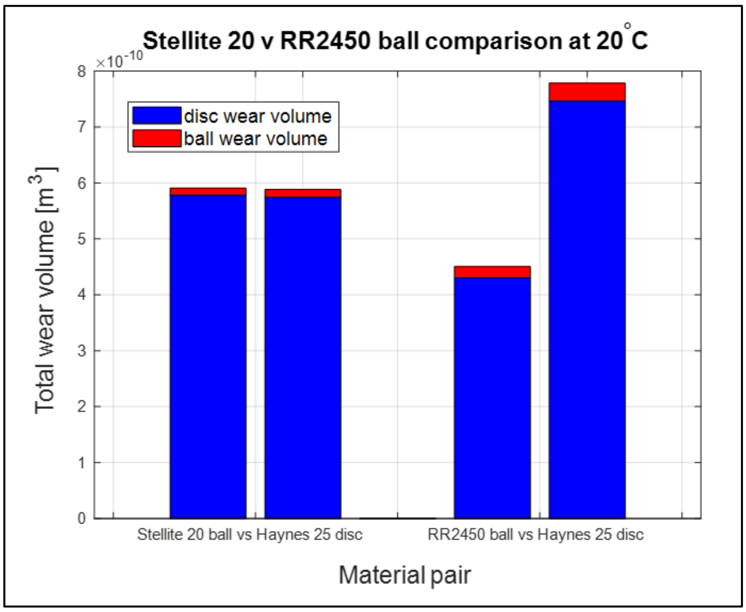

Figure 4.9: Comparing the wear volume produced on experimental components sliding Stellite 20 and RR2450 balls respectively against Haynes 25 discs at room temperature

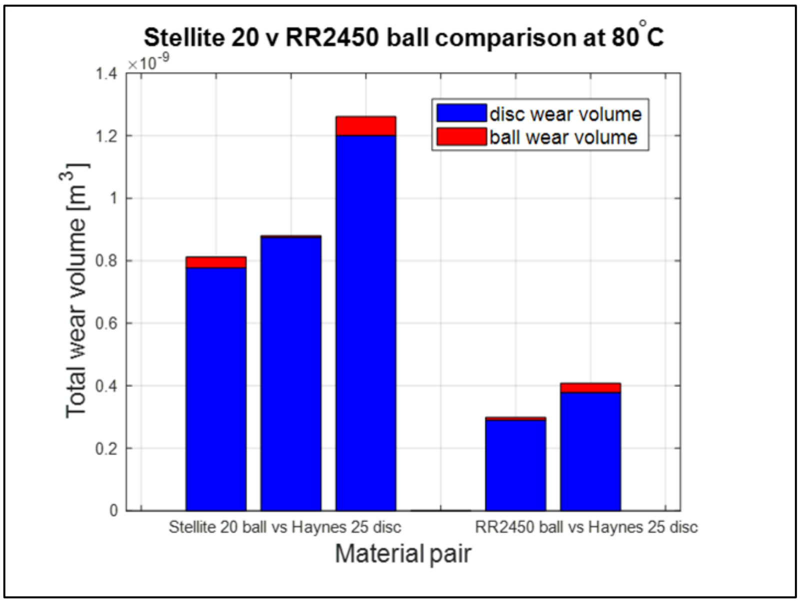

Figure 4.10: Comparing the wear volume produced on experimental components sliding Stellite 20 and RR2450 balls respectively against Haynes 25 discs at 80°C

In the experimental conditions tested, within the bounds of experimental error, the volume of material lost for the RR2450-Haynes 25 ball-on-disc experiments is considered acceptable when compared to the Stellite 20-Haynes 25 combination. With an increase in temperature to 80°C wear resistance demonstrate by the RR2450-Haynes 25 combination is superior to the wear resistance exhibited in the Stellite 20-Haynes 25 experiments. This was anticipated as RR2450 demonstrated good comparative wear resistance across all experimental conditions in results presented in Chapter 3.

Figures 4.11 and 4.12 (a)-(d) present a ball scar and section of a disc track produced as a result of the experiments conducted. Figures 4.11 and 4.12 (e) present a sample of a disc track profile using data measured on the surface of discs with the deepest tracks.

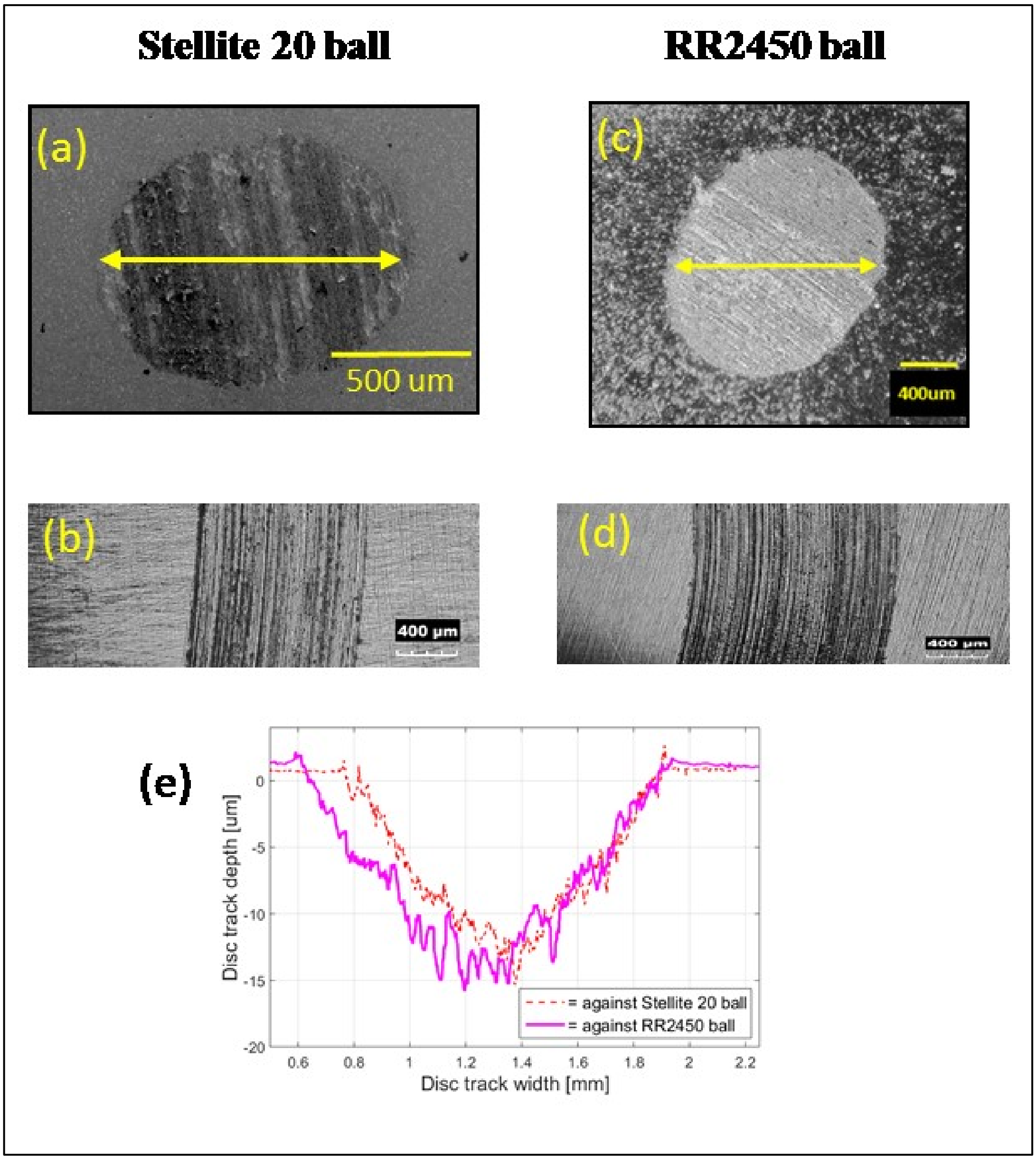

Figure 4.11: Ball scar, disc track and disc track profiles produced under a normal load of 10 N at room temperature

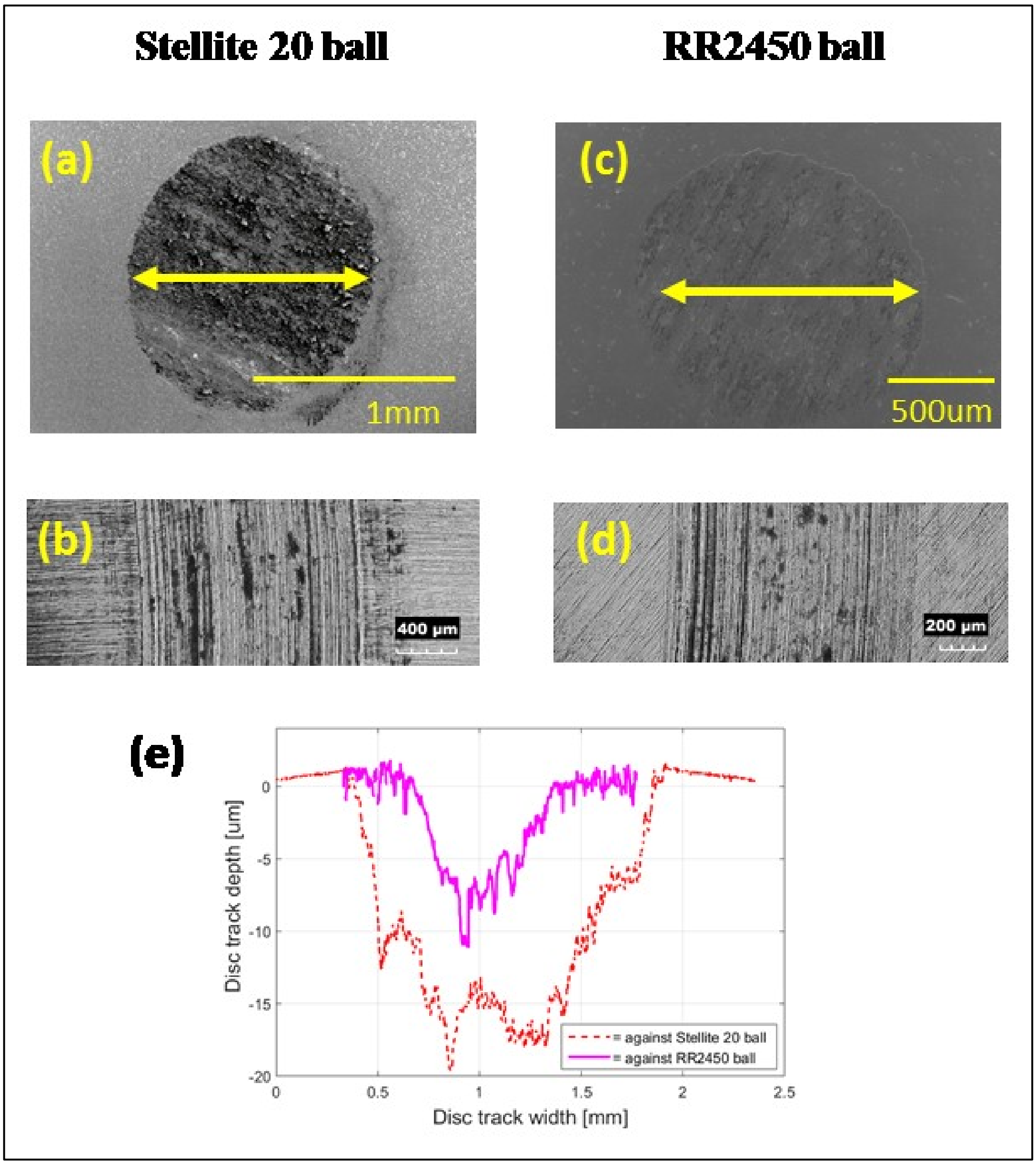

Figure 4.12: Ball scar, disc track and disc track profiles produced under a normal load of 10 N at 80°C

Comparing the maximum wear depth measured on the disc tracks produced at room temperature, the ball material did not have a significant impact on the disc track profile. With an increase in temperature however, Figure 4.12 (e) once again demonstrates the overall superior wear performance of the RR2450-Haynes 25 ball and disc combination which led to a more shallow wear track than that produced on the surface of the Haynes 25 disc from the Stellite 20-Haynes 25 experiment.

4.2.1.5.2 Replacing Haynes 25 disc with discs made from Cronidur 30 and Haynes 230

Figures 4.13 compares the total wear volume measure following experiments conducted using Stellite 20 balls sliding against Haynes 25, Cronidur 30 and Haynes 230 discs at room temperature and 80°C under a 10 N load.

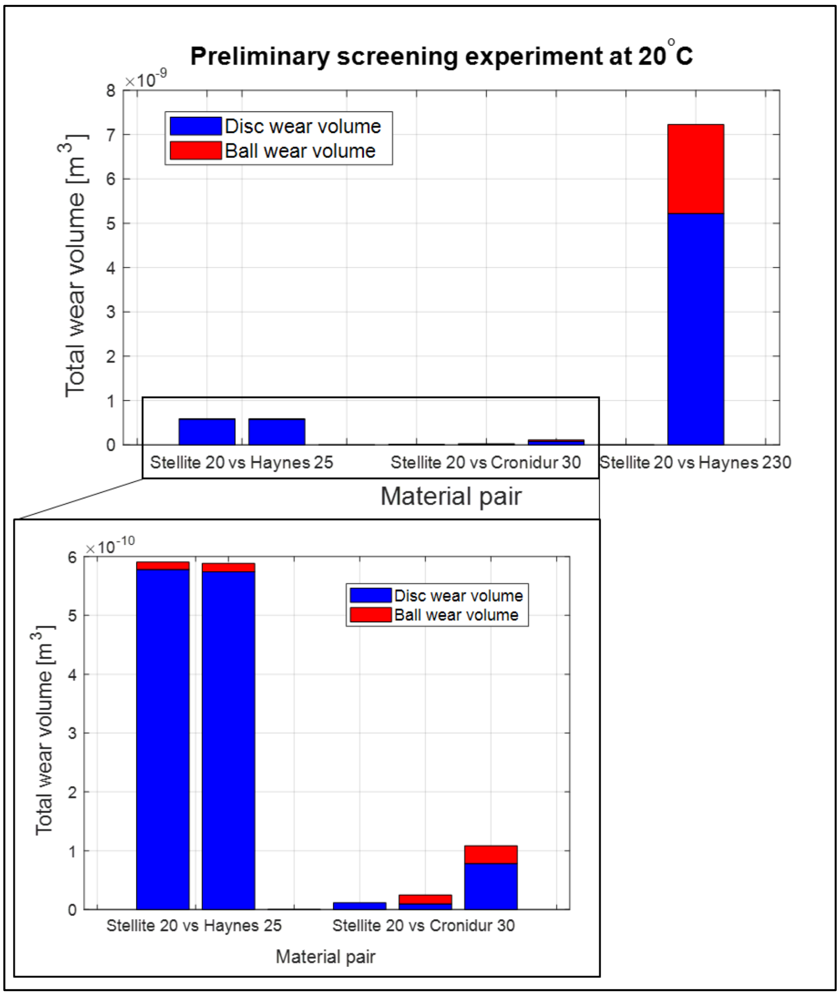

Figure 4.13: Comparing the wear volume produced on experimental components with a Stellite 20 ball against Haynes 25, Cronidur 30 and Haynes 230 discs respectively at room temperature

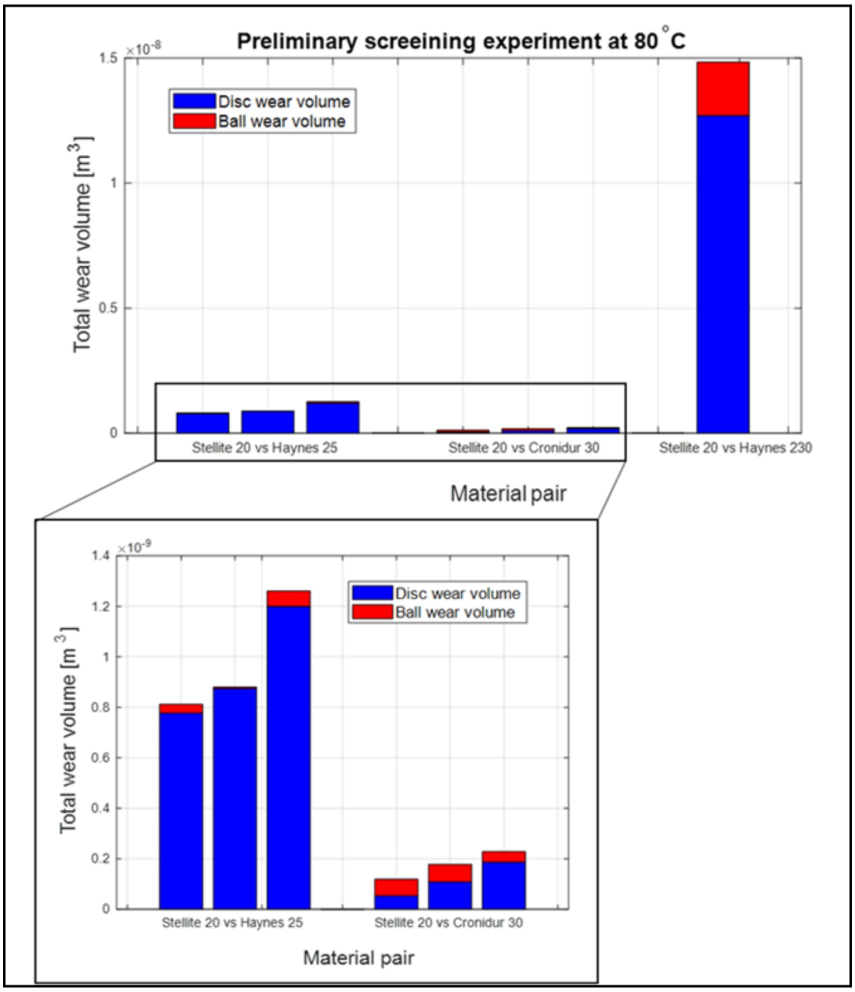

Figure 4.14: Comparing the wear volume produced on experimental components with a Stellite 20 ball against Haynes 25 and Cronidur 30 discs respectively at 80°C

In terms of total wear volume measured, the sliding wear resistance of the Stellite 20–Cronidur 30 ball-on-disc alloy combination was significantly better than the wear resistance of the Stellite 20–Haynes 25 combination in both experimental temperatures. The wear volume of the Stellite 20 ball did not vary significantly, see Figure 4.13 and 4.14. Cronidur 30 exhibited excellent wear resistance compared to Haynes 25 in the conditions tested. As previously discussed, the wear resistance exhibited by Haynes 230 was extremely poor compared to both Haynes 25 and Cronidur 30. The ball wear volumes measured as a result of sliding against the Haynes 230 discs was also significantly higher than from sliding against either Haynes 25 or Cronidur 30.

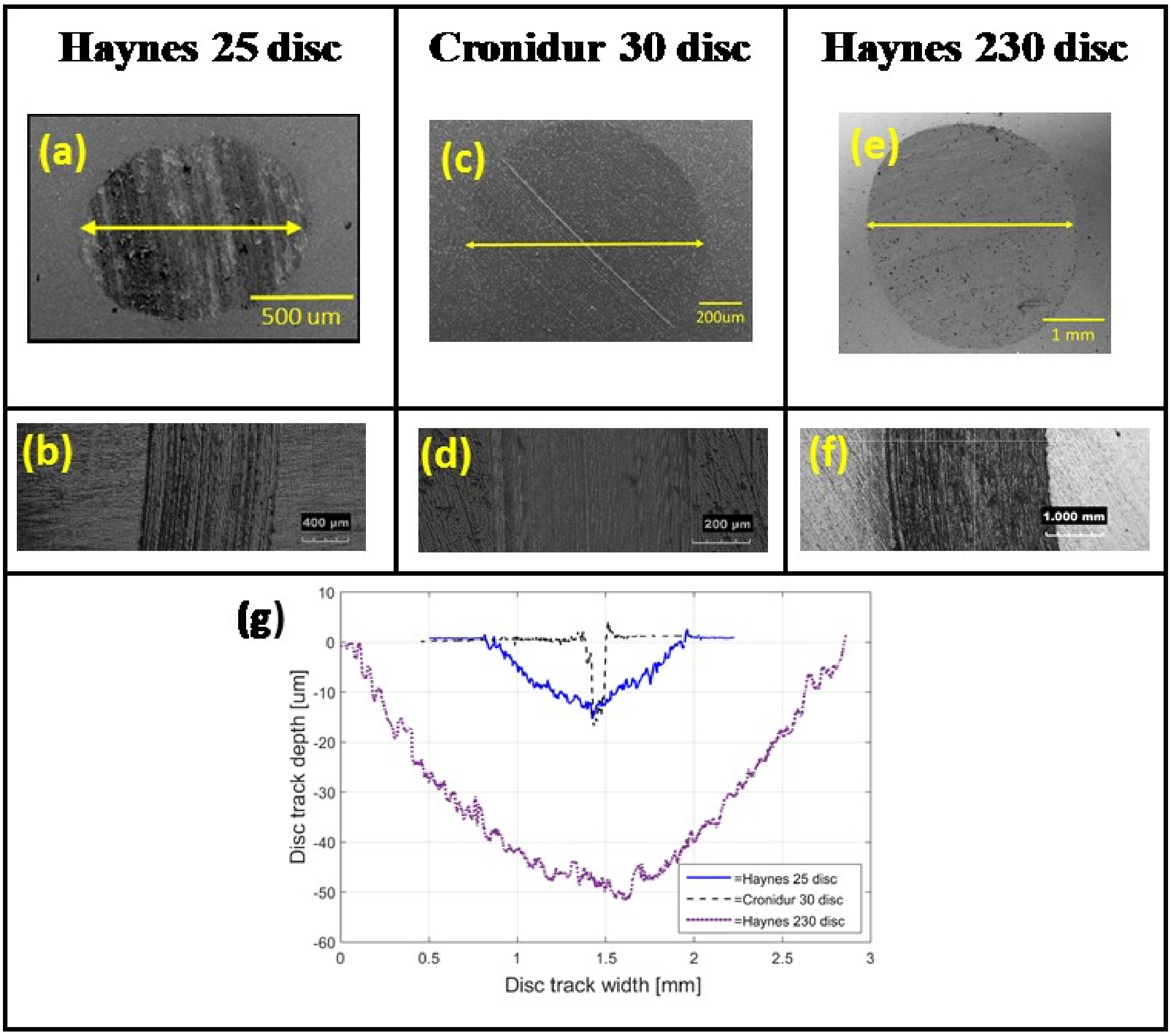

Figure 4.15: Ball scar, disc track and disc track profiles produced under a normal load of 10 N at room temperature

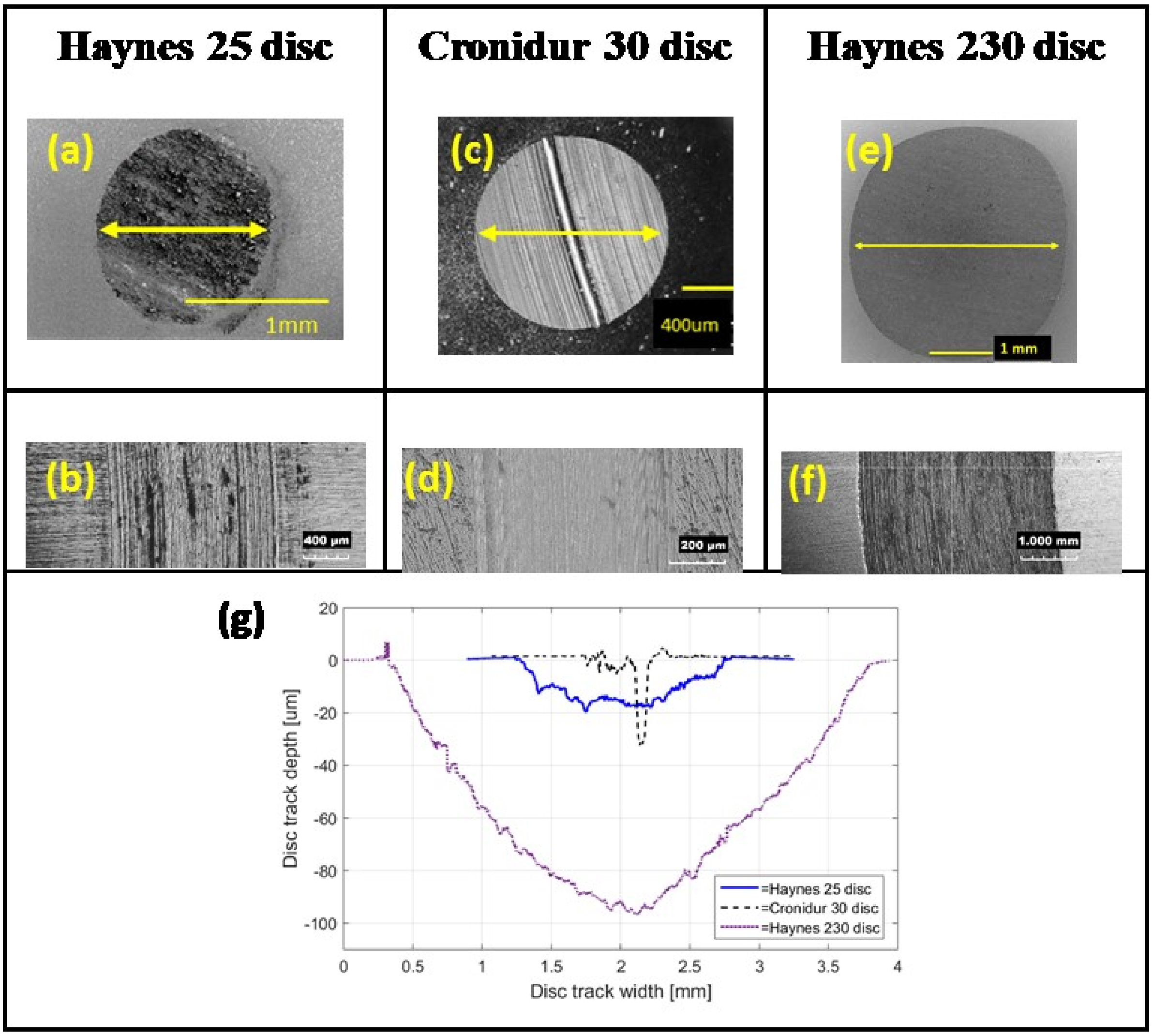

Figure 4.16: Ball scar, disc track and disc track profiles produced under a normal load of 10 N at 80°C

Scars produced on the Stellite 20 balls for both experimental conditions are presented in Figures 4.15 and 4.16 (a) and (c). The diameter of the scars produced following sliding against a Haynes 25 or a Cronidur 30 disc did not vary significantly. Visually however they are notably different as will be further examined in Section 4.2.2. The scars produced on the balls following the Stellite 20-Cronidur 30 experiments contain a deep groove through the centre in the direction of sliding, more severe in the higher temperature condition, see Figure 4.16 (c). This groove appears to agree with the profile of the wear track produced on the Cronidur 30 discs. There was certain difficulty in producing these profiles due to significant material damage at the track edges and the data measured was restored using Veeco software in all cases in order to produce the profile. It is likely that this very uneven, narrow track caused the deep groove through the centre of the ball scars. In terms of wear depth on the disc surfaces, at room temperature the results were fairly similar. At 80°C however, the deepest track produced on the surface of a Cronidur 30 disc was deeper than the same for Haynes 25.

Once again, the poor wear resistance of Haynes 230 can be clearly observed at each experimental temperature. The disc track profiles are significantly wider and deeper than what was produced on the surface of the Haynes 25 and Cronidur 30 discs. The ball scars produced at each experimental temperature were also significantly larger than those produced following experiments with Haynes 25 and Cronidur 30 discs. The ball scar surfaces also appear to be far smoother than those produced in the other experiments. The poor wear resistance of the Haynes 230 is due to its low hardness, relative to Stellite 20, Haynes 25 and Cronidur 30. Haynes 230 in alternative forms *i.e.* not hot rolled solution treated, may offer better wear resistance to the form obtained for the purpose of these experiments. These results demonstrate the effectiveness of the preliminary screening experiment as a means of reducing the volume of time intensive experiments to be conducted using the bespoke tribometer located at the UoN.

4.2.2 Topographical and image analysis of wear surfaces

4.2.2.1 Stellite 20 ball on Haynes 25 disc

Figure 4.17 presents the wear track and scar produced on the disc and ball surface are presented following a sliding wear experiment under a 10 N load at 20°C.

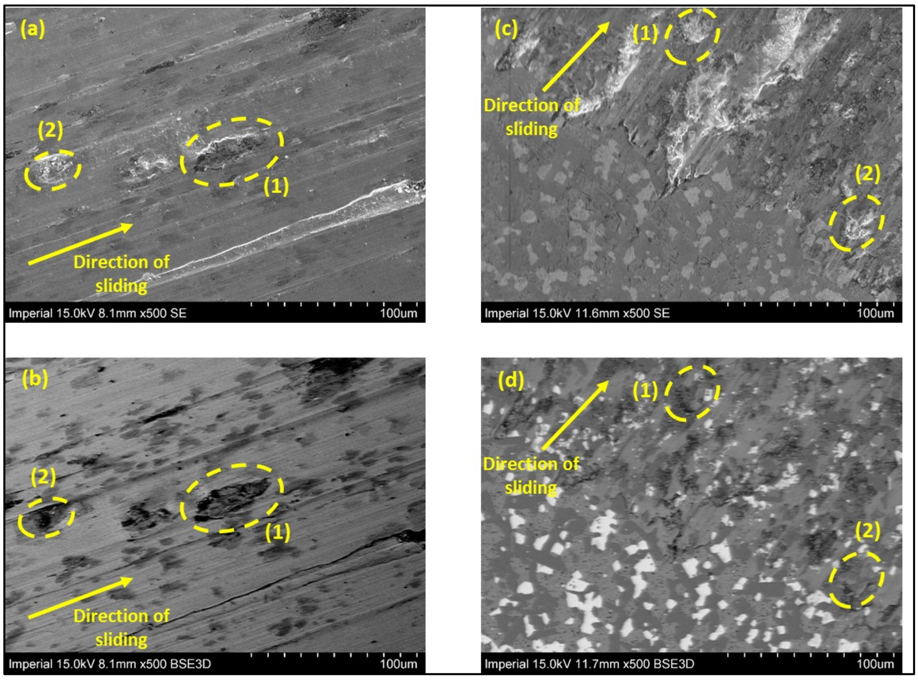

Figure 4.17: (a) and (b) area within disc wear track and (c) and (d) area within ball wear scar from using SE and BSE modes of the SEM of components tested under 35 N at 20°C

In each temperature condition tested, the track and scar produced on the surface of the Haynes 25 disc and Stellite 20 ball were similar to the wear manifestations observed on components tested at the University of Nottingham. At room temperature, the Haynes 25 disc track was fairly smooth with some particles of debris stuck to the surface, see features (1) and (2) highlighted in Figure 4.17 (a) and (b). The topography of the ball scar was not as uniform or smooth as the disc surface, see Figure 4.16 (c), having a slightly polished appearance as a result of the interaction. Wear does not appear to have stabilised on the ball surface with features such as those highlighted (1) and (2) appearing like particles of debris about to be removed from the surface.

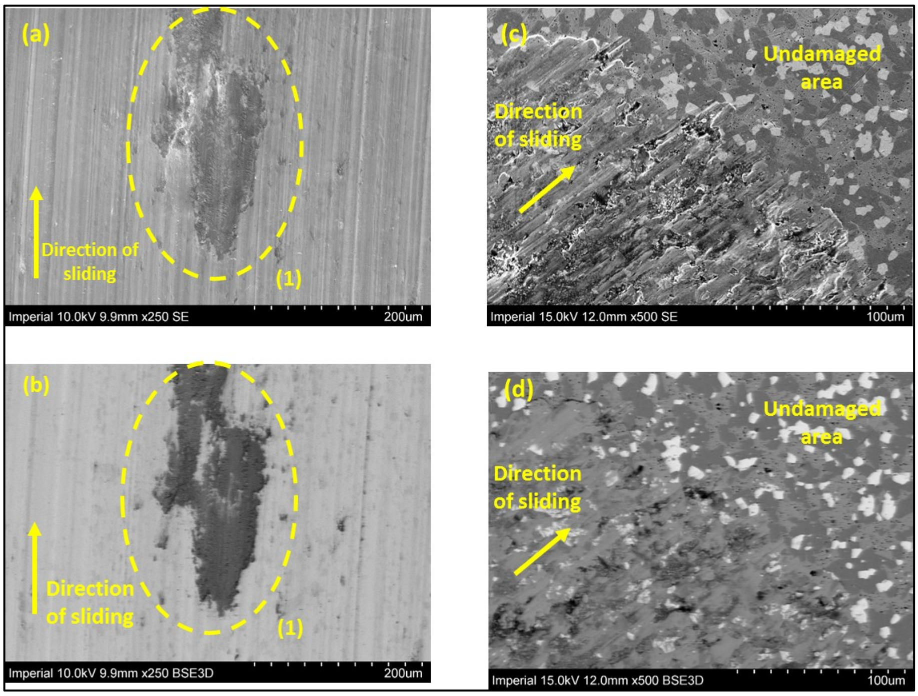

Figure 4.18: (a) and (b) area within disc wear track and (c) and (d) area within ball wear scar from using SE and BSE modes of the SEM of components tested under 35 N at 80°C

At 80°C the appearance of the disc track is smoother than that produced at room temperature. Particles of wear debris were again observed on the track surface although less frequently. In Figure 4.18 (c) and (d), the ball scar has a polished appearance like the lower temperature experiment. This is in agreement with the smooth surface of the track with both surfaces containing grooves, clearly indicating the direction of sliding. Damage to the Stellite 20 microstructure has an even appearance across the ball scar surface. Under the higher temperature experiment this damage seems slightly more severe with the structure of the carbides less clear.

4.2.2.2 RR2450 ball and Haynes 25 disc

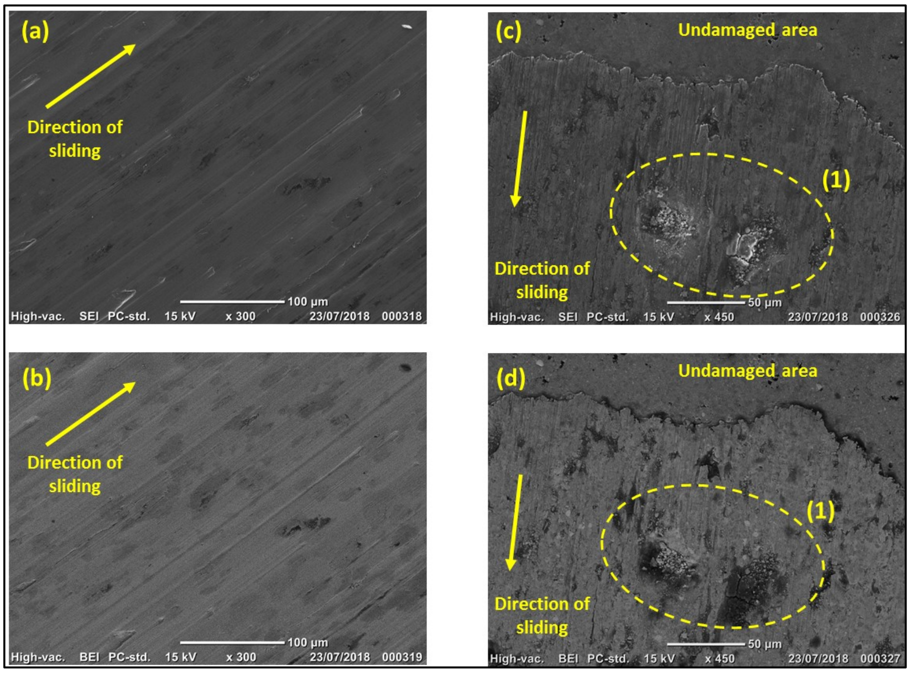

Figure 4.19: (a) and (b) area within disc wear track and (c) and (d) area within ball wear scar using SE and BSE modes of the SEM of components tested under 35 N load at 20°C

In Figure 4.19 (a) and (b), the majority of the Haynes 25 disc track has a fairly uniformly grooved appearance. At infrequent locations what appeared to be wear debris adhering to the surface were observed. Figure 4.19 (a) and (b) present a random location within the track demonstrating this evidence of fairly uniform material removal from the RR2450 ball. The location presented in Figure 4.19 (c) and (d) shows the border between the scar and undamaged area of the ball. The direction of sliding is clear. The two features highlighted, (1), indicate that some of the surface has already been abraded and other locations such as these are about to reach their plastic limit, forming wear debris. Upon closer inspection of feature (1), small particles were observed, of what is likely to be fine particles of debris that have been broken down from the original particle removed during the sliding interaction.

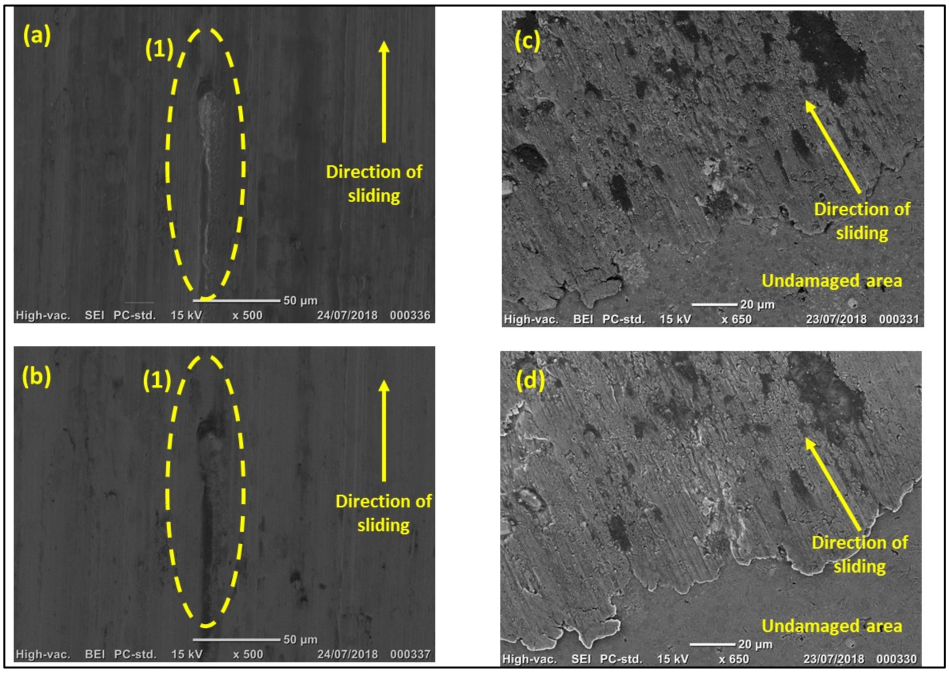

Figure 4.20: (a) and (b) area within disc wear track and (c) and (d) area within ball wear scar using SE and BSE modes of the SEM of components tested under 35 N load at 80°C

Figure 4.20 (a) and (b) present a location on the Haynes 25 disc track toward the outer edge. The overall topography is fairly smooth with some instances where material appears to have been plucked out or about to be removed such as the feature highlighted as (1). Features such as (1) were not frequently observed on the track and when they were, they were generally located towards the track edge. This is reasonable considering the middle of the disc track was in contact with the ball for a longer period than the edges and therefore wear had progressed further in the middle section. Generally the appearance of the track produced on the disc under these experimental conditions was smooth. Figure 4.20 (c) and (d) once again depicts the border between the ball scar and undamaged ball area. Compared to the scar produced on the ball tested at room temperature, the scar appears to be a far more smoothly worn surface with the direction of sliding made more clear by grooves across the surface.

4.2.2.3 Stellite 20 ball and Cronidur 30 disc

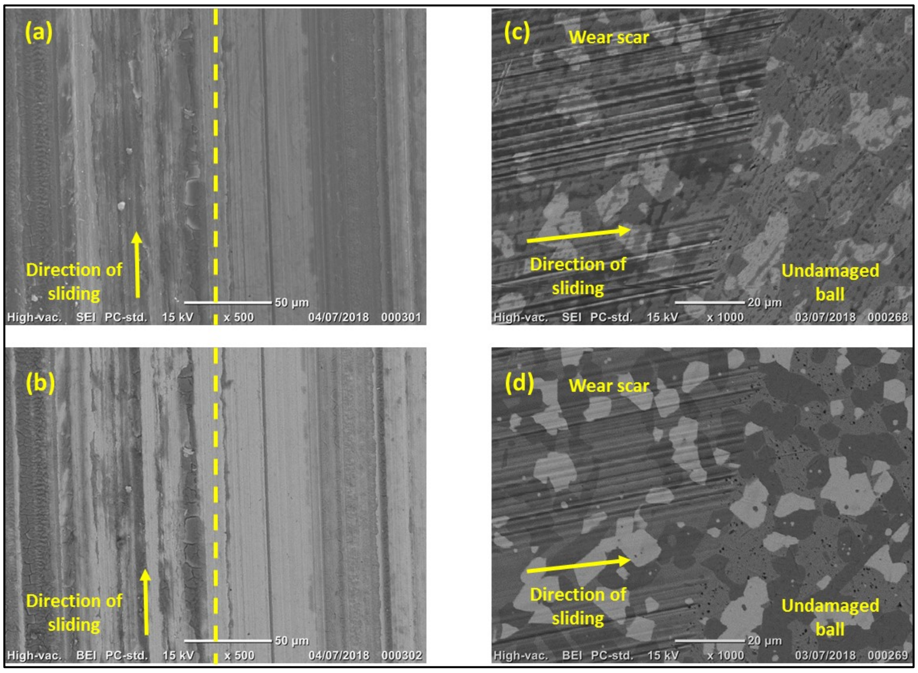

Figure 4.21: (a) and (b) area within disc wear track and (c) and (d) area within ball wear scar from using SE and BSE modes of the SEM of components tested under 35 N at 20°C

Figure 4.21 (a) and (b) presents a location on the outer edge of the disc track where the most severe topographical damage was observed. The surface appears cracked with a clear direction of sliding apparent. There is a significant lack of uniformity along this area of the disc track, some of the surface appearing fractured, some polished and some on the verge of material removal. Central to the wear track, to the right of the serrated line, the topography observed was far more smooth and uniform in appearance in contrast to the rest of the track although the depth of grooves highlighting the direction of sliding are not completely uniform. This contrast in the track topography between the outer edges and the smooth centre correlates to the difficulty in obtaining track profile data using the Veeco white light interferometer. Despite the narrow width of the wear track, a small portion became relatively deep.

Phases of the Stellite 20 microstructure and the solid solution matrix remain visible within the wear scar produced on the ball. The grooves produced on the ball surface indicating the direction of sliding are prevalent however as more of a topographical manifestation than microstructural damage. A deep groove was observed through the centre of the scar with more shallow uniform ones on either side. At the scar edge, minimal topographical damage was observed. The majority of the damage to the microstructure is on the cobalt-chromium-tungsten matrix with the chromium and tungsten rich carbides (dark grey and white in appearance respectively), maintaining their form and structure.

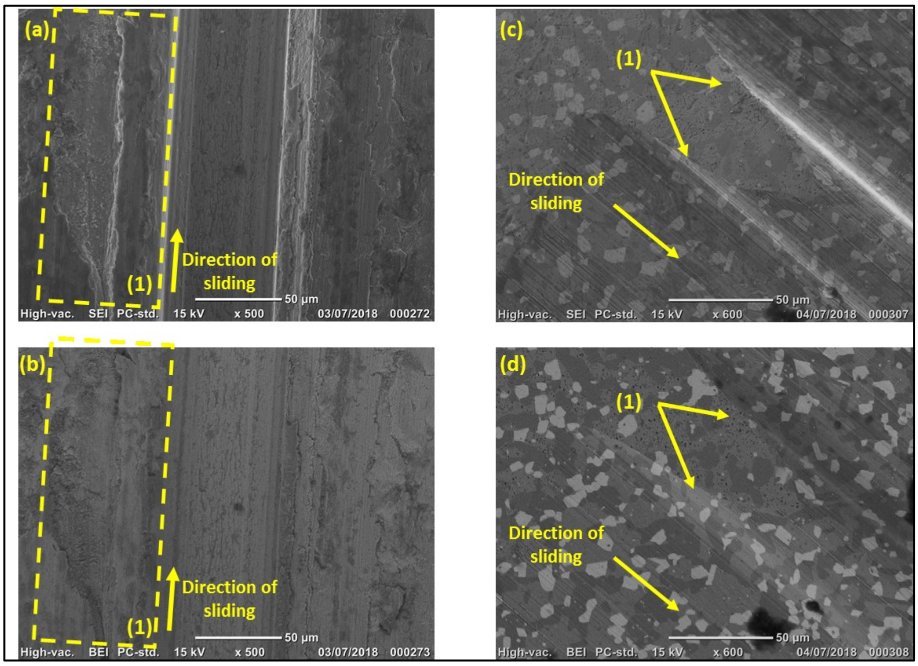

Figure 4.22: (a) and (b) area within disc wear track and (c) and (d) area within ball wear scar from using SE and BSE modes of the SEM of components tested under 35 N at 80°C

A clear and deeply grooved track central to the disc track produced in the 80°C experimental condition was observed. On the edges of the track, as with that produced on the Cronidur 30 disc at room temperature, the surface topography has very little uniformity. Damage and surface fracture on the edges of this deeply grooved track was very clear. In these locations the surface is fragmented and appears like the fragments are piling up.

Similarly to the scar produced on the surface of the Stellite 20 ball at room temperature, two deep grooves were observed across the centre of the ball scar, one more significant than the other. Once again the microstructure of the Stellite 20 ball was largely undamaged save for the crests of the grooves indicated in feature (1) in Figure 4.22 (c) and (d). The distinction between the scar and the undamaged ball surface are made by the presence or absence of these grooves. The overall smooth appearance does not appear to match the significant damage observed on the disc surface although the deep central grooves were likely produced as a result of the 'pile up' damage on the disc track edges. Unacceptably poor wear resistance was exhibited in the Stellite 20-Haynes 230 experiments and therefore a topographical analysis has been excluded.

4.3 Preliminary investigation of rolling wear resistance

4.3.1 Introduction

Rolling wear is of interest to the overall research group investigating the behaviour of the REBs that use Stellite 20 and Haynes 25 in the rolling and race elements, operating in the core of nuclear reactors. The existing set up of the Anton Paar high temperature tribometer at ICL is designed to perform sliding wear experiments only. A ball holder that facilitates rolling wear tests would be extremely useful in understanding wear mechanisms that manifest in the alloys as a result of rolling interactions. A successfully validated rolling wear ball holder design could also be adapted to fit the tribometer located at the UoN, facilitating assessment of the rolling wear behaviour of alloys in the nuclear reactor environment.

In the early stages of the work presented in this chapter a custom ball holder was designed for the tribometer at ICL as the diameter of balls to be tested was greater than what the original ball holder was designed to hold, see Appendix H for drawing. This section presents a second custom ball holder that is designed to facilitate rolling wear experiments using the existing tribometer. Preliminary, short tests were conducted to verify that the holder did indeed facilitate rolling.

4.3.2 Design of ball holder to facilitate rolling wear experiments

Figure 4.23 presents a schematic of the tribometer at ICL with the rolling ball holder.

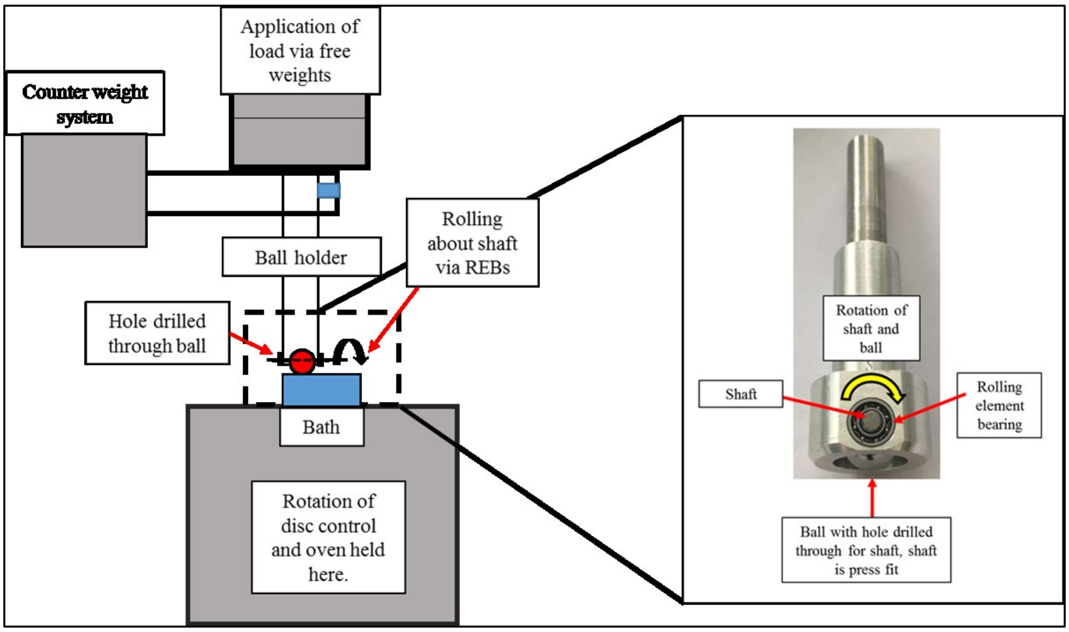

Figure 4.23: Anton Paar High Temperature Tribometer with custom rolling ball holder, image of ball holder inset

Based on the current experimental set up and the diameter of the ball to be tested the SKF Bearing Calculator [123] was used to identify a suitable roller bearing to hold the shaft which was press fit through a hole drilled in the ball. The role of the roller bearing selected was to facilitate rolling of the shaft and therefore the ball against the counter surface.

Table 4.11: Details of rolling element bearing selected using the SKF bearing calculator

Bearing	**Outer diameter (D) [mm]**	**Inner diameter (d) [mm]**	**Breadth (B) [mm]**	**Basic dynamic load rating ‘C’**	**Basic static load rating ‘C_0’**
618/4	9	4	2.5	0.423	0.116

4.3.3 Validation of rolling ball holder

To validate the functionality of the ball holder two short tests were conducted. Firstly, to facilitate rolling, the ball holder was fixed to the tribometer arm so that the ball was free to move in the direction of the rotating disc. Following this, the ball holder was rotated 90° and fixed in the tribometer arm so that the ball was fixed and could not rotate about the axis on which it was fitted. A normal load of 5 N was applied and the disc was set to rotate at 200 rpm, inducing rolling of the ball over a distance of 15 m. The 5 N load was selected to reduce damage to the plate surface which was not adequately hard when compared to the Stellite 20 ball. The ball holder was then adjusted to prevent rolling and the test was run again, the ball sliding against an arbitrarily selected counter surface. Friction from each test was recorded throughout and compared, see Figure 4.24.

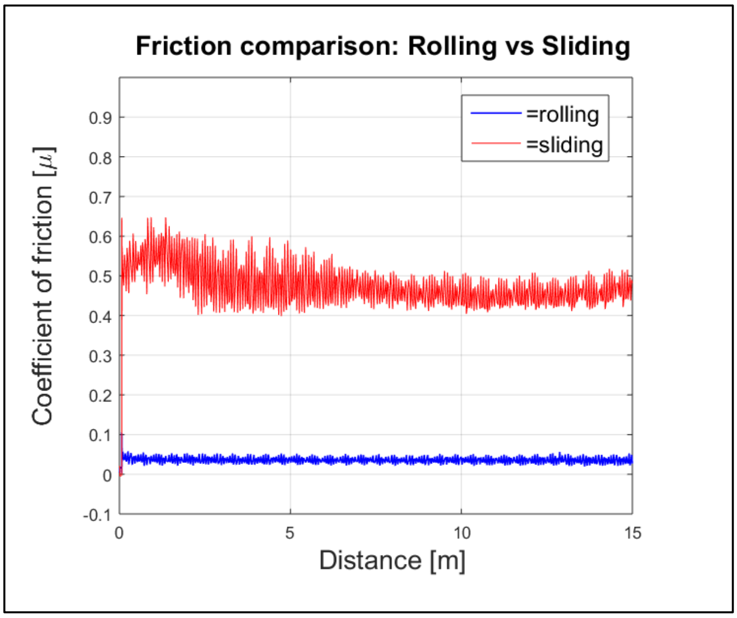

Figure 4.24: Comparison of the coefficient of friction recorded for rolling and sliding tests used to validate the rolling ball holder

The difference between rolling and sliding of the ball is clear from the friction measurements presented in Figure 4.24. As expected rolling friction is much lower than sliding friction. However, this also means that rolling wear may be negligible and difficult to detect under low load and for limited testing times, which would require running much longer tests to be able to systematically investigate this form of wear. Nevertheless, this result validates the functionality of the rolling ball holder and the possibility to conduct rolling wear experiments using the tribometer at ICL.

4.3.4 Next steps

In order to conduct water lubricated rolling wear experiments, a new ‘bath’ is required as the rolling ball holder is bigger than the sliding ball holder and does not fit the current set up. This is a simple modification and should be completed in the future. Following this, water lubricated rolling wear experiments should be conducted using the tribometer at ICL to investigate the rolling wear behaviour of the ball-on-disc alloy combinations investigated in this chapter. The rolling ball holder can be modified slightly to fit the holder at the UoN to investigate the rolling wear behaviour of alloys in the simulated nuclear reactor environment. Results from rolling wear experiments conducted at ICL and the UoN should be compared to establish if the tribometer at ICL can be used as a preliminary screening experiment for rolling wear as well as sliding wear.

4.4 Conclusion

A preliminary screening wear experiment was developed using an Anton Paar high temperature tribometer located at ICL. It was developed to reduce the volume of more time intensive experiments conducted using the tribometer set in an environment designed to simulate nuclear reactor conditions. The preliminary screening experiment was used to evaluate the wear resistance of cobalt-free and low cobalt alloys and compare it to the sliding wear resistance demonstrated by Stellite 20 and Haynes 25 balls and discs. Results were used to make a recommendation for or against further investigation into the wear behaviour of the alloys in the simulated nuclear reactor conditions available using the tribometer located at the UoN. If alloys did not exhibit acceptable wear resistance in the experimental conditions available using the preliminary screening experiment, it is unlikely that they would exhibit acceptable wear resistance in the more extreme environmental conditions of the simulated nuclear reactor conditions.

The preliminary screening experiment was validated by conducting sliding wear experiments at room temperature and 80°C under a normal load of 10 N. Stellite 20-Haynes 25 and RR2450-Haynes 25 ball-on-disc experiments were conducted for the purpose of this validation exercise. The results were compared to results from experiments conducted at the UoN using the same ball-on-disc alloy combinations at room temperature and at 100°C under a normal load of 10 N. The results indicated that the preliminary screening experiment was a valid tool to screen cobalt-free and low cobalt alloys at ICL, reducing the volume of the more time intensive sliding wear experiments. Results from the preliminary screening experiment may be used to make a recommendation for or against further assessment to be conducted on the alloys. The successful performance of an alloy in the preliminary screening experiment will not guarantee a successful result at the UoN, where a load up to 35 N and temperature of 200°C are available.

Results from the validation experiments using Stellite 20 and Haynes 25 balls and discs were used to set a performance benchmark from which the wear resistance of cobalt-free or low cobalt alloys could be compared. Cronidur 30 and Haynes 230, an iron- and a nickel-based alloy respectively, were identified in a review of literature as alloys with mechanical and corrosion resistant properties comparable to the form of Haynes 25 used in this PhD thesis. Experiments were conducted replacing Haynes 25 discs with Cronidur 30 discs and then Haynes 230 discs. The wear resistance exhibited in the Stellite 20-Cronidur 30 ball-on-disc experiments was significantly better than that of the Stellite 20-Haynes 25 experiments. Although the wear depth produced on the Cronidur 30 discs at 80°C was slightly higher than that produced on the Haynes 25 discs, the overall resistance to material removal was excellent by comparison. The microstructure of the scar produced on the ball surface from the Stellite 20-Cronidur 30 experiments was significantly different in appearance than for the Stellite 20-Haynes 25 experiments in both temperatures. Although grooves were produced on the ball surface in the former, the phases present in the Stellite 20 microstructure remained clear. It is recommended that Cronidur 30 is taken forward and tested in more severe environmental conditions at the UoN following the promising results presented in this chapter. There is a possibility that the high level of carbon present in the composition of Cronidur 30 may lead to cracking. However, it has been established as an alloy used in raceways of bearings operating in aircraft engines and it is recommended that further assessment of the alloy in the simulated nuclear reactor environment is continued despite the high carbon level.

As anticipated the wear resistance exhibited in the Stellite 20-Haynes 230 experiments was not deemed acceptable when the results were compared to the performance benchmark set by the Stellite 20-Haynes 25 ball-on-disc experiments. Further investigation of this relatively soft form of Haynes 230 should not be pursued using the tribometer at the UoN. Experiments conducted using Haynes 230 have served to demonstrate the effectiveness of the preliminary screening experiment and it is recommended that this continues to act as a method of screening alloys prior to continuing with more time intensive sliding wear experiments in the simulated nuclear reactor environment. It has also succeeded in demonstrating the importance of hardness in the wear resistance of certain alloys.

A rolling wear ball holder was designed, manufactured and tested as a further development of the preliminary screening tests presented in this chapter. Further validation of this set-up should be conducted as part of future work investigating the behaviour of the relevant cobalt-based alloys and their potential cobalt-free or low cobalt replacement alloys. A successful rolling wear experiment could be used at the University of Nottingham to give further insight into the behaviour of Stellite 20 and Haynes 25 as the rolling and race element of the rolling element bearings that operate in the core of nuclear reactors.

Chapter 5 Sliding wear prediction using semi-analytical and numerical methods

Chapter 5 Sliding wear prediction using semi-analytical and numerical methods

Introduction

In Chapter 3, sliding wear experiments were conducted using a ball-on-disc tribometer. The volume of material removed, maximum wear depth and the ball scar and disc track dimensions were measured from components following the experiments. These measurements were used to develop and validate wear prediction models. The implementation of a comprehensive and validated wear prediction model would greatly reduce the need for the development of complex and expensive environmentally appropriate material and component validation rigs. Wear prediction models based on Archard's wear equation are used extensively throughout the literature describing the relationship between material wear volume lost in a sliding interaction, the load applied to the interaction and the sliding distance. Using Archard's wear equation, these parameters are used to obtain the wear coefficient of a material, which is specific to the experimental environment. The wear coefficient obtained from the experiments conducted and presented in Chapter 3 was used in the development of the wear prediction models presented in this chapter. Two approaches were taken in the development of these wear prediction models.

The first model was developed using information presented by Hegadekatte and co-workers that took a semi-analytical approach [7]. This approach applied a combination of Hertzian contact mechanics, Archard's wear equation and experimental parameters to predict wear depth following a sliding interaction. The approach was developed using MATLAB and was relatively simple to implement; however, it did not give a comprehensive insight of material behaviour throughout the sliding interaction as it was based on several simplifying assumptions and provides limited information about, for example, stress and displacement fields and their evolution. A second approach taken to develop a more comprehensive wear prediction model used commercial finite element software, ABAQUS. ABAQUS generates far more information throughout the sliding wear interaction, such as the stress fields generated in the ball or disc and the impact of wear progression on these fields [101, 124]. FE models can be developed further to incorporate other phenomena such as the effects from surface oxidation, thermo-mechanics or material plasticity including microstructural effects [108, 111]. Barzdajn and co-workers, for example, developed a finite element model to predict galling frequency in rough, normally loaded, metal to metal contacting surfaces that underwent sliding [106]. The model presented by Barzdajn et al, Ref [106], considered a range of factors understood to influence the wear behaviour of the materials in the interaction including adhesion, material plasticity, material hardening, surface roughness and asperity geometries and spacing. The model description highlighted the complexity in the development of such finite element formulations and, the opportunity offered by software such as ABAQUS to simulate such phenomena. Two 2-D FE, or numerical, wear prediction models were developed that predicted wear depth on the ball and on the disc and are discussed in this chapter.

The formation of an oxide glaze on the surface of some components in nuclear reactor environments is a phenomenon that has been related to the excellent wear resistance of some cobalt-based alloys. It was concluded by Déforge and co-workers that any work undertaken to model wear in a nuclear reactor environment should include both the mechanical and electrochemical phenomena [115]. The relationship between the formation of such glazes, particularly during latent periods when the component is at rest, and the impact of mechanical wear on the component surface is an interesting one which has received some attention in literature [21, 114]. As part of this research project, the disc wear model was developed further to demonstrate the capability of FE models in simulating the impact of surface oxidation on the mechanical wear of components exposed to sliding wear. This development successfully demonstrated the versatility of using FE analyses to simulate interactions in which there are a number of factors that combine, often in a non-linear fashion, influence component behaviour.

5.1 Methodology

5.1.1 Semi-analytical wear model

The semi-analytical wear models presented in this chapter were developed based on models presented in [1] to which the interested reader should refer to for supplementary background information. The models used a combination of Hertzian contact stress theory and Archard's wear equation to predict the wear depth on ball and disc components following a sliding wear interaction. Hertz theory of elastic contact presented expressions facilitated analysis of stresses in the contact region between two elastic solids [58]. The two cases are presented in Figure 5.1 (a) and (b) followed by graphs demonstrating the distribution of contact pressure for each condition using arbitrary values. In the case of a line contact, the load along the z-direction is distributed evenly and can there be considered as a 2-D system.

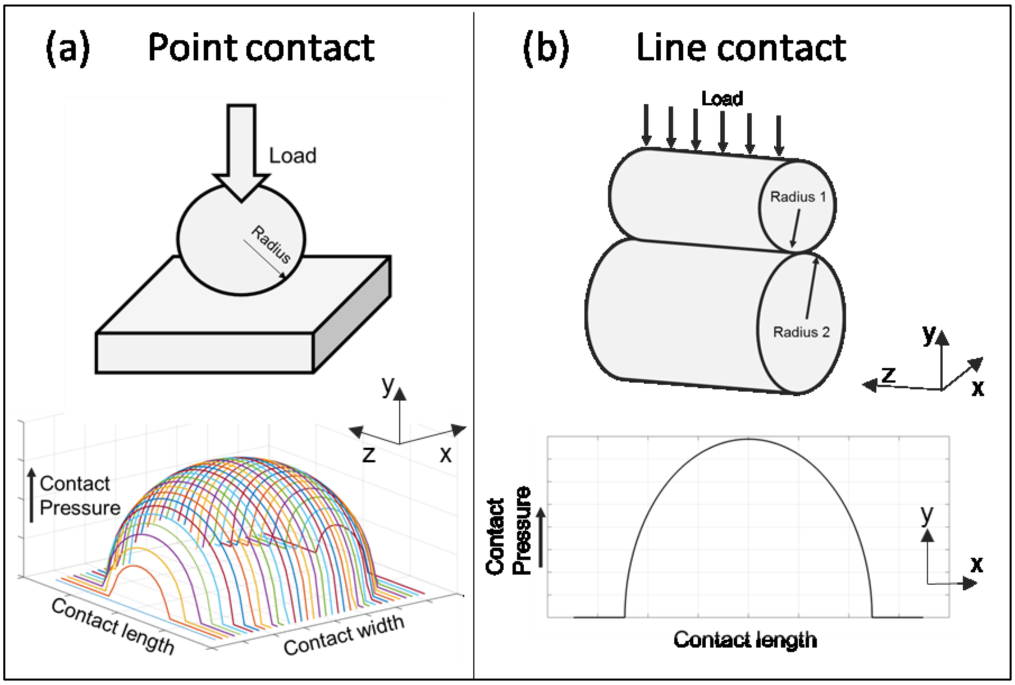

Figure 5.1: (a) and (b) A point contact and a line contact for two elastic bodies and the resultant contact pressure distribution based on Hertz contact theory

Equations 5.1 and 5.2 (a) and (b) present the expressions for the contact radius and average contact pressure generated between elastic bodies illustrated in Figure 5.1 (a) and (b) under a normal load [105].

For a point contact the contact radius and the average contact pressure can be calculated as follows:

$$a_i = ((0.75) * \left(\frac{F_n * R}{E_c}\right))^{\frac{1}{3}} \qquad \text{Equation 5.1 (a)}$$

$$p_{ave,i} = \frac{F_n}{\pi * {a_i}^2} \qquad \text{Equation 5.1 (b)}$$

For a line contact, the contact radius and the average contact pressure can be calculated as follows:

$$a_i = ((2) * \left(\frac{F_n * R}{\pi * E_c}\right))^{\frac{1}{3}} \qquad \text{Equation 5.2 (a)}$$

$$p_{ave,i} = \frac{F_n}{2 * a_i} \qquad \text{Equation 5.2 (b)}$$

where a_i is the contact radius, F_n is the normal load applied to the interaction, R is the equivalent curvature based on the radii of the elastic bodies, E_c is the elastic modulus of the equivalent surface or the reduced modulus, based on the Young's modulus of each body and $p_{ave,i}$ is the mean radius.

The semi-analytical model, developed to simulate the ball-on-disc sliding experiments presented and discussed in Chapter 3, applied point contact theory, as it was representative of the 3-D interaction. The values inserted in the model were based on the properties of the ball and disc, Stellite 20 and Haynes 25 respectively. For the first sliding cycle, a_i was used to find the circular contact area between ball and disc. The contact pressure was calculated and a modified version of Archard's wear equation was used to calculate wear depth of the first sliding cycle on either the ball or disc surface, see Equation 5.3 (a) and (b). Throughout the interaction the ball remains in contact with the disc and thus the sliding distance per cycle for the ball was considered to be the entire path length. If we consider the path length on the disc surface in sections, each section only entered contact with the stationary ball once as it rotated and the sliding distance for one cycle was considered as the length of one of these sections, or one 'contact length' [6].

$$h_{ball,i} = \frac{k_{ball} * p_{ave,i} * l_{path}}{H} \qquad \text{Equation 5.3 (a)}$$

$$h_{disc,i} = \frac{2 * k_{disc} * p_{ave,i} * l_{contact}}{H} \qquad \text{Equation 5.3 (b)}$$

where h is maximum wear depth on the ball or disc surface, k is the experimentally obtained wear coefficient of the ball or the disc, l is sliding length or contact length and H is the hardness of the softer material. As wear progressed on the ball surface, the ball began to flatten, increasing the contact area, which in turn decreased the contact pressure. To find the changing geometry of the ball scar, it was assumed that a spherical dome is removed as the result of wear. This can be obtained using Pythagoras' theorem, see [7], and the relationship obtained was also used to predict the new wear scar diameter.

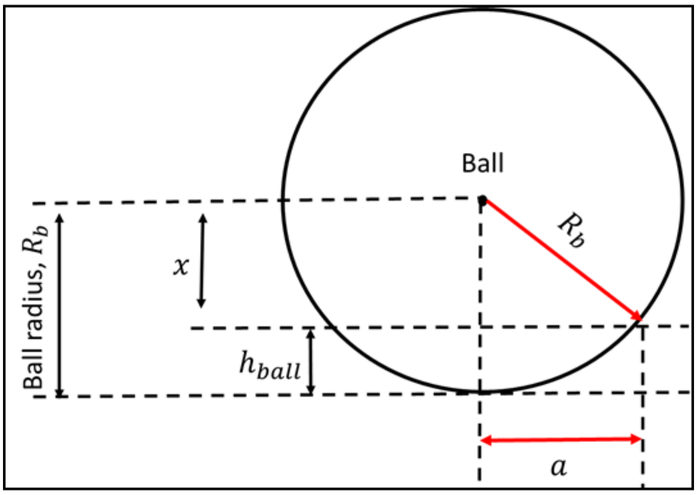

Figure 5.2: Schematic of ball demonstrating how the development of the contact area and thus the ball scar geometry was calculated [7]

The value *a,* identified in Figure 5.2, represents the radius of the circular contact area and thus the ball scar radius. It was found using the following set of equations;

$$R_b = h_{ball} + x \qquad \text{Equation 5.4 (a)}$$

$$x = R_b - h_{ball} \qquad \text{Equation 5.4 (b)}$$

$$R_b{}^2 = a^2 + x^2 \text{ (Pythagoras' theorem)} \qquad \text{Equation 5.4 (c)}$$

$$R_b{}^2 - a^2 = (R_b - h_{ball})^2 \qquad \text{Equation 5.4 (d)}$$

$$a_{i+1} = \sqrt{2R_b h_{ball} - h_{ball}{}^2} \qquad \text{Equation 5.4 (e)}$$

where R_b was the initial ball radius and x was the distance between the centre of the sphere and the wear scar after wear depth was calculated. Equations 5.4 (a) – (e) were used for all iterations of the semi-analytical model predicting wear of the ball following the first sliding cycle.

5.1.1.1 Model validation

The results from the semi-analytical wear models were compared to data measured following experiments conducted and presented in Chapter 3. The maximum wear depth of each ball and disc, the width of the disc wear track and ball scar diameter were measured. Table 5.1 presents the parameters and data measured and presented in Chapter 3.

Table 5.1: Ball and disc components information, wear coefficient calculated with Archard's wear equation

	Diameter [mm]	Depth [mm]	Hardness [Hv]	Young's modulus [GPa]	Poisson's ratio
Stellite 20 ball	9.525		649-867	257	0.3
Haynes 25 disc	30	10	572	225	0.3
Experimental condition	**Load [N]**	**Temperature [°C]**	**Wear coefficient (ball)**	**Wear coefficient (disc)**	
1	10	20	8.281E-15	3.078E-12	
2	10	100	1.006E-13	6.898E-12	
3	10	200	2.038E-11	2.078E-11	
4	35	20	8.898E-13	2.221E-11	
5	35	100	1.435E-11	1.59E-11	
6	35	200	4.14E-11	1.267E-11	

5.1.2 Two dimensional numerical wear prediction model

The simplest iteration of the FE wear model is presented in this section. Two, 2-D models were developed to predict the maximum wear depth of the ball and disc respectively based on the same experimental parameters applied to the semi analytical wear models using Equations 5.3 (a) and (b). There were three significant stages involved in building the wear model using FE software, ABAQUS (version 6.14-4) [125]. The FE model was used to simulate the interaction between the ball and the disc. A fine mesh was applied to one of the component surfaces. Within the region of the contact, the mesh applied was 'adaptive'. This means that as wear progressed and the geometry of the experimental component(s) changed within the adaptive mesh domain, the nodes on the mesh adapted on the component surface in line with the wear depth calculated for each sliding cycle. This change in geometry was the result of the application of Equation 5.3 (a) or (b), adapted from Archard's wear equation. Adaptive meshing worked by running a user defined subroutine, UMESHMOTION in parallel to the ABAQUS simulation. ABAQUS solved the contact problem between the two interacting components and UMESHMOTION used data from ABAQUS and applied the wear equation to calculate the wear depth at each surface node on the wearing component.

5.1.2.1 Model description

(i) Model definition

In the first stage, 'pre-processing', the model was defined in ABAQUS/CAE. The geometry was created in the 'Part' module, see Figure 5.3 (a) and (b), where mechanical wear of the ball and disc were simulated separately. In the model presented in Figure 5.3 (a), the 'disc' was defined as an analytical rigid surface which meant that it would not undergo any mechanical wear during the sliding interaction. In this first stage, the ball was defined as a fully elastic, 'deformable shell planar' part, and the component in the interaction that would undergo wear.

The 'Property' module was used to define the materials from which the parts were defined. As the current iteration of this model defines the deformable part as fully elastic, the Young's modulus and Poisson's ratio are the only inputs. Because ball and disc FE wear models were developed separately, the reduced modulus, E_c was set as the Young's modulus of the deformable part in each model to account for changes due to the rigid part definition. The 'Assembly' module assembles the separate parts that have been created, referred to as 'instances' of parts.

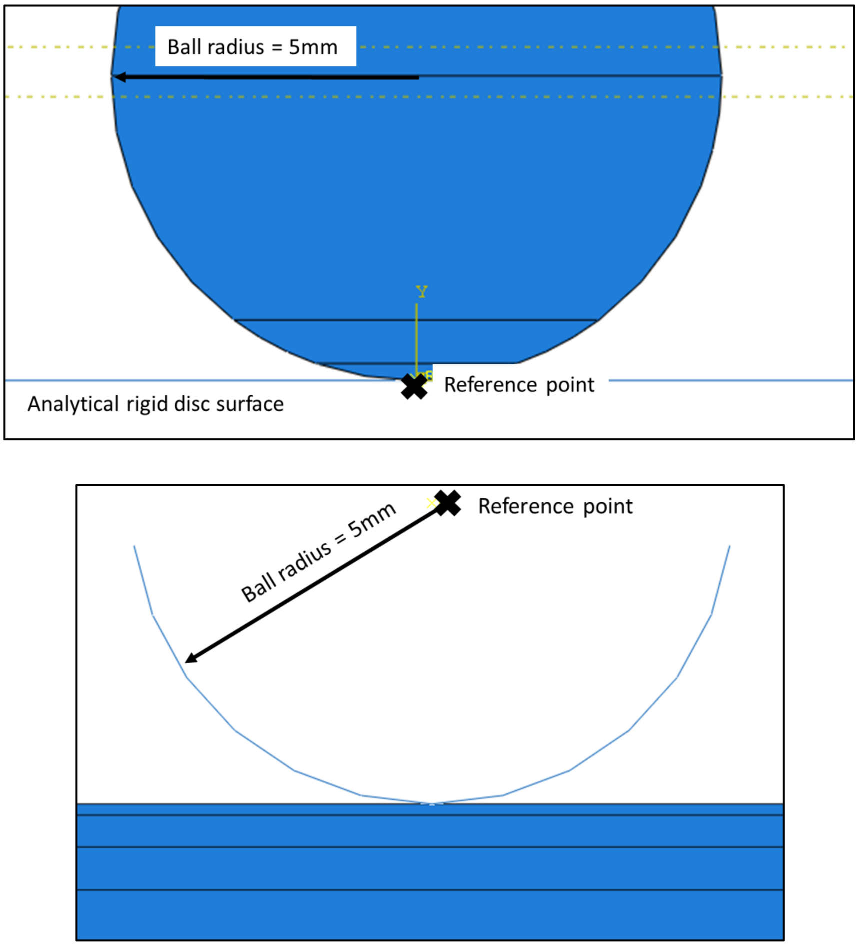

Figure 5.3: (a) Assembly module in ABAQUS CAE; model definition of deformable ball and rigid disc (b) Assembly module in ABAQUS CAE; model definition of deformable disc and rigid ball

The part dimensions and properties for each model are listed in Table 5.2.

Table 5.2: Dimensions and properties of the pin and disc for each wear model

	Ball wear	Disc wear
Ball diameter	10 mm	
Disc length	6 mm (an arbitrary value to facilitate sliding)	
Ball type	2D planar deformable shell part	2D planar analytical rigid body
Disc type	2D planar analytical rigid body	2D planar deformable shell part
Material behaviour of deformable instance	Mechanical, elastic, frictionless behaviour	
Reduced modulus; E_c	131840 MPa	

(ii) Boundary conditions and steps

The FE model was developed with reference to literature published by McColl and co-workers that focussed on fretting wear [58, 126]. The relative tangential displacement between two components in contact that characterises fretting wear is up to approximately 300 µm [126]. To establish a sliding interaction for the 2-D models presented the minimum tangential displacement accepted was at least two times greater than the contact length which also exceeded the fretting wear displacement criterion and mimics sliding wear conditions. It is reasonable to assume that, although a reciprocating scenario is simulated here, the wear recorded at the centre of the stroke length after every cycle coincides with the wear measured for every pin rotation at every point on the disc for every full revolution performed by the disc. The total sliding distance completed in experiments presented in Chapter 3 and by the semi-analytical wear models was not simulated. This was to increase the computational efficiency of the models.

(a) FE ball wear prediction model

In the first part of the analysis, displacement of the ball was constrained by applying boundary conditions for displacement around the perimeter, highlighted in Figure 5.4. This was done in order to replicate the effect of the holder on the ball in the ball-on-disc experiments. The boundary conditions were not applied to the adaptive mesh domain as wear occurred in this region and therefore displacement of this surface nodes could not be prevented.

A reference point was fixed to the upper surface of the disc, as indicated in Figure 5.3 (a). Load, normal and tangential displacements of the rigid disc were applied at this reference point.

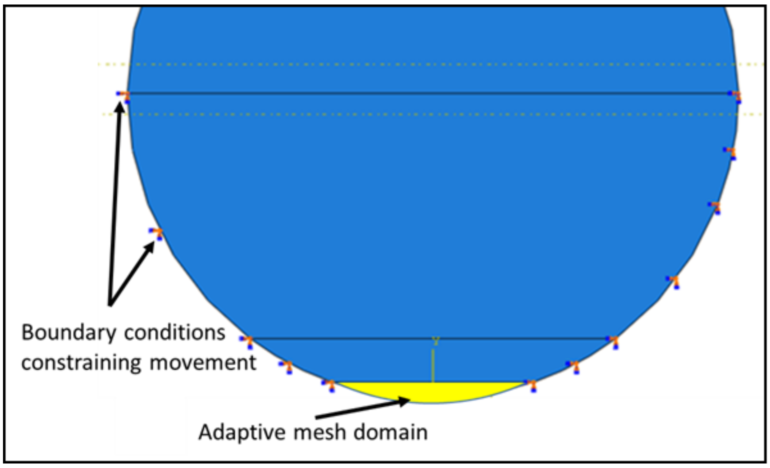

Figure 5.4: Demonstrating boundary conditions applied to ball constraining movement

The loading conditions and sliding cycles were applied in ‘Steps’ as follow;

1. *Make contact*: contact was established between the ball and the disc in the first step, displacing the disc in the positive normal direction, via the reference point.

2. *Apply load*: the normal load was applied in the interaction via the disc, once again via the reference point.

3. *Tangential displacement*: the disc was displaced tangentially to the ball surface, under the exerted normal load. This step was repeated, in the case of this analysis, nine times to simulate nine sliding cycles, an arbitrary number. It was within these sliding cycles that wear of the ball would occur.

The adaptive mesh region highlighted in Figures 5.4 and 5.5 and the adaptive mesh controls, were also defined within the 'Step' module.

(b) FE disc wear prediction model

The disc was constrained during the analysis by applying boundary conditions to the bottom and sides, preventing movement or rotation in any direction (encastred). A reference point was fixed to the rigid ball. Load and normal and tangential displacement of the ball were applied to this point. The loading and sliding cycles followed the same format as described for the ball wear model. The boundary conditions of the disc wear analysis set-up and those applied within the step module are presented in Table 5.3.

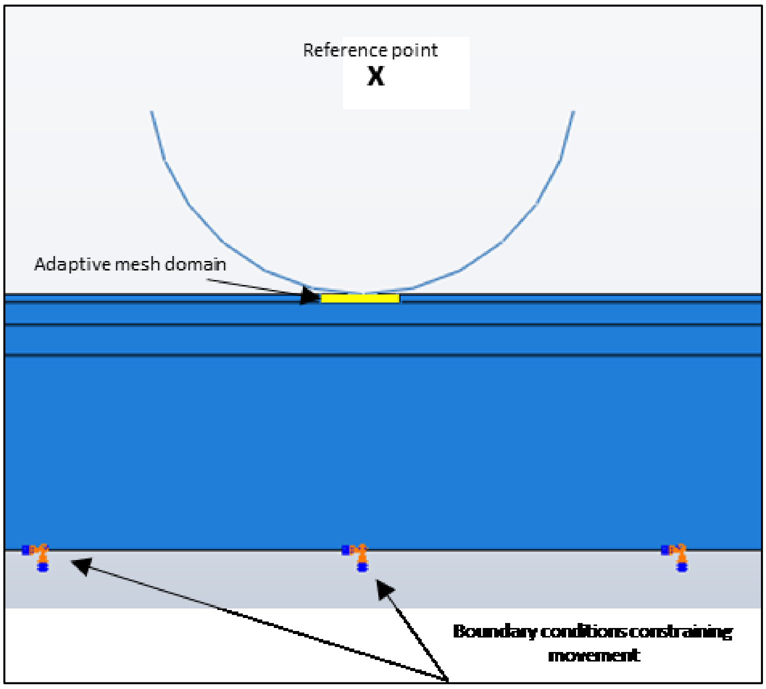

Figure 5.5: Demonstrating boundary conditions applied to disc constraining movement

Table 5.3: Boundary conditions defined within the step module of ABAQUS

Step	Point of application	X	Y	Rotation
Initial	Sides and bottom of disc	0	0	0
Contact	RP	0	-0.0001 mm	0
Apply load	RP	0	-35 N	-
Sliding cycle (*9)	RP	Amplitude	-	-

The sliding steps were controlled by displacement, in an oscillatory movement. An amplitude table was created in ABAQUS, applied in the x-direction via the reference point. Table 5.4 presents the amplitude displacement. The magnitude of sliding was defined within the boundary condition module of each step.

Table 5.4: Amplitude table for the sliding boundary conditions

Time (s)	0	0.25	0.5	0.75	1
Amplitude (mm)	0	1	0	-1	0

(iii) Application of mesh and mesh refinement studies

The Mesh module was used to generate the finite element mesh on parts and assemblies in ABAQUS [125]. This involved selecting suitable element size, type and shape. How coarse or fine the mesh was would strongly impact the quality of the results. The more refined the mesh was, the more accurate the results would be at the expense of increased computational cost. Given the impact of the mesh on accuracy of results and computational expense of the simulations, a balance was struck in order to develop an accurate and efficient model. Biased mesh seeding was applied in the 2-D ball and disc case i.e. the element size decreased gradually in size as the elements approached the area of importance; the location of the contact interaction. This helped to avoid drastic dimensional changes between adjacent elements when adaptive meshing began. A coarse mesh was used outside areas of interest to reduce the computational expense of the simulation. Seeds are ‘markers’ input by the user specifying element density in a region [125].

The second consideration was the element type that was defined. A 2-D region shall have either a quadrilateral or triangular element shape [125]. In FE modelling, specific element types are used for different types of analyses such as stress analysis, heat transfer or acoustic analysis, each having a ‘family’ of appropriate elements. Each of the 2-D FE models developed may be considered within Hertz theory for a line contact, see Section 2.4.1. In the parallel cylinder illustration in Figure 5.2 (b), in the z-direction, the bodies can be considered infinitely long with no variation in the load applied. Plane strain in the z-direction is considered zero in this instance. A 4-node bilinear plane strain quadrilateral element, which assumes zero plane strain in the z-direction, was therefore applied to elements in the 2-D analysis.

(a) Mesh size optimisation study

The balance between model efficiency and accuracy influenced by the mesh size was established by carrying out a mesh optimisation study. Each wear analysis was run for a range of mesh sizes from a relatively coarse to a relatively fine mesh. The coarsest mesh with the least deviation in results from the finest mesh should be selected. The number of elements in the area of contact was deemed important to the accuracy of the model.

Table 5.5: Test values in mesh size optimisation study for ball and disc wear

Mesh size (at ball surface) [mm]	0.01	0.015	0.02
Mesh size (at disc surface) [mm]	0.01	0.015	0.02

In each case the deformable ball or disc was divided into sections prior to meshing to ensure that the analysis converged and there were no fatal errors such as severe distortion of elements during steps. The section in contact with the rigid ball or disc during the steps was defined as an Arbitrary Lagrangian-Eulerian (ALE) adaptive mesh region with user defined adaptive mesh constraints. In ALE meshing, the nodes of the mesh can move independently to the material maintaining the mesh quality. Selecting ‘user defined’ mesh constraints diverted the ABAQUS simulation to the user defined subroutine, UMESHMOTION, in which wear depth was calculated incrementally for each sliding cycle. Adaptive meshing was a very important function within the model as it facilitated the change in component geometry resulting from the wear depth calculated.

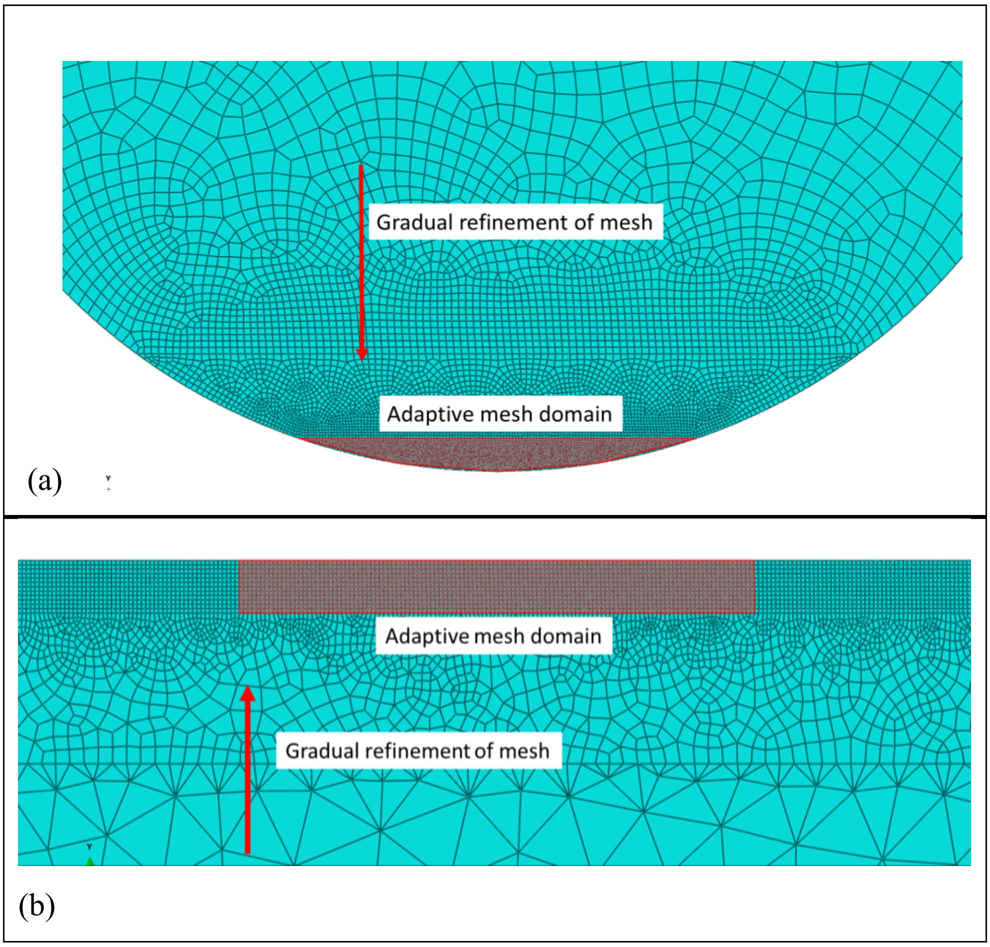

Figure 5.6: (a) Mesh applied to deformable ball (b) Mesh applied to deformable disc

(iv) Solving the contact problem defined

In the second stage of the analysis, the numerical contact problem defined was solved by ABAQUS. In the 'Interaction' module, surface to surface contact was defined between the master surface (the rigid body) and the slave surface (the deformable body). The rigid body was displaced in the direction normal to the surface of the deformable body by a small magnitude in the first step to ensure that contact was established between the components. The normal load was then applied and contact pressure across the 2-D contact length and the distribution of stresses in the deformable component as a result of the interaction were calculated.

(v) Wear calculation by UMESHMOTION

The adaptive mesh controls were assigned to the adaptive mesh region in each sliding step. At the end of each sliding increment, ABAQUS was directed to the user defined subroutine UMESHMOTION that was running in parallel and adaptive meshing was applied. UMESHMOTION was used to define the motion of specific nodes within this adaptive mesh region with respect to the wear equation solved in the code. UMESHMOTION was written in

Fortran code and wear depth as a result of the contact pressure exerted on the surface nodes within each sliding step was calculated within it.

The subroutine written for the purpose of this analysis called utility routines; ‘GETVRN’, ‘GETNODETOELEMCONN’ and ‘GETVRMAVGATNODE’. Access to node point quantities, the list of elements attached to a node and averaged values of material point quantities at the end of each increment were provided by these utility routines in respective order. They provided access to results data produced by ABAQUS/CAE for specific nodes defined within the code such as node geometrical co-ordinates and value of contact pressure (from the output variable CPRESS). The nodes defined within the code that would be adapted or updated according to the wear calculation, were defined as the surface nodes within the adaptive mesh domain, see Figure 5.6 (a) and (b).

ALOCAL is the local co-ordinate system that is assigned to such simulations by UMESHMOTION. It was aligned with the tangent direction to the adaptive mesh domain defined in ABAQUS/CAE. In the case of a 2-D simulation, the two direction system is normal to the surface and for a 3-D simulation the three direction system is normal to the surface [125]. If the adaptive node is on an edge, the three direction system is arbitrary [125]. ULOCAL is the mesh constraint vector variable that was passed into the UMESHMOTION *i.e.* displacement of nodes according to the wear depth calculated was applied to this co-ordinate system.

(a) UMESHMOTION methodology

There were three important sections within the user-defined subroutine.

Firstly, within each increment of the first sliding step, the step number, increment number, node number, contact pressure on the node, time increment and total time from the beginning of the analysis were recorded in a data file. Where there was a zero value of contact pressure, data was excluded to avoid the creation of large files. Figure 5.7 presents a visualisation of non-zero values of contact pressure recorded at nodes within several sliding increments of a sliding step.

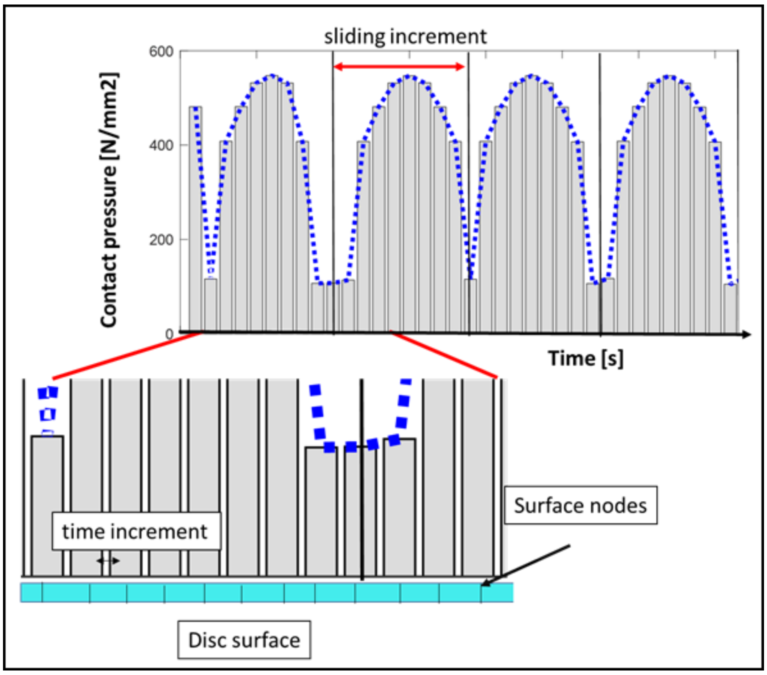

Figure 5.7: Data recorded by UMESHMOTION using data produced in ABAQUS

In the second section, the average contact pressure, P_{ave} across the entire step was calculated using the data recorded *i.e.* the average area under the serrated curve in Figure 5.7.

Equation 5.3 (a) and (b) were adapted to calculate wear depth at each node within a sliding cycle for use within the UMESHMOTION;

$h = k{*}P_{ave}$ Equation 5.5 [58]

h = local* wear depth, k = experimentally obtained wear coefficient, P_{ave}=average contact pressure across all nodes within a sliding cycle.
**local indicating the specific value at a node*

This value was used to update the location of the surface nodes defined within adaptive mesh domain applied to the co-ordinate system ULOCAL;

$U(2) = U(2) - h$ Equation 5.6

where *U(2)* is the location of each node within the region with a direction of moment normal to the surface of the adaptive mesh region. Figure 5.8 demonstrates the interaction and change in location of the surface nodes in the disc. The equation was limited to nodes with a non-zero value of contact pressure.

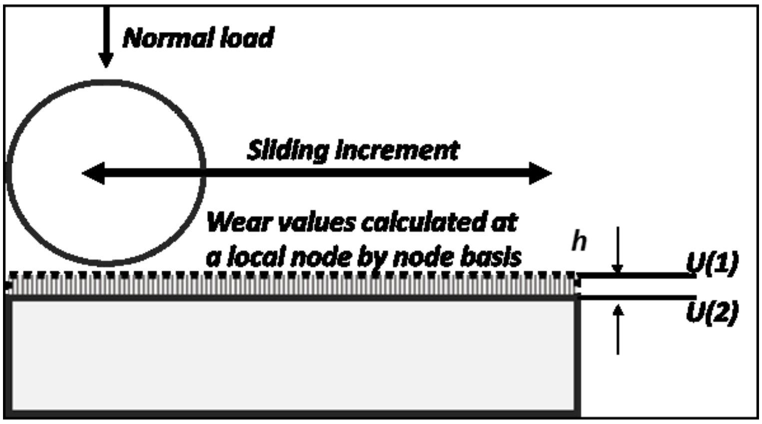

Figure 5.8: Schematic demonstrating material removal from disc surface

The newly calculated nodal location was returned to ABAQUS which progressed to the next sliding step, where the contact problem was once again resolved based on the updated area of contact between the ball and disc. The process was repeated until the final sliding cycle was completed. The same operation was applied in the case of ball wear.

(b) Simulating increased number of cycles within a single sliding step

Within the subroutine, it was possible to mimic more than a single wear procedure by multiplying the wear coefficient by a selected factor. This is described as a more efficient way to model a greater number of cycles, 'cycle jumping' [126]. For example, by multiplying the wear coefficient by nine, the equivalent of nine sliding steps was simulated within one step. Cycle jumping makes an assumption of uniform wear rate throughout the simulation. There is a limit to this value. If a value applied in the subroutine exceeds a certain value, the contact between the interacting surfaces may be lost and the simulation will abort having failed to converge.

5.1.2.2 Validation

The model description in Section 5.1.2.1 was for a 2-D model where either the fully deformable ball or disc underwent wear and the interacting component was defined as a rigid surface. An arbitrary value of 90 sliding cycles was also selected for time efficiency. This incorporated the method of cycle jumping described. It was therefore not possible to perform a direct validation exercise comparing results from the FE analysis with experimental data. As will be seen in Section 5.2.1, the wear depth prediction produced by the 3-D semi-analytical model was in good qualitative and reasonable quantitative agreement with the experimental results. Based on this reasonable validation, the semi-analytical wear depth prediction model was adapted to employ Hertzian contact mechanics for a line contact instead of a point contact, see Figure 5.2 (b) and Equations 5.2 (a) and (b), representative of the 2-D ABAQUS model definition [105].

Results from the modified, 2-D semi-analytical model could therefore be used as a means of validating the wear depth predicted on the disc and ball components by the FE model.

5.2 Results and Discussion

5.2.1 Semi-analytical wear model

The semi-analytical model was executed using data obtained from each environmental condition applied to experiments presented in Chapter 3. The wear coefficient for Stellite 20 balls and Haynes 25 discs at each of these conditions was calculated and used, see Table 5.1. The semi-analytical model calculated the final maximum wear depth on both the ball and disc. The disc wear track width and the ball scar diameter were also calculated. Figures 5.9 and 5.10 illustrate the comparison between the values calculated by this model and the data measured on the post experimental components of the first set of repeated experiments, see Table 3.4, Chapter 3.

The results presented in Figure 5.8 (a)-(f) show that the wear depth predicted is in good qualitative and reasonable quantitative agreement with experimental measurements for the total wear depth. This is an expected outcome as it is the experimental data obtained that is used to calculate the wear coefficient used to predict wear using Archard's wear equation. The percentage error calculated between the measured and predicted ball wear depth remained below 25% under all experimental conditions. The same for the maximum depth of the track produced on the disc surface remained below 30%. The method by which the actual wear depth values were measured was different for the ball and disc component which may explain the discrepancies. As described, the volume per track width was found using the white light interferometer at several points along the track and used to find the total volume lost over entire track length. This gave a good estimation of the material ploughed from the disc surface however, it did not guarantee that this material removal is done uniformly or smoothly. This was evident from looking at the profiles presented in Figures 3.10-3.12, Chapter 3, where unevenness or roughness can be clearly seen in the surface profiles generated. The semi-analytical model did not take this uneven material removal into account.

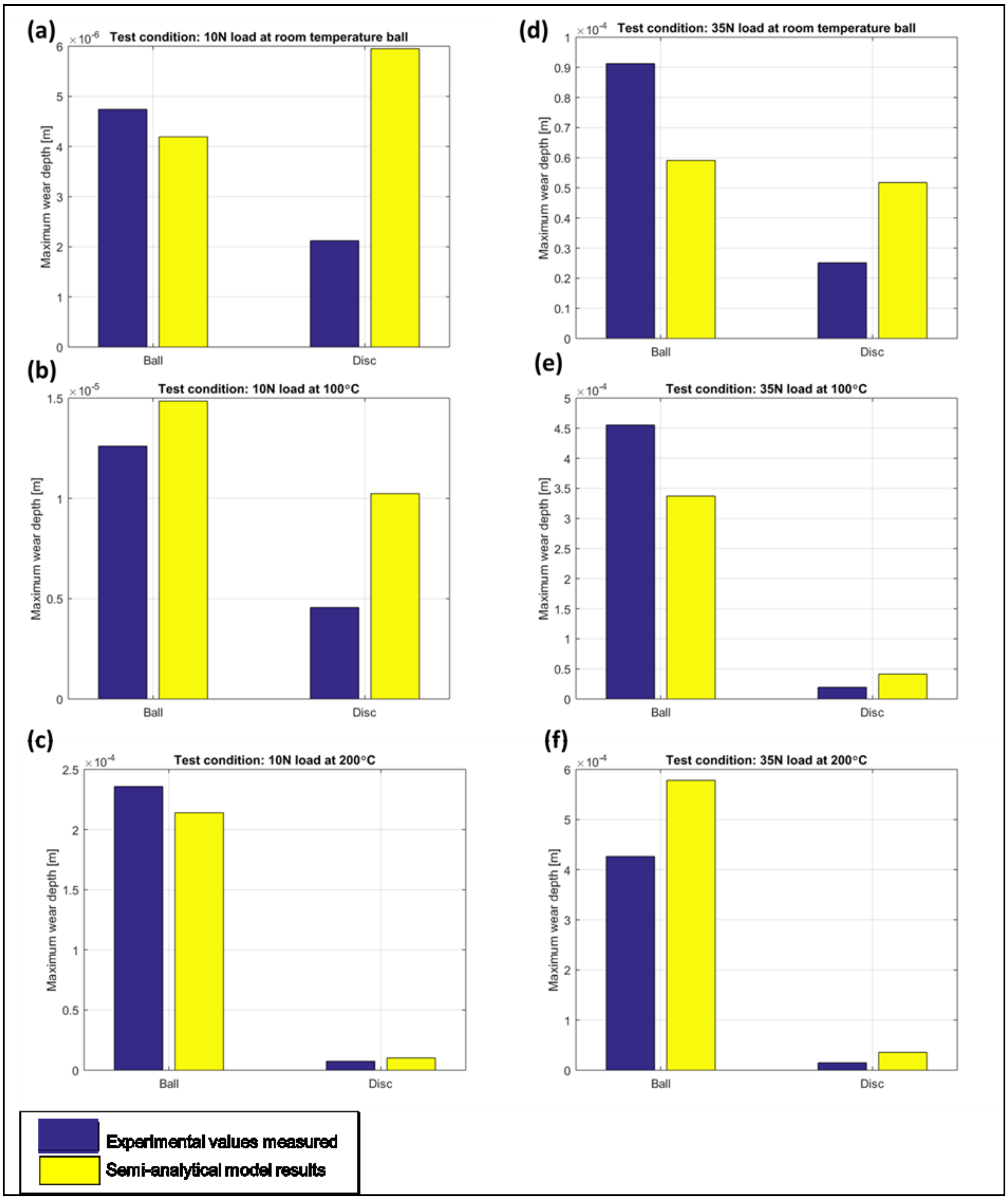

Figure 5.9: (a) – (f): Results from the wear depth computed by the semi-analytical model are compared to the experimental results

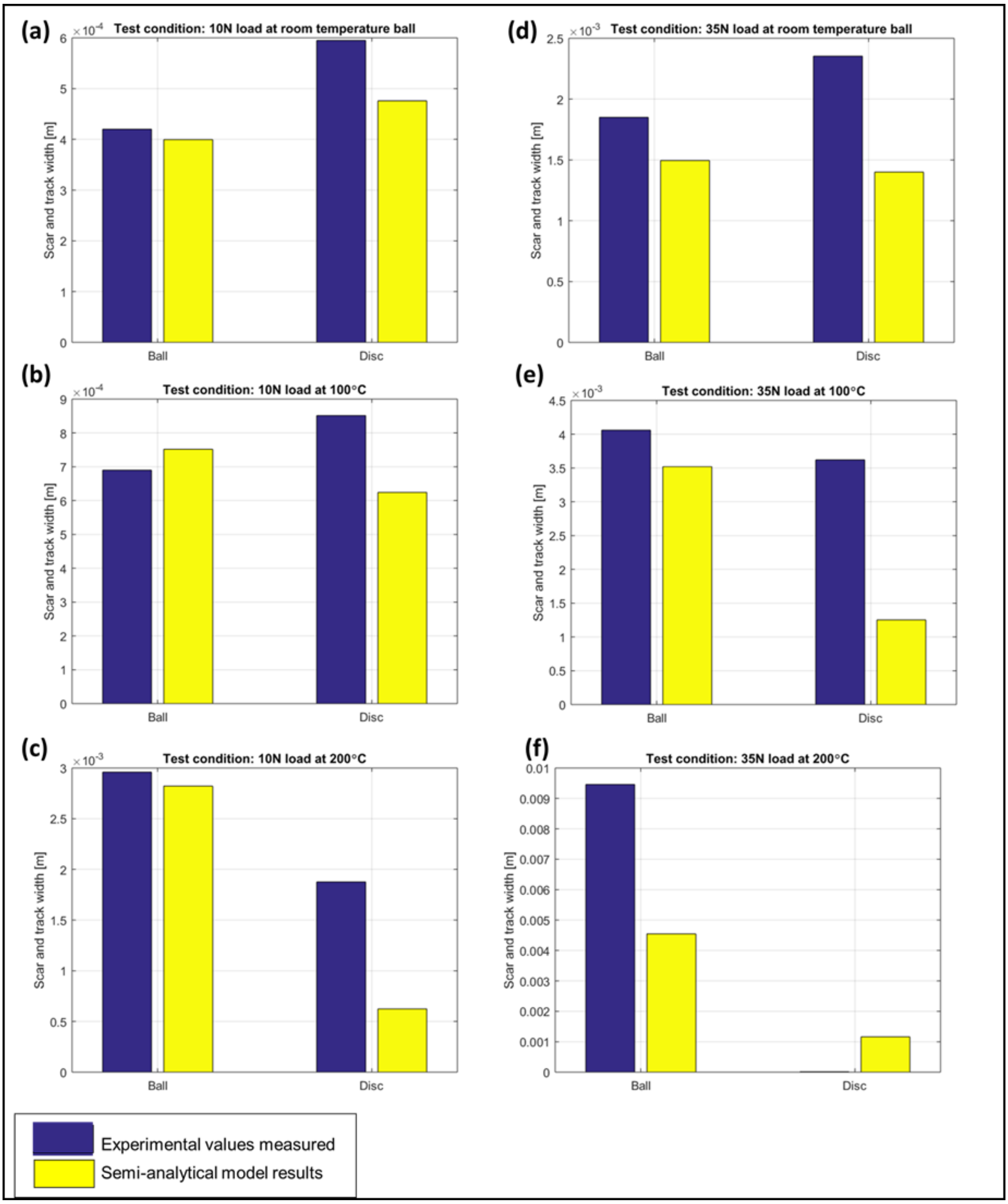

Figure 5.10: (a) – (f): Experimental disc width and ball scar diameter comparison with results from semi-analytical wear prediction model at all experimental conditions

Figure 5.10 (a)-(f) presents the final track width and ball scar diameter measured using measurements on post experimental components in Chapter 3. These values were compared to the values predicted by the semi-analytical model. The values predicted for the width of the disc track exhibit the least agreement of all the values calculated when compared to the experimentally measured values. The ball scars observed were often flat and smooth in appearance. In general, the material on the ball surface appeared to be removed more smoothly than for the disc wear track. As for Figure 5.9, the inconsistency in the track wear prediction may be attributed to the non–uniform ploughing of Haynes 25 by the Stellite 20 ball, which results in grooved surfaces, see Figures 3.10-3.12 (d), and therefore violate the assumption of smoothly evolving surfaces. In order for the model to be improved change in surface roughness should be explicitly captured. The method of calculating the contact area for the disc track throughout the simulation should also be reassessed.

5.2.2 Numerical wear model: 2-D ball and disc models

In the models developed for this project, disc and ball wear were considered separately. The most significant difference between the wear on the ball and disc surfaces during sliding is the progression of contact area between the ball and disc and as a consequence of this, the change in contact pressure and the wear calculated. In the case of disc wear, smooth removal of material was considered and variations such as entrapped wear debris and material plasticity were omitted. A change to the geometry of the surface and therefore a change in contact area was not anticipated. In the case of the ball however, with wear, the geometry of the ball changed or, flattened, increasing the area of contact between the ball and disc and subsequently, the contact pressure changed throughout the simulation. Figure 5.11 (a) and (b) demonstrate how contact pressure changes (or does not) throughout the simulation across the ball and disc contact length. As expected, there was a change in contact pressure for the ball wear case which was not observed for the disc wear case as in 2-D problems the only change in geometry that justifies pressure variation occurs at the end of the stroke, but the pressure remains unaltered in the middle of the stroke where wear is measured in analogy to what would happen in a sector of a pin-on-disc test due to cyclic loading.

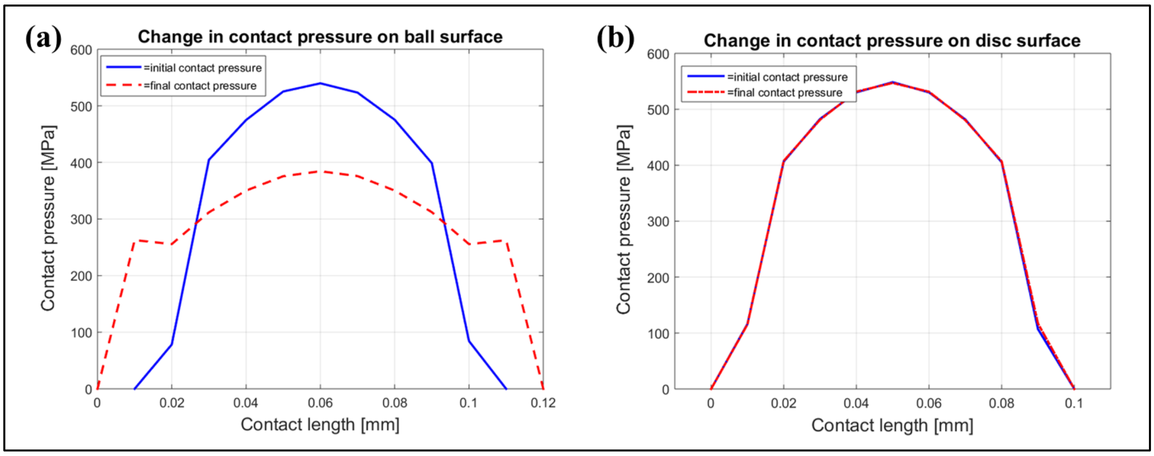

Figure 5.11: (a) and (b): Initial and final contact pressure over a contact length for the ball and disc wear models

In Figure 5.12, the changing stress distribution in the ball can be clearly observed as sliding progresses. As the ball was flattened due to wear induced by the sliding interaction, the contact area between the ball and the disc, represented in this simulation by an analytical, rigid surface, increases and as a result the stress distribution changes, decreasing at the surface where contact pressure is reduced.

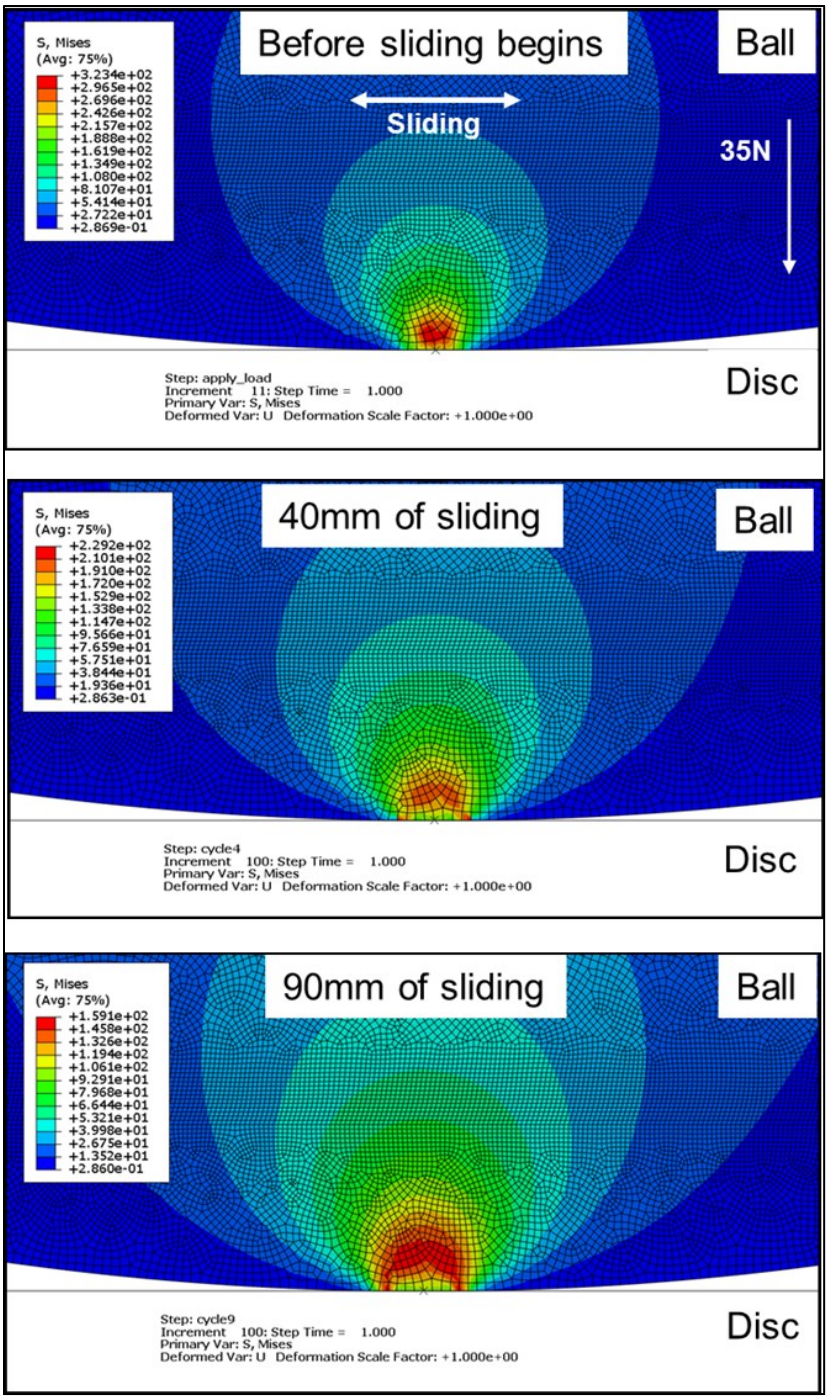

Figure 5.12: Von Mises stress distribution in the fully elastic ball, changing as the contact pressure changes as a result of wear

5.2.2.1 Mesh optimisation study

A mesh optimisation study was carried out for an analysis that represented 90 sliding cycles. Table 5.6 and 5.7 demonstrate the influence of the mesh size on the wear depth prediction result. Each step within all simulations in this study was divided into 100 time increments. The wear coefficient used for both disc and ball components was 1.31E-8, obtained from early wear measurements recorded for experimental conditions of 200°C under a load of 35 N.

Table 5.6: Results from mesh size optimisation study for ball wear

Mesh size (mm)	Total CPU time (hour)	Maximum depth (μm)	Nodes within contact area at start
0.01	19.29	0.846	14
0.015	14	1.005	12
0.02	11	1.005	10

Table 5.7: Results from mesh optimisation study for disc wear

Mesh size (mm)	Total CPU time (hour)	Maximum depth (μm)	Nodes within contact area
0.01	24	0.476	11
0.015	12	0.498	7
0.02	13	0.504	7

5.2.2.1 Wear depth prediction

The 2-D semi-analytical model developed specifically for validating the FE wear models calculated a wear depth of 0.949 μm and 0.526 μm for the ball and disc respectively over a sliding distance of 90 mm under a normal load of 35 N. The most accurate results were anticipated for the FE model with the largest number of nodes in the area of contact. In the mesh optimisation study for the FE ball wear model, three alternative mesh sizes were implemented in the area of contact i.e. the adaptive meshing region; 0.01 mm, 0.015 mm and 0.02 mm. The total CPU time did not vary significantly from wall clock time recorded in any case, indicating that it was representative of time spent executing the simulation. The results indicate that a mesh size of 0.01 mm is optimal for the ball wear simulation as there was a relatively big variation when compared to the coarser meshes applied. In the mesh optimisation study for disc wear, three mesh sizes were implemented in the FE model; 0.01 mm, 0.015 mm and 0.02 mm. The results indicate that a mesh size of 0.015mm is optimal for this simulation as the CPU time taken for most fine and probably the most accurate model (0.01 mm mesh) was significantly longer and therefore not considered acceptable. The average local wear depth recorded on the discs at the end of the final sliding cycle was 0.478 μm and 0.498 μm for mesh sizes of 0.01 mm and 0.015 mm respectively, in good agreement with the semi-analytical validation model, see Figure 5.13.

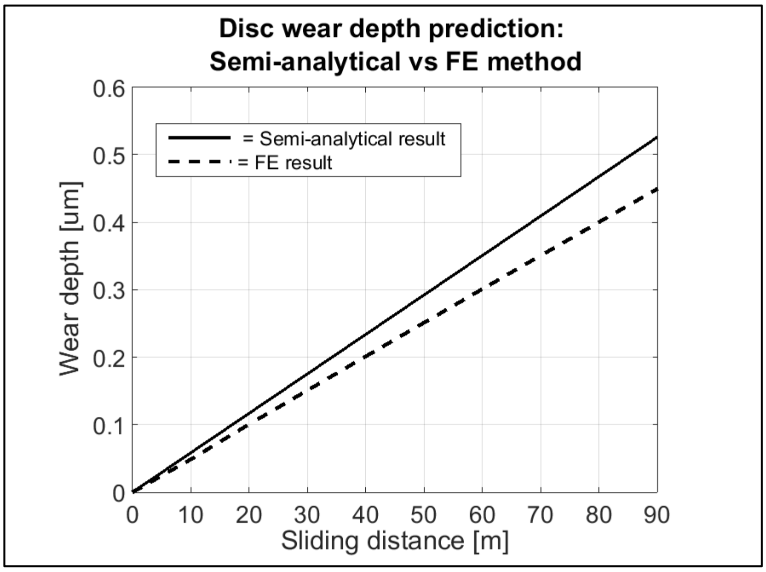

Figure 5.13: Comparison between the wear depth predicted for the disc over the sliding cycles completed using semi-analytical and FE methods

5.3 Further development and future work of the numerical wear model

5.3.1 Introduction

A limitation of using the semi-analytical model presented is that while the wear coefficient value used will be influenced by the experimental environment, the material behaviour will not be considered such as material plasticity, heat generated, wear debris or the presence/absence of oxide layers. Furthermore, the semi-analytical results simulating wear of the ball or ball and disc are limited by the Hertz approximation which hardly holds when the contact size becomes comparable to the disc thickness and oxide layers are introduced. It has been a useful tool to validate the wear depth recorded following sliding wear simulations using FE methods. If a wear prediction model alone was required, the results indicated that the model does not compromise accuracy and is a very time efficient tool for this purpose.

A wear prediction model that succeeds in incorporating variables beyond the removal of material from smooth, elastic surfaces would be useful in reducing the necessity for numerous and complicated validation experiments. Literature from Benea et al [37] shared the curve mapping the growth of an oxide layer on the surface of a Stellite 6 component immersed in a fluid with the same chemistry of nuclear reactor primary water over time, see Figure 2.4, Chapter 2. The growth of an oxide layer on surface components in the reactor environment and how this might affect the rate of mechanical wear is of interest in the overall study of the wear behaviour of cobalt-based alloys. A logarithmic trend function was used to find an equation of the curve provided by Benea and co-workers which fit with basic logarithmic growth kinetics of oxide layers [127]. This agrees with the time dependent Arhennius equation which is presented in a simple form by Equation 5.7;

$$x = A + Bln(t) \qquad \text{Equation 5.7 [127]}$$

where x = film thickness, t = time and A and B are constants found using the data presented in [37]. The growth of an oxide layer on the surface component, when the growth kinetics have been experimentally established, can therefore be simulated using ABAQUS/CAE and UMESHMOTION. Combining this phenomenon with the mechanical wear simulated within a single UMESHMOTION subroutine was also explored. The earlier subroutine described in Section 5.2 invoked Archard's wear equation for surface nodes in the condition of a non-zero value for contact pressure. The modified version presented here activated the displacement of nodes with zero contact pressure, invoking Equation 5.7. This meant that if contact pressure is greater than zero the nodes will be displaced in the negative direction as per the coefficient of wear prescribed, or, if contact pressure on a node is zero the oxide growth kinetics will be applied to 'grow' the surface in the positive direction.

5.3.2 Methodology

Using online tool 'WebPlotDigitizer' at www.automeris.io, data measured for growth in one minute and presented by Benea and co-workers was extracted and used to plot Figure 5.14.

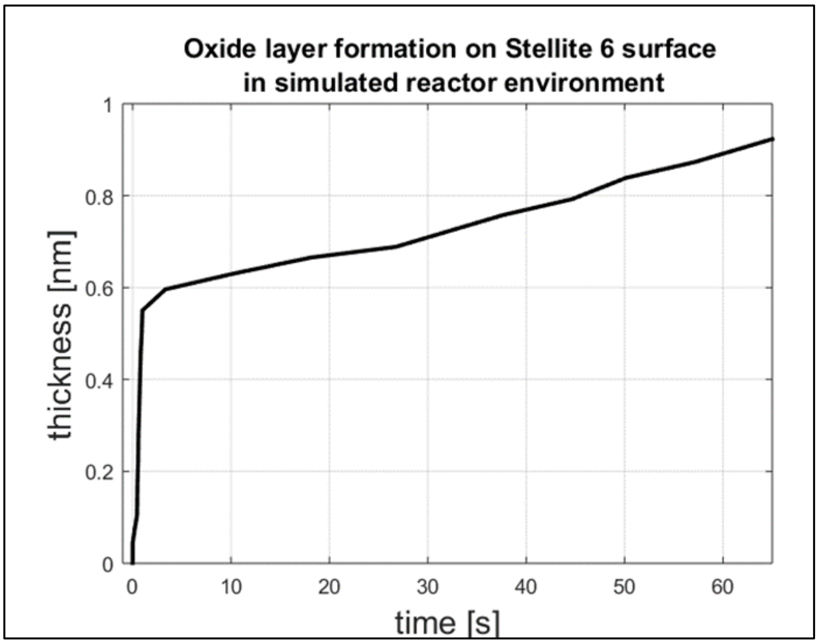

Figure 5.14: Data extracted from Figure 2.4 with permission of the authors demonstrating the growth of an oxide layer over time

Using the Format Trendline function in MS Excel, a logarithmic equation was extracted from the data plotted to describe the growth of the oxide thickness as a function of time, see Equation 5.8.

$$thickness = 0.391 + (0.0784) * ln(time) \qquad \text{Equation 5.8}$$

where the *thickness* of the layer is in nanometers.

In the user-defined subroutine, UMESHMOTION, nodes on the component surface, recorded as 'ULOCAL', adapt in the normal direction with respect to the surface of the adaptive mesh region. In the wear models, displacement of these nodes was in a negative direction as material was 'removed' from the component surface. In the first iteration that attempted to incorporate oxide growth kinetics into the numerical wear model, Equation 5.8 defined the motion of the surface nodes in the positive direction as the layer 'grew' on the surface. The growth of the layer over time on the disc surface was plotted and compared to the data presented by Benea and co-workers.

The next step in developing the model that combined both mechanical wear and the growth of an oxide layer on the component surface was to incorporate the 'wear' and 'growth' equations, previously used separately, within one user-defined subroutine. The ABAQUS wear model was modified with a 'latent' Step inserted between each sliding cycle. In each latent Step, the ball was not displaced although contact was maintained between the ball and disc. The user defined subroutine was modified to simulate growth during the latent periods. The existing subroutine invoked the wear equation removing material from the disc surface when there was a non-zero value for contact pressure. The modification caused the surface to 'grow' when there was a zero value for contact pressure *i.e.* during the latent Steps. The wear depth at the end of each sliding cycle was recorded and results from the wear only model were compared to the results from the model that also included latent periods.

5.3.3 Further improvements and need for future development

The model presented in this section was relatively simple to implement, requiring a wear coefficient and a time related growth equation. Work by Dréano and co-workers presented a far more comprehensive analysis that could be applied in a scenario where more environmental and material data is available [21]. Further experimental data investigating the oxide growth kinetics in the relevant environment would facilitate the development of a more detailed and accurate model focussing on growth of the oxide layer over time. A more in depth understanding of the interplay between the growth kinetics and mechanical wear could be explored by conducting interrupted sliding wear experiments in the nuclear reactor environment, comparing the results to continuous sliding wear experiments and experiments designed to measure oxide growth only.

5.3.3.1 Preliminary results capturing oxide layer formation using FE

(i) Growth only numerical model

To demonstrate the growth of an oxide layer on the surface of a component, a simple ABAQUS/CAE model was created with a single 2-D part, representing the disc. Boundary conditions were applied, preventing displacement of the disc apart from on the surface. A mesh was applied to the part, defined as an adaptive mesh in the region close to the surface. A single Step was created without any further boundary conditions applied. Figure 5.15 compares growth of an oxide on the surface simulated in the ABAQUS model to the data presented by Benea and co-workers [37]. The Fortran code applied in in this FE model can be found in Appendix H. In the user defined subroutine that simulated wear only, the wear equation was invoked only when the local contact pressure at a node in the mesh was greater than zero. In the case of the model that simulated the growth of an oxide layer, the wear growth equation was invoked

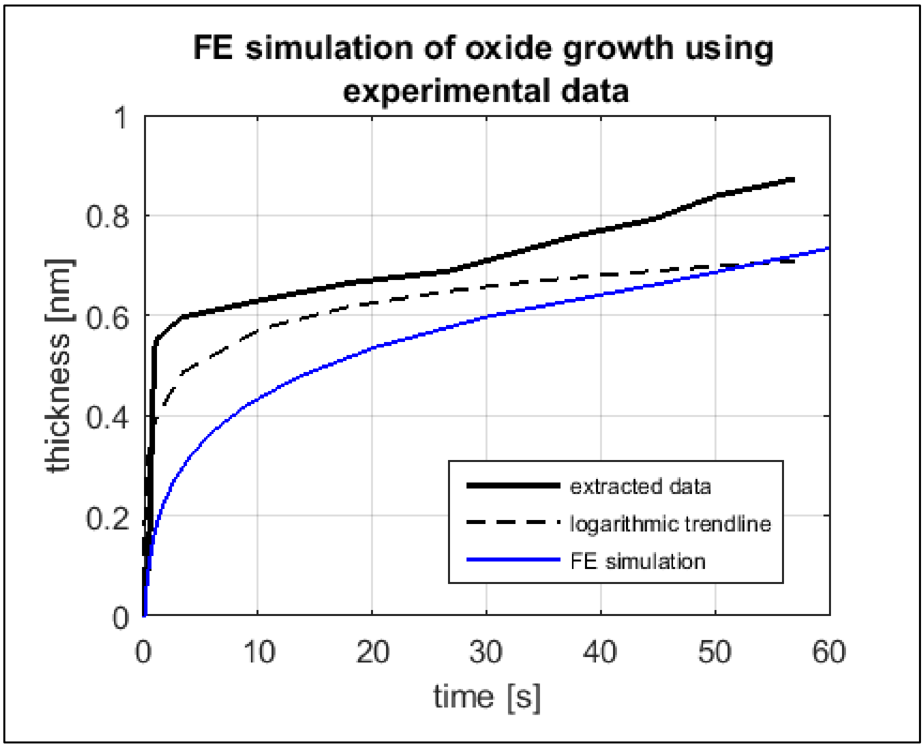

Figure 5.15: FE simulation of oxide layer growth on disc surface using data presented by Benea et al [37]

Figure 5.15 demonstrates that the growth of an oxide layer on a component surface can be simulated in ABAQUS by the application of user-defined subroutine, UMESHMOTION, with experimentally obtained data for oxide layer growth kinetics.

(ii) Combined numerical model

The 2-D disc wear model described in this chapter was used to demonstrate the impact of including the oxide growth kinetics. Nine arbitrary sliding cycles were simulated and the wear depth of a node on the disc surface was recorded and plotted following each sliding cycle. Figure 5.16 demonstrates the difference between the wear only model and the model that included latent periods between each sliding cycle. Although the oxide growth value was arbitrary to be used for demonstrative purposes, the comparison is successful in demonstrating that it is possible to simulate the impact of oxidation on the mechanical wear of a component.

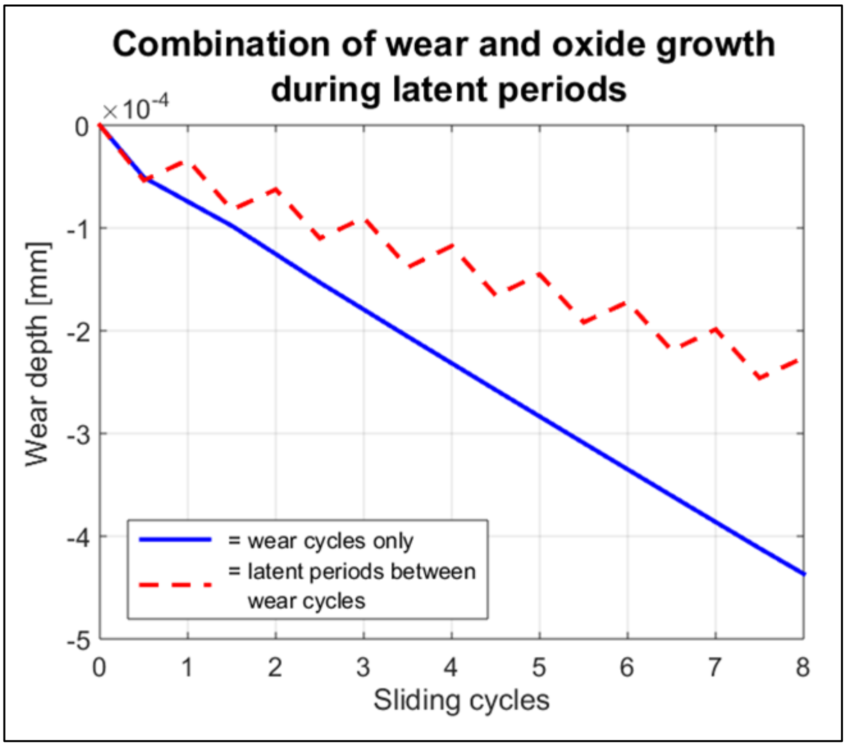

Figure 5.16: Comparing the wear depth of a model that simulated wear only and a model that combined the impact oxidation during latent periods with wear

Figure 5.16 also demonstrates that it is possible to simulate latent periods and how they might impact sliding wear of components in an environment in which oxide films grow on component surfaces.

5.4 Conclusion

Wear prediction models using semi-analytical and numerical methods were developed using information presented in literature. The semi-analytical model is an efficient tool used to predict wear depth and the geometry of disc tracks and ball scars. The results were compared to experimental data recorded and presented in Chapter 3. Overall, the wear depth predicted was in good qualitative and reasonable quantitative agreement with experimental results. The ball scar diameter predictions were also in good qualitative agreement with experimental measurements; however, the model fails to provide a reasonable prediction of track width. This may be due to the uneven nature of material removal on disc track surfaces when compared to the same for the balls. It may also be attributed to the method by which the contact area development was calculated in the case of disc wear which should be reassessed to improve this aspect of the semi-analytical model.

A second more computationally expensive approach to building a wear prediction model was then taken. Two separate numerical wear models were developed using finite element software ABAQUS. To minimise computational expense, the models developed were 2-D analyses of the sliding wear interaction. The sliding distance of the interaction simulated an arbitrary number of cycles, substantially shorter than the sliding distance of the experiments conducted, again to minimise computational expense. As discussed, the wear depth predicted by the semi-analytical wear model for a ball was in reasonable quantitative agreement to the experimental data measured. Although the results of the semi-analytical model developed for the disc was not in as good quantitative agreement with the experimental results as the ball model, it was still adapted to simulate the 2-D interaction. The semi-analytical model was amended to simulate the 2-D interaction using Hertzian contact mechanics for a line contact and used to validate both the FE ball and disc wear models. The successful validation of the FE model gave a platform from which a more comprehensive wear model could be developed, not possible using the relatively simple semi-analytical model. The quantitative agreement between the results produced by the semi-analytical and FE models, highlighted that in order to develop an accurate disc wear model, it would be necessary to build a more complex simulation.

As with the model developed by Hegadekatte et al Ref [7], the wear depth calculated by the semi-analytical model was slightly more conservative than the results produced by the FE wear models. The difference was not however significant, and the semi-analytical model is a reasonable tool to predict wear depth efficiently for both ball and disc components. The limitations of using this model have, however been discussed and it is clear that there is a lot more information and versatility offered by models developed using FE methods.

As discussed in Chapter 2, the growth of an oxide layer on the surface of some cobalt-based alloys in certain environmental conditions can have an impact on the wear behaviour of the alloys. Using data extracted from literature the growth of an oxide layer over time was applied to a component surface using UMESHMOTION, the user defined subroutine used to simulate component wear in the FE wear prediction models presented in this chapter. This was followed by the execution of a model that combined both oxide growth and wear of the component surface. The model was relatively simple; however, it is easily executed and does not rely on detailed environmental parameters. It should be developed further including more material and environmental information as per the model recently presented by Dréano and co-workers for a more comprehensive simulation of the nuclear reactor environment.

Chapter 6 Conclusion

Chapter 6 Conclusion

6.1 Summary

Cobalt-based alloys offer excellent resistance to wear and corrosion in high temperature and pressure, water lubricated environments. Owing to these exceptional properties they are often used for bearing surfaces in nuclear applications. Rolling element bearings (REBs) lubricated by the primary water circulating in the core of nuclear reactors facilitate movement of key structural components. The rolling and race elements of these REBs are made from Stellite 20 and Haynes 25, two cobalt-based alloys. Cobalt behaves unfavourably in the radioactive environment, producing a radioactive isotope cobalt-60, therefore there is an industry drive to minimise the use of components made from cobalt-based alloys that operate in nuclear reactor cores. Any cobalt-free or low cobalt alloy selected to replace Stellite 20 or Haynes 25 must exhibit wear and corrosion resistance equal to or better than the existing alloys in the high temperature, high pressure, and water lubricated environment of the nuclear reactor core.

The main objective of this project was to identify cobalt-free or low cobalt alloys that have the potential to replace Stellite 20 or Haynes 25 as the rolling or race elements in the REBs. Wear behaviour of Stellite 20 and Haynes 25 was assessed in order to set the performance benchmark from which any cobalt-free or low cobalt replacement alloys could be compared and then qualified or, disqualified. The wear behaviour of alloys is commonly evaluated by the weight or volume of material loss from a wear inducing interaction such as ball-on-disc sliding wear experiments. The influence of experimental conditions on wear behaviour is often examined by changing parameters such as temperature, lubrication, load and the total sliding distance. The impact of the interactions on the surface topography of different alloys is also used to compare them. The sliding wear behaviour of Stellite 20 and Haynes 25 was investigated using a bespoke tribometer designed and built to simulate a nuclear reactor environment at the University of Nottingham (UoN). The experiments were conducted under two normal loads, 10 N and 35 N, at room temperature, at 100°C and at 200°C to quantitatively assess wear under severe load and environmental conditions. Using the results from these experiments the wear behaviour of cobalt-free or low cobalt alloys proposed as suitable replacements was investigated and compared to the benchmark set. Tribological properties of a Rolls-Royce plc patented alloy, RR2450, alloy was studied to replace Stellite 3. RR2450 is an iron-based cobalt-free alloy that has demonstrated desirable mechanical properties for nuclear applications from previous studies conducted by the company. A second series of ball-on-disc experiments was conducted with RR2450 balls and Haynes 25 discs over the same range of experimental conditions applied to the Stellite 20-Haynes 25 experiments. The purpose of these experiments was to gain an understanding of the sliding wear behaviour of RR2450 in the simulated reactor environment and to compare it to the performance of Stellite 20.

The experiments conducted using the tribometer located at the UoN were very time intensive as the tribometer was enclosed in an autoclave. A preliminary screening experiment using a tribometer located at Imperial College London (ICL) was subsequently developed to reduce the number of time intensive experiments conducted. The maximum normal load available using the tribometer at ICL was 10 N. The tribometer was not enclosed in an autoclave unlike the tribometer at the UoN and therefore water lubricated experiments were limited to 80°C so that the water didn't evaporate. Experiments conducted using this tribometer were validated by investigating the wear resistance of the Stellite 20-Haynes 25 and RR2450-Haynes 25 ball and disc combinations under a load of 10 N, at room temperature and at 80°C. In both experimental conditions, total wear volume measured was compared to the results from the 10 N, room temperature and the 100°C experiments conducted at the UoN. Prior to the investigation using the tribometer at the UoN, any further alloys proposed to replace either Stellite 20 or Haynes 25 should be screened using these less time intensive experiments. Alloys that demonstrate acceptable wear resistance relative to the benchmark set by Stellite 20-Haynes 25 sliding wear experiments should be recommended for further investigation in the simulated nuclear reactor conditions available using the tribometer at the UoN. A low cobalt and a cobalt-free alloy, Cronidur 30 and Haynes 230, were identified using available literature and data sheets as having mechanical and corrosion resistant properties in good comparison to Haynes 25, see Section 2.5, Chapter 2. As the wear behaviour of these alloys could not be investigated in the simulated nuclear reactor conditions due to restricted availability of the tribometer at the UoN, we decided to conduct preliminary screening experiments [of the alloys] at ICL. Cronidur 30 and Haynes 230 discs were obtained and Stellite 20-Cronidur 30 and Stellite 20-Haynes 230 ball-on-disc experiments were conducted. Results from the Stellite 20-Haynes 25 ball-on-disc experiments conducted using the tribometer at ICL served to provide a performance benchmark from which the sliding wear resistance of Cronidur 30 and Haynes 230 could be compared.

Prior to this project, the tribometers at the UoN and ICL facilitated sliding wear experiments only. Rolling wear was also of interest in this project as Stellite 20 and Haynes 25 are used in rolling element bearings in the nuclear reactor core. A ball holder that facilitated rolling wear tests was designed and manufactured. Short tests were run using the rolling ball holder to demonstrate the difference between rolling and sliding experiments based on the friction recorded for each.

Following the experimental phase of this project, experimental data was used to develop wear prediction models. Wear prediction models can provide the opportunity to reduce the need for complicated and expensive environmentally appropriate material and component validation rigs. The wear volume measured on Stellite 20 and Haynes 25 balls and discs tested in each environmental condition were inserted in Archard's wear equation to calculate the wear coefficient for each component and experimental condition. Each wear coefficient was inserted in a 3-D semi analytical wear prediction model, developed in MATLAB, that was based on work presented by Hegadekatte and co-workers [6]. A second more computationally expensive wear prediction model was also developed using commercial finite element (FE) software ABAQUS and simulated the 2-D sliding wear interaction between a ball and a disc. Two versions of the model, one simulating the wear of the ball and the other the disc were presented in Chapter 5. Wear was simulated by running a user-defined subroutine in parallel to the ABAQUS model. The component surfaces were adapted with respect to the progression of wear, based on Archard's wear equation, which calculated the wear depth following each sliding cycle defined in the model. The numerical wear prediction model was not set up to replicate the entire experimental sliding distance as this would have been extremely computationally expensive. Instead, the semi analytical model was adapted to simulate the 2-D interaction and used to validate the numerical model. The semi analytical model developed was far more computationally efficient than the FE model. However, while the wear coefficient used to calculate the wear depth was influenced by the experimental environment, material behaviour such as plasticity, heat generation in the contact, formation of wear debris or the presence or absence of an oxide glaze were omitted. The development of a more comprehensive model could be executed using ABAQUS, for example using the subroutine to simulate the growth of oxide layers on component surfaces in the nuclear reactor environment. The formation of oxide glazes on component surfaces in certain environmental conditions has been described as influential on the wear behaviour of certain cobalt-based alloys. The numerical wear prediction model developed for this project was modified to simulate the change in component geometry due to the growth of such a glaze. An equation defining the growth of the glaze with respect to time was extracted from data presented in literature and was applied to the user-defined subroutine that ran in parallel to ABAQUS. Two models were executed that incorporated the oxide growth equation extracted. The first simulated the growth of an oxide glaze on the surface of a disc without the application of sliding cycles and thus without inducing mechanical wear. Secondly, Archard's wear equation and the oxide growth equation were applied within the same user-defined subroutine to simulate mechanical wear on a component where the growth of an oxide growth influenced the final wear depth. This is an example of how the numerical wear prediction model can be further developed to provide a better visualisation of material behaviour throughout the experiments.

6.2 Achievements

- The sliding wear behaviour of Stellite 20 and Haynes 25 was investigated for the first time using the sliding wear tribometer set in the simulated nuclear reactor environment at the UoN.
- Developmental iron-based alloy, RR2450, was used to manufacture balls for experiments conducted in this project. The sliding wear behaviour of RR2450 was investigated for the first time with results highlighting its potential as a wear and corrosion resistant alloy to replace Stellite 3* in the rolling element of the REBs that operate in the nuclear reactor environment. However, the risks identified to the manufacture and finishing of RR2450 components should be taken into account.
- Following both sets of experiments conducted in the range of experimental conditions using the tribometer at the UoN, the influence of the ball alloy on the wear of the Haynes 25 discs was assessed. The results indicated that changing the ball from Stellite 20 to RR2450 did not significantly influence the wear behaviour of Haynes 25, in terms of either wear resistance or topographical damage. Compositional analyses of Haynes 25 disc tracks indicated the presence of wear debris adhering to the surface which may have protected the surface and contributed to the decrease in disc wear observed with an increase in experimental temperature, under a normal load of 35 N.
- Cobalt-free or low cobalt alloys proposed as potential alternatives to Stellite 20 or Haynes 25 should be screened using the preliminary screening experiment developed and validated using a tribometer at ICL. The experiment developed was less time intensive than experiments conducted in the simulated nuclear reactor environment. The wear behaviour of alloys that exhibit equal to or superior wear resistance than either Stellite 20 or Haynes 25 should be investigated further at the UoN. This will reduce the volume of time intensive experiments conducted using alloys that have relatively low wear resistance.
- Stellite 20-Cronidur 30 ball-on-disc experiments were conducted with the results demonstrating excellent wear resistance of Cronidur 30, relative to the results produced

using Stellite 20 and Haynes 25 balls and discs in the same experimental conditions. The wear volume of Cronidur 30 was significantly lower than Haynes 25 in both temperatures applied. The wear volume of the Stellite 20 ball was fairly consistent for both sets of experiments which indicated that changing the disc material from Haynes 25 to Cronidur 30 did not have a significant impact on the wear resistance of Stellite 20. The microstructural changes observed on the surface of the Stellite 20 ball scars, however, were very different compared to those produced during the Stellite 20-Haynes 25 experiments. The microstructure of the Stellite 20 balls used had three distinct phases that can be clearly observed in SEM images presented in Chapter 3 and 4. This microstructure underwent significant topographical change following sliding wear experiments conducted with Haynes 25 discs. The microstructure observed on the ball scar produced as a result of the Stellite 20-Cronidur 30 experiments remained distinct. It was clear from the experiments conducted that Cronidur 30 has very good wear resistance compared to Haynes 25 and it was recommended that further experiments are conducted using Cronidur 30 discs in the more extreme conditions available using the tribometer at the UoN. The behaviour of the Stellite 20 balls, sliding against the Cronidur 30 discs, should be observed closely to ensure that its wear performance is not compromised.

- It was not possible to obtain a sample of Haynes 230 in the cold rolled form identified in the literature review that had good mechanical properties relative to cold rolled and aged Haynes 25. Hot rolled solution treated Haynes 230 was available, which was far softer due to the treatment processes used to manufacture it. Experiments were conducted with the softer form of the alloy and as anticipated, the wear resistance was extremely poor compared to either Haynes 25 or Cronidur 30. The experiments did serve to demonstrate the effectiveness of the preliminary screening experiment as a method of reducing the volume of time intensive experiments conducted at the UoN. It is recommended that this continues to act as a method of screening alloys prior to continuing with more time intensive sliding wear experiments in the simulated nuclear reactor environment. It has also succeeded in demonstrating the importance of hardness in the wear resistance of certain alloys.
- Following sliding wear experiments conducted at ICL, a ball holder that facilitated rolling instead of sliding wear experiments was designed. Prior to this work, rolling wear experiments were not possible using the standard tribometer set up.

- Results produced by the 3-D semi analytical wear prediction model were compared to experimental results comparing maximum wear depth, disc wear track width and diameter of the ball scar. The wear depth prediction for balls and discs was in good qualitative and reasonable quantitative agreement with experimental data and the ball scar diameter predicted was in good qualitative agreement with experimental data. The wear track width produced was not in good qualitative or quantitative agreement with the experimental results. The semi analytical wear prediction model was extremely computationally efficient. The results indicated that it may be used as a wear depth prediction model for ball and disc components. However, in its current form it should not be used to predict the width of the track produced on a disc surface as the results were not in good quantitative or qualitative agreement. This may be attributed to the non–uniform ploughing of discs by the balls which resulted in grooved surfaces and therefore violate the assumption of smoothly evolving surfaces. In order for the model to be improved change in surface roughness should be explicitly captured. The method of calculating the contact area for the disc track throughout the simulation should also be reassessed.
- As discussed, a model developed using FE methods has the potential to provide more insight into the material behaviour of components during sliding wear interactions compared to the semi analytical method. Two 2-D numerical wear prediction models predicting wear depth on the ball and disc components were produced. The models were very computationally inefficient when compared to the semi analytical model. The models were not, however, developed to simulate the total sliding distance completed in the experiments and therefore this inefficiency was not as limiting. The 2-D models were validated using the semi analytical model, adapted to simulate a 2-D interaction.
- Following validation of the FE models simulating component wear, a model simulating the growth of an oxide layer on the disc surface was developed using data presented in a study by Benea and co-workers [37]. A second iteration of the model was successfully developed combining the impact of mechanical wear and oxide growth on the disc surface within one simulation. This is relevant to the work investigating the wear behaviour of the cobalt-based alloys in the nuclear reactor core as studies have shown that the growth of oxides on component surfaces can have a deleterious impact their overall wear performance.

6.3 Future work

The highest environmental temperature available for the experiments conducted using the tribometer at the UoN was 200°C, approximately 110°C lower than the temperature of a nuclear reactor core. The increase in wear of Stellite 20 and RR2450 with an increase in experimental temperature, particularly from 100°C to 200°C, was significant. It is highly probable that a further increase in wear volume would be observed if the experimental temperature was increased from 200°C, although the rate of increase in wear might not be as significant. An experimental temperature of 250°C is now available using the tribometer at the UoN and further experiments at this increased temperature should be conducted as it is closer to the operating temperature of the reactor core. The wear volume of Haynes 25 did not increase as significantly with an increase in temperature in either set of experiments *i.e.* when sliding against a Stellite 20 or an RR2450 ball. Experimental analysis suggested that debris formed on the surface of the Haynes 25 discs may have provided some protection of the surface from wear. Literature suggests that debris compacted and sintered on a wear surface might form a hard protective oxide glaze in certain environmental conditions [21, 62, 63]. Increasing the experimental temperature for both the Stellite 20-Haynes 25 and RR2450-Haynes 25 alloy combinations may also present the opportunity to investigate conditions in which this phenomenon might occur.

RR2450 is a developmental alloy and prior to this work, had not yet been used to produce balls. The surface finish of the balls used in the experiments conducted in this project was not uniform due to inexperience manufacturing components from the alloy and perhaps, the presence of the large niobium carbides. The balls were made from bars produced by hot-isostatic pressing RR2450 in powder form and it is thought the lack of uniformity can be partially attributed to coarse grains in the powder. Further experiments should be conducted with balls manufactured from a finer powder, which are currently in production. Results from a second set of experiments with the new balls should give an indication to the impact of the manufacturing process and powder grain size on wear behaviour of RR2450 balls.

Following successful preliminary screening experiments conducted at ICL, it was recommended that the wear behaviour of Cronidur 30 is investigated using the ball-on-disc tribometer at the UoN. Experiments conducted using hot rolled Haynes 230 as the disc material demonstrated very poor relative wear resistance and the alloy in this form should not be tested further. Cold rolled Haynes 230 for use as disc components should be obtained and screened using the tribometer at ICL.

There are small modifications necessary to facilitate water lubricated rolling wear experiments using the tribometer at ICL. These should be made and the rolling ball holder designed in this project should be used to assess the rolling wear behaviour of the cobalt-based alloys. Following this, the holder can be adapted to fit the tribometer at the UoN. This will facilitate rolling wear experiments in the simulated nuclear reactor environment, currently set up to conduct sliding wear experiments only. Information is not readily available which investigates rolling wear of cobalt-based alloys in a simulated nuclear reactor environment whereas there is a significant volume of literature available investigating the sliding wear behaviour of the alloys.

Wear models predicting wear depth on components were presented throughout the literature reviewed. However, models that combine the phenomena of mechanical wear and oxide growth kinetics were not presented or discussed as frequently. To develop the combined model presented in Chapter 5, an equation was extracted from data presented by Benea and co-workers to simulate the growth of an oxide layer over time [37]. Further investigation should be conducted to gain a better understanding of this growth and the subsequent impact it can have on mechanical wear rates. Results from experiments conducted for this purpose could be used to develop a far more comprehensive numerical oxide growth model than what was developed for this project. Interrupted rolling or sliding wear experiments may also provide insight on the impact latent periods have on the wear of components which would simulate periods where the REBs are at rest in the nuclear reactor core.

References

1. Ishida, T., Imayoshi, S., Yoritsune, T., Nunokawa, H., Ochiai, M., Ishizaka, Y., *Development of in-vessel type control rod drive mechanism for marine reactor.* Journal of NUCLEAR SCIENCE and TECHNOLOGY, 2001. **38**(7): p. 557-570.
2. Kusunoki, T., et al., *Design of advanced integral-type marine reactor, MRX.* Nuclear Engineering and Design, 2000. **201**(2): p. 155-175.
3. Freund, G.A., *Materials for Control Rod Drive Mechanisms.* 1963.
4. Ocken, H., *Reducing the cobalt inventory in light water reactors.* Nuclear Technology, 1984. **68**: p. 18-28.
5. Podra, P. and S. Andersson, *Simulating sliding wear with finite element method.* Tribology International, 1999. **32**: p. 71-81.
6. Hegadekatte, V., Huber, N., Kraft, O., *Modeling and simulation of wear in a pin on disc tribometer.* Tribology Letters, 2006. **24**(1): p. 51-60.
7. Hegadekatte, V., et al., *A predictive modeling scheme for wear in tribometers.* Tribology International, 2008. **41**(11): p. 1020-1031.
8. Riddihough, M., *Stellite as a wear resistant material.* TRIBOLOGY, 1970(November): p. 211-215.
9. Klarstrom, D.L., *Wrought cobalt - base superalloys.* Journal of Materials Engineering and Performance, 1993. **2**(4): p. 523-530.
10. Antony, K.C., *Wear-resistant Cobalt-Base Alloys.* JOM, 1983. **25**(2): p. 52-60.
11. Malayoglu, U., Neville, A., Beamson, G., *Characterisation of the passive film on HIPed Stellite 6 alloys using X-ray photoelectron spectroscopy.* Materials Science & Engineering A, 2005. **393**: p. 91-101.
12. Davis, J.R., *Handbook of materials for medical devices*, ed. A. International. 2003, Materials Park, Ohio: ASM International.
13. Liu, R., et al., *Relations of Chemical Composition to Solidification Behavior and Associated Microstructure of Stellite Alloys.* Metallography, Microstructure, and Analysis, 2015. **4**: p. 146-157.
14. Shin, J.-C., et al., *Effect of molybdenum on the microstructure and wear resistance of cobalt-base Stellite hardfacing alloys.* Surface and Coatings Technology, 2003. **166**(2): p. 117-126.
15. Frenk, A. and W. Kurz, *Microstructural effects on the sliding wear resistance of a cobalt-based alloy.* Wear, 1994. **174**(1): p. 81-91.
16. Kapoor, S., Liu, R., Wu, X.J., Yao, M.X., *Temperature - Dependence of Hardness and Wear Resistance of Stellite Alloys.* International Journal of Materials and Metallurgical Engineering, 2012. **6**(7): p. 592-601.
17. Fleitman, A.H., R.B. Herchenroeder, and J.G.Y. Chow, *Cobalt base alloys for use in nuclear reactors.* Nuclear Engineering and Design 1971. **15**: p. 345-362.
18. Bowden, D., et al., *A high-strength silicide phase in a stainless steel alloy designed for wear-resistant applications.* Nature Communications, 2018. **9**(1): p. 1374.
19. Rosalbino, F. and G. Scavino, *Corrosion behaviour assessment of cast and HIPed Stellite 6 alloy in a chloride-containing environment.* Electrochimica Acta, 2013. **111**: p. 656-662.
20. Bowden, D., *Assessment of cobalt-free hardfacing stainless steel alloys for nuclear applications*, in *School of Materials*. 2016, University of Manchester: Manchester. p. 258.
21. Dréano, A., S. Fouvry, and G. Guillonneau, *A tribo-oxidation abrasive wear model to quantify the wear rate of a cobalt-based alloy subjected to fretting in low-to-medium temperature conditions.* Tribology International, 2018. **125**: p. 128-140.
22. Cachon, L., et al., *Tribological qualification of cobalt-free coatings for pressurised water reactor primary circuit gate valve applications.* Surface and Coatings Technology, 1996. **85**: p. 163-169.
23. International, H., *Haynes 25 Alloy*. 2004.
24. Balls, R., *Stellite 20PMH Alloy Balls*, in *RGP Balls*, R. Balls, Editor.: Milan, Italy.

25. Crook, P., *Cobalt and Cobalt Alloys*. ASM Handbook. 1990.
26. Amateau, M.F. and W.A. Glaeser, *Survey of materials for high-temperature bearing and sliding applications.* Wear, 1964. **7**: p. 385-418.
27. McCarron, R., Stewart., D, Shipway, P., Dini., D, *Sliding wear analysis of cobalt-based alloys in nuclear reactor conditions.* Wear 2017. **376-377**: p. 1489-1501.
28. Knezevic, M.C., J. S.; Lovato, M. L.; McCabe, R. J., *Deformation behaviour of the cobalt-based superalloy Haynes 25: Experimental characterization and crystal plasticity modeling.* Acta Materialia, 2014. **63**: p. 162-168.
29. Teague, J., E. Cerreta, and M. Stout, *Tensile properties and microstructure of Haynes 25 alloy after aging at elevated temperatures for extended times*. 2003, Los Alamos National Laboratory: Los Alamos National Laboratory.
30. Coutsouradis, D., A. Davin, and M. Lamberigts, *Cobalt-based Superalloys for Applications in Gas Turbines.* Materials Science and Engineering, 1987. **88**: p. 11-19.
31. Sandrock, G.D. and C.W. Andrews, *Effects of cold work and aging on the substructure and precipitation phenomena in the cobalt-base alloy L-605*, NASA, Editor. 1971, NASA: Washington DC.
32. Ayagaki, M., et al., *Development of Superior Resistant Materials by HIP Process and Their Applications*, in *Technical Report No. 68*, N. Steel, Editor. 1996, Nippon Steel.
33. Yu, H., et al., *Influence of manufacturing process and alloying element content on the tribomechanical properties of cobalt-based alloys.* Journal of Tribology, 2008. **131**(1).
34. Yu, H., R. Ahmed, and H. de Villies Lovelock, *A comparison of the tribo-mechanical properties of wear resistant cobalt-based alloy produced by different manufacturing processes.* Journal of Tribology, 2007. **129**(3): p. 586-594.
35. Ahmed, R., et al., *Influence of Re-HIPing on the structure–property relationships of cobalt-based alloys.* Tribology International, 2013. **57**(Supplement C): p. 8-21.
36. Rabinowicz, E., *Friction and Wear of Materials*. 2nd edition ed. 1995: Wiley-Interscience.
37. Benea, L., et al., *Tribocorrosion Mechanism Study of Stellite-6 and Zircaloy-4 - A Comparison in LiH-H3BO3 Solutions.* Annals of the University Dunarea de Jos of Galati: Tribology, 2005.
38. Roberts, W.H., *Tribology in nuclear power generation.* Tribology International, 1981. **14**(1): p. 17-28.
39. Bhushan, B., *Introduction to Tribology*. Second Edition ed, ed. Wiley. 2013, New York, US: John Wiley & Sons Ltd.
40. Pauschitz, A., M. Roy, and F. Franek, *Mechanisms of sliding wear of metals and alloys at elevated temperatures.* Tribology International, 2008. **41**(7): p. 584-602.
41. Benea, L., et al., *Tribocorrosion of stellite 6 in sulphuric acid medium: electrochemical behaviour and wear.* Wear, 2004. **256**(9-10): p. 948-953.
42. Lemaire, E. and M. Le Calvar, *Evidence of tribocorrosion wear in pressurized water reactors.* Wear, 2001. **249**: p. 338-344.
43. Stachowiak, A. and W. Zwierzycki, *Tribocorrosion modeling of stainless steel in a sliding pair of pin-on-plate type.* Tribology International, 2011. **44**(10): p. 1216-1224.
44. Cao, S., S. Guadalupe Maldonado, and S. Mischler, *Tribocorrosion of passive metals in the mixed lubrication regime: theoretical model and application to metal-on-metal artificial hip joints.* Wear, 2015. **324-325**: p. 55-63.
45. Kanavalli, B., *Application of user defined subroutine UMESHMOTION in ABAQUS for simulating dry rolling / sliding wear*. 2006, Royal Institute of Technology (KTH_: Stockholm, Sweden. p. 58.
46. Spiegelberg, C., *Friction and wear in rolling and sliding contacts*, in *School of Industrial Engineering and Management*. 2005, ka: Sweden. p. 45.
47. Ko, P.L., et al., *Friction and wear studies of nclear power plant components in pressurized high temperature water environments*. 1997, EDF: France.

48. Vernot, J.P. and D. Kaczorowski, *9 - Analysis of mechanisms induced by sliding and corrosion: Dedicated apparatus for pressurized water reactor environments*, in *Electrochemistry in Light Water Reactors*. 2007, Woodhead Publishing. p. 167-178.
49. Lina, A., et al., *The influence of water flow on the impact/sliding wear and oxidation of PWR control rods specimens.* Wear, 2001. **251**(1): p. 839-852.
50. El-Thalji, I. and E. Jantunen, *A descriptive model of wear evolution in rolling bearings.* Engineering Failure Analysis, 2014. **45**: p. 204-224.
51. Bodini, I., et al., *Evaluation of wear in rolling contact tests by means of 2D image analysis.* Wear, 2018. **400-401**: p. 156-168.
52. Akchurin, A., et al., *Analysis of Wear Particles Formed in Boundary-Lubricated Sliding Contacts.* Tribology Letters, 2016. **63**(16).
53. Lim, S.C. and M.F. Ashby, *Wear-mechanism maps.* Acta Metallurgica, 1987. **35**(1): p. 1-24.
54. Hegadekatte, V., N. Huber, and O. Kraft, *Finite element based simulation of dry sliding wear.* Modelling and Simulation in Materials Science and Engineering, 2005. **13**(1): p. 57-75.
55. Rasool, G. and M.M. Stack, *Mapping the role of Cr content in dry sliding of steels: Comparison between maps for material and counterface.* Tribology International, 2014. **80**(Supplement C): p. 49-57.
56. Quinn, T.F.J., *Review of oxidational wear: Part I: The origins of oxidational wear.* Tribology International, 1983. **16**(5): p. 257-271.
57. Bhansali, K.J., *Adhesive wear of nickel and cobalt-based alloys.* Wear, 1979. **60**: p. 95-110.
58. Quinn, T.F.J., *Review of oxidational wear: Part I: The origins of oxidational wear.* Tribology International, 1983. **16**(5): p. 257-271.
59. International, A., *ASM Handbook*. Friction, Lubrication and Wear, ed. P.J. Blau. Vol. 18. 1992, United States of America: ASM International.
60. Mishina, H. and A. Hase, *Wear equation for adhesive wear established through elementary process of wear.* Wear, 2013. **308**(1-2): p. 186-192.
61. Renz, A., et al., *High-temperature sliding wear behaviour of Stellite®12 and Tribaloy®T400.* Wear, 2018. **402-403**: p. 148-159.
62. Inman, I.A., *Compacted oxide layer formation under conditions of limited debris retention at the wear interface during high temperature sliding wear of superalloys*, in *Advanced Materials Research Institute*. 2004, Northumbria University p. 369.
63. Stott, F.H., *High-temperature sliding wear of metals.* Tribology International, 2002. **35**(8): p. 489-495.
64. Inman, I.A. and P.S. Datta, *Studies of high temperature sliding wear of metallic dissimilar interfaces III: Incoloy MA956 versus Incoloy 800HT.* Tribology International, 2010. **43**(11): p. 2051-2071.
65. Kapoor, S., *High-Temperature Hardness and Wear Resistance of Stellite Alloys*, in *Mecanical Engineering*. 2012, Carleton University: Ottowa, Ontario. p. 197.
66. Franklin, F.J., I. Widiyarta, and A. Kapoor, *Computer simulation of wear and rolling contact fatigue.* Wear, 2001. **251**(1): p. 949-955.
67. Fernandes, P.J.L., *Contact fatigue in rolling-element bearings.* Engineering Failure Analysis, 1997. **4**(2): p. 155-160.
68. Sadeghi, F., et al., *A review of rolling contact fatigue.* Journal of Tribology, 2009. **131**.
69. Lau, J.L.B., Dini, D. , *Water Lubrication of Rolling Element and Journal Bearings.* 2014.
70. Zhou, Y.-H., M. Harmelin, and J. Bigot, *Sintering behaviour of ultra-fine Fe, Ni and Fe-25wt%Ni powders.* Scripta Metallurgica, 1989. **23**(8): p. 1391-1396.
71. Rose, S.R., *Studies of the high temperature tribological behaviour of some superalloys*. 2000, Northumbria University: Northumbria University.
72. Amateau, M.F. and W.A. Glaeser, *Survey of materials for high-temperature bearing and sliding applications.* Wear, 1964. **7**(5): p. 385-418.

73. So, H., Chen, C.T., Chen, Y.A., *Wear behaviours of laser-clad stellite alloy 6.* Wear, 1996. **193**: p. 78-84.
74. Landolt, D., S. Mischler, and M. Stemp, *Electrochemical methods in tribocorrosion: a critical appraisal.* Electrochimica Acta, 2001. **46**(24-25): p. 3913-3929.
75. Guadalupe Maldonado, S., et al., *Mechanical and chemical mechanisms in the tribocorrosion of a Stellite type alloy.* Wear, 2013. **308**(1-2): p. 213-221.
76. Inglis, I. and E.V. Murphy, *Performance of wear-resistant iron base hardfacing alloys in valves operating under prototypical pressurised water reactor conditions.* Surface and Coatings Technology, 1992. **53**: p. 101-106.
77. Garcia, D.D. and J.P. Celis, *Corrosion wear of passivating materials in sliding contact based on the concepts of active wear track area.* Wear, 2001. **249**: p. 452-460.
78. Wenger, F., et al., *11 - Tribocorrosion of stellite 6 alloy: Mechanism of electrochemical reactions*, in *Electrochemistry in Light Water Reactors*. 2007, Woodhead Publishing. p. 195-211.
79. Quinn, T.J.F., *Role of oxidation in the mild wear of steel.* British Journal of Applied Physics, 1962. **13**(1): p. 33-37.
80. Ebert, F.-J., *An Overview of Performance Characteristics, Experiences and Trends of Aerospace Engine Bearings Technologies.* Chinese Journal of Aeronautics, 2007. **20**(4): p. 378-384.
81. Jin, J. and T. Shao, *Effects of single- and dual-element ion implantation on tribomechanical properties of Cronidur 30 bearing steel.* Surface and Coatings Technology, 2018. **344**: p. 303-311.
82. Group, F.K., *Rolling Bearings Made of Cronidur 30*, in www.fag.de, F.K. Group, Editor., FAG Kugelfischer: Germany. p. 4.
83. Franz-Josef, E., *An Overview of Performance Characteristics, Experiences and Trends of Aerospace Engine Bearings Technologies.* Chinese Journal of Aeronautics, 2007. **20**: p. 378-384.
84. Trojahn, W., Streit, E., Chin, H.A., Ehlert, D. , *Progress in bearing performance of advanced nitrogen alloyed stainless steel, Cronidur 30.* Materials Science & Engineering Technology, 1999. **30**: p. 605-611.
85. Gavriljuk, V.G., B.D. Shanina, and H. Berns, *A physical concept for alloying steels with carbon+nitrogen.* Materials Science and Engineering: A, 2008. **481-482**: p. 707-712.
86. Bhadeshia, H.K.D.H., *Steels for bearings.* Progress in Material Science, 2012. **57**(2): p. 268-435.
87. Shankar, V., Bhanu Sankara Rao, K., Mannan, S.L., *Microstructure and mechanical properties of Inconel 625 superalloy.* journal of nuclear materials, 2001. **288**: p. 222-232.
88. *Alloy 625 Datasheet*, in *JACQUET*, JACQUET, Editor., JACQUET: USA.
89. *Alloy 825 Datasheet*, in *Datasheets*, JACQUET, Editor., JACQUET: USA.
90. Mulligan, C.P., et al., *Microstructure and age hardening of C276 alloy coatings.* Surface and Coatings Technology, 2015. **270**(299).
91. *Alloy C276 Datasheet*, in *JACQUET*, JACQUET, Editor., JACQUET: USA.
92. Barrett, P.R., Raasheduddin, A., Mamballykalathil, M., Hassan, T. , *Isothermal low-cycle fatigue and fatigue-creep of Haynes 230.* International Journal of Solids and Structures, 2016. **88-89**: p. 146-164.
93. Veverkova, J., et al. *High temperature microstructural degradation of Haynes Alloy 230*. in *Superalloys*. 2008. Pennsylvania, US: TMS.
94. HaynesInternational, *Haynes 230 Alloy Principle Features*, H. International, Editor.: Haynes International.
95. Guo, Y.B., Liu, C. R. , *Mechanical properties of hardened AISI 52100 steel in hard machining processes.* Journal of Manufacturing Science and Engineering, 2015. **124**(1).
96. *Cronidur 30*, E. Essen, Editor. 2003.
97. Metals, S., *Inconel 625*, S.M. Corporation, Editor. 2013, Special Metals Corporation.
98. Metals, S., *Incoloy alloy 825*, S.M. Corporation, Editor. 2004, Special Metals Corporation.

99. Burdett, W.B., *Stainless steel alloy*. 1997, Rolls-Royce Marine Power Operations Ltd.
100. Meng, H.C. and K. Ludema, *Wear models and predictive equations: their form and content.* Wear, 1995. **181**: p. 443-457.
101. McColl, I.R., Ding, J., Leen, S.B., *Finite element simulation and experimental validation of fretting wear.* Wear, 2004. **256**: p. 114-1127.
102. Williams, J.A., *Wear modelling: analytical, computational and mapping: a continuum mechanics approach.* Wear, 1999. **225-229**(Part 1): p. 1-17.
103. Elleuch, K. and S. Fouvry, *Experimental and modelling aspects of abrasive wear of a A357 aluminium alloy under gross slip fretting conditions.* Wear, 2005. **258**(1): p. 40-49.
104. Done, V., et al., *Semi analytical fretting wear simulation including wear debris.* Tribology International, 2017. **109**: p. 1-9.
105. Johnson, K.L., *Contact Mechanics*. 1985, Cambridge: Cambridge University Press.
106. Barzdajn, B., et al., *A crystal plasticity assessment of normally loaded sliding contact in rough surfaces and galling.* Journal of Mechanics and Physics of Solids, 2018. **121**: p. 517-542.
107. Archard, J.F., *Contact and rubbing of flat surfaces.* Journal of Applied Physics, 1953. **24**(981).
108. Fouvry, S., et al., *An energy description of wear mechanisms and its applications to oscillating sliding contacts.* Wear, 2003. **255**(1): p. 287-298.
109. Cruzado, A., et al., *Finite element simulation of fretting wear and fatigue in thin steel wires.* International Journal of Fatigue, 2013. **55**: p. 7-21.
110. Arjamndi, M., et al., *Finite element modelling of sliding wear in three-dimensional woven textiles.* Tribology International, 2017. **115**: p. 452-460.
111. Gonzalez, C., et al., *Numerical analysis of pin on fisc tests on Al-Li/SiC composites.* WEAR, 2005. **259**: p. 609-612.
112. Martinez, F., et al., *Finite element implementation and validation of wear modelling in sliding polymer-metal contacts.* Wear, 2012. **284**: p. 52-64.
113. Suh, N.P., *The Delamination Theory of Wear.* Wear, 1973. **25**: p. 111-124.
114. Jiang, J., M.M. Stack, and A. Neville, *Modelling the tribo-corrosion interaction in aqueous sliding conditions.* Tribology International, 2001. **35**: p. 669-679.
115. Déforge, D., et al., *10 - Tribocorrosion in pressurized water reactor environments: Room temperature results and finite element modeling*, in *Electrochemistry in Light Water Reactors*. 2007, Woodhead Publishing. p. 179-194.
116. SKF, *Rolling Bearings*, in *Roll*, S. Group, Editor. 2018, SKF Group: skf.com
117. *Standard Test Method for Wear Testing with a Pin-on-Disk Apparatus*.
118. Schneider, C.A., W.S. Rasband, and K.W. Eliceiri, *NIH IMage to IMageJ: 25 years of image analysis.* Nature methods, 2012. **9**(7): p. 671-670.
119. Liu, R., Yao, J.H., Zhang, Q.L., Yao, M.X., Collier, R., *Sliding wear and solid-particle erosion resistance of a novel high-tungsten Stellite alloy.* Wear, 2014. **322-323**: p. 41-50.
120. Motallebzadeh, A., Atar, E., Cimenoglu, H., *Sliding wear characteristics of molybdenum containing Stellite 12 coating at elevated temperatures.* Tribology International, 2015. **91**: p. 40-47.
121. Blank, H., Hall, A. M., Hackson, J. W., Anderson, W. K., *The heat treatment and working of Haynes 25 alloy*. 1953: United States Atomic Energy Commission.
122. Hempel Special Metals, *Cronidur 30 Datasheet*, Hempel Metals, Editor. 2014, Hempel Metals. p. 2.
123. SKF. *SKF Bearing Calculator*. [Online Calculator] 2018 30/07/2018 30/07/2018]; Online tool that provides basic bearing analysis]. Available from: http://webtools3.skf.com/BearingCalc/.
124. Cruzado, A., Urchegui, M.A., Gómez, X., *Finite element modeling and experimental validation of fretting wear scars in thin steel wires.* Wear, 2012. **289**: p. 26-38.
125. Systemes, D., *ABAQUS Documentation*, Simulia, Editor. 2011, Simula: Providence, RI, USA.
126. Madge, J.J., *Numerical modelling of the effect of fretting wear on fretting fatigue*. 2009, The University of Nottingham. p. 215.

127. Seyeux, A., V. Maurice, and P. Marcus, *Oxide Film Growth Kinetics on Metals and Alloys I. Physical Model.* Journal of the Electrochemical Society, 2013. **160**(6): p. C189-C196.

Appendix A

Datasheet: Stellite 20

The following datasheet was provided by RGP Balls. The balls purchased from RGP were used in experiments discussed in Chapters 3 and 5.

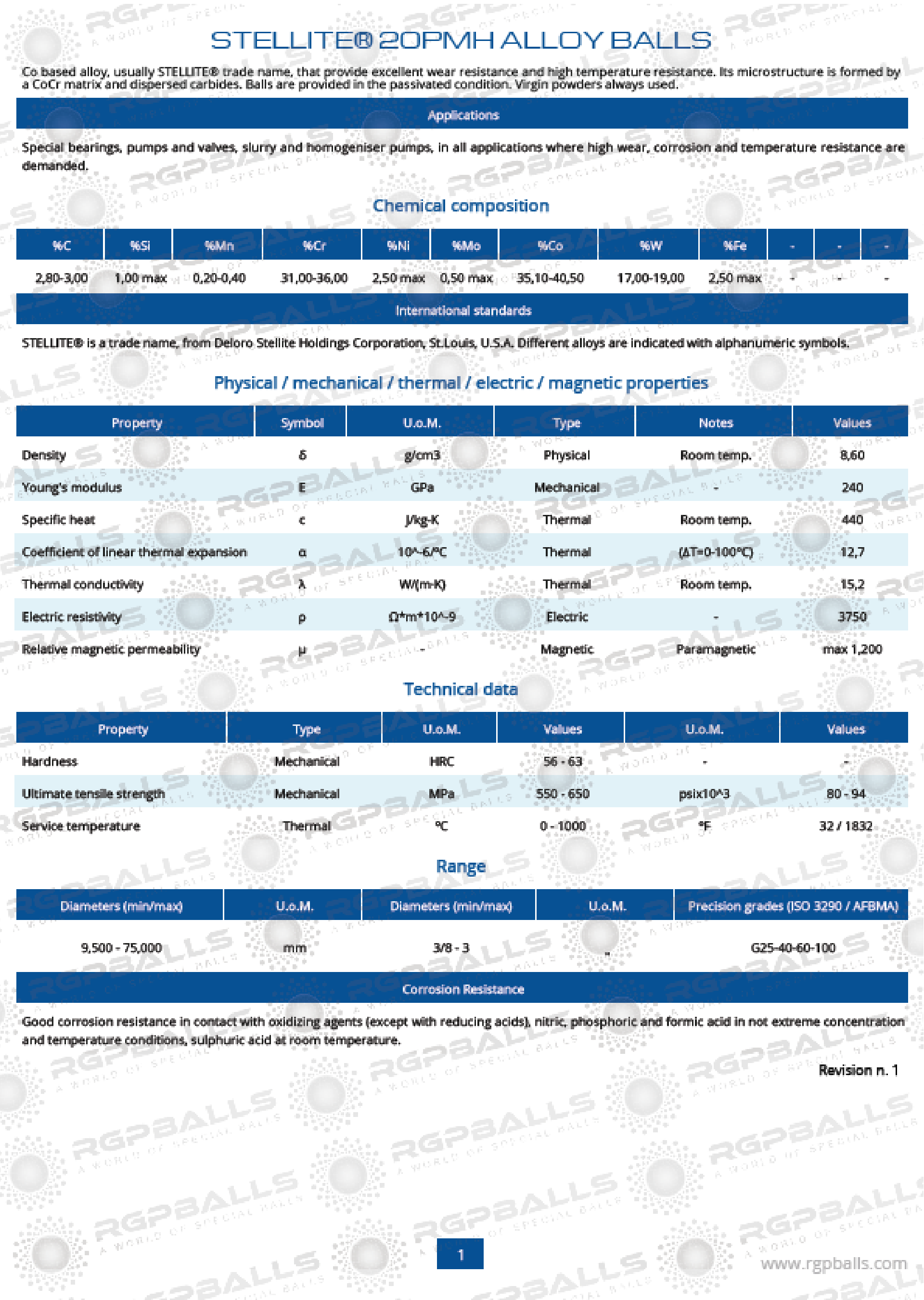

STELLITE® 20PMH ALLOY BALLS

Co based alloy, usually STELLITE® trade name, that provide excellent wear resistance and high temperature resistance. Its microstructure is formed by a CoCr matrix and dispersed carbides. Balls are provided in the passivated condition. Virgin powders always used.

Applications

Special bearings, pumps and valves, slurry and homogeniser pumps, in all applications where high wear, corrosion and temperature resistance are demanded.

Chemical composition

%C	%Si	%Mn	%Cr	%Ni	%Mo	%Co	%W	%Fe	-	-	-
2,80-3,00	1,00 max	0,20-0,40	31,00-36,00	2,50 max	0,50 max	35,10-40,50	17,00-19,00	2,50 max	-	-	-

International standards

STELLITE® is a trade name, from Deloro Stellite Holdings Corporation, St.Louis, U.S.A. Different alloys are indicated with alphanumeric symbols.

Physical / mechanical / thermal / electric / magnetic properties

Property	Symbol	U.o.M.	Type	Notes	Values
Density	δ	g/cm3	Physical	Room temp.	8,60
Young's modulus	E	GPa	Mechanical	-	240
Specific heat	c	J/kg-K	Thermal	Room temp.	440
Coefficient of linear thermal expansion	α	10^-6/°C	Thermal	(ΔT=0-100°C)	12,7
Thermal conductivity	λ	W/(m-K)	Thermal	Room temp.	15,2
Electric resistivity	ρ	Ω*m*10^-9	Electric	-	3750
Relative magnetic permeability	μ	-	Magnetic	Paramagnetic	max 1,200

Technical data

Property	Type	U.o.M.	Values	U.o.M.	Values
Hardness	Mechanical	HRC	56 - 63	-	-
Ultimate tensile strength	Mechanical	MPa	550 - 650	psix10^3	80 - 94
Service temperature	Thermal	°C	0 - 1000	°F	32 / 1832

Range

Diameters (min/max)	U.o.M.	Diameters (min/max)	U.o.M.	Precision grades (ISO 3290 / AFBMA)
9,500 - 75,000	mm	3/8 - 3	„	G25-40-60-100

Corrosion Resistance

Good corrosion resistance in contact with oxidizing agents (except with reducing acids), nitric, phosphoric and formic acid in not extreme concentration and temperature conditions, sulphuric acid at room temperature.

Revision n. 1

Appendix B

Datasheet: Haynes 25

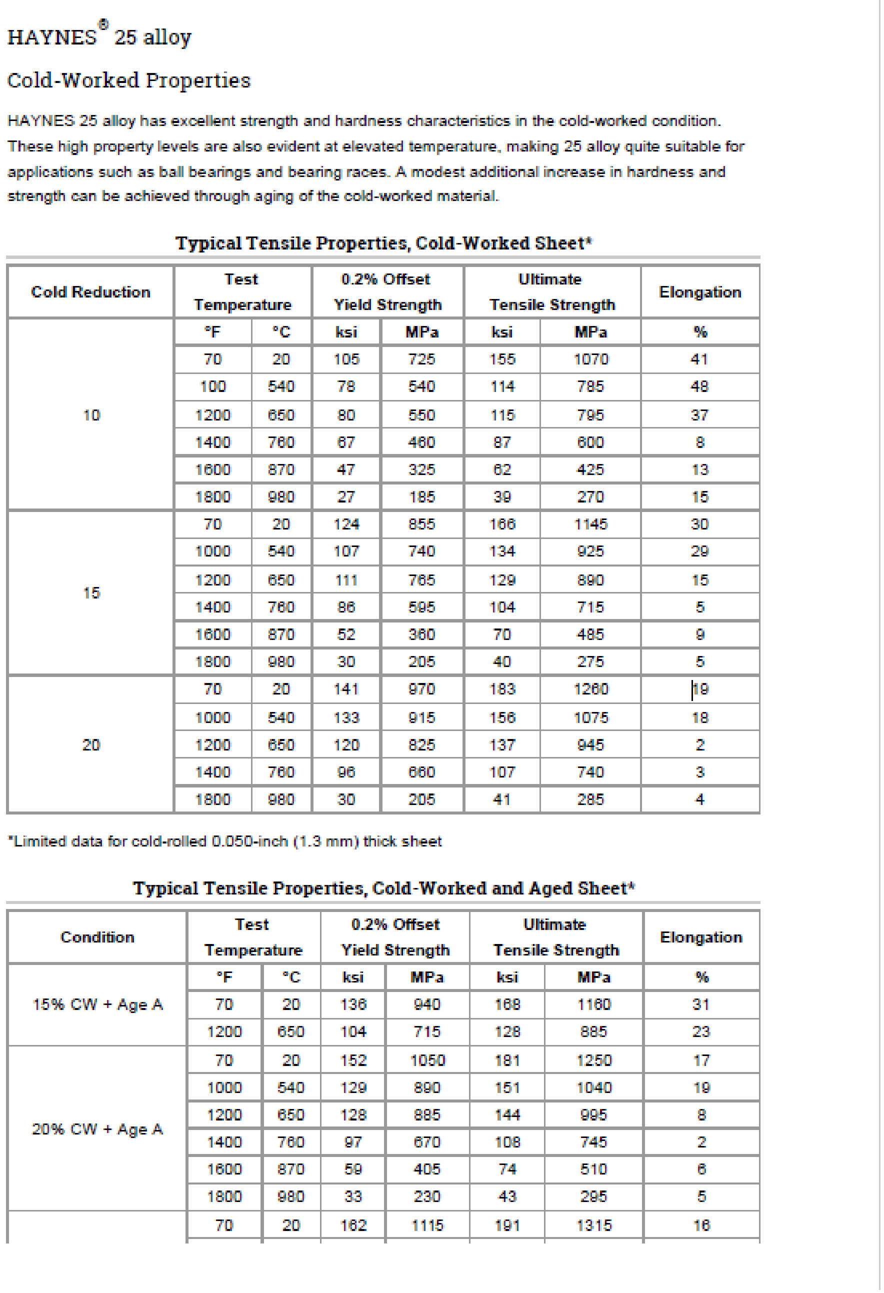

HAYNES® 25 alloy

Cold-Worked Properties

HAYNES 25 alloy has excellent strength and hardness characteristics in the cold-worked condition. These high property levels are also evident at elevated temperature, making 25 alloy quite suitable for applications such as ball bearings and bearing races. A modest additional increase in hardness and strength can be achieved through aging of the cold-worked material.

Typical Tensile Properties, Cold-Worked Sheet*

Cold Reduction	Test Temperature		0.2% Offset Yield Strength		Ultimate Tensile Strength		Elongation
	°F	°C	ksi	MPa	ksi	MPa	%
10	70	20	105	725	155	1070	41
	100	540	78	540	114	785	48
	1200	650	80	550	115	795	37
	1400	760	67	460	87	600	8
	1600	870	47	325	62	425	13
	1800	980	27	185	39	270	15
15	70	20	124	855	166	1145	30
	1000	540	107	740	134	925	29
	1200	650	111	765	129	890	15
	1400	760	86	595	104	715	5
	1600	870	52	360	70	485	9
	1800	980	30	205	40	275	5
20	70	20	141	970	183	1260	19
	1000	540	133	915	156	1075	18
	1200	650	120	825	137	945	2
	1400	760	96	660	107	740	3
	1800	980	30	205	41	285	4

*Limited data for cold-rolled 0.050-inch (1.3 mm) thick sheet

Typical Tensile Properties, Cold-Worked and Aged Sheet*

Condition	Test Temperature		0.2% Offset Yield Strength		Ultimate Tensile Strength		Elongation
	°F	°C	ksi	MPa	ksi	MPa	%
15% CW + Age A	70	20	136	940	168	1160	31
	1200	650	104	715	128	885	23
20% CW + Age A	70	20	152	1050	181	1250	17
	1000	540	129	890	151	1040	19
	1200	650	128	885	144	995	8
	1400	760	97	670	108	745	2
	1600	870	59	405	74	510	6
	1800	980	33	230	43	295	5
	70	20	162	1115	191	1315	16

20% CW + Age B	600	315	132	910	165	1140	28
	1000	540	124	855	149	1025	23
	1200	650	119	820	140	965	13
	1400	760	92	635	116	800	7
	1600	870	50	345	71	490	9
	1800	980	31	215	42	290	12

*Limited data for cold-rolled 0.050-inch (1.3 mm) thick sheet

Age A = 700°F (370°C)/1 hour

Age B = 1100°F (595°C)/2 hours

Typical Hardness at 70°F (20°C), Cold-Worked and Aged Sheet*

Cold-Work	**HRC, After Indicated Level of Cold Work and Subsequent Aging Treatment**		
	-	**900°F (480°C)**	**1100°F (595°C)**
%	**None**	**5 h**	**5 h**
None	24	25	25
5	31	33	31
10	37	39	39
15	40	44	43
20	44	44	47

*Limited data for cold-rolled 0.070-inch (1.8 mm) thick sheet

HRC = Hardness Rockwell "C".

Appendix C

Immersive etching method for Haynes 25

Chemicals:

HCL (32%), H2O2 (30%), Methanol (cleaning agent).

Equipment:

Dryer, fume hood, PPE

Method:

1. Immerse sample for a few seconds in a fume hood in a solution of 100 ml HCL (32%) and 5 ml H2O2 (30%).

2. Remove sample and rinse with water, followed by methanol. Place sample under dryer until it is thoroughly dry.

Result:

Haynes 25 cross section before etching (using SEM):

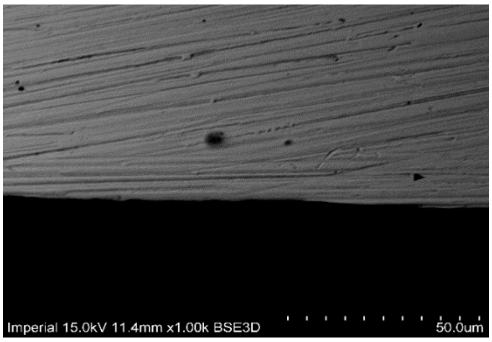

Haynes 25 cross section after etching (using optical microscope):

Appendix D

Patent document: RR2450

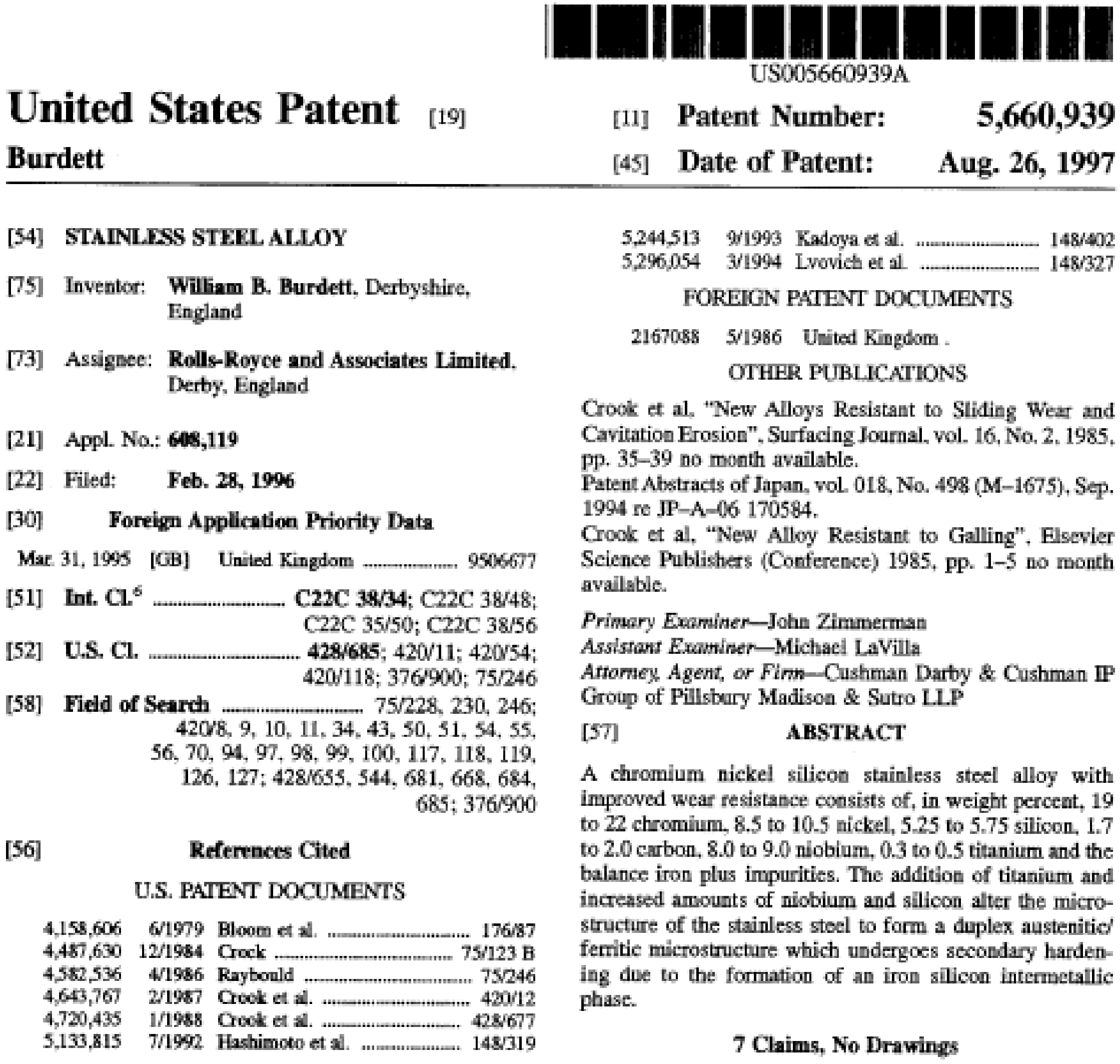

US005660939A

United States Patent [19]

Burdett

[11] **Patent Number: 5,660,939**

[45] **Date of Patent: Aug. 26, 1997**

[54] **STAINLESS STEEL ALLOY**

[75] Inventor: **William B. Burdett**, Derbyshire, England

[73] Assignee: **Rolls-Royce and Associates Limited**, Derby, England

[21] Appl. No.: **608,119**

[22] Filed: **Feb. 28, 1996**

[30] **Foreign Application Priority Data**

Mar. 31, 1995 [GB] United Kingdom 9506677

[51] **Int. Cl.^{6}** **C22C 38/34**; C22C 38/48; C22C 35/50; C22C 38/56

[52] **U.S. Cl.** **428/685**; 420/11; 420/54; 420/118; 376/900; 75/246

[58] **Field of Search** 75/228, 230, 246; 420/8, 9, 10, 11, 34, 43, 50, 51, 54, 55, 56, 70, 94, 97, 98, 99, 100, 117, 118, 119, 126, 127; 428/655, 544, 681, 668, 684, 685; 376/900

[56] **References Cited**

U.S. PATENT DOCUMENTS

4,158,606	6/1979	Bloom et al.	176/87
4,487,630	12/1984	Crock	75/123 B
4,582,536	4/1986	Raybould	75/246
4,643,767	2/1987	Crook et al.	420/12
4,720,435	1/1988	Crook et al.	428/677
5,133,815	7/1992	Hashimoto et al.	148/319
5,244,513	9/1993	Kadoya et al.	148/402
5,296,054	3/1994	Lvovich et al.	148/327

FOREIGN PATENT DOCUMENTS

2167088 5/1986 United Kingdom .

OTHER PUBLICATIONS

Crook et al, "New Alloys Resistant to Sliding Wear and Cavitation Erosion", Surfacing Journal, vol. 16, No. 2, 1985, pp. 35–39 no month available.

Patent Abstracts of Japan, vol. 018, No. 498 (M-1675), Sep. 1994 re JP-A-06 170584.

Crook et al, "New Alloy Resistant to Galling", Elsevier Science Publishers (Conference) 1985, pp. 1–5 no month available.

Primary Examiner—John Zimmerman
Assistant Examiner—Michael LaVilla
Attorney, Agent, or Firm—Cushman Darby & Cushman IP Group of Pillsbury Madison & Sutro LLP

[57] **ABSTRACT**

A chromium nickel silicon stainless steel alloy with improved wear resistance consists of, in weight percent, 19 to 22 chromium, 8.5 to 10.5 nickel, 5.25 to 5.75 silicon, 1.7 to 2.0 carbon, 8.0 to 9.0 niobium, 0.3 to 0.5 titanium and the balance iron plus impurities. The addition of titanium and increased amounts of niobium and silicon alter the microstructure of the stainless steel to form a duplex austenitic/ferritic microstructure which undergoes secondary hardening due to the formation of an iron silicon intermetallic phase.

7 Claims, No Drawings

STAINLESS STEEL ALLOY

FIELD OF THE INVENTION

The present invention relates to a stainless steel alloy and in particular relates to a chromium nickel silicon stainless steel alloy that is especially suited for use as components in nuclear reactors, particularly in the components used in the steam generating plant of nuclear reactors.

BACKGROUND OF THE INVENTION

Currently cobalt based alloys are used in the steam generating plant of nuclear reactors, but cobalt has a long half life making the use of cobalt undesirable for use in such applications. Some known iron base alloys have good wear properties, but insufficient corrosion resistance. Some known nickel base alloys have good corrosion resistance but poor wear resistance.

One known stainless steel potentially suitable for use in components of nuclear reactors is disclosed in UK patent 2167088, and this comprises broadly speaking 15 to less than 25 wt % chromium, 5 to 15 wt % nickel, 2.7 to 5.5 wt % silicon, 1 to 3 wt % carbon, 5 to 15 wt % niobium plus vanadium, up to 0.15 wt % nitrogen, up to 1.5 wt % cobalt and the balance iron plus impurities. This alloy contains very little or no cobalt thus having a low half life.

The particular stainless steel alloy available commercially from Deloro Stellite, St Louis, Mo. USA under the trade name Tristelle 5183, comprises in weight percent 19–22 chromium, 8.5 to 10.5 nickel, 4.5 to 5.5 silicon, 6.5 to 7.5 niobium, 1.8 to 2.2 carbon, up to 0.1 nitrogen and balance iron plus impurities.

The alloys suitable for use in steam generating plant of nuclear reactors must have high wear resistance and high corrosion resistance. The alloys disclosed in UK patent 2167088 have been tested and it has been found that they have a hardness of 350–450 Vickers (38–44 Rockwell C performed on a Rockwell hardness testing machine).

SUMMARY OF THE INVENTION

The present invention seeks to provide a stainless steel alloy suitable for use in nuclear reactors which has greater hardness than the known stainless steel alloys.

Accordingly, the present invention provides a stainless steel alloy consisting of, in weight percent, 15 to 25 chromium, 5 to 15 nickel, 2.7 to 6.0 silicon, 1 to 3 carbon, 5 to 15 niobium, 0.3 to 0.5 titanium and the balance iron plus impurities.

The most preferred stainless steel alloy consists of, in weight percent, 19 to 22 chromium, 8.5 to 10.5 nickel, 5.25 to 5.75 silicon, 1.7 to 2.0 carbon, 8.0 to 9.0 niobium, 0.3 to 0.5 titanium and the balance iron plus impurities.

Preferably the alloy is hot isostatically pressed.

The alloy may be used for making article or components or may be used for coating articles or components.

DETAILED DESCRIPTION OF THE INVENTION

The present invention will be more fully described by way of reference to the following example.

The basic commercially available stainless steel sold under the trade name Tristelle 5183 was modified principally by the deliberate addition of titanium to the stainless steel alloy, and further modified by increasing the amounts of niobium and silicon present in the stainless steel alloy. In particular the titanium was added such that the stainless steel alloy consisted of 0.3 to 0.5 weight percent titanium, the niobium was increased such that the stainless steel alloy consisted of 8.0 to 9.0 weight percent niobium and the silicon was increased such that the stainless steel alloy consisted of 5.25 to 5.75 weight percent silicon.

These controlled additions of titanium, niobium and silicon alter the structure of the stainless steel compared to that in the commercially available Tristelle 5183. The additions of titanium, niobium and silicon produce a duplex auszenitic/ferritic microstructure which undergoes secondary hardening due to the formation of an iron silicon intermetallic phase which has been identified by electron transmission spectroscopy. Further hardening as achievable by hot isostatic pressing (HIPPING) of the stainless steel alloy in powder form. The stainless steel alloy of the present invention creates a duplex microstructure within which secondary hardening occurs. The secondary hardening only occurs in the ferrite phase.

The actual stainless steel alloy consists of, in weight percent, 19–22 chromium, 8.5 to 10.5 nickel, 5.25 to 5.75 silicon, 1.7 to 2.0 carbon, 8.0 to 9.0 niobium, 0.3 to 0.5 titanium and the balance iron plus incidental impurities. The impurities may be up to 0.2 weight % cobalt, up to 0.5 weight % manganese, up to 0.3 weight % molybdenum, up to 0.03 weight % phosphor, up to 0.03 weight % sulphur, and up to 0.1 weight % nitrogen.

The stainless steel alloy of the present invention has been prepared and tested and it has been found that it has a hardness of 475–525 Vickers. Thus it can be seen that the stainless steel alloy of the present invention is considerably harder than those of the prior art, making the stainless steel alloys of the present invention more suitable for use in nuclear reactor steam generating plant, or other applications where high wear resistance is required.

The additions of titanium, niobium and silicon may also be applied to the broad stainless steel alloy range of UK patent no 2167088. The stainless steel alloy of the present invention may be used in the form of cast articles or components, in weldings or hard facing materials applied to articles or components, in wrought articles or components or in powder metallurgy articles or components.

I claim:

1. A stainless steel alloy consisting essentially of 19 to 22 percent by weight chromium, 8.5 to 10.5 percent by weight nickel, 5.25 to 5.75 percent by weight silicon, 1.7 to 2.0 percent by weight carbon, 8.0 to 9.0 percent by weight niobium, 0.3 to 0.5 percent by weight titanium and the balance iron.

2. A stainless steel alloy as claimed in claim **1** wherein the alloy has been hot isostatically pressed.

3. An article comprising a stainless steel alloy as claimed in claim **1**.

4. An article having a coating comprising a stainless steel alloy as claimed in claim **1**.

5. An article as claimed in claim **3** wherein the article is selected from the group comprising a cast article, a wrought article and a powder metallurgy article.

6. An article as claimed in claim **4** wherein the coating is selected from the group comprising a hard facing and a welding.

7. A steam generating plant having at least one component comprising a wear resistant stainless steel consisting essentially of 19 to 22 percent by weight chromium, 8.5 to 10.5 percent by weight nickel, 5.25 to 5.75 percent by weight silicon, 1.7 to 2.0 percent by weight carbon, 8.0 to 9.0 percent by weight niobium, 0.3 to 0.5 percent by weight titanium and the balance iron.

* * * * *

Appendix E

Datasheet: Cronidur 30

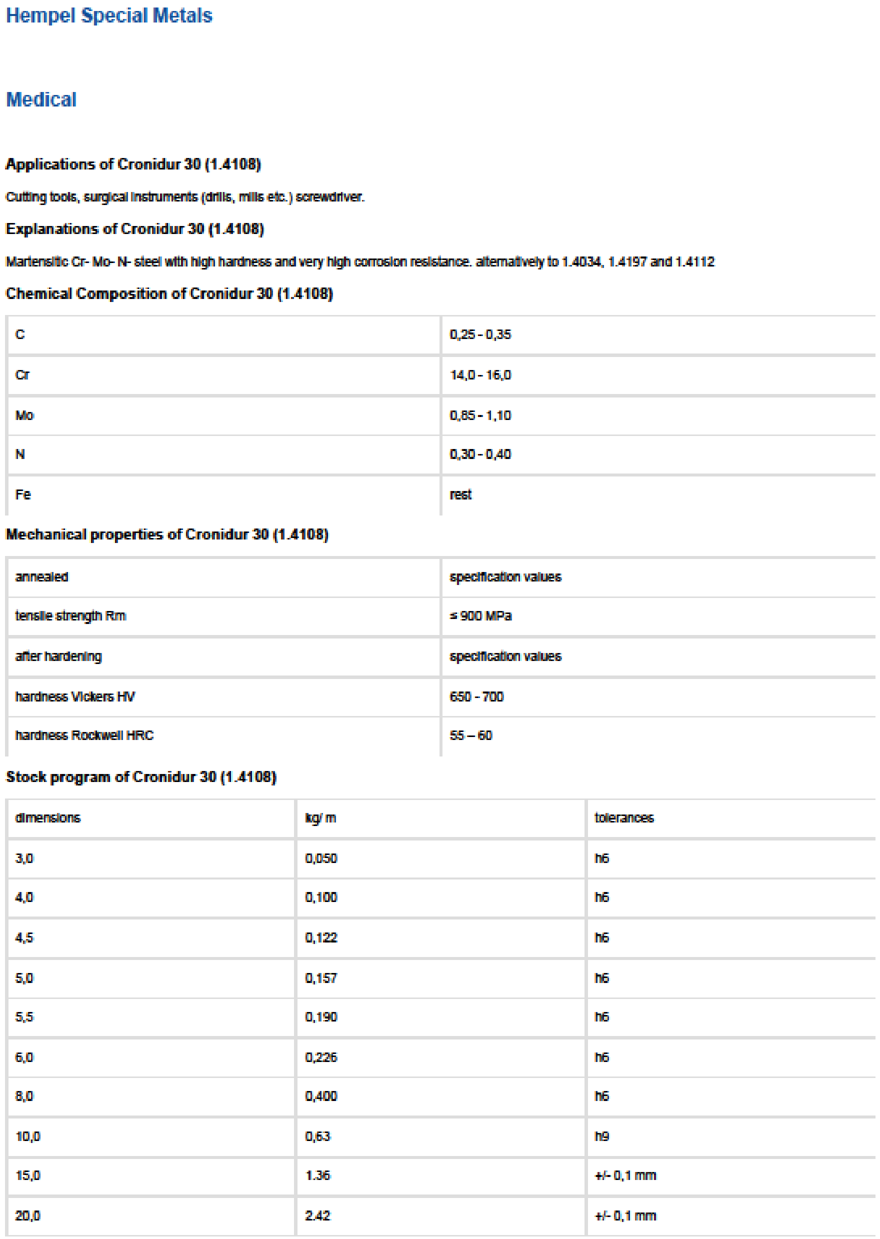

Hempel Special Metals

Medical

Applications of Cronidur 30 (1.4108)

Cutting tools, surgical instruments (drills, mills etc.) screwdriver.

Explanations of Cronidur 30 (1.4108)

Martensitic Cr- Mo- N- steel with high hardness and very high corrosion resistance. alternatively to 1.4034, 1.4197 and 1.4112

Chemical Composition of Cronidur 30 (1.4108)

C	0,25 - 0,35
Cr	14,0 - 16,0
Mo	0,85 - 1,10
N	0,30 - 0,40
Fe	rest

Mechanical properties of Cronidur 30 (1.4108)

annealed	specification values
tensile strength Rm	≤ 900 MPa
after hardening	specification values
hardness Vickers HV	650 - 700
hardness Rockwell HRC	55 – 60

Stock program of Cronidur 30 (1.4108)

dimensions	kg/ m	tolerances
3,0	0,050	h6
4,0	0,100	h6
4,5	0,122	h6
5,0	0,157	h6
5,5	0,190	h6
6,0	0,226	h6
8,0	0,400	h6
10,0	0,63	h9
15,0	1.36	+/- 0,1 mm
20,0	2.42	+/- 0,1 mm

Appendix F

Ball wear – UMESHMOTION subroutine

```fortran
      SUBROUTINE UMESHMOTION(UREF,ULOCAL,NODE,NNDOF,
     *    LNODETYPE,ALOCAL,NDIM,TIME,DTIME,PNEWDT,
     *    KSTEP,KINC,KMESHSWEEP,JMATYP,JGVBLOCK,LSMOOTH)

      INCLUDE 'ABA_PARAM.INC'

      DIMENSION ULOCAL(NDIM)
      PARAMETER (NELEMMAX=1000)
      DIMENSION JELEMLIST(NELEMMAX),JELEMTYPE(NELEMMAX)
      DIMENSION ALOCAL(NDIM,*),TIME(2)
      DIMENSION JMATYP(*),JGVBLOCK(*)
      DIMENSION ARRAY1(15)
      DIMENSION ARRAY2(20)
      DIMENSION STORE(2)
      REAL*8    CPRESS, DIST, CIRC


cccccccccccccccccccccccccccccccccccccccccccccccccccccccccccccccccccccccccccccccccccccc
cccccccc
         REAL  CPRESSA,DTIMEA,SUM,AVE,J,TIMEA
         INTEGER STEPA, INCA, NODEA,I,FLAG,K,N

      OPEN (UNIT=509,FILE='/home/rm5314/ball_ten/dipl.dat')

      OPEN (UNIT=511,FILE='/home/rm5314/ball_ten/data4ave_long1.dat')
      OPEN (UNIT=512,FILE='/home/rm5314/ball_ten/data4ave_long2.dat')
      OPEN (UNIT=513,FILE='/home/rm5314/ball_ten/data4ave_long3.dat')
      OPEN (UNIT=514,FILE='/home/rm5314/ball_tendata4ave_long4.dat')
      OPEN (UNIT=515,FILE='/home/rm5314/ball_ten/data4ave_long5.dat')
      OPEN (UNIT=516,FILE='/home/rm5314/ball_ten/data4ave_long6.dat')
      OPEN (UNIT=517,FILE='/home/rm5314/ball_ten/data4ave_long7.dat')
      OPEN (UNIT=518,FILE='/home/rm5314/ball_ten/data4ave_long8.dat')
      OPEN (UNIT=519,FILE='/home/rm5314/ball_ten/data4ave_long9.dat')
      OPEN (UNIT=520,FILE='/home/rm5314/ball_ten/data4ave_long10.dat')


         OPEN (UNIT=500,FILE='/home/rm5314/ball_ten/debug.dat')



ccccc set parametres in umeshmotion
      JTYP=0
      NELEMS = NELEMMAX
ccccc call functions in umeshmotion
      CALL GETVRN(NODE,'COORD',ARRAY1,JRCD,JGVBLOCK,LTRN)
         CALL GETNODETOELEMCONN(NODE,NELEMS,JELEMLIST,JELEMTYPE,
     1 JRCD,JGVBLOCK)
         CALL GETVRMAVGATNODE(NODE,JTYP,'CSTRESS',ARRAY2,JRCD,
     1 JELEMLIST,NELEMS,JMATYP,JGVBLOCK)

ccccc                  store the data for averaging
cccccccccccccccccccccccccccccccccccccccccc
        DIST=ARRAY1(1)**2 + (ARRAY1(2)-5)**2
        CIRC= SQRT(DIST)
      IF   ((ARRAY1(2).LE.0.280).AND.
     1    ((CIRC-5).LE.0.01).and.(KMESHSWEEP.EQ.1)) THEN
            CPRESS = ARRAY2(1)
            IF (CPRESS.NE.0)THEN
```

```
                     DO K=1,50
                            IF ((TIME(2).GE.(1+K+0.001)).AND.
     1                      (TIME(2).LE.(K+2-0.001))) THEN
c                                  N=MOD(K,10)
                                   WRITE
(UNIT=(510+K),FMT='(I3,I6,I6,F18.8,F10.4,F20.14)')
     1                      KSTEP,KINC,NODE,CPRESS,DTIME,TIME(2)
                                   EXIT
                            ENDIF
                     ENDDO
              ENDIF
c             WRITE (500,*) (510+N)

         ENDIF
ccccc                   calculate average and move
ccccccccccccccccccccccccccccccccccccccccccccc
      IF  ((ARRAY1(2).LE.0.280).AND.
     1    ((CIRC-5).LE.0.001)) THEN
              SUM=ARRAY2(1)*DTIME
              J=DTIME
              DO K=1,50

                     IF ((TIME(2).LT.(K+2+0.001)).AND.
     1               (TIME(2).GT.(K+2-0.001))) THEN
c                           N=MOD(K,10)
                            WRITE(500,*) TIME(2), KINC
                            REWIND ((510+K))
                            DO I=1,10000
                                   READ (UNIT=(510+K),FMT=*,IOSTAT=FLAG)
     1                      STEPA, INCA, NODEA,CPRESSA,DTIMEA,TIMEA

                                   IF (FLAG.LT.0) THEN
                                          WRITE(500,*) 'end',FLAG
c                                         CLOSE ((510+N),STATUS='delete')
                                          EXIT
                                   ELSEIF (NODE.EQ.NODEA) THEN
                                          SUM=SUM+CPRESSA*DTIMEA
                                          J=J+DTIMEA
                                   ENDIF
                            ENDDO

                            IF ((J.NE.0).AND.(SUM.NE.0)) THEN
                                   AVE=SUM/J
                            ELSE
                                   AVE=0
                            ENDIF

ccccc move the node and record the displ of the nodes
                            ULOCAL(2)=ULOCAL(2)-3*0.00000001308646*AVE
                            WRITE(509,'(I5,F14.8,F14.8,I7,I7)')
     1               NODE,ULOCAL(2),AVE,KINC,KMESHSWEEP
                            EXIT

                     ENDIF
              ENDDO
         ENDIF
         ULOCAL(1)=0
      LSMOOTH=1

         RETURN
         END
```

Appendix G

Disc wear – UMESHMOTION subroutine

```
      SUBROUTINE UMESHMOTION(UREF,ULOCAL,NODE,NNDOF,
     *    LNODETYPE,ALOCAL,NDIM,TIME,DTIME,PNEWDT,
     *    KSTEP,KINC,KMESHSWEEP,JMATYP,JGVBLOCK,LSMOOTH)

      INCLUDE 'ABA_PARAM.INC'

      DIMENSION ULOCAL(NDIM)
      PARAMETER (NELEMMAX=1000)
      DIMENSION JELEMLIST(NELEMMAX),JELEMTYPE(NELEMMAX)
      DIMENSION ALOCAL(NDIM,*),TIME(2)
      DIMENSION JMATYP(*),JGVBLOCK(*)
      DIMENSION ARRAY1(15)
      DIMENSION ARRAY2(20)
      DIMENSION STORE(2)
      REAL*8    CPRESS

cccccccccccccccccccccccccccccccccccccccccccccccccccccccccccccccccccccccccccccccccccccc
cccccccc
         REAL  CPRESSA,DTIMEA,SUM,AVE,J,TIMEA
         INTEGER STEPA, INCA, NODEA,I,FLAG,K,N

      OPEN (UNIT=509,FILE='/home/rm5314/c50_0.1/dipl.dat')

      OPEN (UNIT=511,FILE='/home/rm5314/c50_0.1/data4ave_long1.dat')
      OPEN (UNIT=512,FILE='/home/rm5314/c50_0.1/data4ave_long2.dat')
      OPEN (UNIT=513,FILE='/home/rm5314/c50_0.1/data4ave_long3.dat')
      OPEN (UNIT=514,FILE='/home/rm5314/c50_0.1/data4ave_long4.dat')
      OPEN (UNIT=515,FILE='/home/rm5314/c50_0.1/data4ave_long5.dat')
      OPEN (UNIT=516,FILE='/home/rm5314/c50_0.1/data4ave_long6.dat')
      OPEN (UNIT=517,FILE='/home/rm5314/c50_0.1/data4ave_long7.dat')
      OPEN (UNIT=518,FILE='/home/rm5314/c50_0.1/data4ave_long8.dat')
      OPEN (UNIT=519,FILE='/home/rm5314/c50_0.1/data4ave_long9.dat')
      OPEN (UNIT=520,FILE='/home/rm5314/c50_0.1/data4ave_long10.dat')


         OPEN (UNIT=500,FILE='/home/rm5314/c50_0.1/debug.dat')



ccccc set parametres in umeshmotion
      JTYP=0
      NELEMS = NELEMMAX
ccccc call functions in umeshmotion
      CALL GETVRN(NODE,'COORD',ARRAY1,JRCD,JGVBLOCK,LTRN)
         CALL GETNODETOELEMCONN(NODE,NELEMS,JELEMLIST,JELEMTYPE,
     1 JRCD,JGVBLOCK)
         CALL GETVRMAVGATNODE(NODE,JTYP,'CSTRESS',ARRAY2,JRCD,
     1 JELEMLIST,NELEMS,JMATYP,JGVBLOCK)

ccccc                  store the data for averaging
ccccccccccccccccccccccccccccccccccccccccc
         IF ((ARRAY1(2).GE.-12.81).AND.(ARRAY1(1).GT.-2.5).AND.
     1(ARRAY1(1).LT.-0.4).AND.(KMESHSWEEP.EQ.1)) THEN
              CPRESS = ARRAY2(1)
              IF (CPRESS.NE.0)THEN
                     DO K=1,50
                            IF ((TIME(2).GE.(1+K+0.001)).AND.
```

```
     1                      (TIME(2).LE.(K+2-0.001))) THEN
c                                  N=MOD(K,10)
                                   WRITE
(UNIT=(510+K),FMT='(I3,I6,I6,F18.8,F10.4,F20.14)')
     1                      KSTEP,KINC,NODE,CPRESS,DTIME,TIME(2)
                                   EXIT
                            ENDIF
                     ENDDO
              ENDIF
c             WRITE (500,*) (510+N)

         ENDIF
ccccc                   calculate average and move
ccccccccccccccccccccccccccccccccccccccccccccc

         IF ((ARRAY1(2).GE.-12.81).AND.(ARRAY1(1).GT.-2.5).AND.
     1 (ARRAY1(1).LT.0.4)) THEN
              SUM=ARRAY2(1)*DTIME
              J=DTIME
              DO K=1,50

                     IF ((TIME(2).LT.(K+2+0.001)).AND.
     1               (TIME(2).GT.(K+2-0.001))) THEN
c                           N=MOD(K,10)
                            WRITE(500,*) TIME(2), KINC
                            REWIND ((510+K))
                            DO I=1,10000
                                   READ (UNIT=(510+K),FMT=*,IOSTAT=FLAG)
     1                      STEPA, INCA, NODEA,CPRESSA,DTIMEA,TIMEA

                                   IF (FLAG.LT.0) THEN
                                          WRITE(500,*) 'end',FLAG
c                                         CLOSE ((510+N),STATUS='delete')
                                          EXIT
                                   ELSEIF (NODE.EQ.NODEA) THEN
                                          SUM=SUM+CPRESSA*DTIMEA
                                          J=J+DTIMEA
                                   ENDIF
                            ENDDO

                            IF ((J.NE.0).AND.(SUM.NE.0)) THEN
                                   AVE=SUM/J
                            ELSE
                                   AVE=0
                            ENDIF

ccccc move the node and record the displ of the nodes
                            ULOCAL(2)=ULOCAL(2)-10*0.00000001308646*AVE
                            WRITE(509,'(I5,F14.8,F14.8,I7,I7)')
     1               NODE,ULOCAL(2),AVE,KINC,KMESHSWEEP
                            EXIT

                     ENDIF
              ENDDO
         ENDIF
         ULOCAL(1)=0
      LSMOOTH=1

         RETURN
         END
```

Appendix H

Oxide growth only UMESHMOTION SUBROUTINE

```
      SUBROUTINE UMESHMOTION(UREF,ULOCAL,NODE,NNDOF,
     *    LNODETYPE,ALOCAL,NDIM,TIME,DTIME,PNEWDT,
     *    KSTEP,KINC,KMESHSWEEP,JMATYP,JGVBLOCK,LSMOOTH)

      INCLUDE 'ABA_PARAM.INC'

      DIMENSION ULOCAL(NDIM)
      PARAMETER (NELEMMAX=1000)
      DIMENSION JELEMLIST(NELEMMAX),JELEMTYPE(NELEMMAX)
      DIMENSION ALOCAL(NDIM,*),TIME(2)
      DIMENSION JMATYP(*),JGVBLOCK(*)
      DIMENSION ARRAY1(15)
      DIMENSION ARRAY2(20)
      DIMENSION STORE(2)
      REAL*8     CPRESS, OXIDE

cccccccccccccccccccccccccccccccccccccccccccccccccccccccccccccccccccccccccccccccccccccc
cccccccc
         REAL  CPRESSA,DTIMEA,SUM,AVE,J,TIMEA
         INTEGER STEPA, INCA, NODEA,I,FLAG,K,N

      OPEN (UNIT=509,FILE='/home/rm5314/arh_only/dipl.dat')

      OPEN (UNIT=511,FILE='/home/rm5314/arh_only/data4ave_long1.dat')
      OPEN (UNIT=512,FILE='/home/rm5314/arh_only/data4ave_long2.dat')
      OPEN (UNIT=513,FILE='/home/rm5314/arh_only/data4ave_long3.dat')
      OPEN (UNIT=514,FILE='/home/rm5314/arh_only/data4ave_long4.dat')
      OPEN (UNIT=515,FILE='/home/rm5314/arh_only/data4ave_long5.dat')
      OPEN (UNIT=516,FILE='/home/rm5314/arh_only/data4ave_long6.dat')
      OPEN (UNIT=517,FILE='/home/rm5314/arh_only/data4ave_long7.dat')
      OPEN (UNIT=518,FILE='/home/rm5314/arh_only/data4ave_long8.dat')
      OPEN (UNIT=519,FILE='/home/rm5314/arh_only/data4ave_long9.dat')
      OPEN (UNIT=520,FILE='/home/rm5314/arh_only/data4ave_long10.dat')


         OPEN (UNIT=500,FILE='/home/rm5314/arh_only/debug.dat')



ccccc set parametres in umeshmotion
      JTYP=0
      NELEMS = NELEMMAX
ccccc call functions in umeshmotion
      CALL GETVRN(NODE,'COORD',ARRAY1,JRCD,JGVBLOCK,LTRN)
         CALL GETNODETOELEMCONN(NODE,NELEMS,JELEMLIST,JELEMTYPE,
     1 JRCD,JGVBLOCK)
         CALL GETVRMAVGATNODE(NODE,JTYP,'CSTRESS',ARRAY2,JRCD,
     1 JELEMLIST,NELEMS,JMATYP,JGVBLOCK)

ccccc                  store the data for averaging
ccccccccccccccccccccccccccccccccccccccccc
      IF ((ARRAY1(2).GE.-12.81).AND.(ARRAY1(1).GT.-31.3).AND.
     1(ARRAY1(1).LT.28.5).AND.(KMESHSWEEP.EQ.1)) THEN
              CPRESS = ARRAY2(1)
              IF (CPRESS.NE.0)THEN
                     DO K=1,50
                            IF ((TIME(2).GE.(1+K+0.001)).AND.
     1                      (TIME(2).LE.(K+2-0.001))) THEN
```

```
c                                  N=MOD(K,10)
                                   WRITE
(UNIT=(510+K),FMT='(I3,I6,I6,F18.8,F10.4,F20.14)')
     1                      KSTEP,KINC,NODE,CPRESS,DTIME,TIME(2)
                                   EXIT
                            ENDIF
                     ENDDO
              ENDIF
c             WRITE (500,*) (510+N)

         ENDIF
ccccc                   calculate average and move
ccccccccccccccccccccccccccccccccccccccccccccc
      OXIDE =  0.000000001*LOG(TIME(2)) + 0.000000005
         IF ((ARRAY1(2).GE.-12.81).AND.(ARRAY1(1).GT.-31.3).AND.
     1 (ARRAY1(1).LT.28.5)) THEN
              SUM=ARRAY2(1)*DTIME
              J=DTIME
              DO K=1,50

                     IF ((TIME(2).LT.(K+2+0.001)).AND.
     1               (TIME(2).GT.(K+2-0.001))) THEN
c                           N=MOD(K,10)
                            WRITE(500,*) TIME(2), KINC
                            REWIND ((510+K))
                            DO I=1,10000
                                   READ (UNIT=(510+K),FMT=*,IOSTAT=FLAG)
     1                      STEPA, INCA, NODEA,CPRESSA,DTIMEA,TIMEA

                                   IF (FLAG.LT.0) THEN
                                          WRITE(500,*) 'end',FLAG
c                                         CLOSE ((510+N),STATUS='delete')
                                          EXIT
                                   ELSEIF (NODE.EQ.NODEA) THEN
                                          SUM=SUM+CPRESSA*DTIMEA
                                          J=J+DTIMEA
                                   ENDIF
                            ENDDO

                            IF ((J.NE.0).AND.(SUM.NE.0)) THEN
                                   AVE=SUM/J
                            ELSE
                                   AVE=0
                            ENDIF

ccccc move the node and record the displ of the nodes
                IF (AVE.GT.0) THEN
                  ULOCAL(2)=ULOCAL(2)
                  WRITE(509,'(I5,F14.8,F14.8,I7,I7)')
     1            NODE,ULOCAL(2),AVE,KINC,KMESHSWEEP
                  EXIT
                ELSEIF (AVE.EQ.0) THEN
                  ULOCAL(2)=ULOCAL(2)+ OXIDE
                ENDIF
                     ENDIF
              ENDDO
         ENDIF
         ULOCAL(1)=0
      LSMOOTH=1

         RETURN
         END
```

Appendix I

Combined wear UMESHMOTION subroutine – latent periods

```
      SUBROUTINE UMESHMOTION(UREF,ULOCAL,NODE,NNDOF,
     *    LNODETYPE,ALOCAL,NDIM,TIME,DTIME,PNEWDT,
     *    KSTEP,KINC,KMESHSWEEP,JMATYP,JGVBLOCK,LSMOOTH)

      INCLUDE 'ABA_PARAM.INC'

      DIMENSION ULOCAL(NDIM)
      PARAMETER (NELEMMAX=1000)
      DIMENSION JELEMLIST(NELEMMAX),JELEMTYPE(NELEMMAX)
      DIMENSION ALOCAL(NDIM,*),TIME(2)
      DIMENSION JMATYP(*),JGVBLOCK(*)
      DIMENSION ARRAY1(15)
      DIMENSION ARRAY2(20)
      DIMENSION STORE(2)
      REAL*8    CPRESS, OXIDE

cccccccccccccccccccccccccccccccccccccccccccccccccccccccccccccccccccccccccccccccccccccc
cccccccc
         REAL  CPRESSA,DTIMEA,SUM,AVE,J,TIMEA
         INTEGER STEPA, INCA, NODEA,I,FLAG,K,N

      OPEN (UNIT=509,FILE='/home/rm5314/M2_50/dipl.dat')

      OPEN (UNIT=511,FILE='/home/rm5314/M2_50/data4ave_long1.dat')
      OPEN (UNIT=512,FILE='/home/rm5314/M2_50/data4ave_long2.dat')
      OPEN (UNIT=513,FILE='/home/rm5314/M2_50/data4ave_long3.dat')
      OPEN (UNIT=514,FILE='/home/rm5314/M2_50/data4ave_long4.dat')
      OPEN (UNIT=515,FILE='/home/rm5314/M2_50/data4ave_long5.dat')
      OPEN (UNIT=516,FILE='/home/rm5314/M2_50/data4ave_long6.dat')
      OPEN (UNIT=517,FILE='/home/rm5314/M2_50/data4ave_long7.dat')
      OPEN (UNIT=518,FILE='/home/rm5314/M2_50/data4ave_long8.dat')
      OPEN (UNIT=519,FILE='/home/rm5314/M2_50/data4ave_long9.dat')
      OPEN (UNIT=520,FILE='/home/rm5314/M2_50/data4ave_long10.dat')


         OPEN (UNIT=500,FILE='/home/rm5314/M2_50/debug.dat')



ccccc set parametres in umeshmotion
      JTYP=0
      NELEMS = NELEMMAX
ccccc call functions in umeshmotion
      CALL GETVRN(NODE,'COORD',ARRAY1,JRCD,JGVBLOCK,LTRN)
         CALL GETNODETOELEMCONN(NODE,NELEMS,JELEMLIST,JELEMTYPE,
     1 JRCD,JGVBLOCK)
         CALL GETVRMAVGATNODE(NODE,JTYP,'CSTRESS',ARRAY2,JRCD,
     1 JELEMLIST,NELEMS,JMATYP,JGVBLOCK)

ccccc                  store the data for averaging
ccccccccccccccccccccccccccccccccccccccccc
         IF ((ARRAY1(2).GE.-12.81).AND.(ARRAY1(1).GT.-31.3).AND.
     1(ARRAY1(1).LT.28.5).AND.(KMESHSWEEP.EQ.1)) THEN
              CPRESS = ARRAY2(1)
              IF (CPRESS.NE.0)THEN
                     DO K=1,50
                            IF ((TIME(2).GE.(1+K+0.001)).AND.
     1                      (TIME(2).LE.(K+2-0.001))) THEN
```

```
c                                  N=MOD(K,10)
                                   WRITE
(UNIT=(510+K),FMT='(I3,I6,I6,F18.8,F10.4,F20.14)')
     1                      KSTEP,KINC,NODE,CPRESS,DTIME,TIME(2)
                                   EXIT
                            ENDIF
                     ENDDO
              ENDIF
c             WRITE (500,*) (510+N)

         ENDIF
ccccc                   calculate average and move
ccccccccccccccccccccccccccccccccccccccccccccc

         IF ((ARRAY1(2).GE.-12.81).AND.(ARRAY1(1).GT.-31.3).AND.
     1 (ARRAY1(1).LT.28.5)) THEN
              SUM=ARRAY2(1)*DTIME
              J=DTIME
              DO K=1,50

                     IF ((TIME(2).LT.(K+2+0.001)).AND.
     1               (TIME(2).GT.(K+2-0.001))) THEN
c                           N=MOD(K,10)
                            WRITE(500,*) TIME(2), KINC
                            REWIND ((510+K))
                            DO I=1,10000
                                   READ (UNIT=(510+K),FMT=*,IOSTAT=FLAG)
     1                      STEPA, INCA, NODEA,CPRESSA,DTIMEA,TIMEA

                                   IF (FLAG.LT.0) THEN
                                          WRITE(500,*) 'end',FLAG
c                                         CLOSE ((510+N),STATUS='delete')
                                          EXIT
                                   ELSEIF (NODE.EQ.NODEA) THEN
                                          SUM=SUM+CPRESSA*DTIMEA
                                          J=J+DTIMEA
                                   ENDIF
                            ENDDO

                            IF ((J.NE.0).AND.(SUM.NE.0)) THEN
                                   AVE=SUM/J
                            ELSE
                                   AVE=0
                            ENDIF

ccccc move the node and record the displ of the nodes
                              IF (AVE.GT.0) THEN
                  ULOCAL(2)=ULOCAL(2)-10*0.00000001308646*AVE
                  WRITE(509,'(I5,F14.8,F14.8,I7,I7)')
     1            NODE,ULOCAL(2),AVE,KINC,KMESHSWEEP
                  EXIT
                ELSEIF (AVE.EQ.0) THEN
                                     ULOCAL(2)=ULOCAL(2)+0.0000658
                ENDIF
                     ENDIF
              ENDDO
         ENDIF
         ULOCAL(1)=0
      LSMOOTH=1

         RETURN
         END
```